UNIVERSITÉ DE MONTRÉAL

TOWARD COLD ATOM GUIDANCE IN A HOLLOW-CORE PHOTONIC CRYSTAL FIBRE USING A BLUE DETUNED HOLLOW LASER BEAM

JÉRÔME POULIN

DÉPARTEMENT DE GÉNIE PHYSIQUE

ÉCOLE POLYTECHNIQUE DE MONTRÉAL

THÈSE PRÉSENTÉE EN VUE DE L'OBTENTION

DU DIPLÔME DE PHILOSOPHIÆ DOCTOR

(GÉNIE PHYSIQUE)

SEPTEMBRE 2015

UNIVERSITÉ DE MONTRÉAL

ÉCOLE POLYTECHNIQUE DE MONTRÉAL

Cette thèse intitulée:

TOWARD COLD ATOM GUIDANCE IN A HOLLOW-CORE PHOTONIC CRYSTAL FIBRE USING A BLUE DETUNED HOLLOW LASER BEAM

présentée par: POULIN Jérôme
en vue de l'obtention du diplôme de: Philosophiæ Doctor
a été dûment acceptée par le jury d'examen constitué de:

M. TEYSSEDOU Alberto, Ph. D., président
M. KASHYAP Raman, Ph. D., membre et directeur de recherche
M. LUITEN Andre N., Ph. D., membre et codirecteur de recherche
M. DUBÉ Pierre, Ph. D., membre
M. KAISER Robin, Doctorat, membre externe

UNIVERSITÉ DE MONTRÉAL

ÉCOLE POLYTECHNIQUE DE MONTRÉAL

TOWARD COLD ATOM GUIDANCE IN A HOLLOW-CORE PHOTONIC CRYSTAL FIBRE USING A BLUE DETUNED HOLLOW LASER BEAM

Submitted to

Département de Génie Physique

École Polytechnique de Montréal

in Partial Fulfillment of the Requirements

for the Degree of Doctor of Philosophy

for successful completion of the co-supervised dissertation with

The University of Western Australia

by

JÉRÔME POULIN

September 2015

DEDICATION

I dedicate this Thesis to Sarah, for her support and encouragements through every step.

Je dédie cette thèse à Sarah, pour son inestimable support et de m'avoir accompagné à chacune des étapes.

ACKNOWLEDMENTS

This work would not have been possible without the help and support from a large number of people encountered at Polytechnique Montreal, The University of Western Australia and The University of Sydney. This was truly an international effort from the beginning!

First and foremost, I would like to thank my supervisor Raman Kashyap for his incredible support, for his enthusiasm toward my projects and his faith in my capabilities. Your presence and advice were always a beacon and guidance in the troubled waters of learning scientific research and accomplishing an international level PhD.

I deeply acknowledge my supervisor Andre Luiten involvement in my project from the beginning. I admire his edge to always push me into getting more precise answers and going to the bottom of things. The level of exigence he would set for me always paid off when I was able to answer his questions from the full-scale model to an amazingly simplified but accurate model... and making both agree together. He would just say: "Physics works!" and I will always remember that.

Without the implication of my co-supervisor Philip Light, this project would have been experimentally impossible. The complexity of building a Magneto-Optical Trap and laser guiding of atoms from an empty optical table would have been impossible on my own. His amazing technical and computing skills made everything possible! I admire his determination, his patience after multiple failures to always try to find a solution even when that solution meant taking two steps back and adding even more complexity into our work. We made a good team!

I would like to deeply thank Prof. Maryanne C.J. Large at the University of Sydney for supervising me in the science and art of fabricating and characterising hollow core photonic crystal fibers. She was also an extraordinary support in challenging times and her friendship and sense of humor proved invaluable in my discovery of Australian culture and way of life.

I would also like to thank all the mPOF group at the Australian Technology Park and USyd: Alex, Sergio, Anna, Xin, Simon Fleming, Leon Poladian, Boris Khulmey and Geoff "goff I would say" Barton. Special Thanks to Richard Lwin for welcoming me in his home and for being such a good friend!

I would like to also thank the entire FSM group at UWA: Gar-wing, Jimmy, Sascha, Keal, Fred, Weng, Chris, Dan, Dustin, Jean-Michel and many others who were there for shorter periods. I will always remember our Friday evenings drinking beer on top of the Physics building! Perfect relaxation not too far away from our experiments, haha!

Additionally, I have had a great chance to be part of the APCL group and would like to thank all of them for making me feel part of the group even though I was far away most of the time! Thanks to Mathieu, Jerome, Aissa, Elton, Sebastien, Meenu, Victor, Tahereh, Ameneh, Mamoun, Galina and from the earlier days, Yannick and Lutfu.

I am grateful for the support of all the schools officials who supported me and my co-tutelle Canada-Australia. Thanks to Alan Dench and Jean Dansereau for finally making this possible. Special thanks to Lyne Dénommée and Paul Abbott for being so comprehensive and working through the hurdles of this collaboration.

Finally, I would like to thank my family for being so comprehensive and supportive with the distance and especially my partner in life Sarah for her incredible sacrifice and everything she endured so I can realize my dreams and achieve my potential. I will never forget and be eternally grateful. I can never thank you enough!

RÉSUMÉ

Cette thèse décrit les progrès et techniques réalisées pour obtenir un couplage efficace d'atomes froids ^{85}Rb dans une fibre optique en cristaux photonique à coeur vide et utilisant un guidage atomique à l'aide d'un faisceau laser creux de premier ordre décalé en fréquence vers le bleu. Dans le système proposé, la faible diffraction de ce faisceau de premier ordre lui permet d'agir comme un entonnoir optique à potentiel répulsif servant à guider les atomes froids, avec l'aide de la gravité, dans le coeur de la fibre optique. L'utilisation d'une fibre optique à faible perte, plutôt qu'un capillaire permet de développer le potentiel de guider les atomes sur une trajectoire arbitraire et des distances à l'échelle du laboratoire. Ceci permettrait ainsi plusieurs nouvelles applications en nanofabrication et en métrologie optique.

Pour réaliser cet objectif, un piège Magnéto-Optique de ^{85}Rb a été bâtit de zéro et en utilisant les techniques les plus avancées de refroidissement laser par gradient de polarisation a permis d'atteindre régulièrement des températures de 9 μK dans une mélasse optique contenant 10^7 atomes. Ces atomes froids furent guidés au-delà de 23 cm dans un faisceau creux collimé et décalé vers le bleu et au travers de ce faisceau focalisé de manière à reproduire les conditions d'entrée dans une fibre optique tout en permettant une observation précise des dynamiques de couplage. Trois classes d'atomes furent observées : perdus, piégés et guidés. Les dynamiques de ce système ainsi que les conditions optimales de couplage ont été identifiés grâce au modèle physique numérique ayant été développé.

Une nouvelle approche au problème de la modélisation de la dynamique des atomes froids dans l'entonnoir optique a été développée au cours de cette thèse. Ce nouveau modèle a permis de reproduire la dynamique des atomes observés dans l'expérience mais a aussi pu être appliqué dans la simulation d'atomes froids dans le piège Magnéto-Optique et à la prédiction des températures atteintes dans diverses conditions expérimentales. Ceci a été réalisé grâce à la modélisation 3D des composantes conservatives and non-conservatives des forces optiques agissant sur les atomes. L'implémentation des mécanismes d'échauffement connu des atomes : la diffusion de lumière et de leur quantité de mouvement, fût aussi cruciale à cette fin. Ce modèle nous a aidé à identifier les meilleures conditions de couplage dans ce système, corroboré par l'expérience, et qu'il existait un potentiel optique optimal, pour une distance de couplage déterminé, qu'il ne fallait pas dépasser.

Un faisceau LG_{01}, monomode et de haute pureté fût généré avec une efficacité supérieure à 50% en utilisant un hologramme à valeurs complexes généré par ordinateur et rendu grâce à un modulateur de phase spatiale à base de cristaux liquides. Une conversion à l'échelle du

système, de la sortie laser à l'entrée dans la chambre à vide, a été réalisée à 35% d'efficacité.

Plusieurs fibres optiques microstructurées en polymère et en silice ont été fabriquées et évaluées pour devenir la fibre candidate au guidage atomique. C'est finalement une fibre de 50 microns de diamètre à défaut unique de coeur et à microstructure Kagome qui s'est avérée être la plus performante pour guider le faisceau creux décalé vers le bleu servant de matrice de transport aux atomes froids de rubidium. Ce mode LG_{01} produit par le modulateur de phase à cristaux liquides a été couplé dans le coeur vide de la fibre avec une efficacité de couplage et transmission à 43% et l'on obtint 76% pour le mode Gaussien. Pour réaliser ceci, on a tiré profit du haut niveau de contrôle de la période du masque de phase virtuel et du contrôle de la taille du faisceau généré avant l'optique de couplage.

Toutes ces réalisations ont ouvert la voie à la réalisation du guidage atomique par fibre optique dans un système optimal qui a démontré que l'échauffement des atomes se produisait à un ordre de grandeur inférieur aux systèmes comparables de guidage Gaussien décalés vers le rouge. Cette technique de guidage permet aussi de conserver seulement les atomes les plus froids parmi une population piégée et qu'elle n'interagisse que minimalement avec le potentiel-guide. Cette approche promet aussi la réalisation du guidage des ondes atomiques dans un mode spatial unique avec moins de contraintes expérimentales que dans les approches décalées vers le rouge.

ABSTRACT

This thesis describes advances and techniques toward the efficient coupling of cold ^{85}Rb atoms into a low loss hollow core photonic crystal fibre using a blue-detuned first order hollow beam. In the proposed system, the low diffraction of the blue-detuned first order hollow beam acts as a repulsive potential optical funnel that allows the coupling of cold atoms under the influence of gravity into the fibre's hollow core. Using a low loss fibre with a blue detuned hollow beam shows potential for guiding atoms over an arbitrary path and longer distances on the laboratory scale, which would enable several new applications in nanofabrication and optical metrology.

To realize this objective, a Magneto-Optical Trap of ^{85}Rb was built from scratch and by using advanced polarization gradient cooling techniques was turned into a 9 μK cold optical molasses containing 10^7 atoms. These cold atoms were guided over 23 cm in a collimated blue detuned hollow beam tunnel and through a focused hollow beam mimicking as closely as possible the coupling conditions for a hollow core optical fibre. Three classes of atoms were observed: lost, trapped and guided atoms. The dynamics of the system as well as the optimal coupling conditions were identified through the use of a numerical model.

A novel approach to modelling cold atom dynamics in an optical funnel was developed during the course of this thesis. This new model was not only able to reproduce the dynamics of atoms in the experiment but also simulate dense cold atoms cooled into the MOT and predict final temperatures attained. This was achieved by 3D modelling of the conservative and non-conservative components of optical forces acting on atoms but also through the implementation of known heat mechanisms: light scattering and momentum diffusion. The model identified the best coupling conditions of this system, confirmed by experiment, and an optimal light potential for a given distance of coupling that must not be exceeded.

A single mode, high purity, LG_{01} beam was generated with over 50% conversion efficiency from a Gaussian mode using a complex-valued computer generated hologram (CGH) rendered on a phase-only liquid-crystal spatial light modulator (SLM). A system-wide 35% conversion efficiency was achieved from the laser output to the vacuum chamber input.

Several micro-structured polymer optical fibres and silica hollow-core band-gap photonic crystal fibres with Kagome claddings were evaluated. A single defect, large hollow core ($\sim 50\mu$m diameter) Kagome cladding fibre was identified as a suitable solution for guiding cold ^{85}Rb atoms. The LG_{01} mode generated by the SLM was coupled into a single first order hollow mode with a high efficiency of 43% and 76% for the Gaussian mode by controlling the

blazed grating period and the input beam size with the CGH.

All these achievements opened a way for the challenging realisation of cold atom fibre guidance in this optimal system which has shown to have an order of magnitude less heating than in comparable red-detuned coupling and guidance. This guiding scheme also allows the keeping of the coldest atoms within the distribution to interact minimally with the guiding potential, showing promise of enabling single mode atomic wave guiding with less experimental constraints than red detuned schemes.

TABLE OF CONTENTS

LIST OF TABLES

LIST OF FIGURES

LIST OF SYMBOLS AND ACRONYMS

Acronyms

AOM	Acousto-Optical Modulation
AWG	American Wire Gauge
CCD	Charge-Coupled Device, a type of digital imaging sensor.
DDS	Direct Digital Synthesizer, a type of frequency synthesizer used for creating waveforms from a fixed-frequency reference clock.
EMF	Electromotive force
EOM	Electro-Optical Modulation
fps	Frame-per-second, a camera video imaging rate.
FSM	Frequency Standards & Metrology, our research group at UWA.
HC-PCF	Hollow-Core Photonic Crystal Fibres
HWP	Half-Wave Plate
MBR	Monolithographic Birefringent Resonator, a ring cavity CW tunable Ti:Sapphire laser.
MOT	Magneto-Optical Trap
MTS	Modulation Transfer Spectroscopy
NPBS	Non-Polarising Beam Splitter
OCF	Optical Capillary Fibres
OM	Optical Molasses
PBS	Polarising Beam Splitter
PCX	Plano-Convex lens
PCV	Plano-Concave lens
PGC	Polarisation Gradient Cooling
PID	Proportional-Integral-Derivative controller, a control loop feedback mechanism.
QMC	Quantum Monte Carlo, a cold atom modelling approach.
QWP	Quarter-Wave Plate
SAS	Saturation Absorbtion Spectroscopy
SC	Semiclassical
SC-FP	Semiclassical Fokker-Planck
SC-VV	Semiclassical Velocity-Verlet
SEM	Scanning Electron Microscope

SLM	Spatial Light Modulator
TEC	Thermoelectric Cooler, or Peltier Cooler.
TVS	Transient Voltage Suppressor, a type of ultrafast diode.
UHV	Ultra-High Vacuum
UWA	University of Western Australia

Physical Constants

g	Earth's Standard Gravity, 9.80665 m/s^2
k_B	Boltzmann constant, $1.38064852 \times 10^{-23}$ m^2 kg s^{-2} K^{-1}
c	Speed of light in vacuum, 2.99792458×10^8 m/s
$\hbar$	Planck's constant over 2π, $1.054571800(13) \times 10^{-34}$ J·s
m	Atomic mass; for ^{85}Rb $= 1.409993199(70) \times 10^{-25}$ kg

Symbols

r	Fibre core diameter or radial position in free space
R	Radius of coil
z	Distance along core axis or in free space
x, y	Planar coordinates in plane perpendicular to fibre or laser optical axis
d	Distance between two coils
N_i	Number of wire turns in coil construction
a	electrical conducting coil wire radius supporting current I_B
I_B	Current driving the coil and generating magnetic field
B	Total Magnetic field in space
L	Inductance of a coil (measured/calculated in SI units of Henry)
τ	Radiative lifetime
τ_p	Optical pumping time
Γ	Spontaneous decay rate, natural linewidth
Γ'	Spontaneous decay rate, natural linewidth, power-broadened
Γ''	Mean fluorescence pumping rate, ground state width
γ_s	Light scattering rate
δ	Laser detuning from resonance frequency
Ω	Rabi frequency

ω_a	Atomic transition frequency
ω_l	Laser frequency
ω_r	Recoil frequency
ω_D	Doppler shift
I_s	Saturation intensity
s	Saturation parameter, off-resonance
s_0	Saturation parameter, on-resonance
β	Damping coefficient (Doppler mechanism)
α	Friction coefficient (sub-Doppler mechanism)
T	Atomic velocity distribution temperature(K)
T_r	Recoil temperature
T_D	Doppler temperature
$\bar{v}$	Thermal velocity (rms)
v_c	Critical velocity
v_D	Doppler velocity
v_r	Recoil velocity
r_c	Trap capture radius
N	Number of atoms captured in trap
n	atomic density, $n(r,t)$ is the atomic density distribution
σ	cloud size parameter; time-dependant Gaussian distribution variance parameter of expanding (when released) atom cloud
σ_0	initial cloud size parameter; initial variance parameter of atomic distribution in space
t	time parameter; of ballistic expansion, of exposure

LIST OF APPENDIXES

CHAPTER 1 INTRODUCTION

1.1 History of atom optics

Over the last hundred years, our technological progress has been closely linked with our ability to improve precision measurements of every physical quantity. Precision instruments have allowed the development of metrology standards (distance, frequency) that drive industrial quality of production. They have also deepened our knowledge of the physical world which in turn has allowed us to innovate and develop new technologies. In this respect, the laser has revolutionized optical metrology of distances and dimensions, acceleration, temperature, frequency and time [1].

The first *particle-optics* device, the scanning electron microscope (SEM), was the culmination of efforts initiated 39 years before its invention by Louis de Broglie's controversial hypothesis (1924). He postulated the dual wave-particle nature of light. Their associated wavelength is expressed by the relation:

$$\lambda_{Br} = \frac{h}{Mv} \tag{1.1}$$

where *h, M, v* are the Planck's constant, the particle's mass and its velocity, respectively. This hypothesis was verified experimentally three years later by Davisson and Germer in 1927 with the observation of electron diffraction through a thin metal film [2]. In microscopy, a SEM can achieve resolutions a thousand-fold superior to the best optical microscope. In its essence, SEM is similar to the optical microscope but it exploits the wave nature of massive particles (electrons) to resolve features much beyond the capabilities of visible light.

After electron optics came the development of neutron optics with a striking difference to its predecessor: gravity had to be accounted for, making the experiments much more challenging. Diffraction of neutrons was used to study the crystalline organization of matter and to produce a neutron interferometer [3] and microscope [4]. Neutron optics was limited in its scope because of the neutron insensitivity to external electric and magnetic fields. Therefore, interest in the field shifted to performing optics with neutral atoms, particles that are sensitive to externally applied fields which also benefit from being more massive and therefore featuring a smaller *de Broglie* wavelength for equivalent velocity.

In 1982, following theoretical proposals, the first atomic mirror was demonstrated [5]; atom optics was born. Later, controlling the motion of atoms with optical electromagnetic fields, nearly every element of photon optics was duplicated in their atomic-equivalent: from

lenses [6] and collimators [7], to beam splitters [8] and gratings [9]. Atomic interferometers [10], such as Sagnac gyroscopes [11] and Mach-Zehnder interferometers [12] demonstrated the potential of atom optics metrology to go beyond the performance of its optical counterpart. Atom interferometers can also measure physical quantities like gravity [13] and electrical polarisability [14] which had been impossible to measure with an optical interferometer.

Extraction of atoms from the source is performed at high temperature and the velocity of atoms, even when cooled to room temperature, requires very strong fields and therefore limits the potential of this new technology. The development of laser cooling of neutral atoms was a game-changer and interest in atom optics sparked after the realization of the first Bose-Einstein Condensate (BEC) over 15 years ago [15] and the subsequent Nobel prizes awarded for laser cooling of atoms in 1997 [16] and 2001 [15]. BEC, its warmer cousin optical molasses and Magneto-Optical Traps (MOT) [17], became common tools in atom optics experiments further enabling the capabilities of atomic interferometers [18].

1.2 Motivation

The motivation for this Thesis came from the realisation that one key element was still missing from the atom optics arsenal: the long distance atom guiding optical fibre. The field of atom optics has produced matter-wave equivalents for almost every conventional optical component [5, 19, 20]. However, a hollow core optical fibre which supports an electromagnetic mode capable of steering the atoms away from the fibre walls can enable guidance of atoms over long distances and ideally through an arbitrary path.

The loading and guiding of atoms into short straight lengths of fibres has been realized many times in the last 20 years as will be reviewed in chapter 2. However, long distance guidance, over 1 meter and in curved paths is still challenging because of high losses, both of the optical mode and guided atomic populations. One of the goals of research in this Thesis on atom guidance in fibres is to achieve the most efficient coupling/guiding of atoms while keeping losses low in bends and over longer propagation distances. The goal is to be able to deliver cold atoms to a second location in a coherent single mode matter-wave beam, which could serve several purposes, such as to load an optical lattice, to deliver atoms to a second trap devoid of background vapour, for atomic interferometry setup or even an atomic chip [21].

1.3 Applications driven motivation

An objective for guiding atoms is to use cold ensembles of atoms to perform high resolution spectroscopic measurements and study ultra-efficient single atom-single photon interactions [22, 23].

The realisation of an efficient atomic optical fibre allowing guidance of atoms over lengths at the laboratory scale and in arbitrary paths is a key element for many future applications. Calls for improved gravity sensors could be answered by the sensitivity expected from large area atomic interferometers. A fibre-guided source of atoms could provide a highly coherent beam that would allow such large area atomic interferometers and therefore an improved precision in the measurement of G [10]. It was also proposed theoretically that atoms guided in a U-bent fibre could make a sensitive device that would enable the detection of gravity waves [24].

One of the most promising features given a cold enough cloud in a micron-sized fibre, is the guidance of a single matter-wave mode. Such a mode would produce an ideal wavefront for interferometric experiments with matter-waves [25]. The resolution achieveable with atom optics would enable the development of a promising new technology in microfabrication, e.g., atomic lithography [26, 27]. Atoms coupled and guided coherently in a single atomic mode fibre could enhance the capabilities of atomic lithography by allowing the direct etching (without a mask), selective doping of specific areas in a chip, or writing-in structures almost atom-by-atom [28].

Due to the very precise requirements for the frequency of the guiding optical force, an atom guiding fibre also acts as the ultimate atom filter leading to a pure mono-isotopic source of atoms. This fibre could be fed into a second vacuum chamber, which is devoid of hot background atoms from the source, typical of the cooling and trapping chamber environment. This would provide an ideal setup for ultrasensitive applications. Coherently ejected atoms from the fibre could also be inserted into specific inputs of a designed atom-chip for further manipulations [21].

Already, first spectroscopic experiments of coupled cold atoms into a fibre core [22, 29, 30], probed in situ, have demonstrated that it is a promising environment to study quantum interactions between light and matter. The combination of high densities of cold atoms interacting with very intense guided laser pulses, brings us closer to conditions where atom-photon interactions could be studied [31]. Electromagnetically induced transparency with fibre coupled atoms was recently demonstrated [30]. Efforts into loading colder atoms from a BEC instead of a MOT could lead to the realisation of a Tonks-Girardeau gas of atoms

[32], essentially a BEC in 2D with fermionization of bosons in 1D, along the fibre axis [33]. Improvements into coupling and preventing heating of the guided atoms are essential to attain this objective.

Finally, it is envisioned that the highly efficient interaction between guided atoms within the fibre and probe light could also lead to a novel optical atomic clock in a fibre cavity where accuracy and stability are improved over their free-space counterparts [23].

1.4 Problem statement

Until recently, atoms have only been guided in an optical capillary fibre (OCF) or a hollow-core photonic crystal fibre (HC-PCF) by a red-detuned fundamental mode (HE_{11} or Gaussian). This attractive potential concentrates guided atoms in the centre of the beam. However, this poses a problem because of the losses induced by light scattering which heat atoms during loading and transport. One way to circumvent this problem was demonstrated by Vorrath et al. using a 2.3 watts of a very far, 100 THz, red-detuned laser [34]. A proof of concept by using such a powerful beam is not a practical and efficient solution to the problem as it presents new issues. The fibre used for guiding at a wavelength of 1067 nm cannot be used to guide a probe beam at 780 nm. Indeed, the energy levels being Stark-shifted during guidance, require the guiding beam to be extinguished before measurements, causing significant losses.

The purpose of the blue-detuned hollow beam as a guide is two-fold: to minimize heating losses triggered by spontaneous absorption events by guiding atoms in the dark; and to minimize the offsetting of the atoms energy levels by Stark effect caused by the guiding field electric potential. Therefore, the blue-detuned hollow beam presents a strong advantage of not needing to interleave pulses of the guiding and probing light. A review of the literature (section 2.7) shows that there is a gain of between 3 and 10× in guidance efficiency, as well as a reduction in light scattering by an order of magnitude.

Blue-detuned hollow guidance has only been performed in a vacuum and in capillary glass fibres. A capillary fibre is not suitable for the applications envisioned in the previous section because of its strong attenuation of light guided in the core and high bend loss, limiting its useful length to a few 10ś of centimetres of guidance in a straight fibre. With the advent of HC-PCF technology, guiding efficiency increased significantly with red-detuned guidance demonstration, detailed in the literature review in the next chapter. HC-PCF technology made possible the guidance of a low order Laguerre-Gaussian-like mode [35], and confinement of atoms in HC-PCF using blue-detuned hollow beams for high resolution

spectroscopy [22, 23], was also demonstrated; however their experimental setup did not allow for blue-detuned transmittance through the fibre.

What is also unclear is how efficient is the diffraction of the blue-detuned hollow mode from the fibre for the task of loading the atoms into the fibre core. This Thesis also aims to answer this question.

1.5 Thesis objectives

This thesis proposes an approach to improve the guidance of cold atoms into a Kagome lattice HC-PCF by using a low-order blue-detuned hollow beam while minimizing heating through the fibre coupling stage. Therefore, the objective of this thesis is to build the experimental foundations and techniques, supported by a numerical model, leading to the realisation of the blue-detuned hollow beam atom guiding experiment through a HC-PCF. More precisely, the first objective was to realise a stable and efficient Rubidium Magneto-Optical Trap along with imaging and fibre mounting hardware in the vacuum chamber. Secondly, to build a setup to generate a low order Laguerre-Gaussian mode and use this setup to excite a closely-related hollow mode supported by an appropriate HC-PCF. Thirdly, to model the experimental setup to couple atoms from the MOT to the fibre core and identify the optimal parameters to achieve this in the lab. This thesis also aims to evaluate the efficiency of this task compared to using a red-detuned Gaussian mode.

1.6 Thesis structure

Chapter 2 reviews the literature of atom guidance with an analysis of the results obtained to give the reader a firm understanding of this subfield of atom optics.

Chapter 3 presents the theory of several topics essential to the foundation of this work: laser cooling, laser spectroscopy and magneto-optical trapping with practical calculations applied to the guidance of ^{85}Rb.

Chapter 4 describes the numerical model of the experiment to couple and guide atoms from the MOT to the fibre using a diffracting LG01 beam. An investigation of the dynamics of the atoms in the optical funnel as well as the particular challenges of this approach is presented. The results of a numerical simulation have been published in reference [36].

Chapter 5 constitutes the core experimental chapter. An overview of the experimental setup is presented with details about the MOT design and fabrication. Next, the experimental results in aligning, trapping and guiding atoms in vacuum are presented along with advanced

techniques used to image the atoms.

Chapter 6 discusses the efficient generation of a hollow beam and its coupling into a hollow core optical fibre. Earlier works, in the design and fabrication of a hollow atom guiding fibre, are also discussed.

Finally, Chapter 7 concludes by summarizing the experimental achievements and their significance for future atom optics experiments.

CHAPTER 2 LITERATURE REVIEW OF ATOM GUIDANCE

2.1 Historical developments and atom guidance propositions

In 1871, James Clerk Maxwell deduced theoretically that light exerts pressure upon any surface exposed to it. Later, in 1901, J. N. Lebedev [37] measured the movement induced by light on a suspended metallic mirror in a high vacuum. This first quantitative proof of Maxwell's electromagnetic theory was confirmed the same year by Nichols and Hull [38].

The possibility of interaction between atoms and a laser standing-wave was first introduced by Letokhov in 1968 [39]. The concept of cooling and trapping atoms by using light's radiation pressure was developed extensively by Arthur Ashkin [40–42], who is considered the father of the topical field of optical tweezers, and whose pioneering theoretical work led to the first experimental realizations of cooling [43] and trapping [44] atoms with lasers, for which Steven Chu, Claude Cohen-Tannoudji and William Daniel Phillips received the Nobel Prize in Physics in 1997.

In 1982, Cook and Hill [5] proposed an atomic mirror which used the evanescent field of reflected electromagnetic radiation to reflect and trap atoms within an illuminated cubic vacuum space in a glass medium. For a laser irradiance of $1\,\mathrm{W/cm^2}$ ($8\,\mathrm{mW}$ for a $1\,\mathrm{mm}$ diameter beam), atoms of speeds up to $4\,\mathrm{m/s}$ could be contained in this trap. Cook and Hill also proposed that atoms could be reflected, diffracted, focused and manipulated like light, therefore: "a complete optics of atomic beams could be constructed on the basis of such reflecting elements". In comparison, rubidium atoms cooled down to their Doppler temperature ($141\,\mu\mathrm{K}$) have a velocity of $0.2\,\mathrm{m/s}$, making these atomic mirrors very efficient in reflecting cold atoms. What is different in atom optics, compared to light optics, is the strong effect of gravity on slow atoms, which must be considered in interferometer designs, even for paths of a few centimetres.

In 1987, Cohen-Tannoudji et al. [45] demonstrated experimentally, that it is possible to guide atoms between the low potential nodes of a laser standing-wave. Balykin et al. [46] further demonstrated that it is possible to channel the atoms in a spherical path by using a spherical wave. In 1983, Balykin and Letokhov proposed the idea of guiding atoms with a laser through a hollow-core optical fibre. This theoretical paper proposed to create a potential well in the centre of the fibre by using a red-detuned laser beam. The potential was calculated for sodium atoms, showing that a propagation of 10 m could be achieved (assuming all atoms are propagating along the fibre axis with no transversal velocity) [47]. However,

the effect of light scattering had not been taken into account; these spontaneous absorption events increase the energy along the laser propagation axis (and in the transversal direction). Additionally, when atoms are in an excited state, the effect of the dipolar force is reversed and leads to a transversal energy escalation over the absorption-emission events, ultimately resulting in direct atom guidance loss. This form of heating is called viscous dipole heating and was discovered by Dalibard et al. [48]. Its effect in laser guided atoms was reported by Renn et al. (1997) [49] (see Figure 2.1).

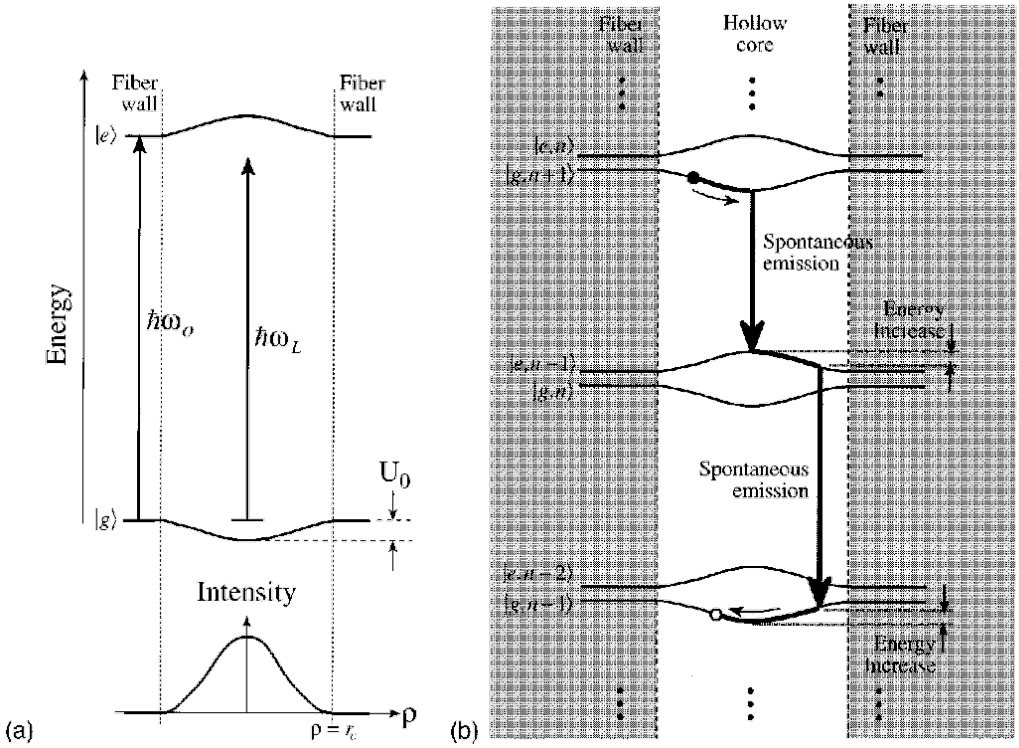

Figure 2.1: (a) Variation of the energy levels in a two-level atom according to its position in a red-detuned field from the first guided mode of a fibre. (b) This dressed state picture shows the atom completing a spontaneous absorption cycle from a ground state to an excited state and back to its ground state. During its time in a particular level, the atom moves transversally to reach the minimum potential, gaining transversal kinetic energy in each transition. *Figure modified from [49].*

A year later, Marksteiner et al. [50] developed a more complete simulation of the requirements of the atom-guiding hollow optical fibre. There was one major difference between Marksteiner's theory and the model of Balykin [47]. Marksteiner suggested guiding the light in the cladding of the capillary at a blue-detuned frequency, arguing that losses caused by

light scattering could be prevented by using repulsive evanescent wave guiding. A more realistic model addressing the issue of optical modes in a multimode hollow-core capillary used for evanescent guiding of Rb atoms was published by the Japanese group (Ito et al. [51]) a year later.

Over the years, many original proposals and experimental achievements have been published to improve the evanescent field (metal coating the fibre cladding [52]), to further confine the atoms in the fibre using gravity [24] or by tapering a capillary [53]. Atoms have also been guided in free space over short distances by red-detuned Gaussian beams [54, 55]), blue-detuned dark hollow beams [56, 57] and over magnetic wires [58, 59].

In the interest of brevity, the following subsections will focus on the literature on atom guidance in optical capillary fibres (OCF) and hollow-core photonic crystal fibres, including Kagome lattices (HC-PCF). OCF, often called capillary or fibre (which can lead to confusion) glass tubes of the same size as an optical fibre but with a hollow core and silica cladding, which can be composed of multiple layers of different refractive indices [60]. For a thorough review of laser-guided atoms in vacuum, readers can refer to Song [61] and Noh and Jhe [62]. After reviewing the key publications in this subfield, a comparative table (Table 2.1) along with a summary of the current state-of-the-art of Rb atom guiding experiments will be presented.

2.2 Rubidium guiding experiments in silica capillaries

In 1995, atom guidance through an OCF was demonstrated experimentally for the first time by the University of Colorado group JILA (C. E. Wieman, E. A. Cornell, D. Z. Anderson and others) Renn et al. [63]. They achieved guidance of rubidium (Rb) from a thermal oven source by using a red-detuned laser beam (see experimental setup, upper image of Figure 2.2) coupled into a 3.1 cm long capillary, with a hollow core of 40 μm diameter. The investigation of red-detuned Rb guiding was further extended to study the atom flux vs. detuning while varying two experimental parameters: length (3 and 6 cm) and power coupled in the core (from 0.75 to 60 mW) [49]. Two guiding regimes were identified. At low intensity ($< 5\,\mathrm{MW/m^2}$), the atom flux quickly increases with increasing negative detuning up to a maximum and then slowly decreases (see Figure 2.2 (a)). This is the result of the conservative part of the dipolar force. Thus, for relatively short capillary lengths and a large area core at moderate intensity, the contribution from the non-conservative force is small.

For higher intensity fields, the single peak is shifted into two peaks separated by a dip in guided atom flux (see Figure 2.2 (b)-(d)). This "hole-burning" effect appears in the atom

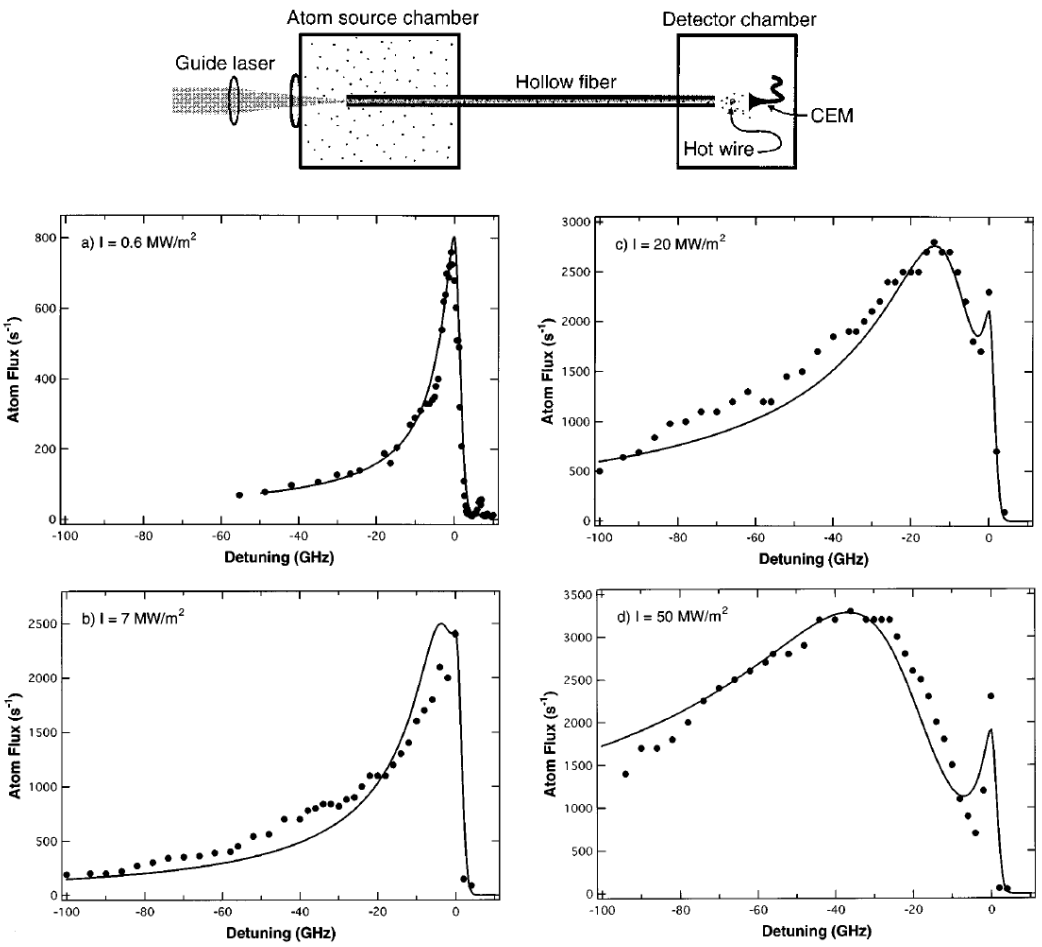

Figure 2.2: (top) Schematic of the experimental apparatus. A rubidium oven chamber is connected through a glass capillary to a second detection chamber. Atoms are detected with an ionising rhenium hot wire and a channeltron electron multiplier (CEM). (a)-(d) Atom flux through the 6-cm-long, 40 μm diameter capillary versus detuning of the guiding laser with increasing intensities. The first maximum spikes rapidly with detuning close to 0 GHz due to the rapid turn off of the laser pressure force and increase of the dipolar guiding force (a). With higher intensities (b)-(d), a quick drop in atom flux after the first maximum appears, similar to spectral hole burning, due to viscous dipole heating. Then, an increasingly important second maximum in the atom flux appears with further detuning as the viscous dipole heating and spontaneous absorption probabilities are both insignificant. *Figure modified from [49].*

flux profile at intermediate detunings because it corresponds to the maximum viscous dipolar heating force. At larger detunings (Figure 2.2 (d)), the non-conservative force quickly decreases as δ^{-2}, while the dipole guiding force only decreases as δ^{-1}. When the viscous

heating is turned off and dipole guiding is only slightly weaker, the atom flux reaches its second maximum and the guiding force is then at its most efficient (> 40 GHz). Keeping the intensity constant, a longer capillary produces greater heating loss which is undesirable for atomic guidance. Because this loss is caused by atoms travelling in the high-intensity regime, they concluded with the results of a numerical model, that guidance over 20 cm is impossible. With a longer OCF, even at a minimal guiding force, all atoms would suffer an increase in transverse velocity that would quench the guidance. This was identified as an important limitation of red-detuned guidance.

The solution proposed, using evanescent wave blue-detuned guidance in a capillary fibre, was demonstrated for the first time in 1996, by the same Colorado group [64]. Using a 10/77 μm (core/cladding diameter) silica capillary, blue-detuned laser light was coupled into the capillary solid glass cladding. Mode-matching constraints made the evanescent field inefficient at guiding the Rb atoms over the first few attenuation lengths in the core (400 μm). Guidance was greatly improved by the use of a second red-detuned "escort" beam focused in the core of the capillary. The proof that atoms were only guided by the evanescent field was clearly demonstrated by turning off the blue-detuned laser (keeping the red-detuned escort beam on) and showing that only ballistic atoms were detected. As opposed to previous experiments (Renn et al. 1995), the red-detuned beam decayed over a much shorter distance because the core was 4 times smaller (attenuation length scales as r^3, core radius). An optical intensity threshold was also observed for guidance to occur, calculated from the penetration of the blue-detuned evanescent field in the core of $\approx \frac{\lambda}{2\pi}$ (124 nm for D_2-guided Rb), which is in the same order of magnitude as the van der Waals forces. Thus, the repulsive potential of the evanescent field must exceed the attractive potential of the van der Waals forces to achieve optical guidance of atoms. A threshold of 5 MW/m^2 (22 mW total optical power) was observed for the capillary dimensions used in the experiment. For such a short evanescent field penetration in the core, atoms are considered to be guided by an almost specular reflection from the potential walls (identified as bounces), like light in a large-core multi-mode step-index fibre [64]. Nonetheless, evanescent field blue-detuned guiding was demonstrated to be at least three times more efficient than previous Rb guiding in a red-detuned laser beam.

In 2000, the JILA Colorado group further deepened their experimental research on blue-detuned evanescent Rb guiding by improving a major parameter: the atomic source [65]. This work was acknowledged as the first guidance of cold Rb atoms through an OCF. Their experimental setup is shown in Figure 2.3 (a). A low-velocity intense source (LVIS) of laser-cooled Rb atoms was used. The more efficient atom coupling and a larger core (100/160 μm

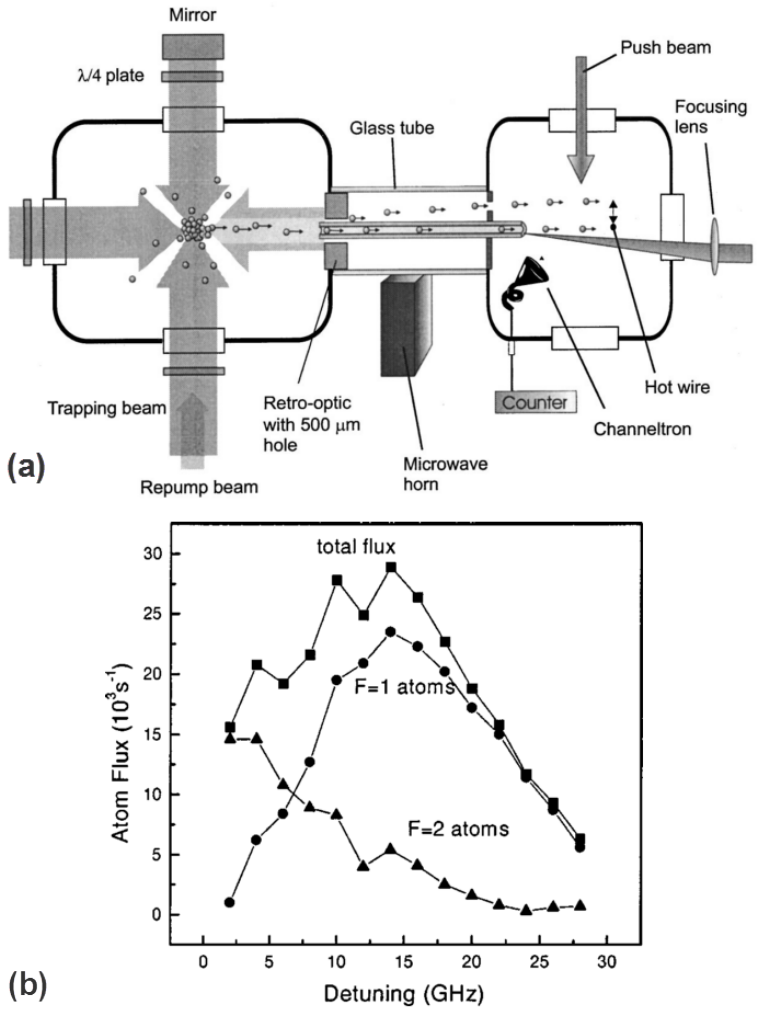

Figure 2.3: (a) Experimental setup consisting of two vacuum chambers connected with a capillary. First chamber contains the LVIS beam setup. In the second chamber, the guiding beam is coupled into the capillary cladding. The guided and unguided atoms can be counted separately using a hotwire and channeltron detector setup. The internal state of the atoms can be probed using a transversal laser push beam. (b) Guided atoms internal state dependence with detuning. In small detunings, a lot of guided atoms go through spontaneous emission cycles and end up in the F=2 ground state. At larger detunings (> 15 GHz), total flux contains more than 90% atoms in the F=1 state indicating suppression of spontaneous emission during guidance. *Figure modified from [65].*

core/capillary diameter), made an escort beam unnecessary. Guiding of a flux of 590 000 Rb atoms/s was demonstrated for 30-cm-long capillaries using a 55 mW beam, 6 GHz detuned to the blue. Two major loss mechanisms were identified: collisions with background atoms

because the vacuum in the core was not perfect and collision losses because of the interference generated speckle pattern in the evanescent fields of the multimodes coupled in the capillary. Guiding efficiency was shown to be 3% at best [65]. They also identified the ground state of the guided atoms depending on the detuning and found it is mostly F=1 atoms that are guided as shown in Figure 2.3 (b).

A Japanese group also realized similar evanescent field, blue-detuned atomic guidance experiments using a hot oven source of rubidium in 1996 [66] and 1997 [67]. The main difference was that they used a very small core capillary (2 and 7 μm diameter) with a thin higher-index doped region of 4 μm around the core and a high power beam (280 mW) coupled to the thin region. However, the thin doped region supported only 3 modes: $LP_{01}, LP_{11}, LP_{21}$. The restricted light guiding region generated a high gradient potential wall allowing atomic modes with high transverse velocities. Guiding efficiencies of 40% in a 3-cm-long OCF were reported with a channeltron electron multiplier detection technique. The main loss mechanism was identified to be modal interference leading to a modulated and irregular evanescent field along the core. They also developed interesting coupling techniques. In one scheme, the beam directed orthogonally to the capillary end-face was coupled with a mirror which had a hole in its center [66]. In a second experiment, the end-face was cleaved and polished at a 45° angle and the beam was coupled directly without the use of a mirror [67].

2.3 Blue-detuned meta-stable helium guiding experiments

In 1999, an Australian group [68] demonstrated the first and only experimental guidance of He*. It was also the first blue-detuned evanescent wave guidance of cooled atoms. Helium was the second meta-stable/excited atom guided in OCF after the Neon guiding experiments in 1998-1999 [69, 70]. The cooled atom source was a low-velocity intense source (LVIS) beam of He* produced from a Bose-Einstein condensate (BEC). Since Helium has a low vapour pressure, loading from background vapour is highly inefficient and results in small MOTs, hence the earlier effort into producing a cold atomic beam. In meta-stable helium guidance, a high efficiency single-frequency InGaAs laser diode with a distributed Bragg reflector (DBR) cavity was used. This laser diode can produce 50 mW at 1083 nm [68]. Powerful Ytterbium 1-Watt fibre lasers are also used to cool down and collimate the beam [71].

The experimental setup used is illustrated in Figure 2.4 (a). Two, 5-cm long capillaries, were used with 40/110 and 10/150 μm core/cladding diameters. Light was coupled orthogonally to the end face that was cut at 45° of its axis using the coupling technique developed by the Japanese group [67]. Figure 2.4 (b) is an SEM image of the 45° cut and polished

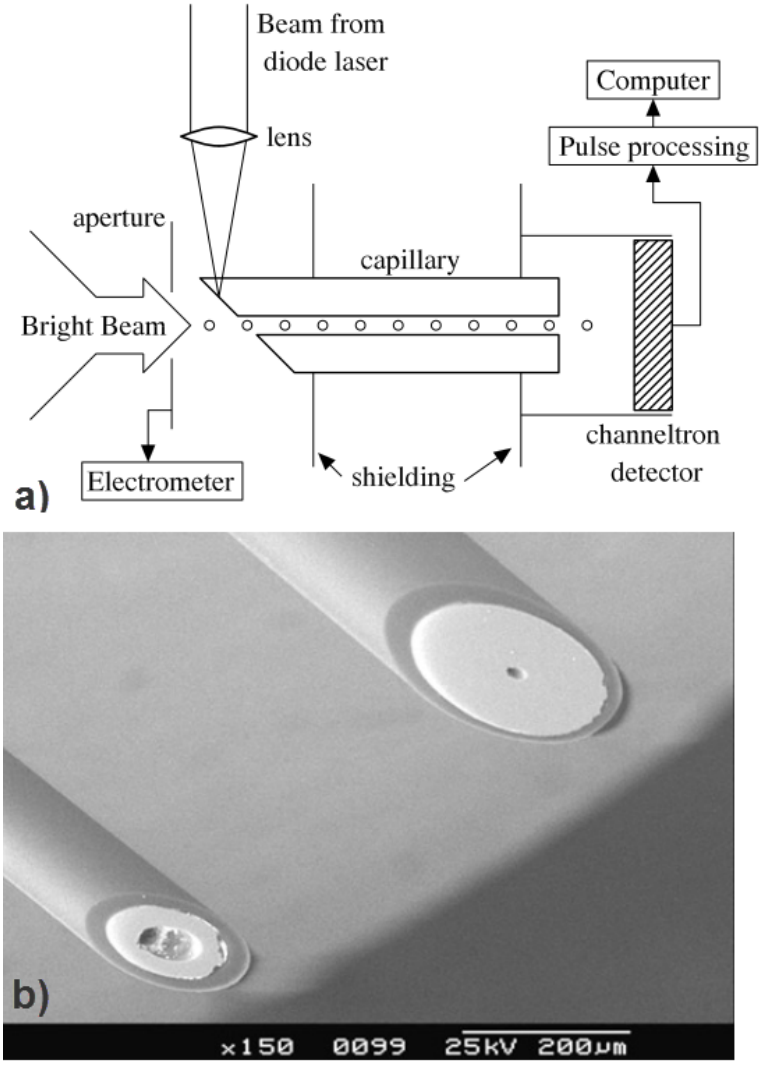

Figure 2.4: a) Sketch of the experimental setup showing how light is coupled into the 45° bevel capillary. (b) SEM image of the capillaries showing the smooth angled polishing results. *Figure modified from [68].*

capillaries. The light coupling efficiency was around 10% but it still managed to guide the atoms. When turning off the field, there were still ballistic atoms coming through because of the high coherence of the atomic source (and the short capillary used). It was observed that the decrease of guided atoms with respect to detuning was more important than expected because of multimodal propagation in the cladding leading to modal interferences and irregular evanescent wave intensity along the capillary. The coupling direction of the laser beam, with respect to the propagation direction of the atoms, was shown to have no impact on the guiding efficiency of He* [68].

After the initial guiding experiment, an important part of Dall's thesis [71] focused on the enhancement of the magneto-optical trap and the improvement of the LVIS beam [72]. While the flux of the atom beam was kept around 1-3 $\times 10^{10}$ at./s, its focus was improved from a 10 mm to a 2 mm beam diameter and by slowing down the average velocity from 100 to 26 m/s. The beam divergence slightly increased from 10 to 15 mrad, but its resultant parameter, the transverse velocity, was reduced from 1 to 0.4 m/s which is almost the Doppler limit of He* (0.29 m/s) for the $2^3S_1 \rightarrow 2^3P_2$ transition [72]. This much improved beam could help to efficiently couple atoms to small core fibres in order to achieve "few-moded" *de Broglie* wave guiding.

2.4 Atom guidance in photonic crystal fibres

In 2007, micro-structured hollow-core photonic crystal fibre (HC-PCF) [73] were used in atom guidance for the first time by Takekoshi et al. [74, 75]. Rubidium atoms injected from a thermal oven were guided over 6 cm of fibre by a red-detuned beam far from resonance of the D_2 line. Atoms were very hot at the coupling input end of the fibre (up to 9 times the longitudinal speed of previous Rb guiding experiments [65]). Another limiting factor in the guidance was the inefficient coupling of the laser light into the fibre core (10-30%) because all the lenses were located outside the vacuum chamber. Nonetheless, it was the first atom guiding experiment in a fibre using a single mode low loss guiding field. The achieved guiding efficiency of over 70%, was impressive given the non-collimated thermal source used and it demonstrates well the potential of HC-PCF over simple capillaries.

One of the solutions suggested to reduce events of light scattering of atoms and enhance atom guidance over longer distances was to use a far detuned guiding beam. The photon scattering rate decays as the inverse square of the frequency detuning as opposed to the dipolar force that decays as the inverse of the detuning. Thus, for an intensity sufficient to ensure guidance, a large detuning light scattering is preferable because of this favourable scaling of the forces. Vorrath et al. [34] pushed this solution to extremes by using an ultra-far red-detuned beam, 100 THz below resonance (or +300 nm detuned), to demonstrate guidance of cold atoms in an 8.8-cm long 12-μm diameter HC-PCF. The experimental setup is detailed in Figure 2.5 (a). A ^{85}Rb MOT was cooled to 10 μK in an optical molasse phase and brought closer to the fibre end by moving the zero-point of the magnetic field. The fibre was aligned horizontally with the MOT. The cold atoms are attracted into the core by the action of the longitudinal component of the dipolar field from the diffracting Gaussian beam. The guiding field composed of two orthogonally polarised Gaussian beams of 2.3 W each at 1067 nm

(almost 300 nm off resonance, -100 THz) produces a trapping potential of 8.2 mK. From the time the molasses beam was switched off, they measured a transmission of 7400 atoms with a peak flux of 1.5×10^5 atoms/s.

The transmission of atoms flux as a function of time is shown at Figure 2.5 (b). A constant flux of 1.5×10^4 atoms/s was maintained for >150 ms when the 2D cooling MOT trap at the fibre input was used. They also measured the peak density of atoms in the fibre at 5×10^{11} atoms/cm^3, a factor 3× higher than the MOT peak density.

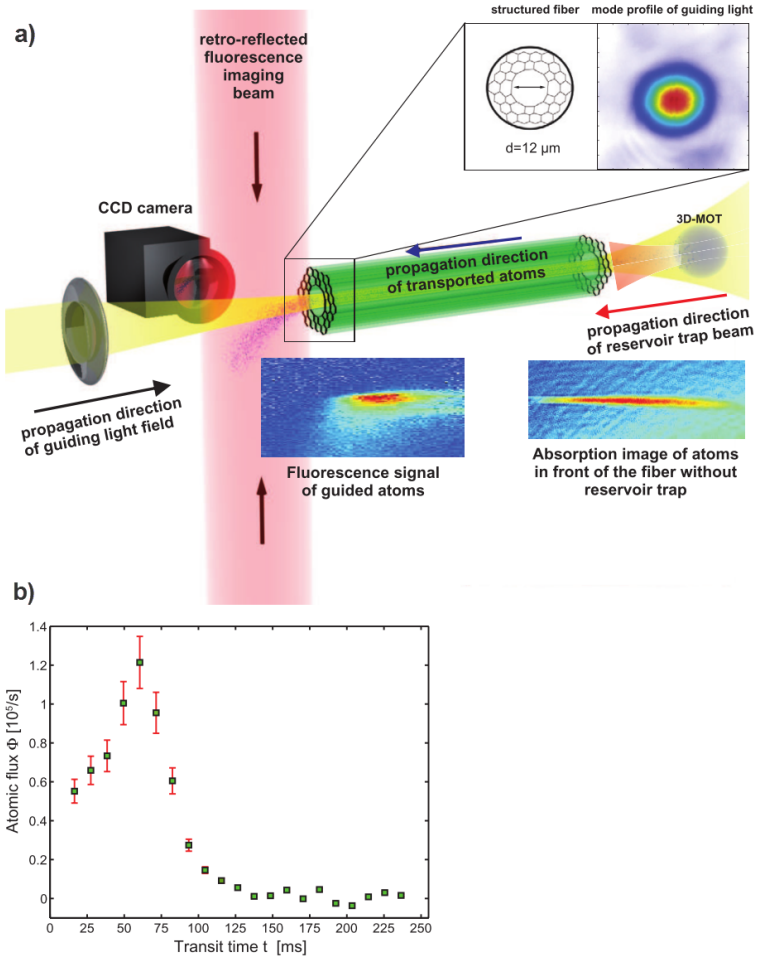

Figure 2.5: a) Schematic of the experimental setup. A MOT is moved magnetically in the trapping region of a fibre guiding two 2.3 W counterpropagating beams, red-detuned very far off resonance. A retroreflecting laser beam at the end of the fibre is used to capture fluorescence from guided atoms on a CCD camera. b) Captured atomic flux guided through an 8.8-cm-long HC-PCF as a function of time. A peak flux of 1.2×10^5 at./s is obtained after 60 ms. *Figure modified from [34].*

From the data in the paper, an overall coupling efficiency of ∼0.05% is calculated. It is rather low because only atoms emitted within a certain solid angle toward the fibre can be captured by the diffracting Gaussian beam. The effective trapping volume is directly dependant on the beam power. "An unexplained behaviour" (in the words of the author) was observed where only the counter propagating polarised beams contributed to the guiding of the atoms in the fibre. The average transit time in the fibre was 60 ms which corresponds to a longitudinal velocity of 1.5 m/s. The spontaneous scattering rate was calculated to be $\Gamma = 120/\text{s}$ which corresponds to an average of 7 scattering events / guided atom, so the overall resulting loss during guidance is expected to be negligible.

So far guiding has only been realised over short lengths of few cm to a few tens of cm. Hollow metallic guides offer interesting solutions to this peculiar problem as they can guide higher order hollow beams [76]. Pechkis and Fatemi [77] demonstrated guidance in 100 μm core diameter and 3-cm long hollow metallic waveguide and showed that second order hollow beam feature less light scattering at small detunings. However, further simulations showed that at larger detunings (> 100 GHz) the difference between second order and first order hollow beams becomes marginal. Hollow metallic waveguides also proved to be lossier waveguides (~ 1.5 dB/cm when straight) than HC-PCF, and even more so when they are bent.

2.5 Nonlinear optics with cold atoms loaded in a fibre

Light interaction with thermal atoms in hollow fibres was observed through electromagnetically induced transparency for applications in high resolution spectroscopy [78, 79]. Similar applications with cold atoms were also explored by Bajcsy et al. [22] but the efficient coupling of atoms requires additional steps to control the atoms in space. These techniques could also benefit atom guidance applications.

In 2008, Christensen et al. [29] demonstrated the first loading of a sodium BEC into a hollow core optical fibre. By adjusting the focal point of the optical dipole trap beam (Gaussian red-detuned) between the front and the core of the fibre, they were able to move atoms from the BEC into the fibre and back into space. They achieved 5% transfer efficiency.

Bajcsy et al. [30] used a ^{87}Rb MOT cooled down to 40 μK, and loaded atoms by simultaneously using the diffracting Gaussian beam from the fibre and a magnetic quadrupole funnel shaped with four electrical wires. Atoms from the MOT are then released and gravity pulls them down toward the bi-force funnel. Figure 2.6 shows a schematic of their experimental setup. They measured 3000 atoms loaded into the fibre core. Two years later, they were

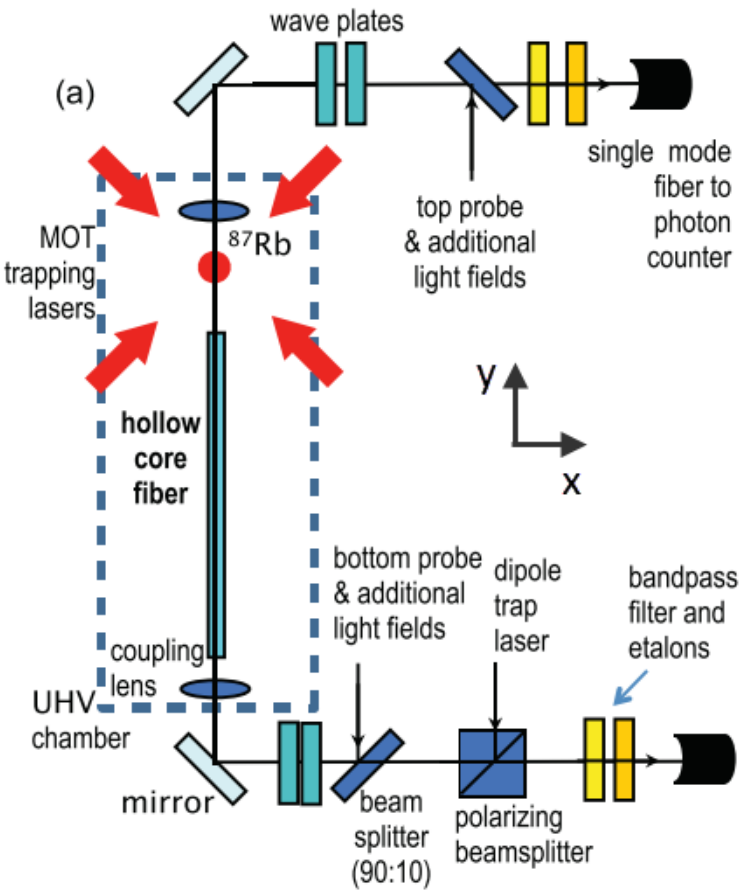

Figure 2.6: Schematic of the experimental setup. A Rb MOT is realized 10 mm above a vertically mounted HC-PCF. Top and bottom probe and guiding beams are coupled into the fibre with the help of control and detection optics. *Figure modified from [22].*

able to improve the loading technique by a factor of ten [22]. They replaced the magnetic quadrupole funnel by a collimated 0.5 mm diameter blue-detuned hollow beam with a repulsive sheet beam positioned 1-mm in front of the fibre. A cross section of its intensity and MOT confinement results are shown for the experimental setup to generate the hollow beam, in Figure 2.7 (a-d). This technique lowers the MOT much closer to the fibre while still strongly confining them in space and the sheet beam dissipates the kinetic energy gained from the drop. Figure 2.7 (e) shows the absorption image of the atoms stopped by the sheet beam and confined in the hollow blue-detuned beam. I named it the "optical elevator technique" because it is a representative imagery of the occurring atoms dynamics and makes it simpler to refer to this precise technique later on.

Most recently, Okaba et al. [23] pushed the limits of atomic coherence spectroscopy by

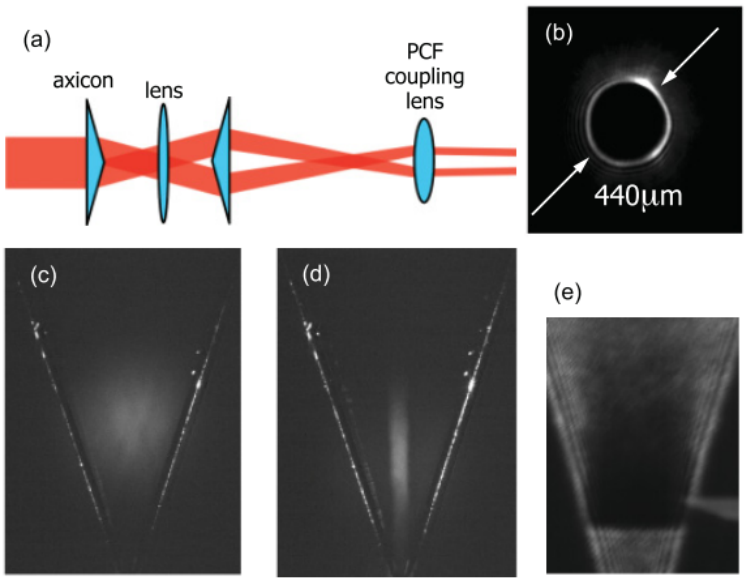

Figure 2.7: Experimental results of the optical elevator technique to improve atom coupling. (a) Schematic of the optics to generate the hollow beam. (b) Image of the intensity cross-section of the hollow beam. (c) Fluorescence image of the atomic cloud 20 ms after release without the hollow beam. (d) Same imaging as in (c) with the addition of the blue-detuned hollow beam. (e) Absorption image of the atoms collected 1 mm above the fibre by the sheet beam and confined with the hollow beam. *Figure from [22].*

loading Strontium atoms one-by-one from a MOT into a hollow Kagome fibre core in an optical lattice which confines atoms in the axial and transversal dimensions. This scheme allows an increase in the optical depth in precision spectroscopy while preserving the atomic coherence time by preventing atom collisions with the walls and between atoms.

2.6 Single-mode guidance of de Broglie waves

The prospect of single mode atomic wave guiding [50] is most promising for applications in atomic lithography and a large area atom interferometer because the atoms can maintain their coherence for a short distance outside of the fibre [28, 71]. To date, single spatial mode guiding of atoms has never been achieved in a fibre but it was demonstrated experimentally by magnetic guidance of sodium atoms over a distance of 12 mm [58]. The atoms were loaded directly from a magnetic microtrap on a substrate where the BEC was transferred using optical tweezers. It was demonstrated that only a transverse confinement is necessary to guide matter waves in a single spatial mode, even if the longitudinal velocity is significant.

The conditions to achieve single-mode guidance are challenging but may be within reach in the near future. Renn et al. [63] calculated that atoms at 200 nK launched into a 2-μm-diameter fibre would propagate in a single transverse atomic mode.

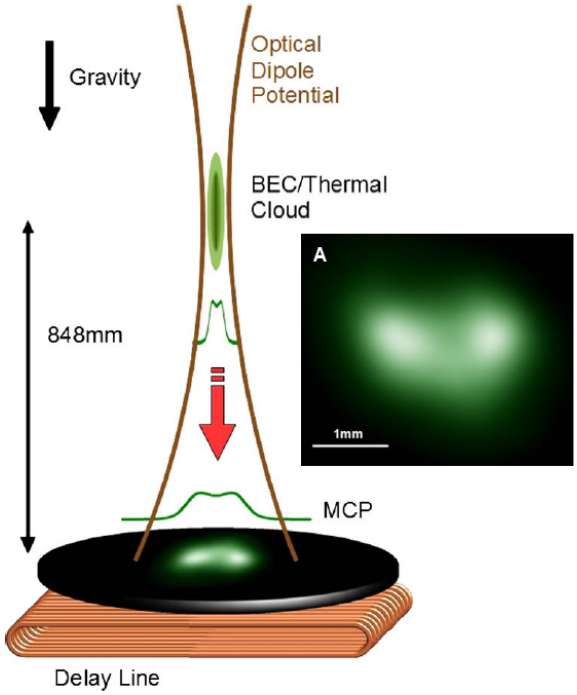

Figure 2.8: Experimental setup. A thermal cloud is guided in the focal point of a single mode 1550 nm laser beam and down toward a microchannel plate (MCP) and delay line detector. [Subset A] Image of the intensity of the guided atoms, propagating in a distribution of multiple atom modes, imprinted on the MCP. *Figure modified from [25].*

More recently, Dall et al. [25] guided a BEC of He* in vacuum in a single atomic mode (see experimental setup in Figure 2.8). Atoms were guided into a Gaussian optical dipole potential. They measured a near perfect Gaussian spatial intensity profile from the guided matter waves. When they used warmer atomic ensembles, they could observe speckled patterns in the density distribution of the guided atoms (see Figure 2.8 (a). This speckle originates from interference of the atomic modes. When the number of modes is too large, the interference becomes too fine to be measured. This experiment demonstrated that atomic speckle patterns appear like their photonic equivalents and can be observed with a single atom micro-channel plate detector. With the appropriate fibre, achieving single-mode atomic guidance may be the next step that could open the door to high coherence atom interferometers.

Table 2.1: Summary of results from Rb atom guiding experiments in the literature

Reference	Atom source	Capillary / Fibre / light tunnel	Guiding beam	Atom flux and efficiency	Peak density
Renn 1995,1997 [49, 63]	Thermal Rb oven	Capillary core/cladding diam. 40/144 μm 3.1 cm long	Gaussian red detuned 45 mW / -6 GHz $U_0 = 71$ mK	2 x 10^4 at./s	N/A
Renn 1996 [64]	Thermal Rb oven	Capillary 20/144 μm 6 cm long	Evanescent wave blue detuned 500 mW / +3 GHz	6 x 10^4 at./s	N/A
Ito 1996 [66]	Thermal Rb beam 10^6 at./s $v_l = 300$ m/s $v_{tr} = 0.3$ m/s	Doped ring hollow fibre hollow/ring/cladding diam. 7/15/150 μm 3 cm long	Evanescent wave blue detuned 280 mW / +3 GHz	3.5 x 10^5 at./s Guiding eff. 40%	N/A
Ito 1997 [67]	Thermal Rb beam 10^6 at./s	Doped ring hollow fibre hollow/ring/cladding diam. 7/15/150 μm 4 cm long	Evanescent wave blue detuned 38 mW / +3 GHz	2 x 10^5 at./s	N/A
Muller 2000 [65]	^{87}Rb LVIS (Cold beam) 10^9 at./s Temp. transverse: 50 μK (8 cm/s)	Capillary 100/160 μm 23.5 / 30.5 cm long $v_{tr} = 9.4$ cm/s	Evanescent wave blue detuned 55 mW / +6 GHz	5.9 / 5 x 10^5 at./s Guiding eff. 3%	N/A
Takekoshi 2007 [74]	Thermal Rb beam Peak density: 1.1 x 10^7 cm^{-3}	Hollow core PCF (Blaze HC800-01) core/mode diam.: 7 / 3.8 μm 6.1 cm long	Gaussian red detuned 0.5 - 4 mW / 10 - 350 GHz Coupling eff. 10 - 30%	5 x 10^4 at./s Guiding eff. 70%	N/A
Bajcsy 2009 [30]	^{87}Rb MOT 10^7 atoms, temp.: 40 μK	Same as Takekoshi 2007, 3 cm long Additional magnetic quadrupole guide	Gaussian red detuned few mW, $U_0 = 10$ mK in core	N/A	Optical Density = 30 3000 atoms in fibre
Vorrath 2010 [34]	^{85}Rb MOT Temp.: 10 μK Peak density: 1.5 x 10^{11} cm^{-3}	HC-PCF (Crystal Fibre Air-12-1060) Guide at 1060 nm, 12 μm core 8.8 cm long	Gaussian very far red detuned Two counterpropagative beams orthogonally polarized 2.3 W each, 1067 nm, $U_0 = 2$ - 8 mK Coupling eff. 80%	Peak: 1.2 x 10^5 at./s Cont.: 1.5 x 10^4 at./s $v_l = 0.45$ - 1.5 m/s	5 x 10^{11} cm^{-3} 7400 atoms in fibre
Bajcsy 2011 [22]	Same as in Bajcsy 2009	Same as in Bajcsy 2009 No magnetic guide, Optical elevator tech.	Same as in Bajcsy 2009 Coupling eff. 25%	$v_l = 0.35$ - 1.4 m/s Atoms temp. in fibre: 1.6 mK No guiding data	Optical Density = 180 30 000 atoms in fibre Gaussian only = 5000 at.
Pechkis 2012 [77]	^{85}Rb MOT 10 μK	3-cm-long, 100-micron-diameter hollow rod with silver-coated walls	Red detuned HE_{11} loading and guide + Hollow TE_{01} guide	Opt. eff. 45% Hollow: 10x less scatt.	HE_{11}: 10^6 TE_{01}: 10^5
Okaba 2014 [23]	^{88}Sr MOT few μK	32-mm-long kagome cladding lattice HC-PCF with hypocycloid core shape	813 nm optical lattice lasers Counterpropagative	up to 53 mm/s	10^4 atoms loaded
Wolschrijn 2002 [55]	^{87}Rb MOT Temp.: 4 μK Cloud RMS diam.: 0.4 - 1.4 mm	NO FIBRE, light tunnel Beam diam.: 1.1 mm Propagated on: 6.5 mm (28 ms)	Gaussian red detuned 85 mW / -70 GHz $U_0 = 22\mu$K	Guiding eff. 40%	2 x 10^9 cm^{-3}
Mestre 2010 [57]	^{87}Rb MOT 10^7 atoms, temp.: 20 μK Cloud RMS diam.: 0.3 mm	NO FIBRE, light tunnel Beam diam.: 0.3 - 1 mm Propagated on: 10 mm (45 ms)	Laguerre-Gaussian LG_0^l blue detuned 200 mW / 25 - 250 GHz $U_0 = 3$ - 88 μK	Guiding eff. up to 25 %	N/A

2.7 Analysis and state-of-the-art summary

Thermal and cold Rb atoms have been guided both in OCF and HC-PCF to varying degrees of efficiency. Table 2.1 highlights the results obtained in atomic guidance with thermal and cold atoms through capillaries (OCF) and fibres (HC-PCF). Results from two staple publications on guiding atoms in vacuum using Gaussian and Laguerre-Gaussian beams are also listed for comparison. Of particular interest are the results of peak guided atom flux, guiding efficiency and peak density in the hollow core.

So far, atomic guidance studies are difficult to compare because setups, atom sources and coupling techniques can be quite different. There is no standard methodology to count the guided atom flux; there could be important systematic errors involved depending on the detection method whether it is with a micro-channel plate, hot wire, CEM, sheet beam probing or MOT recapture. There is also a problem of methodology in assessment of the guidance efficiency; all guided isotopes including ballistic atoms are counted in the transmission efficiency rather than only the atoms targeted for guidance. This issue was made clear by Ito et al. [66] in a detailed analysis of atom flux. In their calculations, they corrected their measurements for solid angle captured by the detector and multiplied the value by the quantum efficiency of the detector. They repeated the flux for each guided atom species and its excitation state. They also added the background signal from ballistic atoms. In other publications, details on how the guided atom rates were calculated are missing. Also missing was whether it was a transmission or guidance efficiency. This makes it difficult to compare the numbers across publications.

An example that perfectly illustrates the challenge of comparing the efficiency of atom guidance techniques is the latest free-space guidance literature. Results from Wolschrijn et al. [55] using Gaussian red-detuned collimated guidance and Mestre et al. [57] Hollow blue-detuned collimated guidance of ^{87}Rb are summarized at the bottom of Table 2.1. First, they both have MOT sources but in the red-detuned case the temperature is $4\,\mu$K and in the blue-detuned case, it is five times warmer at $20\,\mu$K. A warmer cloud will be guided with reduced efficiency compared to a colder ensemble. The cloud size, guiding beam diameter and trapping potential are all on a comparable scale but the guiding length is almost twice as long in the blue case when compared to the red case. Overall, the guiding efficiency of the hollow blue guide is 25% whilst the Gaussian red guide reached 40% but with a shorter guide and a MOT 5 times colder. Thus, we can infer that the hollow blue guidance is a technique with significant advantages over the red-detuned scheme.

In previous experiments involving vacuum and capillary guidance of atoms, hollow blue-

detuned beams have always outperformed Gaussian red-detuned guidance. The most convincing evidence are the experiments of Renn et al. [63, 64] (see the first two entries in Table 2.1) at JILA in Colorado. They used the same source of Rb and the same coupling technique (a red-detuned Gaussian funnel). Using a capillary twice as long with a diameter half as big in the blue case, they enhanced Rb atom flux by a factor of 3 with blue-detuned evanescent waves compared with a red-detuned Gaussian beam [64]. Moreover, when Bajcsy et al. [22] used a collimated blue-detuned hollow beam to assist the atomic coupling to the fibre; they improved it by a factor of ten. Pechkis et al. [77] also guided atoms in OCF and observed a reduced light scattering by a factor of ten in blue-detuned hollow guidance vs. red-detuned beams.

There are historical reasons for the type of waveguide used for the optical dipole trap. Before 2007, OCFs were the only atomic waveguides in use. Not being a true optical fibre, OCFs are limited in useful length because only grazing incidence modes are transmitted in the core (it is an antiguide). The mode intensity decays significantly with the propagation distance and is characterized by an attenuation length: $L_e = 2.4r^3/\lambda^2$ [80], a distance at which the intensity is reduced to $1/e$ of its input level. Since the attenuation length is proportional to the cube of the radius of the capillary core, it is necessary to have at least a $20\,\mu$m radius to guide the dipole trap beam over a distance of a centimetre.

Guiding light in the cladding of the OCF presents some problems. The cladding is a true waveguide and supports low loss optical modes but at the same time it is not single-moded. Thus, the many modes interfere creating a non-uniform evanescent field with regions of destructive interference. This non-uniformity caused by the evanescent field speckle is an important source of atom guidance loss [64]. Also, the coupling technique focusing light into a single zone of the cladding requires at least 0.4 mm, a distance called the equilibrium length, to produce a guided mode that can guide atoms. This is the reason why Renn et al. [64] used a Gaussian red-detuned escort beam focused into the core to achieve the atomic coupling. The doped ring fibre in Ito et al. [66] was used to produce a thinner guidance region supporting just a few modes.

In the 2000s, the development of photonic crystal fibres [81] and hollow band gap guidance [73], allowing very low loss optical transmission in a hollow core, made these fibres available for new experiments for atom guidance. In these hollow core photonic crystal fibres (HC-PCF), the optical modes are much smaller than the core itself i.e., $3.8\,\mu$m $1/e^2$ in a $7\,\mu$m diameter core for Blaze Photonics HC-800-01. For the first time, the dipole trap beam had a constant potential during its propagation in the fibre. The HC-PCF yielded a very high

guidance efficiency (70%) despite the poor laser coupling efficiency and the thermal Rb source at high temperature (160°C). A similar PCF fibre can also support a hollow laser mode in the core given the proper band gap design [35], although it has not yet been used in an atom guidance experiment.

HC-PCFs are the most interesting for research in atom guidance, but there are very few commercial products available (Blaze Photonics^{TM}/Crystal Fiber^{TM}). Therefore there has been limited choice in selecting an optimal core diameter. However, even with an optimal core diameter fibre, there is a trade-off between atomic coupling efficiency (that ultimately depends on the cooling mode coupling efficiency and the source temperature and density) and limiting available atomic modes to achieve speckle-free propagation.

The best peak flux was achieved with a 100 μm diameter fibre by Muller et al. [65] which guided 5.9×10^5 at./s over 23.5 cm in the fibre. They also obtained 5.0×10^5 at./s in a 30.5-cm-long capillary. Extrapolating a reported loss of 0.13×10^5 at./(s·cm), according to calculations they would have achieved up to 8.2×10^5 at./s in a 6-cm-long capillary, a length comparable to other atom guidance experiments in the literature. The LVIS source they used was the determining factor for this achievement as it was able to output 10^9 cooled at./s which yielded a high atom flux, even considering the poor coupling efficiency of the experiment at under 3%.

Currently, the experiment by Muller et al. [65] demonstrated guided atoms over the longest distance in a 30.5-cm-long OCF. But this is not representative of what could be achieved because so far there have been challenges to guide atoms over longer distances. Mostly the length of fibre is selected according to the space available in the vacuum chamber to mount a straight fibre. We believe a guidance over 50 cm could be achieved with HC-PCF, if space is available in the vacuum chamber setup.

For study of nonlinear interactions between light and matter and, eventually, atomic single-mode guidance, experiments by Vorrath et al. [34] and Bajcsy et al. [22] are atom guiding/coupling achievements. In the publication by Vorrath et al., they obtained up to 7400 atoms simultaneously in the fibre for a density of 5×10^{11} at./cm^3, which were transmitted horizontally at longitudinal velocities up to 1.5 m/s. This density is three times higher than the peak density in their MOT source. Nonetheless, because of the longitudinal movement and the absence of background vapour we suspect that there are less Rb-Rb collisions as well as repulsive interactions than in the MOT. With their optical elevator technique, Bajcsy et al., demonstrated the best coupling technique of atoms from a MOT into the fibre core. In a fibre 3 times shorter and an area 3 times smaller than Vorrath et al., they coupled 4 times

as many atoms (30 000). The calculated atomic density from the beam area and spread of the cloud gives a density 36 times higher, probably close to $2 \times 10^{13}\,\mathrm{cm}^{-3}$. Such a density is 2 orders of magnitude above the peak density in a standard Rb MOT [82]. Data on the transmission of atoms was not part of this study. It is possible that at this density Rb-Rb collisions dominate to such an extent that few atoms are guided out of the fibre. There was no other information related to the atom dynamics within the fibre, except for interactions with photons.

CHAPTER 3 COOLING, TRAPPING AND GUIDING ATOMS: A THEORETICAL BACKGROUND

This chapter will present the theoretical and experimental framework behind the interaction between neutral atoms and coherent optical fields that serves as the foundation of this thesis. The material and equations developed in this chapter follows mainly from reference books in atomic physics [83], laser cooling [84] and atom optics [85]. Specifically, it will describe the optical forces to achieve cooling and guiding of atoms. These elements will be integrated and then shown how they are applied to realise a magneto-optical trap in order to produce an experimental source of cold atoms to couple into a fibre. Specific characteristics of the energy level structure of rubidium will be discussed. Then, will be reviewed the saturated absorption spectroscopy technique to measure the atom hyperfine levels and use them to stabilize the laser frequency in order to achieve laser cooling.

3.1 Atom optics: controlling atoms using laser light

Atom optics is a subfield of atomic physics that concerns the control of atomic motion, in an analogous way to the control of photons, by the use of electromagnetic fields. Beams of atoms can be reflected, focused, split and applied in atomic interferometry experiments. Considering an atom in a light field, interaction with a coherent light field can generate two different forces: a non-conservative on-resonance force called spontaneous force and a conservative off-resonant force called the dipolar force.

3.1.1 Spontaneous emissions: lighting the way to atom cooling

The first one is the most used in atomic physics and is responsible for laser cooling. The realisation of optical molasses and the cooling mechanism theory gave Claude Cohen-Tannoudji, Steven Chu and William D. Philipss the 1997 Nobel prize in Physics. It further led to the realization of Magneto-Optical traps [86] and Bose-Einstein Condensates [15], cooling atoms to less than 500 picoKelvin [87].

The spontaneous force (originally called light pressure force, resonance radiation pressure or light scattering force) relies on the absorption of coherent light by atoms. Each time a photon is absorbed, it transfers a momentum kick $\Delta\mathbf{p} = \hbar\mathbf{k}$ to the atom. The rate of absorption, and therefore the spontaneous force, is strongest when the light frequency is resonant with a closed atomic transition. The force gets its name from the spontaneous

emission event that follows when the electron in the excited state relaxes back to the ground state. The relaxation occurs at a rate of $\Gamma = \tau^{-1}$, the natural linewidth of the transition that is equal to the inverse excited state lifetime. This force relies on spontaneous emission to release excess energy. It is dissipative because its action cannot be reversed, spontaneous absorption being impossible.

The direction of a spontaneous emission event is random so that over many recoil events, it doesn't result in any net movement, $<\Delta\mathbf{p}> = 0$. There is still some accumulated energy from these events as $<\Delta p^2> \neq 0$. A way to visualize this recoil heating effect is to imagine that these spontaneous emission events are such that they propel the atom in a circular motion, no net movement comes from the emissions but each event has the effect of propelling the atom faster in the circular orbital, increasing its total kinetic energy.

The Doppler shift key to atom cooling

To summarize, when atoms are scattering coherent light because it is resonant with an atomic transition, they gain (or lose) momentum $\hbar\mathbf{k}$ depending on their own velocity and the direction of the laser beam wave vector. Spontaneous emissions also heat the atom from the recoil of spontaneously emitted photons without any preferential direction. The key to produce laser cooling is to have the atoms only absorb counterpropagating photons such that their momentum will be dampened along that direction by absorption photon recoil. This is accomplished by opposing the laser relative detuning, δ, to the Doppler shift of counterpropagating atoms:

$$\delta + \omega_D = \omega_l - \omega_a - \mathbf{k} \cdot \mathbf{v} = 0 \tag{3.1}$$

where, ω_l is the laser absolute frequency and ω_a the transition resonance frequency. The Doppler shift ω_D is the negative dot product of the wave vector $\mathbf{k}$ and the atom velocity vector $\mathbf{v}$. When the frequency of the laser is below the resonance of the transition, the detuning is negative and is described as red detuned. When the frequency is above resonance and detuning is positive, it is said to be blue detuned.

Atoms are cooled in 3D space by arranging laser beams in counterpropagating pairs following three orthogonal directions intersecting in a vacuum chamber containing an atomic vapour. Then, by red detuning the frequency of those lasers, the Doppler shift creates an imbalance in the spontaneous force in such a way that atoms are in resonance mostly with the laser opposite to their movement. In the centre, where all six beams are intersecting, atoms from any direction can be cooled down. Cooled atoms, no longer in resonance with the red detuned beams, start slowly drifting randomly in the beam. This state is called optical

molasses.

Atomic velocity as temperature

In laser cooling, it is convenient to reduce the average kinetic energy of an atom distribution to a temperature. When atoms are emitted from a source they exchange heat with the environment by making contact with the walls of the vacuum chamber. If the source is remotely located from the main chamber, it is adequate to describe the velocity distribution of the atoms as a Maxwell-Boltzmann distribution:

$$f(v) = \sqrt{\frac{2}{\pi}} \frac{m^{3/2} v^2}{(k_B T)^{3/2}} \exp\left(\frac{-mv^2}{2k_B T}\right) \tag{3.2}$$

where $f(v)$ is the probability per unit velocity that an atom has velocity within the interval v, $v + dv$. The temperature T of this distribution would then correspond to a thermodynamic equilibrium temperature. When the atoms start being cooled, they are no longer in a thermodynamic equilibrium but they can achieve steady-state conditions and are adequately characterized by a Maxwell-Boltzmann velocity distribution (in 3D). Thus, describing them by a temperature is a convenient way of describing their velocity distribution. Their average kinetic energy is:

$$< E_r >= \frac{1}{2} m \bar{v}^2 = \frac{3}{2} k_B T \tag{3.3}$$

where $\bar{v}$ is the root mean square (rms) velocity such that:

$$\bar{v} = \sqrt{< v^2 >} = \sqrt{\frac{3k_B T}{m}} \tag{3.4}$$

In a magneto-optical trap, under high density conditions, the atoms will start adopting unorthodox velocity distributions and in this case characterizing them by a temperature isn't adequate and must be interpreted with care.

Recoil temperature

Considering a gas of atoms at $T = 0$K (at rest) that is exposed to a beam of resonant light for τ such that on average each atom experiences only a single absorption-emission cycle. The gas temperature will become $T = 2T_r$ where T_r is the single-photon recoil temperature limit. Simple thermodynamic yields:

$$T_r = \frac{\Delta p^2}{2k_B m} = \frac{\hbar^2 \omega^2}{2k_B m c^2} \tag{3.5}$$

Rubidium atoms cooled on the second resonant transition (D_2 line), would reach a recoil temperature of $0.37\,\mu$K. Further cooling is possible but one has to resort to manipulating the energy state of the atom to strategically tune off the force at certain times.

Spontaneous force

The spontaneous force was formulated by Ashkin in 1970 as the product of the momentum kick imparted by the photon absorbed and the scattering rate of photons from the beam:

$$\mathbf{F}_{sp} = \Delta\mathbf{p}\gamma_s \tag{3.6}$$

The scattering rate γ_s (identified with symbol R in older textbooks) is expressed as the product of Γ, the natural linewidth of the transition, with ρ_{ee} the steady state excited population fraction:

$$\gamma_s = \Gamma\rho_{ee} = \frac{\Gamma}{2}\left(\frac{s}{s+1}\right) \tag{3.7}$$

and the resulting force is:

$$\mathbf{F}_{sp} = \hbar\mathbf{k}\frac{\Gamma}{2}\left(\frac{s}{s+1}\right) \tag{3.8}$$

where s is the saturation parameter, which describes how efficiently the atomic transition gets excited by the laser light. The force is maximum when $s \gg 1$ and the steady state excited population reaches $\frac{1}{2}$.The saturation parameter is defined [84] as

$$s = \frac{\Omega^2/2}{\Gamma^2/4 + \delta^2} \tag{3.9}$$

The Rabi frequency Ω represents the strength of the coupling between a classical light field of intensity I and the atomic transition. It is defined by the expression:

$$\Omega = \Gamma\sqrt{\frac{I}{2I_s}} \tag{3.10}$$

and the saturation intensity I_s [84] is

$$I_s = \frac{\pi hc}{3\lambda^3\tau} \tag{3.11}$$

where h is Planck's constant, c and λ are light's velocity, wavelength and τ is the excited state lifetime.

By combining equations 3.9 and 3.10 into 3.8, the spontaneous force is expressed in terms of the spontaneous decay rate Γ, the transition saturation intensity I_s and the experimental laser parameters of intensity and detuning (Eq. 3.1):

$$\mathbf{F}_{sp} = \hbar\mathbf{k}\frac{\Gamma}{2}\frac{I/I_s}{1 + I/I_s + (2\delta/\Gamma)^2} \tag{3.12}$$

The spontaneous force is strongest when the laser frequency is resonant with the atomic transition ($\delta = 0$) and at large detunings, $\delta >> \Gamma$, decays as the inverse square of the

detuning ($F_{sp} \propto 1/\delta^2$). Increasing the laser intensity at resonance does not increase the force without limit because the excited state population fraction cannot exceed $\frac{1}{2}$, the force saturates at a maximum value of $\hbar k\Gamma/2$.

In this maximum saturation equilibrium state, excited state and ground state populations are equal. A higher population in the excited state is not possible in two-level atoms because the pump rate and the radiative decay rate are the same. Population inversion, a necessary condition for light amplification, can be achieved in three or four level atoms where the decay rate is smaller than the pump rate. In a two-level atom, if the population were greater in the excited state, the amount of electrons relaxing during a time $\frac{1}{\Gamma}$ would be greater than the number of electrons excited at saturation thus returning to a larger ground state population. In laser cooling and atom guiding, the atom is conditioned to a stable or metastable state and a particular transition is targeted, thus, it is effectively behaving as a two-level atom [84]. This is why the equations of light radiation forces, analytically derived from two-level atomic models, are valid approximations.

Above light intensities that saturate the force on-resonance, it still continues to increase off-resonance. This creates power broadening and changes the relationship with detuning. The natural linewidth becomes the power-broadened linewidth:

$$\Gamma' = \Gamma\sqrt{1 + I/I_s} \tag{3.13}$$

and the spontaneous force becomes:

$$\mathbf{F}'_{sp} = \hbar\mathbf{k}\frac{\Gamma}{2}\left(\frac{I/I_s}{1 + I/I_s}\right)\left(\frac{1}{1 + (2\delta/\Gamma')^2}\right) \tag{3.14}$$

In Figure 3.1, the power-broadened spontaneous force has been represented as a function of detuning for 5 different intensities spanning 4 orders of magnitude. Power broadening is noticeable above an intensity of 10 I_s. In real world experiments, other kinds of line broadening effects occurs as well: lifetime broadening (due to the uncertainty principle) and Doppler broadening (due to the movement of the atoms). One must be aware that the measured linewidth can be a convolution of multiple broadening effects. This is examined closely in Sec. 3.5.

Energy and momentum conservation

Earlier was shown that the spontaneous force is dissipative, but when taking into account the energy transfer with the light field, the system conserves energy, momentum and angular momentum.

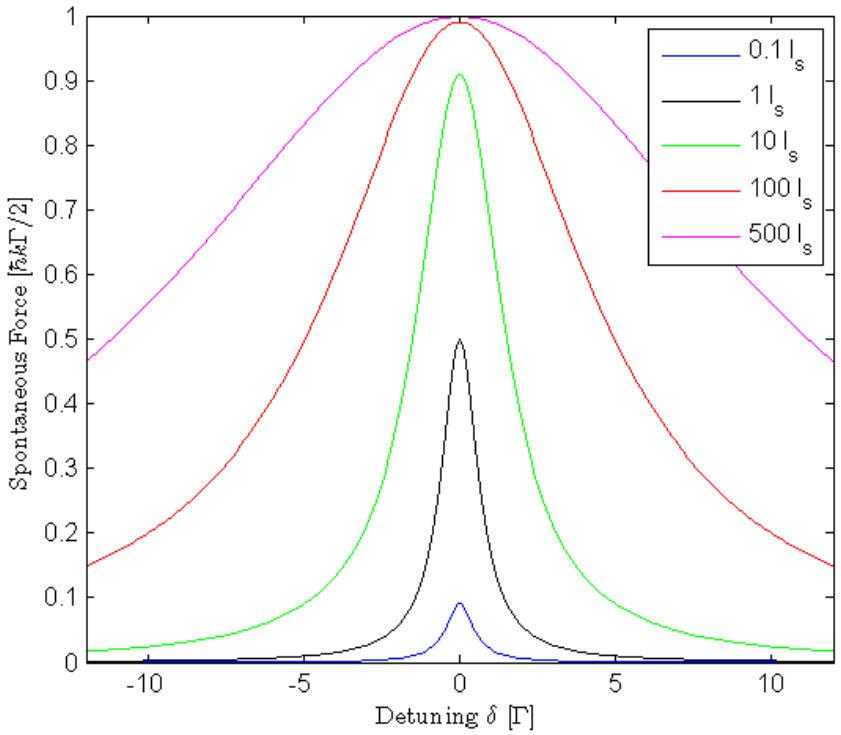

Figure 3.1: Spontaneous force on a two-level atom at rest. The force (in units of the maximum force) is expressed as a function of the laser detuning for 5 different intensities: 0.1, 1, 10, 100 and 500 times I_s the saturation intensity. Power broadening appears above 10 I_s.

A photon carries energy $\hbar\omega$, momentum $\hbar\mathbf{k}$ and angular momentum $\hbar$. When an atom absorbs a photon, the energy is stored by allowing an electron to jump into a higher energy state, the momentum is conserved by recoiling (receiving a momentum kick) and the angular momentum is conserved by internal reconfiguration of the electrons into Zeeman sublevels. When the atom momentum changes by $\hbar k$, its kinetic energy changes by the recoil energy $E_r = \hbar^2 k^2/2m = \hbar\omega_r$. During absorption of a photon, the energy transferred to the atom, averaged over many events, is $\hbar(\omega_a + \omega_r)$ and the energy emitted is $\hbar(\omega_a - \omega_r)$ so that the light field transfers on average $2\hbar\omega_r$ of energy to the atom at each absorption-emission cycle.

Laser absorption through an atomic gas medium

After reviewing light scattering and spontaneous force on two-level atoms at rest in section 3.1.1, the impact of laser intensity will be discussed from an experimental point of view. When a laser beam is going through a vapour of atoms, its intensity decreases with distance

z following the relation:

$$\frac{dI}{dz} = -\hbar\omega_a\gamma_s n \tag{3.15}$$

where n is the atomic density and γ_s is the scattering rate of light. For low to moderate intensity ($I < 10I_s$) and close to resonance, the light scattering rate $\gamma_s \approx \Gamma I/(2I_s)$. Inserting this approximation into Eq. 3.15 gives $dI/dz = -\sigma_{eg} nI$ where the photon-atom scattering cross-section, using I_s definition (Eq. 3.11) becomes $\sigma_{eg} = \hbar\omega\Gamma/(2I_s) = 3\lambda^2/(2\pi)$. The solution of the intensity as a function of distance in the vapour is then:

$$I(z) = I_0 e^{-\sigma_{eg} nz} \tag{3.16}$$

Applying this relation to rubidium atoms to calculate the density to obtain 50% absorption over 1 mm gives $2.5 \times 10^9\,\mathrm{cm}^{-3}$. These densities are realized in optical traps, so its expected that absorption at the edge of the trap will strongly reduce the force in the centre. Reabsorption of spontaneously emitted photons will also cause additional pressure on the inside of the trap resulting in experimental density and trap size limitations.

3.1.2 Dipolar force: conservative guiding of atoms

In atom guiding, the dipolar force (also called gradient force) controls atomic motion perpendicularly to its beam direction, thus making the optical potential field an effective atom waveguide. This force is a direct consequence of the energy conservation in a quasiresonance electric field that induces an AC Stark shift on the energy levels of the atom. The AC term comes from the fact that the electric field of light is oscillating [DC stark shifts occurs when atoms are exposed to static external electric fields]. AC Stark shifts are often labeled as light shifts [84]. To be effective, the force doesn't require the atom to have a permanent electric dipole because the high frequency of the laser field induces a temporary electrical dipole moment, the atom is said to enter a polarised state. This force was predicted by Einstein, in 1909, to be significant in the optical and infrared parts of the electromagnetic spectrum [85].

When the atom is in a blue detuned electric field (higher frequency, lower wavelength than its atomic transition), its ground state energy is shifted up proportionally to the laser field intensity (see Figure 3.2). The atom's potential energy is increased and due to conservation of energy, its kinetic speed is reduced proportionally. An atom travelling toward regions of high field intensity would be slowed down to a halt (if the light shift gradient is large enough) and then pushed back to regions of lowest intensity by the dipole force. It is important to note that if the two-level atom is in an excited state, the effect of the force is completely opposite for the same blue detuned field. The excited atom would be attracted towards regions of

high intensity. For red detuned fields, the effect of the force on atoms, in the ground state or excited state, is the reverse of the case with a blue detuned field.

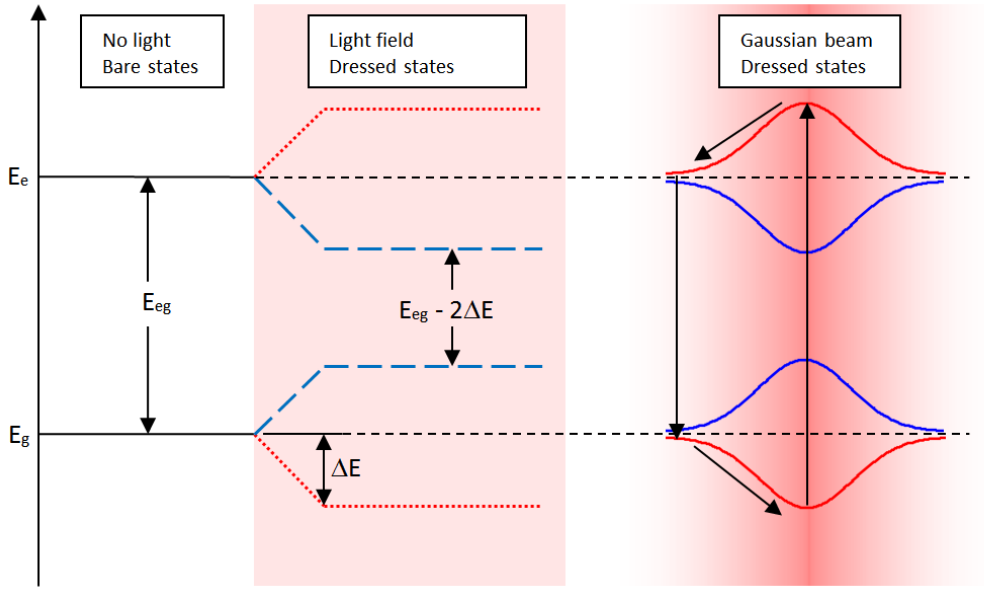

Figure 3.2: Diagram of the energy levels AC Stark shift induced by the laser electric field. The red dotted line corresponds to a red detuned field while the blue dashed line represents the blue detuned field. The amplitude of the light shift ΔE is equal to the dipolar trapping potential U. On the rightmost, the ground and excited state bowing under the AC Stark shift in a Gaussian intensity distribution is shown. The arrows indicate the absorption-emission cycle that would produce the maximum viscous dipolar heating, amounting to twice the trapping potential U. Such heating would allow the atom to immediately escape from the trap.

With the atomic ground state energy modified by the AC Stark effect light shift (ΔE), the resulting dipolar trap potential is given by [88]:

$$U = \frac{\hbar\delta}{2} ln\left[1 + \frac{\Omega^2/2}{\delta^2 + \Gamma^2/4}\right] \tag{3.17}$$

The dipolar force is conservative and therefore its expression can be obtained by the negative gradient of the potential or derived from the solutions of the optical Bloch equations [89]:

$$\mathbf{F}_{dip} = -\frac{\hbar\delta}{4} \frac{\nabla\Omega^2}{\delta^2 + \Gamma^2/4 + \Omega^2/2} \tag{3.18}$$

In the limit of large detunings $\delta \gg \Gamma, \Omega$ which is the usual case in optical dipolar traps, the

potential has a simpler form:

$$U \simeq \frac{\hbar\Omega^2}{4\delta} \tag{3.19}$$

and the large detuning expression of the dipolar force, written in terms of measurable quantities using Eq. 3.10 is:

$$\mathbf{F}_{dip}(r,z) \simeq -\frac{\hbar\Gamma^2}{8\delta I_s}\nabla I(r,z) \propto \frac{I}{\delta} \tag{3.20}$$

Both expressions of the dipolar force (Eqs. 3.18 and 3.20) are illustrated against detuning in Figure 3.3. The solid line represents the exact dipolar force equation while the dashed line is the large detuning approximation. The force against detuning is plotted for 4 intensities (1, 10, 25 and 100 I_s). This conservative force doesn't saturate and just keeps increasing with intensity but it is also observed that the maximum is pushed to larger detunings with increasing intensity. For the lower intensities, the quick agreement between the exact expression and its approximation is noticed. For larger intensities, larger detunings are necessary before observing agreement and satisfying the condition $\delta \gg \Omega$.

Viscous dipolar heating

When using the dipole force for atom trapping and guiding, one must avoid exciting the atoms or else the potential has a reverse effect which results in viscous dipole heating and losses. Favorably, the dipolar force scales with detuning as $\frac{I}{\delta}$ while the spontaneous force scales as $\frac{1}{\delta^2}$. This means that for very large detunings, the spontaneous force becomes increasingly smaller while the dipolar force also decreases but proportionally becomes larger than light scattering. Thus, using large detunings minimize spontaneous emissions as shown in Figure 4.8 and Figure 4.9.

At intermediate detunings, the situation is quite different because there is a certain amount of excitation and there is definitely a stronger conservative trapping potential. In atom guiding experiments that measured the atom flux vs. detuning at different intensities [49], a definite "hole-burning effect" is observed at these intermediate detunings as shown in Figure 2.2 b)-d). This dip in atom flux at intermediate detunings is caused by viscous dipolar heating. Earlier, the discovery of viscous dipolar heating was briefly presented in section 2.1 using Figure 2.1 (b).

In Figure 3.2, the energy levels of an atom bowing under the light shifts caused by the AC Stark effect in a Gaussian light beam are represented. The black arrows show the largest cycle of viscous dipolar heating.

In this cycle, the atom gains transversal kinetic energy equals to twice the potential depth which is more than enough energy to escape the guide. Fortunately, this is an extreme case

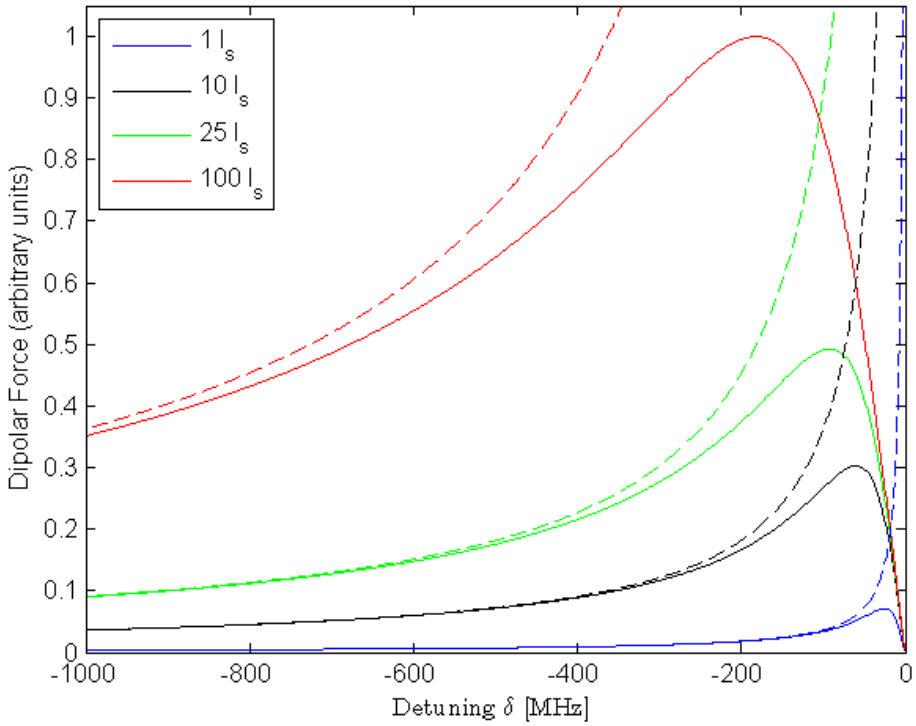

Figure 3.3: Dipolar force as a function of the detuning of the laser at 4 different intensities (1, 10, 25 and 100 I_s). The exact formulation (solid line) is compared with its large detuning approximation (dashed line). The maximum of the force is pushed toward larger detunings with increasing intensity. For a valid approximation, larger detunings are also necessary with increasing intensity to satisfy the large detuning condition and reach agreement with the exact formulation of the force.

of viscous dipolar heating and in most situations the atom will not have time to complete this cycle to its full extent. In this off-resonant excitation, the atom will have an excited lifetime of $\tau_a = 2(\pi\Gamma)^{-1} \simeq 0.64\tau$ before relaxing [49]. Its transversal velocity might also favorably oppose viscous heating forces leading to smaller gains. Nonetheless, this heating effect produces important guiding losses whenever the dipolar trapping is at its strongest but can be reduced with larger detunings.

Evidence of this effect was also observed by measuring atom flux for a fixed detuning while increasing the intensity, as shown in Figure 3.4. For low intensity where the large detuning condition is satisfied, the atom flux increases linearly with intensity. At higher intensity, the atom flux starts to decrease indicating that the amount of viscous heating allowed guided

atoms to escape the trapping potential. This is happening because larger intensities result in larger light shifts as well as increased absorption probability (breaking the large detuning condition). This leads to more cycles of absorption-emission and the energy gains are more important because of the larger trap potential. Therefore, viscous heating becomes more important with increasing intensity.

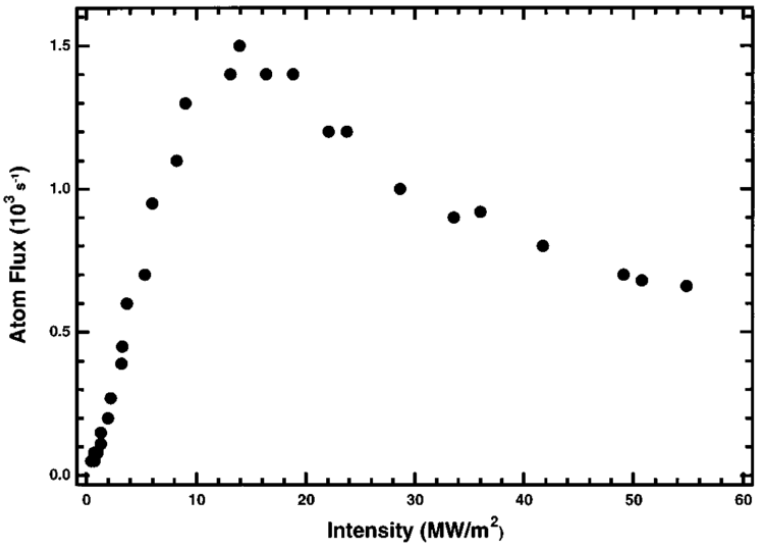

Figure 3.4: Intensity dependence of the guided atom flux for a fixed -8 GHz detuning. Initially, the atom flux will increase linearly with intensity as expected from the conservative component of the dipolar force because the large detuning condition $\delta \gg \Omega$ is satisfied. At a certain intensity, this behavior breaks up and the atom flux starts decreasing with further increases in guiding light intensity. This break up is caused by the viscous dipolar heating which amounts sufficiently to cause guiding losses. *Figure from [49].*

Viscous heating is also a limiting factor in the useful length of the fibre in atom guiding experiments, because a longer fibre means more interaction time with the guiding potential. These forces being nonconservative, the viscous heat is just building up over time with no known mechanism to cool atoms inside the fibre. However, as was previously mentioned, viscous heating can be reduced at larger detunings, eliminating losses and allowing to use longer fibres.

Another strategy consists in using a blue detuned hollow guide such that atoms spend more time guided in the dark, where there is no light shift of their energy levels. Thus, no viscous heating is possible during that time.

3.2 Optical molasses

In previous sections was discussed the key concept in optical cooling of neutral atoms whereby the use of the Doppler effect and a red-detuned laser beam create an imbalance in the spontaneous forces. This imbalance causes the spontaneous force to be dominant in the direction opposite to the atoms propagation direction. When combined in a setup using three pairs of orthogonal and counterpropagating laser beams with orthogonal polarisations, it creates a dissipative force that dampens atoms kinetic energy in all directions. These slowed atoms are called optical molasses. But this is not sufficient to achieve spatial trapping, a local concentration of the molasses. A force component with spatial dependence is necessary to keep the slow atoms in the centre. An efficient way to create this is by generating a magnetic field gradient in 3D that is null where the 6 laser beams overlap. This magneto-optical trap became the most important and widely used of all optical traps because it is quite robust under realistic conditions of operation, i.e., misaligned optical beams, optical interferences, stray magnetic fields along with environmental disturbances. The current theory that serves as the foundation to atom guiding experiments will be reviewed in the following subsections.

3.2.1 The Doppler model

In section 3.1.1 was discussed the spontaneous emission process behind the spontaneous force (Eq. 3.8). Since the ratio of intensity to saturation intensity is heavily used, a symbol is defined for the on-resonance saturation parameter as

$$s_0 = \frac{I}{I_s} \tag{3.21}$$

Considering the situation of a moving atom, in one dimension, in the field of two red-detuned laser beams facing each other, using the expression of the Doppler-shifted detuning (Eq. 3.1), the optical molasses force is expressed:

$$\mathbf{F}_{OM} = \frac{\hbar \mathbf{k} \Gamma s_0}{2} \left(\frac{1}{1 + s_0 + [2(\delta - |\omega_D|)/\Gamma]^2} - \frac{1}{1 + s_0 + [2(\delta + |\omega_D|)/\Gamma]^2} \right) \tag{3.22}$$

This expression is valid as long as stimulated emissions are not important ($s_0 \leq 1$), which is always the case when optical cooling is desired. When the detuning is close to resonance, the force is nearly linear between its two maxima at $v = \pm\Gamma/k$. The expression of the optical molasses force in that range is simply: $\mathbf{F}_{OM} = -\beta \mathbf{v}$ where β is the damping coefficient:

$$\beta = -\frac{8\hbar k^2 s_0 \delta/\Gamma}{(1 + s_0 + [2\delta/\Gamma]^2)^2} \tag{3.23}$$

Red-detuning ($\delta < 0$) close to resonance will create a force that viscously damps atom velocities within the effective range of the force. In this context, it is convenient to define a critical velocity: $v_c = \Gamma/k$, but note that the capture velocity, that is dependent on the geometry of the trap size, is in practice several times the critical velocity. Beyond the critical velocity range, the damping force is nonlinear and weaker than the maximum but it is still efficient. The damping coefficient reaches its maximum value of $\hbar k^2/2$ for $s_0 = 2$ and $\delta = -\Gamma/2$.

In Fig. 3.5, the optical damping force is illustrated in velocity-space in units of the critical velocity for detunings of: $-\Gamma/8$, $-\Gamma/2$, $-\Gamma$ and -2Γ. For the largest detuning, the breakdown of the linear regime can be observed between the two maxima of the force. This is caused by the almost complete separation of the spontaneous force component from each beam. Each of these components is illustrated in the figure by the dashed traces. This lack of overlapping components also allows the force to reach maxima equivalent to the spontaneous force maximum $\hbar k\Gamma/4$ from a single beam at $s_0 = 1$ (see Fig. 3.1). But considering the cooling efficiency, the slope of the optical damping force near zero is the most determinant factor in reaching the lowest temperature. In the figure, the largest damping is obtained at a detuning of $\delta = -\Gamma/2$ and both lower and higher detunings produce a weaker damping.

Such a damping force would cool atoms down to zero, however it is balanced by a velocity-independent heating force: the momentum diffusion caused by spontaneous emissions. The diffusion coefficient is calculated from Brownian motion theory [84]:

$$D_0 = \frac{\Delta(p^2)}{\Delta t} = (\hbar k)^2 \cdot 2\gamma_s = \frac{(\hbar k)^2 s_0 \Gamma}{1 + s_0 + (2\delta/\Gamma)^2} \tag{3.24}$$

where $\Delta p = \hbar k$ is the momentum kick from spontaneous emission, $1/\Delta t = 2\gamma_s$ is the light scattering rate by the two beams where γ_s is defined by Eq. 3.7. By equating the heating and the cooling rates, the steady-state temperature is obtained:

$$k_B T_{ss} = \frac{D_0}{\beta}$$

$$T_{ss} = \frac{\hbar\Gamma}{4k_B} \frac{1 + s_0 + (2\delta/\Gamma)^2}{2|\delta|/\Gamma} \tag{3.25}$$

The temperature has a minimum when intensity $s_0 \ll 1$ and the detuning $\delta = -\Gamma/2$. Applying these parameters to obtain saturation $s = s_0/2$, diffusion coefficient $D_0 = (\hbar k)^2 s_0 \Gamma/2$ and damping coefficient: $\beta = \hbar k^2 s_0$. The lowest temperature achievable in this model, called Doppler temperature is then given as

$$T_D = \frac{\hbar\Gamma}{2k_B} \tag{3.26}$$

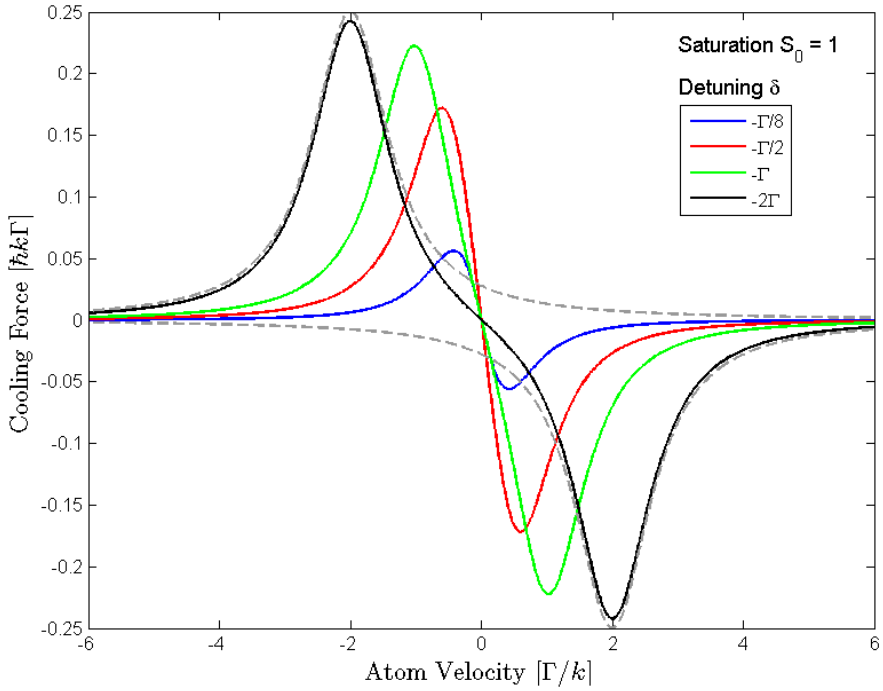

Figure 3.5: One-dimensional velocity dependence of optical damping force for 4 detunings: $-\Gamma/8$, $-\Gamma/2$, $-\Gamma$ and -2Γ. Velocity axis is in units of the critical velocity Γ/k. Dashed-trace illustrates the Doppler-shifted spontaneous force from each of the individual beams that are components of the optical damping force (in this case for $\delta = -2\Gamma$).

and from the expression of kinetic energy, the Doppler velocity is calculated:

$$v_D = \sqrt{\frac{\hbar\Gamma}{2m}} \tag{3.27}$$

From the Doppler velocity (or steady-state velocity) a velocity-independent force that balances the optical damping force at T_D (or T_{ss}) is obtained

$$F_D = \frac{D_0}{mv_D} \tag{3.28}$$

Doppler temperature was believed to be the lowest temperature achievable in optical molasses. This was a truly remarkable theoretical result at the time, as it can be obtained from several other independent ways. Because it was only dependent on the natural linewidth, it was an atomic constant as well for cold atom experiments. Table II.1 lists the Doppler temperature and velocity for some common cold atom species.

It came to quite a shock when the accurate time-of-flight method, developed at NIST to measure 3D optical molasses temperatures, determined that the sodium atoms temperature was as much as 10 times below their Doppler temperature [90]. This is a rare example when unaccounted effects in an experiment produce better results than expected. This led the way to the sub-Doppler refinement of the theory that was developed by Claude Cohen-Tannoudji [16] and Steven Chu [91], less than two years after the realization of the failure of the Doppler model. Both groups published their independent research within the same month and both of their cooling models were in strong agreement with each other.

3.2.2 Polarisation gradient cooling

There are different known mechanisms leading to cooling below Doppler temperatures. One such is magnetic orientational cooling which involves a laser standing wave of uniform polarisation in a dc magnetic field [92]. By far the most popular scheme is *polarisation gradient cooling* which is also the underlying mechanism behind magneto-optical traps. In the following, only this scheme is considered; other methods are beyond the scope of this thesis.

The Doppler model is still a good approximation for fast atoms but breaks down for atoms near and below Doppler velocity. Three key ideas led to understanding the new cooling mechanism below Doppler temperature:

1. Consideration of the fine and hyperfine structure of the atom rather than the simplistic two-level model.

2. Atoms in a standing wave from two orthogonally polarised counterpropagating beams are moving in a polarisation gradient.

3. Optical pumping within a polarisation gradient causes ground state population transfers within the Zeeman substates.

The new cooling process discovered is the link between these 3 key ideas. In fact, when the atom moves at an appropriate velocity, in the polarisation gradient, there is a non-adiabatical following of the population distribution within the ground substates that causes kinetic energy losses when the atom is excited and returns to the ground state. This results in a friction (damping) force that is stronger than the previous Doppler damping force but is effective over a much narrow range of velocities.

General properties of polarisation gradient cooling

When atoms are fast, they are insensitive to polarisation gradients. When they reach Doppler cooled velocities and are weakly pumped ($\Omega \ll \Gamma$), they start to experience the polarisation gradient effect. This effect operates at a new time scale, the optical pumping time $\tau_p = 1/\Gamma''$, which is the mean time an atom is transferred from the ground substate M_j to $M_{j'}$ in a fluorescence cycle. The optical pumping time τ_p is much longer than the radiative lifetime τ ($\Gamma'' \ll \Gamma$) and consequently is defined a new critical velocity where the sub-Doppler cooling mechanism is effective $v_c' \sim \Gamma''/k$ which is much smaller than usual velocities required for Doppler cooling scheme $v_c \sim \Gamma/k$. From these, the friction force is qualitatively expected to be strongest when atoms are travelling a distance $\lambda/4$ (the maximum polarisation gradient distance) during one optical pumping process (τ_p).

Both Doppler and sub-Doppler mechanisms are complementary. So the stronger friction forces of sub-Doppler cooling are only experienced by atoms first slowed by Doppler cooling damping forces. To prevent confusion, the sub-Doppler damping is called friction coefficient and denoted by symbol α as opposed to the Doppler damping coefficient β.

The new replacement of the momentum diffusion (heat) force is much weaker than its Doppler counterpart. It also features different dependences (over intensity and detuning) and will be defined by the type of polarisation gradient involved (lin$\perp$lin or σ^+–σ^-). The final temperature atoms settle to is still determined at the moment the cooling force is balanced by the diffusion force.

To calculate the cooling forces and predict the final temperature, the particular mechanisms involved for the two types of polarisation gradients, lin$\perp$lin and σ^+–σ^-, are considered. The cooling mechanisms of each are strikingly different, but their end result settles to about the same temperature. The scheme with circular polarisation is particularly useful because a magnetic field gradient can be used to add a spatial dependence component to its cooling force, thus, leading to the realization of a magneto-optical trap (MOT).

Linear $\perp$ linear polarisation gradient cooling (sisyphus cooling)

When two counterpropagating orthogonally linearly polarised beams create a standing wave field, the resulting polarisation changes from linear to left-circular to linear to right-circular and back to linear over the course of half a wavelength.

Previously in Sec. 3.1.2 was described how energy levels get shifted in a light field (see Fig. 3.2). The light shift described by Eq. 3.19 was for a far detuned travelling wave. This

equation can be rearranged as:

$$U = \Delta E_g = \frac{\hbar\delta s_0/2}{(2\delta/\Gamma)^2} \tag{3.29}$$

In sub-Doppler theory, the hyperfine structure and the polarisation have an important effect on the energy substates. The light shift equation is rewritten to take into account the fact that two laser beams are present (doubles the intensity) and that the light shift is specific for every substate in a given polarisation field [16]:

$$\Delta E'_g = \frac{\hbar\delta s_0}{(1+(2\delta/\Gamma)^2)} C^2_{ge} \tag{3.30}$$

where C^2_{ge} is the squared Clebsch-Gordan coefficient that describes the strength of the coupling between ground and excited substates. Reference [93] explains how to calculate these coefficients for any transition for any atom. Appendix D of ref. [84] conveniently lists all the Clebsch-Gordan coefficients squared for alkalis. The simplest structure for lin⊥lin cooling is the $J_g = 1/2 \rightarrow J_e = J_g + 1 = 3/2$. In this model, all other hyperfine transitions are ignored. The ground level features two substates $M_j = -1/2, 1/2$ that are simply noted $M_{-1/2}$ and $M_{+1/2}$ states. In a linear polarised field, the light shifts of both states are identical. In σ^+, the light shift of $M_{+1/2}$ is three times larger as the shift for the $M_{-1/2}$. The reverse applies for the σ^- polarisation.

As a result of the selection rules, atoms in σ^+ polarisation will be pumped into the ground level Zeeman substate $\mathrm{M}_{+1/2}$ and conversely a σ^- field will pump atoms into substate $\mathrm{M}_{-1/2}$. In either case, they are pumped in the substate with the lowest energy, corresponding to the largest negative light shift (negative because $\Delta E'_g$ follows the sign of the detuning). The rest of the cooling mechanism can be understood by careful examination of Fig. 3.6.

In the polarisation gradient described above, the two ground substates are oscillating up and down in energy between $-4\Delta E'_g$ and $-12\Delta E'_g$. In a given circular polarisation, atoms in the higher energy substate are pumped down to the lower substate. In the extreme case illustrated, the atom travels a distance of $\lambda/4$ during time τ_p. So it is climbing potential hills between fluorescence cycles converting its own kinetic energy to potential energy. During a fluorescence cycle, that potential energy is lost through radiative decay. The result is a dissipative friction force that is more efficient than the Doppler cooling. From this illustration, it is understood that the origin of the cooling lies in the non-adiabatic following of the atom substate when it travels in a polarisation gradient. It can only really readjust during a fluorescence cycle. This is also why this cooling is only efficient over a limited range of velocities.

This particular mechanism was termed *Sisyphus cooling* after the myth where a Greek

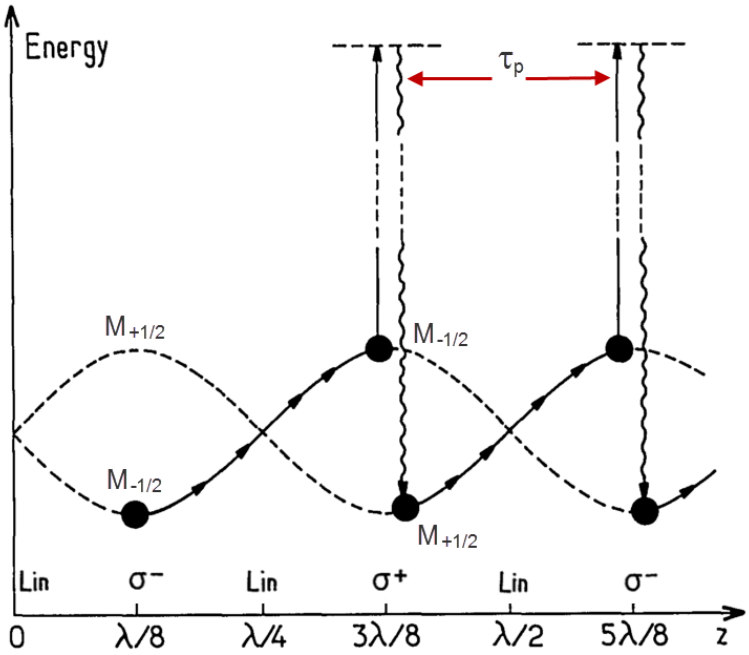

Figure 3.6: Sisyphus cooling mechanism in lin⊥lin configuration. The polarisation is identified in the bottom axis as a function of the spatial position z along the optical axis (in units of wavelength). The energy of states $M_{\pm 1/2}$ are oscillating in the polarisation gradient. The atom experiences maximum cooling because it is climbing potential hills most of the time. *Figure modified from [16]*

king was condemned by the Gods to push a boulder up a hill. This cooling mechanism is stronger than the one from the σ^+–σ^- configuration. But its momentum diffusion is also stronger, resulting in a similar steady-state sub-Doppler temperature.

σ^+–σ^- circular polarisation gradient cooling

The cooling mechanism in the circular polarisation gradient configuration is quite different, yet the resulting temperature is strikingly similar. Experimentally, this configuration is much more important because, with the addition of a magnetic field gradient, it can alter this mechanism to produce a *Magneto-Optical Trap* (MOT).

Circular polarisation is produced when linearly polarised light passes through a birefringent material (e.g. Calcite). The orthogonal axis of such a material are usually labeled fast (lower index of refraction, a direction perpendicular to the molecular chains) and slow axis (higher index of refraction, parallel to the molecular chains). By carefully selecting the thickness of this material to produce a phase difference of $\lambda/4$ at the wavelength of interest, the

resulting electric field (and magnetic field) of the traveling wave will spiral in space. From the laboratory point of view, looking at a fixed position, the electrical field vector will rotate in a clockwise or counterclockwise direction. Depending on the observer point-of-view, the rotational direction of the beam will be perceived differently. At this point, it is helpful to review the notations and definitions of circularly polarised light.

The sigma notation comes from the mathematical formulation of the polarisation vectors [84]. In the standard right-handed coordinate system:

$$\hat{\mathbf{x}} \times \hat{\mathbf{y}} = \hat{\mathbf{z}}$$

$$\sigma^+ : \hat{\mathbf{e}}_+ = \frac{-1}{\sqrt{2}}(\hat{\mathbf{x}} + i\hat{\mathbf{y}}) \tag{3.31}$$

$$\sigma^- : \hat{\mathbf{e}}_- = \frac{+1}{\sqrt{2}}(\hat{\mathbf{x}} - i\hat{\mathbf{y}}) \tag{3.32}$$

Circular polarisation is a special case of the more general elliptical polarisation. Elliptical polarisation is obtained whenever the two orthogonal linearly polarised components of the electric field are phase shifted (other than a multiple of $\pi/2$). Experimentally, circularly polarised light is produced when the angle between the quarter-wave plate fast axis (or slow axis) and the linear polariser axis is 45°.

In the laboratory, there are two designation conventions of circularly polarised light. The most commonly used in optics, followed in this thesis, is the *handedness convention* where the light is described from the source point-of-view. Taking the right hand and pointing the thumb in the propagation direction of the beam, the curl of the fingers indicates the clockwise direction of rotation to label the light *right-handed* (RH). If it is opposite (counterclockwise), it is *left-handed* (LH). In the handedness convention, σ^+ is right-handed and σ^- is left-handed.

On the opposite, the *screw convention* looks at the light beam as if it was a screw from the point-of-view of the target looking toward the source. The labeling is therefore opposite to the *handedness convention* and called *right-circularly polarised* (RCP) and *left-circularly polarised* (LCP).

When the axis of the quarter-wave plates used to produce the circular polarisation are not identified, it can be difficult to identify the true handedness of a circular polarisation but it is easy to tell one handedness from the other. So, in practice, the polarisations are often labeled right and left arbitrarily and this is correct (the physics being fully symmetric) as long as the method to label them is consistent across the experiments.

Taking two orthogonally circular polarised beams, creates a standing wave with a strong linear polarisation gradient. The polarisation vector is fixed in time but rotates uniformly

in space with a period of one wavelength (see Fig. 3.7). When looking from the point of view of any beam, the linear polarisation gradient rotates in the opposite direction as the polarisation of the beam observed.

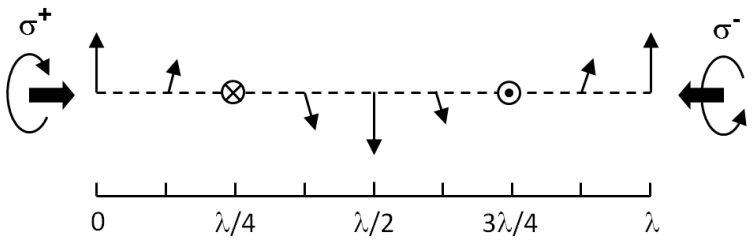

Figure 3.7: Polarisation gradient field resulting from two orthogonally circular polarised beams counterpropagating. The linear polarisation rotates in space in the opposite handedness to the beams.

For $J_g = 1/2$, in a linearly polarised field, the light shift is identical in all ground states and no atomic alignment is possible, but this is not the case when $J_g = 1$ or higher, which is a necessary condition to cool atoms in the σ^+–σ^- configuration.

The new cooling mechanism arises from the combination of two factors. The first factor is based on the atomic alignment of the ground state, i.e. population differences among the Zeeman sublevels. The rotation of the linear polarisation induces a population difference between M_{-1} and M_{+1} states. For an atom propagating at low velocity toward $z > 0$ (toward the σ^- beam), the imbalance is such that the state M_{-1} will be more populated. From the atom's point-of-view, the linear field rotation is σ^- (left-handed), which is the reason why the M_{-1} state is more populated. The reverse applies for an atom propagating in the opposite direction.

The second factor contributing to the cooling effect is the differential scattering from the two circular beams. Looking at the Clebsch-Gordan coefficients and transition strengths, an atom in the M_{-1} sublevel scatters light from the σ^- polarisation 6 times more efficiently than light from the σ^+ polarisation. The reverse is true for an atom in the M_{+1}. The resultant cooling is similar to the Doppler cooling mechanism in such that the friction forces arise from the differential absorption in which the counterpropagating beam is more scattered than the copropagating beam. The resultant friction is efficient at a much lower velocity range but is stronger than the Doppler damping coefficient. In the low velocity domain ($kv \ll \Gamma' \ll \Gamma$), the full quantum formulation of the force can be simplified to a form $f = -\alpha v$ where α is

the friction coefficient [16]:

$$\alpha = \frac{120}{17}\frac{-\delta\Gamma}{5\Gamma^2 + 4\delta^2}\hbar k^2 \tag{3.33}$$

The force reaches a maximum value of $\sim 0.8\hbar k^2 v$ for a detuning $\delta = -\sqrt{5/4}\Gamma$ ($\sim -1.1\Gamma$). Comparatively the Doppler force was maximal at $0.5\hbar k^2 v$ for a detuning $\delta = -0.5\Gamma$. The friction force is also linear over a new critical velocity range: $v < v'_c = \Delta E'_g/k$.

When considering the complete quantum formulation, taking into account states populations and coherences among those states, one can obtain an expression of the force that is valid for any velocity. Figure 3.8 shows why plots of this force against velocity in all domains (black line) and is compared with previous Doppler cooling force (dotted line). This remarkable quantum model shows that the new force expression is identical to the Doppler model for higher velocity domains but transforms to a stronger friction coefficient (steeper slope) in the low velocity limits.

The new quantum model developed by Dalibard and Cohen-Tannoudji [16] shows that this force is a single mechanism that operates continuously instead of two separate models (Doppler and sub-Doppler cooling) and it is valid only in certain velocity domains as it was initially presented. Taking into account the new momentum diffusion forces as well (see appendix B in [16]), a new expression of the final cooling temperature is obtained as

$$T = \frac{\hbar\Omega^2}{k_B|\delta|}\left[\frac{29}{30} + \frac{254}{75}\frac{\Gamma^2/4}{\delta^2 + \Gamma^2/4}\right] \tag{3.34}$$

The evolution of temperature with detuning and intensity can be broken down into two regimes:

$$\text{for } \Gamma/2 \leq |\delta| < 3\Gamma\text{: } T \propto 1/\delta^3$$

$$\text{for } |\delta| \gg \Gamma\text{: } T \propto I/\delta$$

For large detunings, the temperature is proportional to the light shifts intensity (see Eq. 3.20). For intermediate detunings, this relationship breaks down due to a change in the momentum diffusion forces.

Cooling molasses: temperature and capture range considerations

Note that for both cases of polarisation gradient cooling the resulting dependences are opposite to what was found in Doppler cooling. For Doppler cooling, the damping coefficient was found to be proportional to the laser power. The capture range, defined where the force is linear within the critical velocity limit, is independent of power. Now in polarisation gradient cooling, the friction/damping coefficient is independent of power but the capture range does

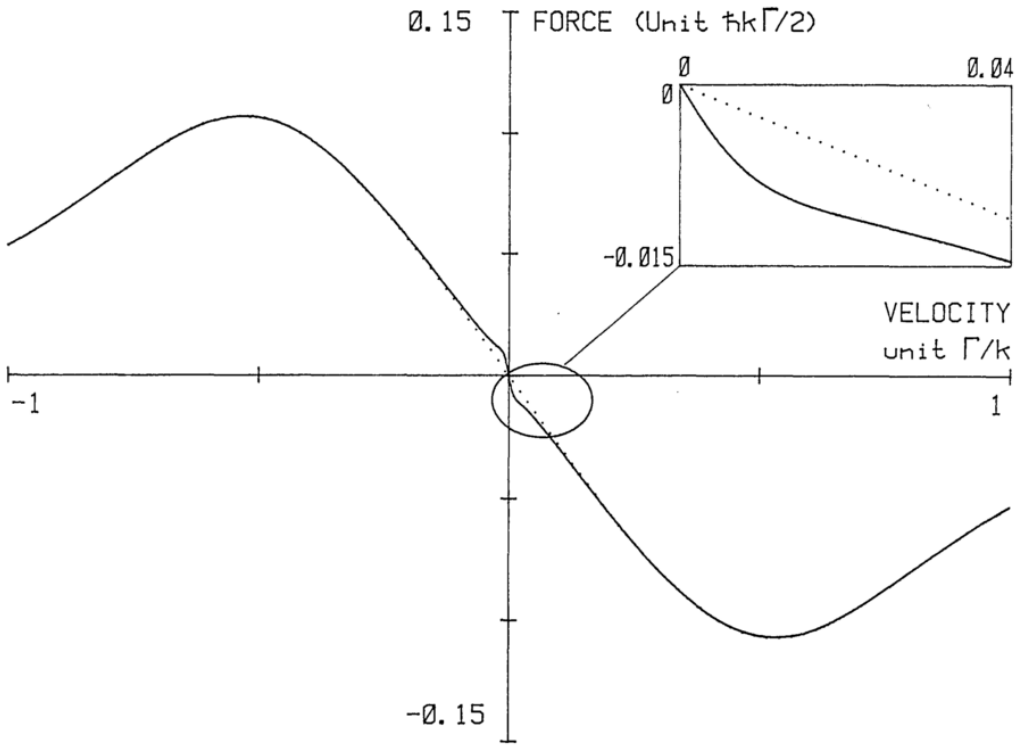

Figure 3.8: Spontaneous radiative force as a function of atom velocity for a $J_g = 1 \rightarrow J_e = 2$ transition in the σ^+–σ^- configuration with intensity $\Omega = \Gamma/4$ and detuning $\delta = -\Gamma/2$. Around $v = 0$ (see also inset), the slope gets steeper in polarisation gradient cooling (solid line) as compared to the Doppler cooling regime (dotted line). The negative slope is a result of the negative detuning (red detuned laser frequency) yielding the force its dissipative/cooling character. *Figure from [16].*

depend on it. Since the diffusion of momentum is also dependent on power, the resulting final temperature will, finally, also depend on the laser power.

A major issue for experimentalists is therefore arising: one cannot produce very large molasses and have it very cold simultaneously. Because optimizing for low temperature (low power, large detuning) also significantly reduces the velocity capture range of the trap and therefore reduces the proportion of atoms cooled.

Another limitation in working with molasses is that there is no localized force so that even when the atoms are cooled, they are not trapped and are just free to drift away, out of the beams. Both of these issues found solutions that will be highlighted in the next section.

3.3 Magneto-optical trapping

The original idea of the magneto-optical trap (MOT), also earlier known as the Zeeman shift optical trap (ZOT), was suggested by Jean Dalibard [84] and was first demonstrated [86] at Bell Laboratories in collaboration with David Pritchard's MIT group. Later, a simpler setup was demonstrated at NIST (Colorado) where the MOT was loaded directly from a background low-pressure vapour in a small glass cell [94].

In this trap, the magnetic field does not contribute directly to the trapping, its magnitude being 100 times below the level required for magnetostatic trapping, so the direct force applied is negligible [86] and cannot support alone the atoms against gravity. The role played by the magnetic field is rather to create a shift in the excited Zeeman substates (denoted M_F in the case of real alkali atoms, or M_J for the simpler case discussed here) such that the absorption imbalance mechanism of the σ^+–σ^- polarisation gradient cooling will be modified to include a localization component to the force around the magnetic field minimum of the chamber. Note that the magnetic field enhances the σ^+–σ^- polarisation gradient cooling mechanism by adding a spatially dependent component, like a spring, to the force. Therefore, using a lin⊥lin beam configuration in a magnetic field gradient will not produce a MOT.

It was also interesting to realize that the new force component had no significant heating or cooling effect on the atoms. The temperature obtained in the MOTs was also below the Doppler limit and in the same range as that achieved with optical molasses [94–97]. Using a magnetic field gradient does not only concentrate the atoms captured, it significantly enhances the velocity capture range of the molasses force and a lot more atoms are slowed, captured in the trap and achieve higher densities. For example, in a typical sodium molasses, the capture velocity is $\sim 6\,\mathrm{m/s}$ but in a sodium MOT, atoms at velocities of $70\,\mathrm{m/s}$ can be captured.

The capture mechanism will be explained in more detail in the following subsections, where the magnetic field and the MOT model are also covered.

3.3.1 Effect of a magnetic field on atom cooling

To produce a 3D trap, it is required to have a magnetic gradient that spans everywhere in space and that is zero at the centre. The simplest and most used is the spherical quadrupole magnetic field that is produced by using two coils with opposite currents, a configuration dubbed anti-Helmholtz (see Fig. 3.9). When the radius-to-distance ratio is equal to $\sqrt{3}$ it produces an ideal constant magnetic field gradient $\mathbf{A} = d\mathbf{B}/dz$ (the anti-Helmholtz condition). The magnetic field gradient in the transverse plane to the coils axis is at half the

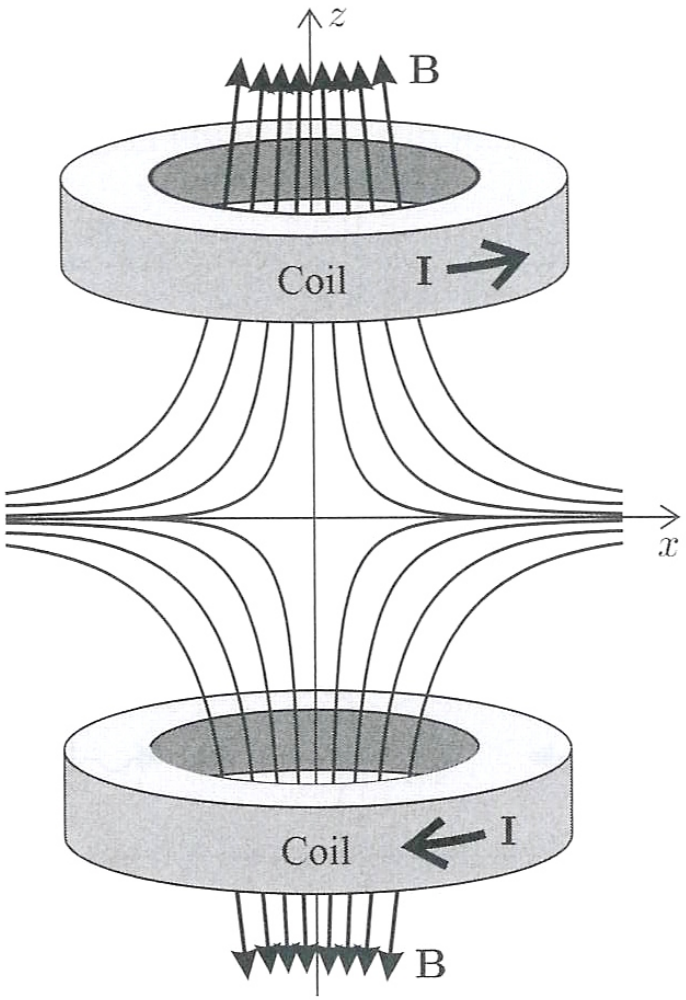

Figure 3.9: A pair of coils with opposite currents generates a magnetic spherical quadrupole field. The field magnitude decreases linearly in every direction until it reaches zero in the centre. Figure from [83].

on-axis gradient (A/2). This is a direct consequence of Maxwell's equation $\nabla \cdot \mathbf{B} = 0$ [83].

Fundamentally, the effect of a static magnetic field on the cooling molasses force is to shift the zero crossing point of the force proportionally to the Zeeman shift. This is illustrated in Fig. 3.10 where for a positive magnetic field, the force profile is shifted positively in velocity space. The atoms in this static magnetic field are now cooled to the velocity-selective resonance $v_{vsr} = \omega_z/k$ where ω_z is the Zeeman shift:

$$\omega_z = \frac{\mu' B(z)}{\hbar} = \frac{(g_e M_e - g_g M_g)\mu_B}{\hbar} Az \tag{3.35}$$

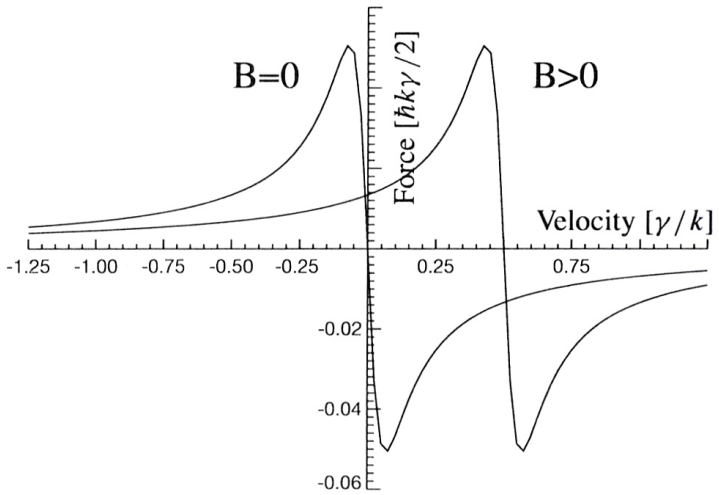

Figure 3.10: Effect of a static positive magnetic field on the σ^+–σ^- polarisation gradient force as a function of velocity. In a magnetic field, atoms are cooled to the velocity selective resonance corresponding to the zero-crossing point of the force. Figure from [84].

where $B(z)$ is the magnetic field at position z, A is the field gradient and μ' is the effective magnetic moment for the transition. For most alkalis cycling transitions (including rubidium), $\mu' = (1/2 * 4 - 1/3 * 3)\mu_B = \mu_B$, Bohr's magnetron.

In experimental conditions, the Earth's magnetic field and the ion pump produce stray magnetic fields in the chamber. While these fields are usually not strong enough to prevent the MOT from functioning, they shift the zero crossing of the quadrupole gradient in space but also increase the velocities of atoms within the trap, leading to increased cooling temperatures. Failure to properly cancel stray magnetic fields in the centre even led early experiments to measure optical molasses and MOTs as hot as Doppler temperature. These particular issues along with observations relative to stray fields cancelling will be discussed in chapter 5.

Now considering a magnetic field gradient, there is an imbalance in the magnetic field shifted force that pushes the atoms toward ever smaller v_{vsr} until it reaches zero in the centre. As it tries to move away from the centre, the shift in the force creates a more efficient capture force with an imbalance that pushes them again toward the centre. The next subsection will present the mathematical formulation of the force leading to these dynamics.

3.3.2 The overdamped oscillator MOT model

The magnetic field gradient creates a spring like force that acts on the atoms to keep them at the centre, but comparatively to the formidable cooling damping force, the restoring spring-like force component is no match. The resulting effect is the MOT is behaving like an overdamped oscillator. The optical molasses force (Eq. 3.22) becomes in the MOT[1] [83]:

$$\mathbf{F}_{MOT} = \frac{\hbar \mathbf{k} \Gamma s_0}{2} \left(\frac{1}{1 + s_0 + [2(\delta - |\omega_D| - \omega_z)/\Gamma]^2} - \frac{1}{1 + s_0 + [2(\delta + |\omega_D| + \omega_z)/\Gamma]^2} \right) \quad (3.36)$$

By numerically integrating the equation of movement of an atom submitted to this force, in a large statistical distribution (like those generated in a Monte Carlo model), solutions of the MOT properties like its velocity capture range are found. This equation is the semiclassical approximation to the complete and more accurate quantum model described in Dalibard et al. [16] Appendix B. The following equations are analytical approximations derived from the semiclassical and/or the quantum model for a restricted set of conditions. They are presented in detail as they are key in understanding the dynamics of the system. Around the zero crossing point of the magnetic field, small atom velocities ($v \ll \Gamma/k$) and small Zeeman shifts ($\omega_z \ll \Gamma$) only are present. Under these conditions is derived an approximation of the force where the spatial and velocity components are decoupled [84]:

$$\mathbf{F}_{MOT} = \alpha \mathbf{v} - \kappa \mathbf{z} \quad (3.37)$$

where α is the friction coefficient from the σ^+–σ^- polarisation gradient (Eq. 3.33) and κ is the spring constant of the MOT:

$$\kappa = \frac{\mu' A}{k\hbar} \alpha \quad (3.38)$$

The particularity of this system, compared to the classical mechanics damped oscillator, is that the spring constant is proportional to the friction coefficient. This is expected since the restoring force is only a component of the cooling force, because the magnetic field, by itself, doesn't exert any force on the atoms. It only splits in energy the degenerate magnetic substates M_J (M_F). For example an atom with J=1 (like in the example of Sec. 3.2.2) in a positive magnetic field, the substate M_J=+1 is shifted up in energy and M_J=-1 is shifted down, proportionally to the Zeeman shift. The substate M_J=0 is unaffected. The inverse applies for a negative magnetic field. The resulting energy splittings in the magnetic field gradient are clearly illustrated in Fig. 3.11. The frequency of the energy levels is represented

[1] In Metcalf [84], there is a sign error: $\omega - (\omega_0 + \omega_z) = \delta - \omega_z$ not $\delta + \omega_z$ for the positive valued Zeeman shift.

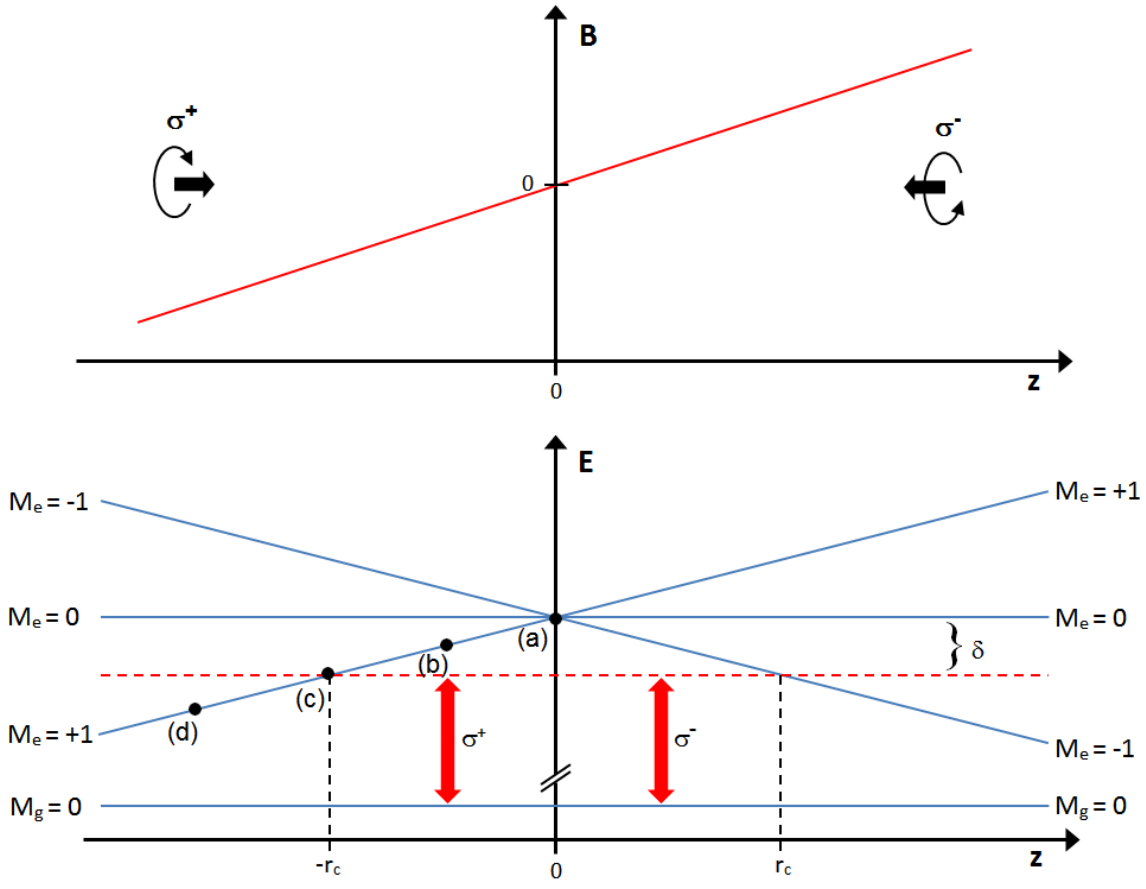

Figure 3.11: Zeeman splitting of the energy levels of an atom in the simple case of a $J_g = 0 \rightarrow J_e = 1$ atomic transition. (Top) Magnetic field gradient in z is shown as well as the polarisation of each beam. (Bottom) Energy of the Zeeman splitted magnetic substates as a function of position z. The capture radius r_c is at the position where the Zeeman splitting is equal to the laser detuning.

from the point of view of an atom at rest. The red-dotted line represents the red detuned cooling laser. The magnetic substates are both modified with the Zeeman shift caused by the magnetic field gradient. In the centre, point (a), the atoms are normally cooled as in an optical molasses. As they move away from the centre (b), the shift of M_J=+1 brings atoms closer to resonance with the σ^+ beam and further from the σ^- beam which first enhances the imbalance and yields a stronger damping. In (c), the most energetic atoms trapped are stopped here and are resonant only with the σ^+ which pushes them back toward the trap centre. Point (c) defines the capture radius, the maximum distance a captured atom can move away from the centre before the damping force turns blue detuned for an atom at rest.

It is obtained by simply equating the Zeeman shift ω_z with the laser detuning δ:

$$r_c = \frac{\hbar\delta}{\mu' A} \tag{3.39}$$

Experimentally, the capture radius is always limited by the cooling beam radius but it is the magnetic field gradient and the detuning that sets the size of the capture volume within the cooling beams overlap. Tuning of the capture radius r_c will affect the number of atoms N captured in the trap. To obtain the largest MOT, the capture radius needs to be set as large as the cooling beam radius.

Finally in point (d), an atom sees the cooling beams as blue detuned so it cannot even be slowed to an optical molasses. This is an effect of the magnetic field, it enhances trapping inside the capture radius but outside of it, it doesn't even cool the atoms, in contrast with optical molasses that can cool atoms, at least in 1D, anywhere in the laser beam.

3.3.3 Capture velocity and MOT size models

The capture velocity is a useful quantity to estimate the number of atoms that can be trapped in the MOT. It is defined as the highest velocity to capture in the MOT an atom propagating in 1D across the capture diameter. The capture velocity can be computed precisely by integrating the equation of velocity in the overdamped oscillator model of the MOT presented earlier. For close detunings, it can be estimated assuming the atoms are subjected to half the maximum optical molasses deceleration in the following formula:

$$v_c = \sqrt{r_c \cdot a_{max}/2} = \sqrt{r_c \frac{\hbar k \Gamma}{8m}} \tag{3.40}$$

where r_c is the capture radius (Eq. 3.39) and a_{max} is the optical molasses maximum force (see Sec. 3.2.1) divided by the atom's mass. This approximation is mostly valid for close detunings ($< 10\Gamma$) because it doesn't take into account that the capture radius is limited by the beam radius. As the detuning increases, the force weakens but the capture radius increases which favors an increase in the capture velocity. When the capture radius cannot increase anymore with detuning, the weakening of the force is no longer being compensated which leads to a steep decrease in the capture velocity (almost like a cutoff).

The number of atoms that can be captured in the MOT is determined by the balance between the capture rate with the loss rate of the trap following this simple rate equation [94]:

$$\frac{dN}{dt} = R - N/\tau \tag{3.41}$$

where R is the trap loading rate, N is the number of atoms in the trap and $1/\tau$ is the loss rate of the trap (1/lifetime). This rate equation has a general solution:

$$N(t) = N_0(1 - e^{-t/\tau}) \tag{3.42}$$

and $N_0 = R\tau$ is the number of atoms at steady-state. Given a Maxwell-Boltzmann velocity distribution, the density n of atoms in the chamber (obtained from the vapor pressure data), the velocity capture v_c and trapping volume V that is characteristic of the trap, one obtains for the MOT loading rate:

$$R = \frac{nv_c^4}{2V^{3/2}} \left(\frac{m}{2k_B T} \right)^{3/2} \tag{3.43}$$

and the loss rate:

$$\frac{1}{\tau} = n\sigma \sqrt{\frac{3k_B T}{m}} \tag{3.44}$$

where σ is the atom-atom scattering cross-section. The steady state number of atoms in the *capture-loss rate* model is then [94]:

$$N_0 = \frac{v_c^4}{\sqrt{6}V^{3/2}\sigma} \left(\frac{m}{2k_B T} \right)^2 \tag{3.45}$$

The next chapter will compare experimental measurements of the number of atoms in the MOT with this theoretical model based on the experimental parameters.

One final remark is that the capture radius is not related to the final rms radius of the MOT. The equipartition theorem states that at steady state conditions, the average kinetic energy is given by [84]:

$$\frac{1}{2}k_B T = \frac{1}{2}mv^2 = \frac{1}{2}\kappa r^2 \tag{3.46}$$

times the degrees of freedom for the system, where v is the root-mean-square (rms) velocity and r is the rms radius which in a normal distribution corresponds to the radius one standard deviation away from the centre (or at a position corresponding to the maximum of the distribution divided by e). In experimental conditions, one cannot solely measure the MOT temperature based on the size of the MOT at equilibrium because this assumes that the trap potential is ideally harmonic which is rarely the case. This would also require knowing the trap spring constant which cannot be inferred just by observing the MOT at equilibrium. In chapter 5, expanding on these notions, the MOT temperature will be measured accurately by observing the thermal expansion dynamics of the MOT from the time it is released from the trap.

3.4 Atomic structure of laser cooled atoms

As seen in the previous section, laser cooling is a process of cyclic absorption-emission in which the momentum of the atom in one direction is reduced by the momentum kicks of absorbed photons from the laser in the opposite direction. Therefore, atoms that can be laser cooled have a two-in-one requirement: having a closed loop (cycling) transition that is at a frequency for which there is lasers available. The atom often also exhibits one or few forbidden/secondary transitions around the cycling transition but they will need to be compensated by lasers that will repump the electron back in the cycling transition.

Before going further into manipulation of the atomic states and how rubidium atoms are cooled, it is helpful, for readers less familiar with atomic physics to consult Appendix I: Review of the quantum mechanical model of the atom. Appendix II: Atom candidates for laser-cooling, details the general characteristics and properties of neutral atoms and molecules suitable for laser-cooling and trapping.

3.4.1 Atomic structure and the cooling cycle of rubidium

The quantum model of the atom presented in Appendix I describe the fine and hyperfine energy level structure of a given atom. This structure is also rigorously confirmed by spectroscopic data. The energy levels of both ^{85}Rb and ^{87}Rb are illustrated by Fig. 3.12 and 3.13 respectively.

Spin-orbit coupling creates a fine structure splitting of the p-orbital doublet 5P separated by 7 THz. These two transitions are identified by spectroscopists as D_1 line, $5^2S_{1/2} \rightarrow 5^2P_{1/2}$ at 795 nm and D_2 line, $5^2S_{1/2} \rightarrow 5^2P_{3/2}$ at 780 nm. At this level, there is only a few MHz of difference between the two isotopes of Rb. The structural differences between the two atoms appear at the hyperfine level caused by the nuclear spin coupling with the electron's magnetic and electric momenta. Their nuclear spin of 5/2 in ^{85}Rb and 3/2 in ^{87}Rb causes the hyperfine splitting, in the latter, to be more than twice as large. Quantum theory also calculates accurately the relative strength of transitions from one hyperfine ground state to each of its permitted transitions. Selection rules state that in dipolar electric coupling (such as the one provided by a single photon absorption) the allowed atomic transitions can only have a momentum change $\Delta J = 0, \pm 1$. Thus, this is why the closed-loop transition from $5^2S_{1/2}$ F=3$\rightarrow 5^2P_{3/2}$ F'=4 is obtained. The electron in this excited state can only relax back to the F=3 ground state. Transition to F=2 ground state cannot be provided by a single photon emission as it would violate conservation of the angular momentum (as stated by the ΔJ selection rule). Transitions between the fine structure excited states $5^2P_{1/2}$ and $5^2P_{3/2}$

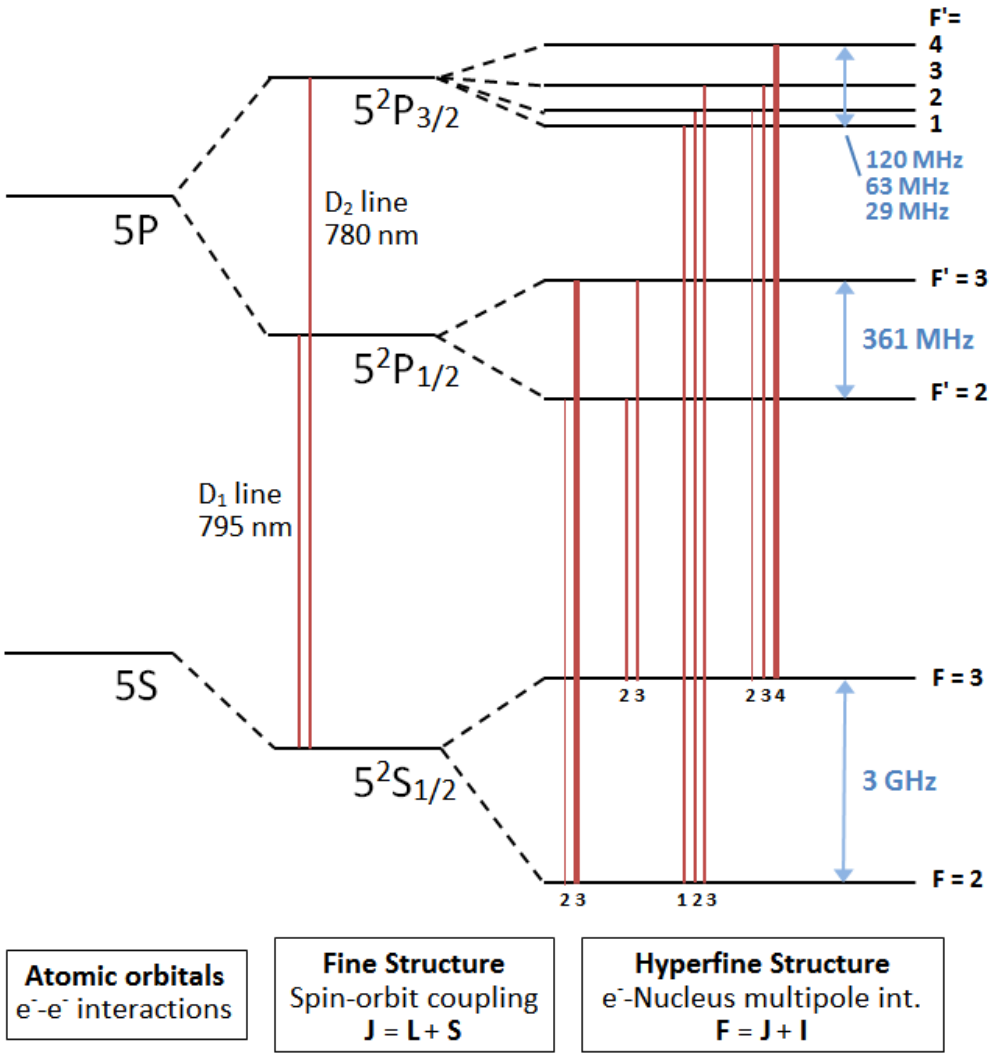

Figure 3.12: Fine and Hyperfine structure of ^{85}Rb for D_1 and D_2 transitions. The vertical lines between the hyperfine ground and excited states show all the permitted transitions according to the atomic selection rules. The small number under each line from the ground states identifies the excited hyperfine F-number. The thickness of the lines also qualitatively shows the transition strength of each transition relative to its neighbours. The figure is not drawn to scale but each hyperfine splitting frequency is identified, as well as the fine structure transition at 795 nm (377 THz) and 780 nm (384 THz).

are also forbidden as they would violate the parity of the angular momentum. In the two figures, each allowed transitions are represented by vertical lines of varying thickness between the hyperfine levels. Numbers at the bottom of each transition represent the excited F' state.

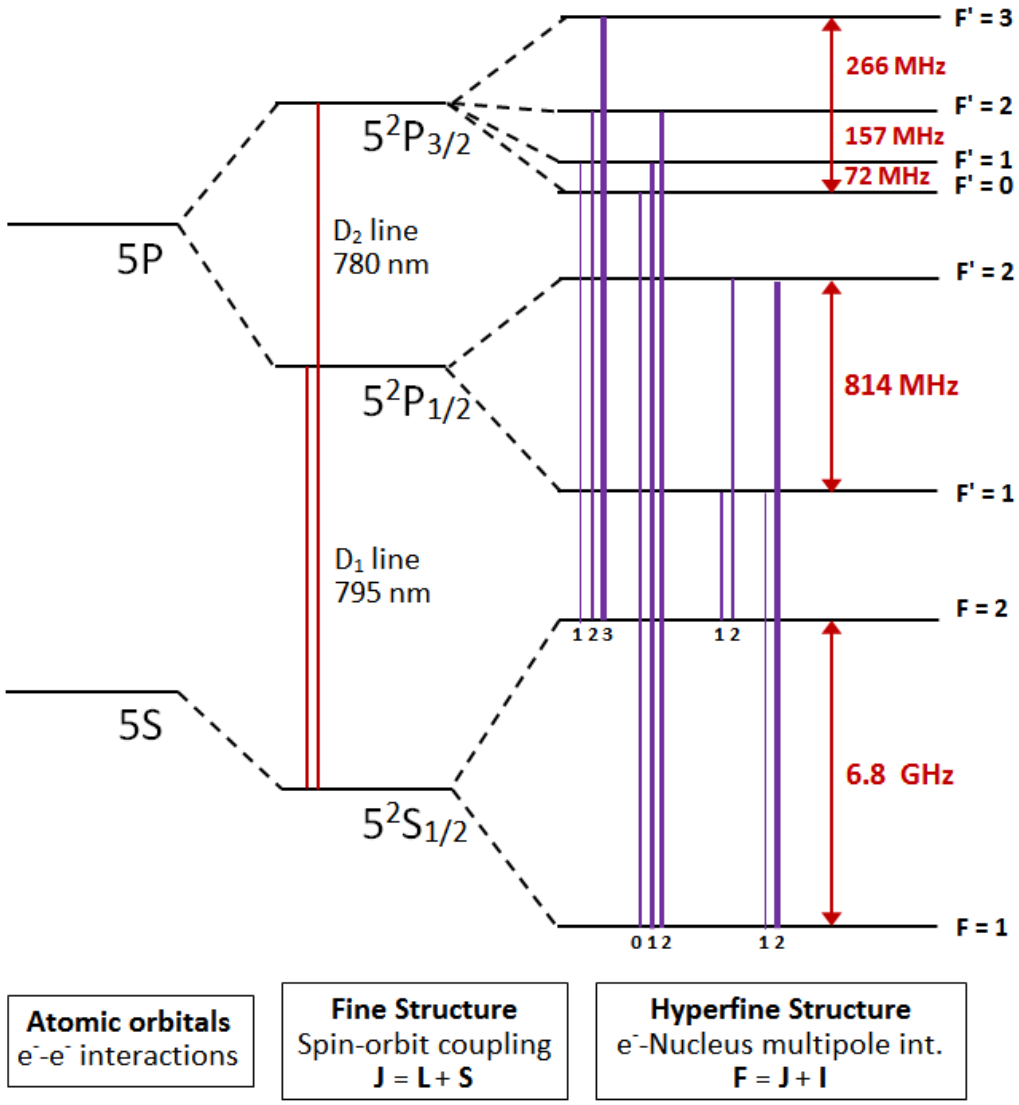

Figure 3.13: Fine and Hyperfine structure of ^{87}Rb for D_1 and D_2 transitions. The vertical lines between the hyperfine ground and excited states show all the permitted transitions according to the atomic selection rules. The small number under each line from the ground states identifies the excited hyperfine F-number. The thickness of the lines also qualitatively shows the transition strength of each transition relative to its neighbours. The figure is not drawn to scale but each hyperfine splitting frequency is identified, as well as the fine structure transition at 795 nm (377 THz) and 780 nm (384 THz). The hyperfine levels separation are also illustrated wider than in the ^{85}Rb figure to reflect the reality where the splittings are almost doubled in the isotope.

The thickness is used to illustrate the relative transition strength between the hyperfine transitions from each ground state. The transition strengths, also calculated by quantum theory, describe how easy it is to excite a given transition when compared to the others.

To a more practical interest to us is the cooling mechanism of ^{85}Rb. Figure 3.14 is a simplified diagram of the D_2 hyperfine transitions. Ideally, the electron should always be

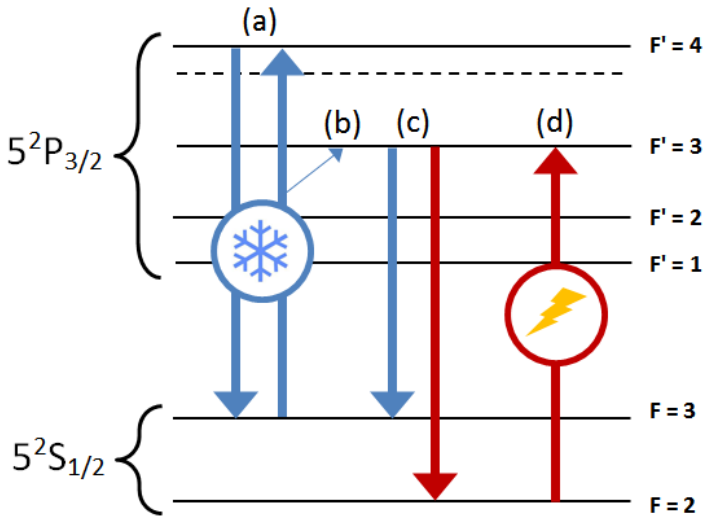

Figure 3.14: The cooling cycle of ^{85}Rb showing only the hyperfine transitions. The closed-loop transition used for cooling (a) and the repump (d) are identified. The dashed level represents the red-detuned transition frequency that has a non-zero overlap with the F'=3 level (b). The possible outcomes of decay from F'=3 levels (c) shows how the electron can fall back into the cooling cycle or go to the "dark state" (F=2) and use the repump excitation to F'=3 for a chance to go back into the cooling cycle. Energy levels separations are not drawn to scale.

recycled into the F=3 $\rightarrow$ F'=4 (transition (a) in Fig. 3.14) for the atom to be laser cooled and ultimately trapped if a magnetic field is added. Since the atoms are moving fast at different velocities (described by the Maxwell-Boltzmann distribution) and the Doppler effect shifts the cooling laser frequency, it is necessary to use red detuned frequencies to interact with them. In the velocity class in close resonance to the red detuned laser, there is a non-zero probability of being excited to the F'=3 level instead of F'=4 (transition (b) in the Fig.). The probability is approximately 1/1000. When this happens, electrons in the F'=3 have approximately equal probability of decaying either to F=3 or F=2 ground state (transition (c)). When decaying back to F=3, the "light state", the atom is back in the cooling cycle with

no effect. But when it decays to F=2, the "dark state", it becomes unaffected by the laser and thus walks out of the cooling process. In practice, the odds of that occurring relatively to the number of transition events per second involved in laser cooling atoms are so high (1/2000) that without a compensating mechanism, it is impossible to cool Rb atoms. A second repump laser is red-detuned to the F=2 $\rightarrow$ F'=3 (transition (d)) because it is forbidden to repump to F'=4. Then it is back to step (c) where it has an equal chance to decay to the light or dark ground state. Because there are only few atoms that decay to this state at any given time, only a weak laser is needed compared to the cooling laser. The repump works easily at saturation with an order of magnitude weaker intensity than the cooling beams.

With this precise understanding, the following section will review the spectroscopy techniques for resolving the hyperfine structure of Rb atoms in motion.

3.5 Spectroscopy

The most critical part of any atomic cooling experiment is the active frequency stabilisation setup used to lock the laser at a specific frequency. The atomic transitions of an atom are known today to a very high degree of accuracy and, contrarily to cavities and interferometers, are quite insensitive to environmental fluctuations such as temperature, vibrations and air currents. Many atomic clocks are now based on hyperfine transitions of Alkalis such as Caesium [98] and rubidium [99, 100]. As such, atomic vapours of neutral atoms are ideal media to produce the reference dispersion signal (also called "error signal") using spectroscopic techniques. In this section are introduced the concepts in atomic spectroscopy upon which our frequency stabilisation setup in Sec. 5.1.5 is built.

3.5.1 Lifetime broadening

Atomic transitions, even at hyperfine resolution, are never monochromatic as they suffer from various broadening effects. The most fundamental, one that cannot be reduced, is caused by the uncertainty principle where the uncertainty in the electron lifetime in an excited state results in consequential energy uncertainty in the transition. Thus, *lifetime broadening* is a normalized Lorentzian density function of the probability of absorption for a given atomic transition expressed by:

$$P_{ab}(\nu) = \frac{1}{\pi} \frac{\gamma/2}{(\nu - \nu_0)^2 + \gamma^2/4} \tag{3.47}$$

Where $\gamma = \Gamma/2\pi$ is the natural linewidth of the transition and $\nu - \nu_0$ is the laser frequency detuning. For Rb, the natural linewidth is 6 MHz.

3.5.2 Power broadening

Another type of linewidth broadening is experienced when the intensity is strong enough to saturate the transition on-resonance but can still increase absorption away from resonance. At this level of stimulation, the line shape will then change because of the on-resonance saturation. To account for power broadening, γ in the previous equation, needs only to be replaced by the power-broadened natural linewidth γ' and the FWHM linewidth becomes:

$$\gamma' = \gamma(1 + I/I_s)^{1/2} \tag{3.48}$$

3.5.3 Doppler broadening

Atoms in motion interact with the laser at frequencies Doppler shifted by their intrinsic velocity. The resonance frequency of a moving atom is:

$$\nu = \nu_0(1 + v_z/c) \tag{3.49}$$

where v_z is the velocity component along the propagation axis of the laser beam. In the laboratory reference frame, this translates into a very large broadening of their atomic transitions.

Considering a gas of atoms with a distribution of velocities, the resonance interaction with laser light will also be a function of that distribution. The probability that an atom has a velocity between v_z and $v_z + dv_z$ is expressed by the Maxwell-Boltzmann distribution:

$$P(v_z)dv_z = \left(\frac{m}{2\pi k_B T}\right)^{1/2} \exp\left(-\frac{mv_z^2}{2k_B T}\right) dv_z \tag{3.50}$$

$$\text{where } v_z = (\nu_L - \nu_0)\frac{c}{\nu_0};\ dv_z = \frac{c}{\nu_o} d\nu_L$$

The probability of absorbing a photon with frequency between $[\nu_L, \nu_L + d\nu_L]$ is given by:

$$P(\nu_L)d\nu_L = P(v_z)\frac{dv_z}{d\nu_L}d\nu_L$$

$$P(\nu_L)d\nu_L = \frac{1}{\nu_0}\sqrt{\frac{mc^2}{2\pi k_B T}} \exp\left(-\frac{(\nu_L - \nu_0)^2}{2\left(\frac{k_B T}{mc^2}\right)\nu_0^2}\right) d\nu_L \tag{3.51}$$

and the FWHM Doppler-broadened linewidth is only a function of the atomic transition frequency ν_0, temperature T and mass m of the atoms:

$$\Delta\nu = \nu_0\sqrt{\frac{8k_B T}{mc^2}\ln 2}. \tag{3.52}$$

Doppler broadening is by far the most important broadening effect at low pressures. For a Rb vapour at 300K, a Doppler broadening (FWHM) of 520 MHz is obtained, enough to merge all the hyperfine transitions from a given ground state into a single Doppler line.

3.5.4 Spectroscopy of the rubidium gas

When Rb vapour is exposed to a laser beam, the transmitted intensity, over 10 GHz, will show 4 Doppler-broadened dips of different intensities. Each of these dips corresponding to one of the two ground state of each isotope of Rb for a particular manifold of the D-line. The absorption spectrum can be easily calculated and fitted to measure the actual density inside the sample. The spectrum is modeled by the sum of the Doppler-broadened profile of each hyperfine transition (using Eq. 3.51). The relative amplitude of each normalized hyperfine line is then calculated from the squared Clebsch-Gordan coefficient of the transition for a particular polarisation, that is normalized over all possible transitions in the line manifold of a particular isotope (Appendix IV of [84] and [93, 101]). The sum of amplitudes for a particular isotope of Rb is then multiplied by its relative natural abundance (73% for ^{85}Rb and 27% for ^{87}Rb). The relative absorption spectrum can be fitted using Eq. 3.16 over spectroscopic data in a known transmission distance to obtain the atomic vapour density. Figure 3.15, shows the relative Doppler absorption spectrum for the Rb D_2 manifold. The Doppler-broadened

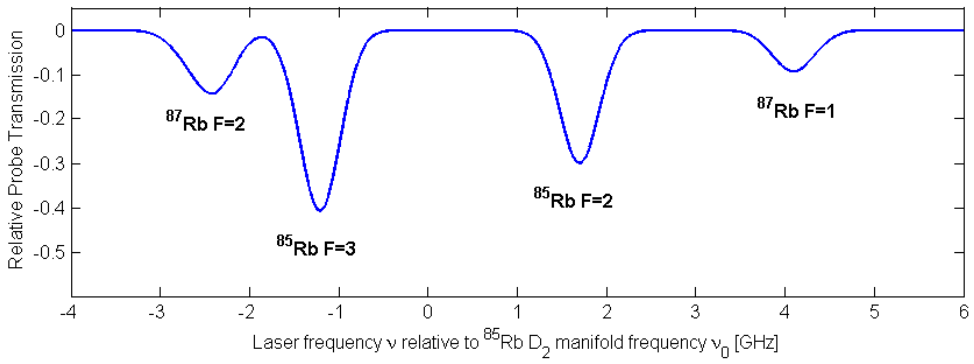

Figure 3.15: Relative transmission spectrum of a probe laser beam as a function of frequency in the D_2 manifold of Rb. The four peaks are caused by Doppler-broadened transitions from the $5^2S_{1/2}$ ground states of, in increasing frequency order: ^{87}Rb F=2, ^{85}Rb F=3, ^{85}Rb F=2, ^{87}Rb F=1. Each peak is a sum of the Doppler-broadened ground state transitions to the allowed hyperfines states of the excited level $5^2P_{3/2}$.

spectrum of each hyperfine transition composing a Doppler dip in transmission is shown in Fig. 3.17.

The next subsection shows that the Doppler broadening effect can be effectively cancelled to resolve hyperfine transitions by constructing a counterpropagating pump-probe spectroscopic setup.

3.5.5 Hyperfine resolution with saturated absorption spectroscopy

Saturated absorption spectroscopy (SAS) is a technique that brings a solution to Doppler broadening whereby a laser probe interacts with atoms that have zero velocity in its propagation axis. Thus, the atom hyperfine transitions can be resolved. To achieve this, the idea is to saturate the atom vapour with a strong laser beam, the "pump" beam. Then, a weak counterpropagating beam, the "probe", is inserted and aligned to spatially overlap with the pump.

Fig. 3.16 shows a typical setup to realize SAS. By scanning the laser over the frequency

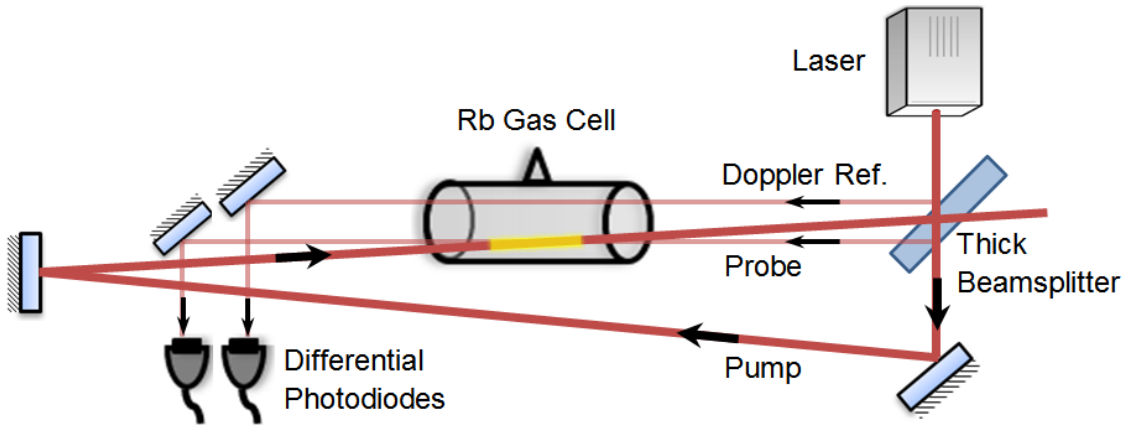

Figure 3.16: Experimental setup to realize saturated absorption spectroscopy. The laser is splitted in two identical weak probe beams and a strong transmitted pump beam using a thick slab of silica. Mirrors are used to overlap one of the probe beam with the pump beam in opposite directions. Both probes are transmitted to a differential photodiode that will subtract the reference Doppler background from the transmitted probe signal through the pumped Rb atoms.

range, only atoms with no velocity along the laser propagation axis will be simultaneously excited by both pump and probe, thereby efficiently eliminating Doppler effects for that particular class of atoms. The action of the pump, saturating this class of atoms, results in reduced absorption of the probe. It creates a *hole burning effect* in the probe signal over each hyperfine transition. Of course, the probe will still be absorbed by all the other moving atoms yielding a Doppler background signal but with a dip in absorption over each hyperfine transition. The intensity of those dips will depend on the particular transition strength, of each hyperfine transition and the polarisation type of the probe beam (linear or circular).

Figure 3.17 shows the transmitted probe signal in a vapour of pumped atoms at the same laser frequency (solid red line).

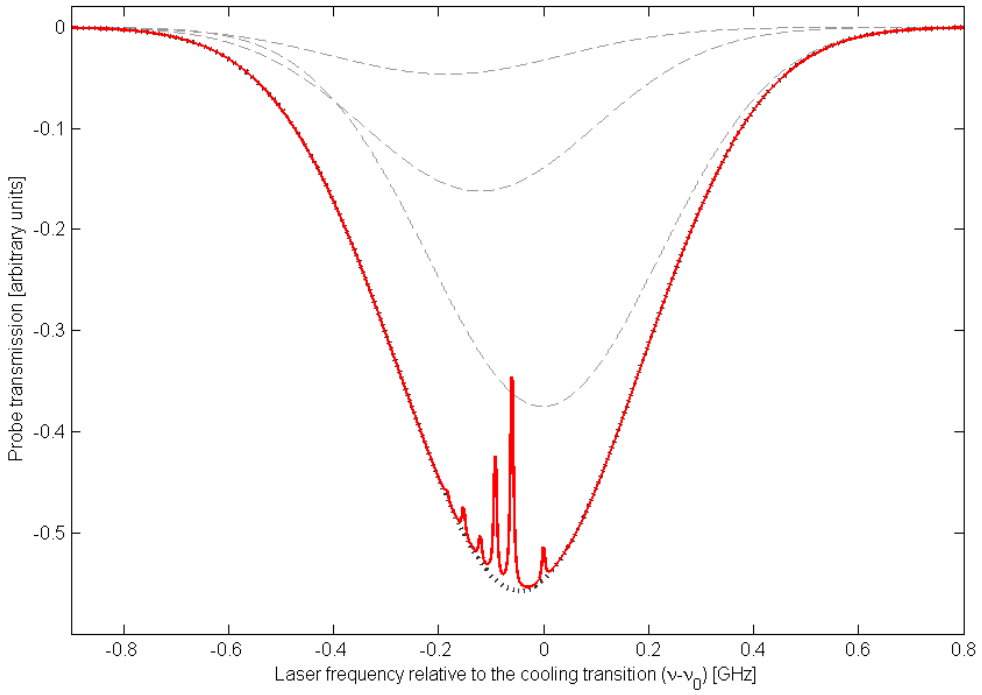

Figure 3.17: Transmission of a weak laser probe through a Rb gas cell where a strong pump beam has been coupled in the opposite direction and at the same frequency. Result is the solid red line showing the hyperfine depleted transitions for the atoms along the laser propagation axis. Because of the pumping, less light is absorbed by the probe over hyperfine frequencies. The dotted line corresponds to the probe transmission without the pump beam. Dashed lines are the Doppler-broadened transitions corresponding to each hyperfine level.

By using a second identical "reference" probe beam that has no overlap with the pump, it can be used to differentiate against the first probe, subtracting the Doppler background over the signal. This produces a Doppler-free signal that only shows the hyperfine transitions against a flat background (see Fig. 3.18). It is not necessary but this helps to better resolve weak transitions.

Although only three transitions are permitted from a given F ground state, 6 lines are observed in the signal. This is one particular artefact of the SAS technique: transmission peaks are also observed when the laser frequency is exactly at mid-point between two "real" hyperfine levels (crossover lines). They are usually stronger and easier to resolve because

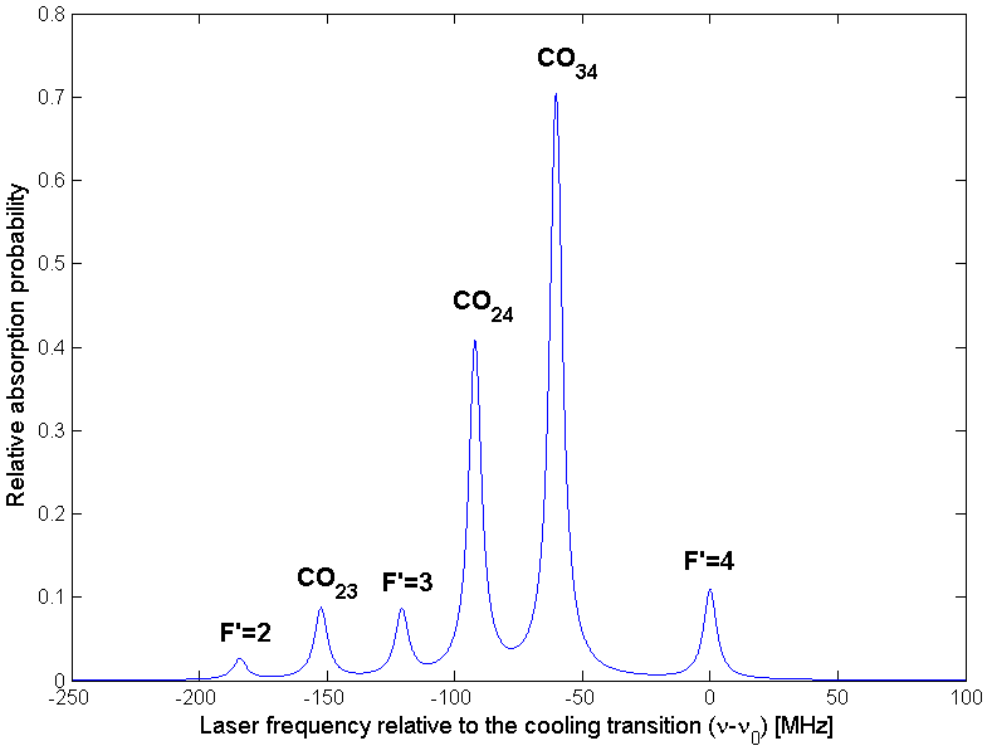

Figure 3.18: Doppler-free saturated absorption spectroscopic signal for the ^{85}Rb $5^2S_{1/2}$F=3 transitions in the D_2 manifold.

of the hyperfine pumping effect [83]. In a multilevel atom with closed hyperfine transition, the pump and probe simultaneously burn two holes in the velocity distribution. When the hole burning for one transition reduces the probe absorption from the other level and vice-versa, a crossover peak is detected. These are generally stronger because they interact with non-zero velocity classes (along the propagation axis) of atoms over two resonant transitions which is a much more numerous population than the zero-velocity class of a single transition. These crossover peaks are as precise in frequency as the hyperfine levels themselves so these extra peaks do not cause confusion in the spectrum interpretation. Because they provide a better signal to noise ratio, they are often used to stabilise the laser frequency. Tuning to the correct transition required for laser cooling and repumping is achieved with an acousto-optic modulator (AOM).

3.5.6 Laser frequency stabilisation techniques

The general approach in laser frequency stabilisation is to convert the probe signal from an atomic vapour, into an error signal where the desired frequency crosses zero, the lock point. Several spectroscopic techniques are available each with their own strengths and weaknesses and the choice of a particular technique is strongly dependent on the application requirements. There is often a trade-off between the frequency stability of the lock and its capture range, which means how far the locking system allows instantaneous frequency deviations and still be able to bring the laser back into the lock point. All techniques are classified into two categories: unmodulated (SAS [102, 103], DAVLL [104], Sagnac Loop [105]) and modulated techniques (FM spectroscopy [106], Pound-Drever-Hall [107, 108] and MTS [109, 110]).

The Doppler free saturated absorption spectrum is a direct and inexpensive way of producing a signal which can be processed by electronics in order to derive a lock point frequency reference to lock the laser frequency. By biasing the DC signal detected by the photodiode, a locking point detuned from resonance is obtained, also called *side-lock*. However, the locking point frequency is very sensitive to intensity. In demanding applications like magneto-optical trapping, a more stable and robust frequency lock is often necessary so the modulation transfer spectroscopy (MTS) became a key technique in atomic physics. The MTS setup used in the experiments along with the frequency lock servo is presented in subsection 5.1.5.

3.5.7 Modulation transfer spectroscopy

Modulation transfer spectroscopy [111] is a modulated spectroscopy technique (like Pound-Drever-Hall and FM spectroscopy). It is considered the most robust technique when one needs to stabilise a laser frequency to an atomic cycling transition [110]. The basic idea is to exploit a nonlinear four-wave mixing effect by modulating a pump laser beam that overlaps within an atomic gas cell with an unmodulated probe beam. When the carrier frequencies of the pump-probe are resonant near an atomic transition, the unmodulated pump, probe and the modulated pump sideband all beats together. This process, due to the $\chi^{(3)}$ susceptibility of the atomic vapour, generates a fourth beam (the probe modulated sideband) [109]. Hence, the "modulation transfer" name given.

Because the nonlinear susceptibility is large only in atomic cycling (closed) transitions, the MTS signal recovered is strong only on these transitions. This process is insensitive to linear absorption so the MTS signal is a flat background with very low noise. There are two components to the MTS signal, the in-phase and quadrature terms which are linked to the absorption and dispersion of the vapour. To produce the desired error signal, one must take

care to set the correct phase of the local oscillator in the RF mixer input of stage B (Fig. 5.14) in order to retrieve the quadrature component of the MTS signal [110].

CHAPTER 4 MODELLING COUPLING EFFICIENCY INTO A HOLLOW FIBRE

4.1 Model presentation

In this chapter, a semi-classical Monte Carlo model of laser cooled atoms is developed. The aim is to support the experimental efforts of coupling cold atoms from a MOT into a HC-PCF using a single blue-detuned hollow beam.

For a repulsive collimated beam the analysis of guided atoms dynamics is straightforward, however, in an optical funnel an axial force appears that modifies the dynamics at work. Fully taking into account heat generation effects such as light scattering events is essential. Momentum diffusion also improves the accuracy of simulated experiments. Through the model and the experiment, only the lowest order hollow beams is demonstrated to be suitable for the experiment because they diffract minimally and allow for the longest capture distance of atoms released from the fibre.

It is demonstrated that there is an optimal magnitude of potential under a given set of initial conditions, to maximize the atomic coupling. In other words, the deepest possible potential does not provide the best coupling of free-space atoms into the optical fibre. Knowledge of these coupling dynamics will improve future implementations of atom loading from a blue-detuned optical funnel.

The next section will briefly review published literature on the models of atom coupling and guiding into fibres. In section 4.2, the 3D Monte Carlo semi-classical model of laser cooling is presented and compared with other models. section 4.3 adds the building blocks to apply this model to the optical funnelling and atom guiding scenarios. section 4.4 deals with the dynamics of the atoms in the funnel and predicts a gravito-optical bottle trapping effect. The system's atom coupling efficiency against experimental parameters is studied in the last section 4.5.

4.1.1 Models of collimated guiding and optical funnelling into fibres

One of the first atom coupling models [112] into a silica capillary, proposed the use of the diffracting field from the cladding to couple the atoms. The low power in the evanescent field required a high-power near-detuned beam ($> 500\,\mathrm{mW}$) with its associated spontaneous emission loss. Neglecting these heating losses, the model predicted over $> 99\%$ coupling efficiency, which has never been realized experimentally. There is also a major issue with this

approach where the atoms are first funneled directly by the optical field, but then at the fibre interface, they are guided by the much weaker evanescent field. The atoms are also exposed to attractive van der Waals forces [113] which were also neglected in this model. Another main obstacle of evanescent blue-detuned guidance was clearly identified first by Renn et al. [64] and later by Dall et al. [68]: Multimodal interference in the capillary cladding led to zones of destructive interference in the evanescent field resulting in heavy guided atom loss.

Development of hollow-core photonic-crystal fibres (HC-PCF) [73, 114] paved the way for efficient guidance of atoms because of their low loss and optical mode guidance in the hollow core itself instead of using the cladding. Fully guiding the hollow beam into the core of the fibre eliminates the previous issue of van der Waal's attractive forces. However, since the guided mode is not single-moded, there is still speckle generated in the guiding potential.

Recently, two approaches were developed to improve the coupling efficiency of cold atoms into small-core HC-PCF. Bajcsy et al. [30] used a quadrupole magnetic funnel to guide the MOT from its launch distance to within reach of the Gaussian beam funnel. Soon after, they improved the atom coupling efficiency by a factor of 6 using a collimated blue-detuned hollow-beam and a repulsive sheet beam. The system effectively acts as an "optical elevator" that lowers the MOT within 1 mm of the fibre input [22]. When the sheet beam is turned off, gravity and a red-detuned Gaussian beam funnels the atoms into the core, of which most are now in a nearly uniform disk-shaped distribution.

For blue-detuned atomic guidance, HC-PCF enables the use of a hollow Laguerre-Gaussian beam itself to guide the atoms instead of just the evanescent-field part that leaks into the hollow core. This allows for a deeper trapping potential at much lower optical power, while keeping the atoms away from the influence of the fibre walls [50, 113, 115]. Collimated Laguerre-Gaussian (LG) beams have also been used to guide cold atoms from a MOT and it was shown that high ℓ-order beams proved to be the most efficient guides, superior to red-detuned Gaussian beams, as they minimize the potential energy provided to atoms at the loading stage [57]. Using the model developed in this chapter, their results were reproduced leading to similar conclusions.

Fatemi et al. [116] have also shown that guided atoms travelling in a collimated blue-detuned hollow beam are exposed on average to 2% of the light guide's total intensity.

To our knowledge, no HC-PCF have been demonstrated to guide high ℓ-order LG beams. On the other hand, low-loss guidance of a LG_{01}-like mode in a 19-m-long HC-PCF was demonstrated in [35]. Models of atom guiding in collimated blue-detuned hollow-beams in vacuum have also been developed and validated with experimental results [57, 117, 118],

although, to our knowledge, no one has yet considered the cold atoms funneling behavior into the diffracted field from the core of a fibre.

4.2 3D laser cooling model

4.2.1 Two modelling approaches

In atom optics, most of the observations are limited by fluorescence imaging. By carefully repeating experiments, videos can be reconstructed frame-by-frame from triggered time-delayed photography to image the atoms but often, this is not enough to get an understanding of the dynamics of the experiment. Even more difficult is finding the optimal parameters. This is why modelling is a necessary tool for atom optics experiments. Since the sub-Doppler cooling theory of a simplified transition model by Dalibard and Cohen-Tannoudji [16], there has not been a more complete theory to predict all the experimental results obtained with optical molasses and magneto-optical traps. Although, there are a number of good theories that can explain one precise parameter, e.g. temperature, density, spatial distribution, but there is no single uniform model which has been able to simulate all the experimental parameters of atoms cooled below the Doppler limit.

There are generally two approaches in the modelling of cold atoms [119]: the Quantum Monte Carlo (QMC), often referred to as the full quantum treatment, and the semi-classical approach (SC).

In QMC, the model takes into account the atom location among spatially computed polarisation gradients where interferences between multiple beams are also taken into account. Loss mechanisms like one-body and two-body losses and multiple scatterings are computed and can therefore resolve complex density-limiting mechanisms in the MOT. The model also keeps track of each atom's state over time. However, this approach is computationally very intensive and care must be taken to formulate adequately the problem's initial conditions in an analytical way. This approach is adequate in predicting accurately a single parameter in laser cooling [119] (temperature, density, etc.), especially in extreme conditions of operation to produce dense and very large MOT (under high magnetic field gradient, high optical power) [120].

In SC modelling, the movement and position of the atoms are treated classically but light-atom interactions are formulated in equations derived from solving the quantum mechanical problem using the stochastic Fokker-Planck equation (which includes a formulation of Brownian motion scattering in periodic potentials) [119]. By far, the most popular computing approach in semi-classical laser cooling models solves the Fokker-Planck equation which

describes the time evolution of the probability density function of the velocity of the atom while taking into account the heating from light scattering altogether (model SC-FP). From this equation other observables such as the spatial distribution can also be calculated. This method is well suited for implementing complex sub-Doppler effects such as coherence between magnetic sub-states and adapting quantum mechanical results such as diffusion tensors into a semi-classical picture. While this approach has yielded accurate predictions of quantitative aspects of MOT such as temperature, density and spatial distribution, it also suffers from many exotic effects not encountered in experiments such as regions of anti-damping, non-Gaussian spatial distributions and non-Maxwell-Boltzmann velocity distributions [121]. Another challenge of this approach, as well as for the full QMC computation, is that a considerable analytical description of the initial problem is required in terms of tensors and observables prior to the simulation.

4.2.2 Semiclassical velocity-Verlet model overview

The simulation model objective was to generate a flexible approach to atom cooling which could adapt to most experiments. No complex formulation of the problem was required prior to simulation which could allow modelling of unorthodox systems. Most importantly, this model was required to be physical in nature over the wide range of the addressed velocities with no regions of anti-damping or spatial and velocity distributions coherent with the trapping or guiding potential.

This model was initially built with the simulation of atom guiding in mind rather than addressing the laser cooling mechanisms. However, the consideration of momentum diffusion and light scattering forces on guided atoms naturally led the model to including elements of laser cooling. The modelling of optical molasses and the magneto-optical trap were then used as a validation of the model rather than as an objective in itself. However, the flexibility of the model to evaluate warm and cold atoms in different coupling and guiding situations, naturally limited its sub-Doppler cooling modelling to the simplest cases in the linear regime.

Following these objectives, the model program, built in Mathworks Matlab R2010b, was called *MOTlab* to enhance the idea that it is a virtual lab where the user can model various atom optics and cooling experiments. As a result of a simulation run, this model produces a 3D video of atoms in motion in the experiment. Afterwards, users can run advanced analytics to examine the temperature, spatial and velocity distributions, densities, capture and coupling efficiencies and so on during the virtual experiment.

This model is the first semi-classical implementation of laser cooling in the framework of a

velocity-Verlet integration of the equations of motion (SC-VV). This integration framework is used today particularly in celestial mechanics and molecular dynamics simulations. Its strongest advantage is that numerical errors in the calculation of position and velocity do not add up during iterative operations, a property manifested in the accurate conservation of Keplerian orbits (see section 3.1 in [122]). It has proven to be the most accurate algorithm for the calculation of a comet's trajectories in a complex space of gravitational forces.

As such, it is particularly suited to the modelling of an atom's orbital-like motion in a funnel of the trapping potential of laser light. In contrast to QMC and SC-FP, SC-VV does not take into account the atom's internal state and local polarisation gradient effects. It uses a macro time-stepping which comprises 1000 or more state-transitions between iterations so that the average statistical behavior always becomes dominant over its quantum behavior. It also assumes that atoms spend most of their time in the ground state so that they are always available to interact with photons (unsaturated transition condition). Nonetheless, taking into account statistical deviations of the absorption and emission rate of photons between iterations, is a quintessential part of simulating precisely the dynamics of atom motion in cooling and guiding experiments.

Finally, in its core, SC-VV sub-Doppler mechanics are based on the analytical formulation of damping and diffusion forces in the linear regime demonstrated by Dalibard and Cohen-Tannoudji [16] with adaptations detailed in subsection 4.2.3. The validity of this model, in the sub-Doppler regime, is restricted to conditions in which a linear damping coefficient and linear Brownian motion response are valid. This Brownian regime, also called diffusive time regime, means that the mean-squared displacement (or velocity kick) grows linearly in time.

4.2.3 3D formulation of the sub-Doppler cooling force applied to ^{85}Rb atoms

Dalibard and Cohen-Tannoudji formulated the semi-classical and quantum theory of sub-Doppler atom cooling in a 1D formulation derived from the simplest transition $J = 1 \rightarrow J' = 2$ [16]. Several authors worked on 3D formulations of the equations in SC-FP and QMC formalism [123–125] but their conclusions suffered from inconsistencies when compared to the experimental results [97].

In a simplification effort, Steane et al. [126] developed a general calculation of the friction force in 1D but could be used for any atomic transition. They showed that for ^{85}Rb $J = 3 \rightarrow J' = 4$ cooling transition, the force is approximately three times larger than in the $J = 1 \rightarrow J' = 2$ case considered in [16].

They also proposed an approach to translate the 1D force into 3D by simply adding

a dimensional scale factor [126]. In a six-beam configuration, atoms are cooled in each dimension independently so they are only dependent on the saturation parameter per axis and not for all 6. On the other hand, as they are exposed to the potential of the other beams, their light shifts (by Stark effect) are still multiplied by a factor of 3, which reduces the population imbalance by the same factor. Overall, this translates to a reduction factor of 3 for each one-dimensional formulation of the cooling force.

Conveniently, for the case of a $J = 3 \rightarrow J' = 4$ cooling transition, as in ^{85}Rb, the scale factor of the cooling transition in 1D cancels the scale factor of the 3D formulation applied to each 1D component. Thus, in this specific case, the polarisation gradient cooling (PGC) friction coefficient shown in Equation 3.33 can be used in a 3D space without any scale factor. This approach will be validated by reproducing in a model, previous experiments and comparing results in subsection 4.5.4.

4.2.4 SC-VV algorithm

As stated earlier, velocity-Verlet (VV) is a time-stepping algorithm resulting from a particular integration of the equations of motion of an object. It produces the future phase-space coordinates (position and velocity at time $t + \Delta t$) of an object based on known initial conditions at time t. The algorithm has been highly successful in celestial mechanics to calculate orbital trajectories because it conserves energy in the absence of dissipative forces. Energy conservancy in iterative time-stepping results from the property that numerical errors do not build up over multiple iterations, unlike Euler integration.

Assuming position r, velocity v and time step Δt at time t, the future position and velocity along dimension i of an object of mass m are expressed:

$$r_i(t + \Delta t) = r_i(t) + v_i(t)\Delta t + \frac{\sum F_i(t)}{2m}\Delta t^2 \tag{4.1}$$

$$v_i(t + \Delta t) = v_i(t) + \frac{(\sum F_i(t) + \sum F_i(t + \Delta t))}{2m}\Delta t \tag{4.2}$$

where the sum of forces includes light scattering forces (Eq. 3.12), gradient/dipolar forces (Eq. 3.18) and optical molasses forces (Eq. 3.22), that may include the Zeeman effect (Eq. 3.36), depending on the configuration of the experiment. Momentum diffusion is not formulated as a heating force at this step but rather as a velocity kick to provide a more instantaneous and chaotic effect on the motion rather than a steering force. Implementation of the VV algorithm for our application is not straight-forward because the damping force is velocity-dependent, which results in the addition of a mid-point velocity calculation. Moreover, momentum dif-

fusion velocity shuffling requires two additional steps of its own. Global integration results in the following core algorithm implementation:

1. Initialization of simulation parameters
2. Rendering geometry and input variables of the atom optics experiment
3. Monte Carlo generation of initial conditions for each atom
4. Assigning an atom to a processing thread, a "matlab worker" enabled for parallel computation, on one of the available processor cores and execute the following time-step loop:
   (a) Calculate the sum of forces acting on the atom at time t
   (b) Calculate VV position at time $t + \Delta t$ (Eq. 4.1)
   (c) Calculate VV mid-point velocity at time $t + \Delta t$ (Eq. 4.3)
   (d) Calculate momentum diffusion and add velocity kick to mid-point velocity
   (e) Re-calculate future forces at future position and mid-point velocity; discard mid-point velocity
   (f) Calculate VV final velocity at time $t + \Delta t$ (Eq. 4.2)
   (g) Re-apply momentum diffusion velocity kick (that was discarded along mid-point velocity step).
   (h) Iterate the time-step, repeat steps (a)-(g) if the atom is still in the computing domain and the maximum number of iterations is not reached
5. Run statistics and analytics, e.g. atom losses, capture rate, coupling efficiency, cloud temperature, etc.
6. (Optional) Produce video of atoms motion in virtual experiments

The first step is to load the simulation parameters which are the number of atoms to simulate (default: 1000), the time-step ($10\,\mu$s), the length of the simulation, events management (change of experimental parameters at certain times of simulation), debugging options, memory allocation and number of simultaneous computing threads for the multi-core parallel execution of the simulation (8 "workers" are supported on an intel core i7 processor). In the second step, the geometry of the virtual experiment (size and step of the computing domain) is loaded along with the physical constants, laser beams and all user-defined experimental

parameters (power, detuning, magnetic field strength, etc.). In the third step, the Monte Carlo generation of the initial conditions determines the 3D positions and velocity vectors of all the atoms and stores them in a memory array. Step 4 is the time loop executed per atom, the computing intensive part of the program. Each worker is assigned an atom to simulate through steps (a)-(g). *The conditions to finish are*, either the atom left the computing domain, or the loop reached the maximum number of iterations defined in step 1. At the end of the loop, the atom position and velocity are recorded into the array and then the computing thread picks another atom from memory and starts time-stepping. It does so until all atoms have been simulated. Step 5 analytics is where the simulation post-processing is executed. For example, the temperature of the atoms is calculated and figures of relevant quantities, such as the velocity distribution, etc. are plotted. The final step is the production and execution of the 3D simulation video, according to many configurable parameters by the user such as frame rate, reading data rate, playback speed, etc.

4.2.5 Mid-point velocity and momentum diffusion

This subsection aims to present the two modifications to the VV algorithm implemented to support atom laser cooling simulation.

The challenge of calculating the velocity is that the forces are dependent on the future velocity which is not known yet. The selected approach is to perform a first pass estimate by assuming the future force is identical to the current force. Eq. 4.2 becomes:

$$v_i(t + \Delta t) = v_i(t) + \frac{\sum F_i(t)}{m}\Delta t \tag{4.3}$$

Later, this is corrected by using this mid-point velocity (future velocity estimated from current force) into future force of Eq. 4.2. The mid-point velocity is then discarded and replaced by the more accurate future velocity just calculated using the future force obtained.

Before executing this calculation, the mid-point velocity and the final velocity will both be modified by the inclusion of the 3D momentum diffusion projected along the dimension used in the calculation (also called velocity shuffling). Previously, Sec. 3.1.1 presented the cooling spontaneous force based on light scattering but without considering fluctuations over time of the scattering and emission processes. The instantaneous force from a single laser beam is described by C. J. Foot [83] as:

$$\mathbf{F} = \mathbf{F}_{abs} + \delta\mathbf{F}_{abs} + \mathbf{F}_{em} + \delta\mathbf{F}_{em} \tag{4.4}$$

where the first two terms, on the right hand side, describe the absorption process and the two last terms, the spontaneous emission process. The average of this force over a time step

t_s becomes:

$$\mathbf{F} = \mathbf{F}_{sp} + \overline{\delta\mathbf{F}_{abs}} + \overline{\delta\mathbf{F}_{em}} \tag{4.5}$$

where the time average of the absorption, $\overline{\mathbf{F}_{abs}} = \mathbf{F}_{sp}$ which represents the spontaneous force from Eq. 3.12 or in the case of two orthogonally polarised counter-propagating beams Eq. 3.22. The emission force averages to zero over many events, $\overline{\mathbf{F}_{em}} = 0$, because photons are spontaneously emitted uniformly in all directions. $\overline{\delta\mathbf{F}_{abs}}$ and $\overline{\delta\mathbf{F}_{em}}$ represent the deviations from the average of each of these processes, which can be counted in units of recoil momentum $\hbar\mathbf{k}$.

This is where the Brownian motion theory becomes useful in describing these fluctuations. If atomic motion considers only the average spontaneous force as a reference, then the light scattering process fluctuations lead to a random walk in velocity. If N photons are scattered, then the mean displacement is $\sqrt{N}$ recoil kicks. This is true because, in the statistical sense, the fluctuations are best described as a Poisson process. Events are numerous enough that this is at the limit of validity. Mandel's Q-factor accounts for the non-Poissonian nature of the statistical fluctuations [127]. In particular, atoms see the two counter-propagating waves as independent triggers of absorption and this is *approximately* correct when the intensity is below saturation; it neglects the fact that these waves also form a standing wave and has additional nonlinear effect over the momentum diffusion, aside from their independent contribution. This is where the Q-factor contributes to compensate for this characteristic. Being nonlinear in laser intensity, its value is determined using the Doppler cooling limit in section 4.2.6 and the current experimental parameters (laser intensity and detuning). At zero laser intensity, Q-factor also goes to zero.

Whether from absorption or emission, the recoil kick has the same order of magnitude, only its direction differs. Fluctuations from absorption are purely one-dimensional along the laser propagation axis. The fraction of total spontaneous emissions along one dimension are identified by η. In the 3D model, when the atoms are illuminated by optical molasses cooling beams from all 6 directions, the velocity spread is formulated in *one-dimension* $i = x, y, z$ as:

$$\delta v_i = \sqrt{1 + 3\eta + Q} \cdot \frac{\hbar k}{m} \cdot \sqrt{2\gamma_s t_s} \tag{4.6}$$

where the first term is the dimensional spread of the recoil events. The 1 means that absorption always gives a kick along the propagation axis of the laser, $\eta = 1/3$ because the spontaneous emissions are isotropic and the factor 3 means that spontaneous emissions from the other directions contribute to recoils along dimension i. $\hbar k/m$ is the magnitude of the recoil velocity kick and the last term is the total number of scattering events during time step

t_s. The factor 2 accounts for the contribution of each counter-propagating laser beam to the light scattering. This application of the momentum diffusion, valid in the linear Brownian motion regime, results in δv_i being independent of its own velocity. This regime breaks down when the atoms are submitted to a laser intensity several times larger than the saturation intensity at small detuning (light force parameter $\Omega^2/|\delta|\Gamma \gg 1$).

The velocity shuffling process is how the magnitude of those fluctuations is calculated during a given iteration:

$$\Delta v_i(t) = \delta v_i \cdot \mathfrak{F}(0,1) \tag{4.7}$$

where $\mathfrak{F}(0,1)$ is a random number generator function that follows a normal distribution of average around zero and standard deviation equal to 1. The momentum diffusion based velocity shuffling is then added to the future velocity for each dimension $i = x, y, z$ at steps 4 (d) and (g) of the algorithm. In the next subsection, momentum diffusion is applied on laser cooled atoms resulting in an equilibrium temperature.

4.2.6 Simulation results of the magneto-optical trap

Before simulating atom optics experiments, the dynamics of the atom cooling model are evaluated by simulating the most documented cold atom experiment: the magneto-optical trap.

The starting point is generated with $N = 1000$ atoms at $T = 300\,\mathrm{K}$, uniformly distributed over the computing domain. Figure 4.1 A shows the initial condition of the MOT simulation. The standard domain used in all simulations is $100 \times 100 \times 100\,\mathrm{mm}$, a compromise which allows the observation of the dynamics of atoms around the trap but not so large as to waste computing time tracking out of reach atoms. Since there are many atoms with too high an energy to be captured, an efficient choice is to randomly re-generate the atom's initial conditions when it walks out of the computing domain. Thus it is effectively as if many more than $N = 1000$ atoms are used initially, without having to track as much, effectively saving memory resources. If atoms that have moved out of bounds are re-generated, the simulation takes this into account to calculate accurately the capture statistics.

Doppler cooling Q-factor determination

The Doppler limit of temperature was used to determine the Q-factor. Running the simulation in the Doppler range only, turning off PGC, the atomic response follows theory where it would be coldest for lowest intensity, $s_0 = 0.05$ and when the detuning is $-\Gamma/2$. Closer or further detuning just increases the final temperature. The equilibrium temperature

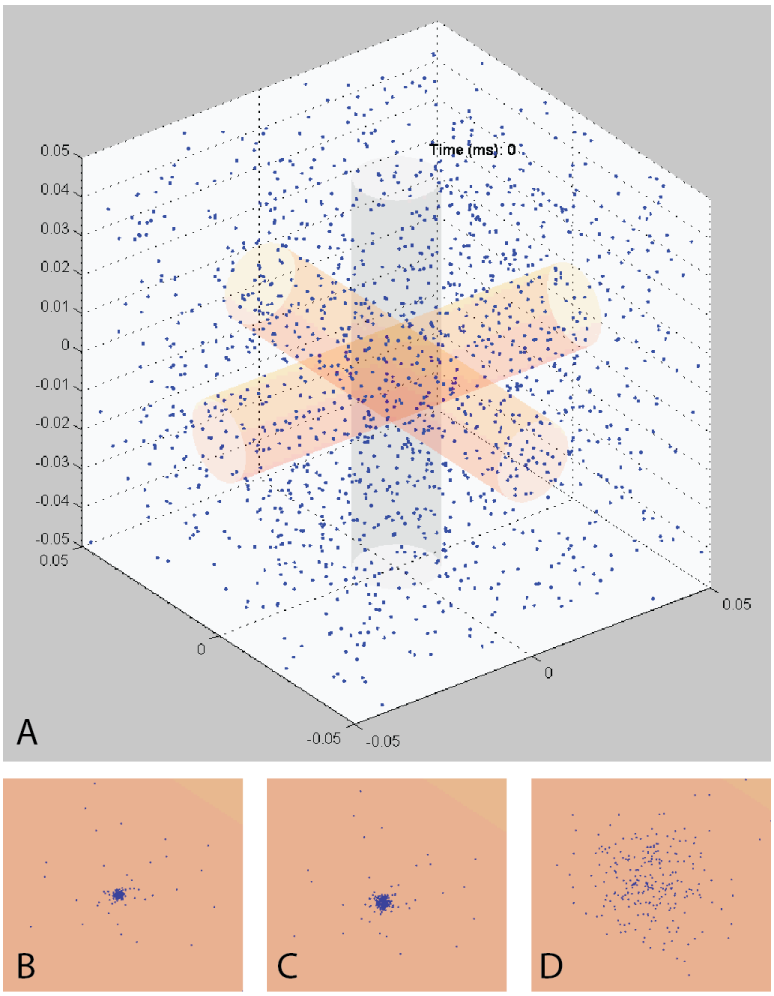

Figure 4.1: A. Screenshot of the video at the start of the simulation of the MOT. B. Zoom on the 33 μK MOT after 200 ms. C. Atoms at 1.5 μK at the end of the cooling expansion phase. D. Atoms released after shutting off the cooling beams.

achieved was around 130 μK, with the Q-factor = 0, which is below the Doppler Temperature of 145 μK for ^{85}Rb. This error comes from the fact that the light scattering is inaccurately represented by assuming it is a purely Poissonian process. By adding a Mandel's Q-factor of 0.2 to the momentum diffusion in Eq. 4.6, the temperature now converges to a value of 145.9 μK. Keeping the same light scattering formula for the sub-Doppler mechanism, the value of Q is not modified later on.

Atom cooling dynamics

Starting with a zero magnetic field, optical molasses are observed and captured atoms exhibit Brownian motion, slowly drifting away from the cooling beams. Outside the beams-path, they move at constant velocities. Atoms eventually walk out of the cooling beams but others are captured to replace them. These atoms are captured in the 6 beam-overlap but do not converge toward the centre of the chamber.

When a magnetic gradient of 3 Gauss/cm is applied, the dynamics change radically. The capture rate is improved markedly and atoms converge toward the centre of the chamber. The atoms stay in the centre but light scattering also induces a Brownian motion that scatters them in the centre creating a dense sphere of agitated atoms. The magnetic field gradient, as well as the number of captured atoms, determine the size of the MOT sphere. Another expected effect observed in the simulation of the MOT, when compared to optical molasses alone, is that atoms outside the capture radius are not slowed, even if they are propagating in a laser beam. The capture process only works in the volume generated by the 6 beam-overlap because of the Zeeman effect that effectively blue-detunes the cooling transition of the atoms, and move them towards the laser beam, when they are outside the capture radius.

The simulated atom dynamics were following the expected experimental response. Laser cooled atoms in a MOT showed that their final temperature was independent of the magnetic field with the same temperature as achieved in an optical molasses simulation. However, the observed temperatures of MOTs in actual experiments are sometimes higher than those of optical molasses due to experimental deviations between the magnetic field zero and the centre of the cooling beam capture volume.

Modified initial distribution to improve computing efficiency

To reduce the computing time and increase the capture probability in an atom cooling simulation, the use of a lower initial temperature was evaluated. Starting with a distribution of atoms at 3 K ($v_{rms} = 30\,\mathrm{m/s}$), most of them still have too high an energy to be captured. However, the tail of the distribution within the capture range being larger than at 300 K, reduces processing time significantly. In Table 4.1, a simulation of 15000 iterations with 1000 atoms using a medium force (light force parameter of 0.5 at a detuning of -3Γ) simulates the number of atoms cooled and their final temperature when compared with their starting Monte Carlo distribution temperature. The results in Table 4.1 show that the starting temperature does neither impact the final cooling temperature nor the velocity distribution of the cooled atoms. However, it does affect capture statistics and efficiency, and is therefore

Table 4.1: Comparison of cooled atoms temperatures for different starting temperatures with or without regeneration of lost atoms. In all six runs, 1000 atoms were simulated using 15000 iteration steps, under a medium cooling force (light force parameter 0.5 at -3Γ detuning). A lower temperature distribution and regeneration of lost atoms only increase the number of atoms captured during a simulation run without affecting the other physical parameters of the MOT.

Init. Temp.	Single run, no regen.		Single run w/ regen.	
300 K	None	-	31 atoms	38.5 μK
30 K	3 atoms	39.42 μK	249 atoms	39.91 μK
3 K	19 atoms	39.87 μK	689 atoms	39.72 μK

only used when these parameters are not evaluated, *which is the case most of the time*. The preferred approach was therefore to use a 3 K distribution with regeneration of atoms when they are out of bounds. Regeneration implies that the longer the simulation runs, the bigger the MOT becomes. Note that the simulation time is always well below the normal lifetime of an atom in the MOT. Another numerical technique that keeps capture statistics valid is a truncated Monte Carlo Thermal distribution but it also extends simulation processing time because room-temperature atoms are still initiated but discarded when found out of capture range.

Cloud temperature calculation

After the MOT/OM simulation, a condition to qualify cooled atoms for the calculation of the ensemble temperature was identified: On their last iteration, they must be under the critical velocity, where the damping force is linear (see Sec. 3.2.1) (< 4.73 m/s for ^{85}Rb) and within a cooling laser beam (for OM) or within 0.5 mm of the chamber centre (for MOT). Considering the light scattering effect on atomic motion, the velocity of an atom on the last iteration is not a realistic evaluation of its average velocity in the trap. Instead, the average

velocity magnitude over the last ten iterations is used:

$$v_{abs} = \frac{\sum_{t_i-10}^{t_i} \sqrt{v_x(t_i)^2 + v_y(t_i)^2 + v_z(t_i)^2}}{10} \tag{4.8}$$

And the temperature of the ensemble is calculated from the 3D Maxwell-Boltzmann distribution:

$$T = \frac{m}{3k_B} \left(\frac{\sum_{j=0}^{n-1} v_{abs,j}}{n} \right)^2 \tag{4.9}$$

where the mass of the atom is multiplied by the mean squared velocity of the cooled atomic ensemble. This approach produces a small error on the temperature evaluation that is caused by atoms that have just been captured but have not yet reached their steady state (their lowest temperature) by the end of the simulation. When the number of atoms in the MOT is large (> 500), this error is negligible but for a small number of atoms (< 50) it can increase the ensemble temperature by 10 to 100 μK *in certain scenarios*. In the post-processing stage, analytics can be used to eliminate atoms in the process of cooling so that they do not contribute to the temperature but they are still counted in the ensemble.

Simulated MOT sub-Doppler temperatures

Management of events was also coded in the program in which after a certain time into the simulation, physical parameter changes like laser intensity, frequency detuning and magnetic field gradient can be triggered. These events allow the simulation of certain experimental protocols to obtain even colder molasses in a concentrated cloud. Such a sequence of events is simulated in Fig. 4.1 B, C and D. In B, a MOT of ~ 300 atoms at $33\,\mu$K is shown. Then the magnetic field is turned off for 1 ms, the intensity is divided by 4 and detuning shifted to -10Γ. During this molasses-cooling expansion phase, the temperature drops to $1.5\,\mu$K and the molasses expand slightly due to Brownian motion and the absence of a localization force (see subset C). Finally, when the lasers are turned off, the optical molasses expands (see figure subset D) and vanish quickly.

The MOT was simulated with variable light force and its temperature plotted in Fig. 4.2. It was compared with the precise experimental results obtained by Gerz et al. [128] with ^{85}Rb optical molasses.

The temperatures predicted by the 3D SC-VV Monte Carlo model of the MOT (blue circles) for light forces between 0.05 and 0.9 with a detuning of -3Γ and -4Γ were in close

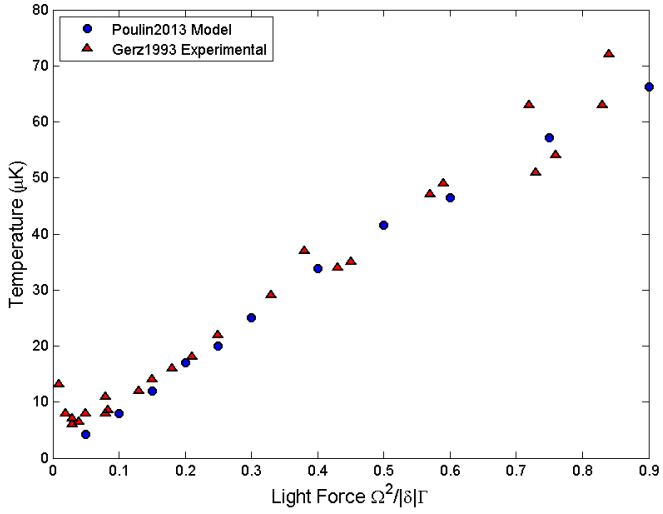

Figure 4.2: Temperature of 3D optical molasses of ^{85}Rb as a function of the light force of the cooling lasers for detuning below -3Γ. Results from our 3D Monte Carlo SC-VV model (blue circles) shows excellent agreement with experimental temperatures (red triangles) measured by Gerz et al. [128] for detunings from -4Γ to -10Γ.

agreement with the temperature of optical molasses of ^{85}Rb measured with the time-of-flight technique (red triangles) for various detuning from -4Γ to -10Γ. For a detuning beyond -3Γ, MOT and optical molasses, temperatures are linear and only depend on the light force. This means that any combination of detuning and intensity at the same light force yields the same temperature. This observation breaks down for closer detuning at which the slope of the temperature vs. light force relation increases inversely with detuning, and was observed in the experimental response [97] in agreement with the simulations.

An experimental MOT in the linear regime also features a Gaussian spatial distribution of atoms with a Maxwell-Boltzmann velocity distribution. The model also correctly demonstrates this characteristic. Fig. 4.3 shows the absolute velocity distribution in a 30 μK MOT of 1500 atoms. The red solid curve represents the probability density function of the Maxwell-Boltzmann distribution, which agrees with the atom-velocity distribution in the simulated MOT. The spatial distribution of the simulated atoms, shown in Fig. 4.4, is also analyzed and fitted to a Gaussian distribution function (solid red curve). The good agreement of the spatial distribution with a Gaussian function is visible in all 3 dimensions and at any time. However, the dimensions of the MOT are much smaller than in the experiment, mainly due to the fact that MOTs with only a few thousands atoms are simulated and compared with

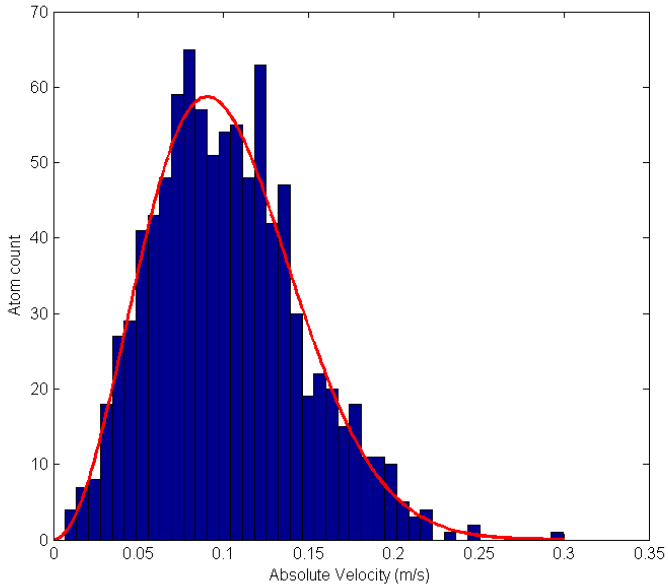

Figure 4.3: Absolute velocity (m/s), averaged over 100 μs, of 1500 ^{85}Rb atoms in a MOT at 30 μK is compared with the probability density function of the Maxwell-Boltzmann distribution (red solid line). The good agreement of the atom velocities with the Maxwell-Boltzmann distribution shows that the simulation accurately model MOT dynamics in the linear regime.

tens of millions in experiments, which under-represents candidates in the tail of the spatial distribution.

4.2.7 Future directions for the 3D laser cooling model

At this stage, the model was developed sufficiently to accurately support the experimental efforts. Further research work is necessary to realise the full potential of this tool. Here is a list of possible future developments:

- Inclusion of stray magnetic fields and non-central magnetic field zero.
- Laser beam intensity profiles to simulate dark hollow beam traps and atom laser configurations
- Non-orthogonal alignment of the cooling beams
- Render laser linewidth effects: randomisation of the laser frequency at each iteration, within the experimental laser linewidth variation.

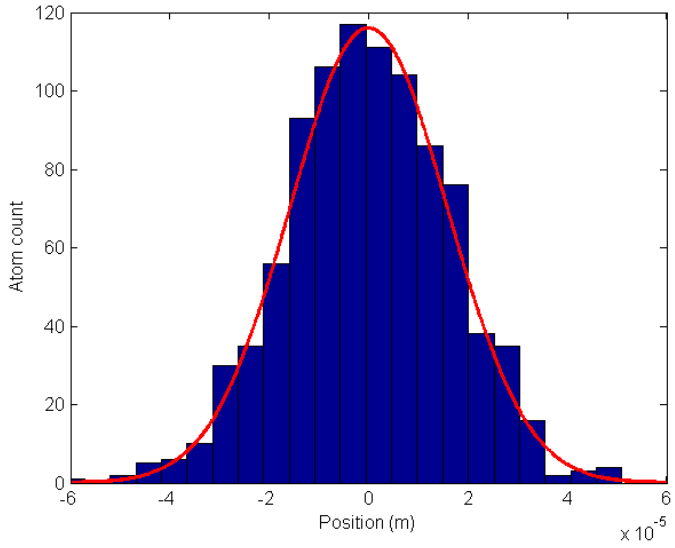

Figure 4.4: Spatial distribution of 1000 atoms in a 30 μK MOT is fitted against a Gaussian function (solid red line). The close agreement again shows that the simulation accurately models MOT dynamics in the linear regime.

- Development of linear damping and diffusion coefficients specific to ^{85}Rb $J = 3 \rightarrow 4$ [129] transitions in a 3D spatial domain [123].
- Integrate density-limiting effects: two-body collisions and multiple scatterings.

With these improvements, a greater range of experimental conditions could be accurately reproduced and could explain which parameters contribute to produce heat in the MOT. Simulating a misaligned MOT, which is the case in most experiments, would allow exploring the dynamics and internal motion or flow of atoms within real MOTs when the forces are unbalanced. It could also be useful when using the magnetic field to steer the MOT close to the fibre.

4.3 Cold atoms fibre coupling model

The SC-VV model was applied to explore the dynamics and the optimal solution of coupling cold atoms into a hollow core fibre. We published the results [36] of using an earlier version of the model that neglected heating effects because of its use of laser guidance with large detuning. The improved and more general model presented here provides an in-depth analysis and detailed results including spontaneous light-scattering and momentum-diffusion

induced velocity-shuffling.

Fig. 4.5 shows the experimental arrangement when a far-detuned low-order Laguerre-Gaussian beam is coupled and guided in a hollow-core photonic-crystal optical fibre. The

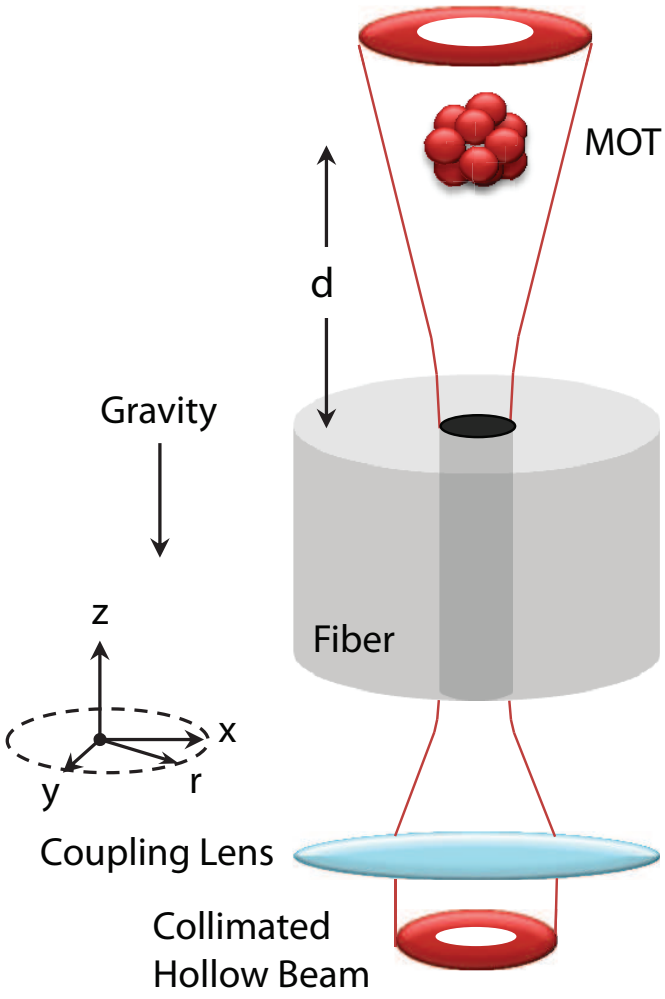

Figure 4.5: Experimental setup for coupling atoms from a MOT into a hollow-core photonic-crystal fibre. The fibre is mounted vertically in the vacuum chamber. A single blue-detuned collimated Laguerre-Gaussian beam is coupled into the fibre core at the bottom of the fibre. At the top end, the beam diffracts into free space acting as a funnel. When the MOT is released, from distance d of the fibre output, the combined action of gravity and the hollow-beam funnels the atoms into the core and guides them down the fibre. The schematic is not drawn to scale.

fibre is aligned vertically, so that its axis is parallel to gravity. A blue-detuned hollow-beam

diffracting from the core acts as a funnel to both couple and guide atoms released from a MOT situated above the fibre.

The term "coupling" is used to describe the process of optically funnelling the atoms into the fibre core. The term "guiding" is exclusively used to describe the optical control of the motion of the atoms when they are inside the fibre core.

4.3.1 Forces in the optical funnel

In this subsection, equations of Laguerre-Gaussian beam diffraction are developed in order to add the optical funnel to the SC-VV mode. A new component of the optical dipolar force is also derived from its intensity gradient.

Rotational symmetry allows the problem to be analysed using cylindrical coordinates: r being the distance to the fibre core central axis and z the axial distance from the fibre end. The extremity of the fibre facing the MOT defines the axial origin ($z = 0$). This form describes the intensity of a single-ringed Laguerre-Gaussian mode (radial order $\rho = 0$, azimuthal order $\ell \neq 0$) [130]:

$$I\left(r,z\right) = \frac{2P}{\pi w^2(z)} \frac{1}{|\ell|!} \left(\frac{2r^2}{w^2(z)}\right)^{|\ell|} exp\left(\frac{-2r^2}{w^2(z)}\right) \tag{4.10}$$

where P is the optical power and $w(z) = w_0\sqrt{1+(z/z_R)^2}$ is the radius of the lowest order beam propagating in free space. The beam waist radius, inside the fibre, is w_0 and $z_R = \pi\omega_0^2/\lambda$ is the Rayleigh range. When the laser frequency is far-detuned ($> 1000\ \Gamma$, $> 40\,\mathrm{GHz}$ for Rb atoms), the trapping potential can be expressed in the two-level approximation [85]:

$$U(r,z) \simeq \frac{\hbar\Gamma^2}{8\delta}\frac{I}{I_s} \tag{4.11}$$

where the laser detuning $\delta = \omega_{laser} - \omega_0$, Γ is the natural line width of the cooling transition, and I_s is the saturation intensity parameter. For this simulation, the energies of atoms are specified in terms of an equivalent thermal energy for ease of comparison between energy scales. The dipolar force is equal to the negative gradient of the potential $U(r,z)$. In the interest of readability, the vector force will be separated into its axial (F_z) and radial (F_r) components. Explicit mention of the variable's dependence in r,z will also be omitted. Deriving the trapping potential from Eq. 4.11 in the context of the LG intensity (Eq. 4.10), in

r and z, gives:

$$F_r = \frac{-\hbar\Gamma^2}{8\delta I_s}\frac{2^{\ell+2}P}{\pi\ell!}\frac{r^{2\ell}}{w^{2(\ell+1)}}\left[\frac{\ell}{r}-\frac{2r}{w^2}\right]exp\left(\frac{-2r^2}{w^2}\right) \tag{4.12}$$

$$F_z = \frac{-\hbar\Gamma^2}{8\delta I_s}\frac{(-2)^{\ell+2}P}{\pi\ell!}\frac{r^{2\ell}}{w^{2\ell+3}}\left[1+\ell-\frac{2r^2}{w^2}\right] exp\left(\frac{-2r^2}{w^2}\right)\frac{w_0 z}{{z_R}^2\sqrt{1+(z/z_R)^2}} \tag{4.13}$$

As an example, when comparing the axial and transverse components of the dipolar force at the same spatial coordinates in an LG_{01} beam with a $1/e^2$ waist diameter of $40\,\mu$m (diffraction half-angle of 1.6°), F_z is found to be at least 3 orders of magnitude weaker than F_r. Nonetheless, F_z can be many times stronger than gravity, even for a realistic trap potential depth of 0.5 mK. This results in F_z having a strong influence on the dynamics of the atoms in the trap. It can be seen from Eq. 4.11 that for large detuning, the potential is merely linearly dependent upon the ratio of the optical power over the detuning. From now on, this parameter will be referred to as the *light force ratio* $\kappa = P/\delta$ (in units of mW/GHz).

The radial force confines atoms within the funnel as gravity pulls them downwards toward the fibre core. Figure 4.6 shows the radial acceleration on ^{85}Rb resulting from a dipolar radial force under typical conditions at three axial distances from the end of the fibre. The force has the form of a trapping potential, which has its maximum at the output of the fibre and decreases with distance proportional to the intensity. An important consequence of the intensity distribution of a blue-detuned hollow-beam is its limited confinement radius. Outside the maximum intensity radius, the decreasing gradient produces a force that repels atoms away from the axis of the beam.

The axial force, F_z, is a manifestation of the gradient of intensity produced by a diverging beam. Therefore, it is null for collimated beams, e.g. inside the fibre. The axial force is always directed away from the end of the fibre for a blue-detuned beam regardless of the optical beam's propagation direction. This force is seen to rise sharply when the atom comes within $1.5\,z_R$ of the end of the fibre. Under typical coupling conditions, the axial force will be many times the gravitational force when close to the radius of maximum intensity. As an example, Fig. 4.7 shows the axial acceleration on a ^{85}Rb atom for three axial distances, z: 0.02, 0.4 and 2.4 mm. The axial acceleration reaches a maximum at 0.4 mm. At distances of 0.02 and 2.4 mm, the axial force maximum is equal to the gravity.

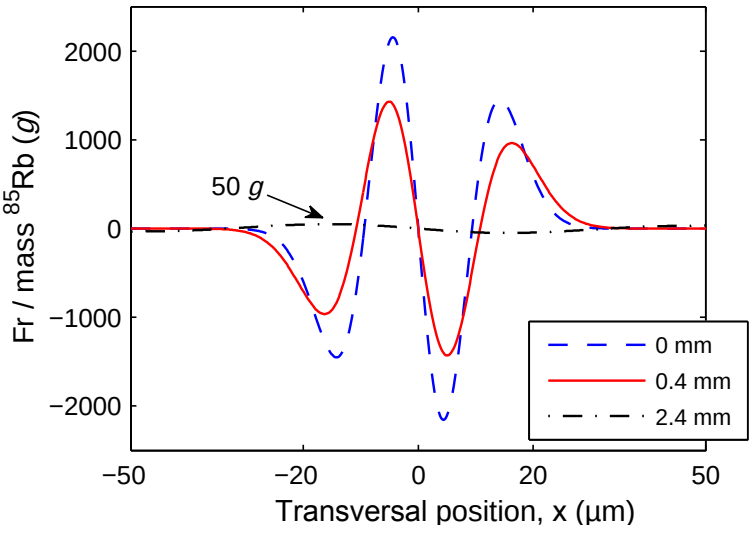

Figure 4.6: Radial component of the blue-detuned dipolar force (see Eq. 4.12) at three distances from the fibre end: 0 mm (blue dashed), 0.4 mm (red solid) and 2.4 mm (black dash-dotted). The force is represented as ^{85}Rb acceleration in units of standard gravity. Positive values mean the force vector is oriented towards increasing values of r, while negative values indicate the force vector points to decreasing values of r (or abs(x)). The location of the zero-crossings of the force function correspond to the minimum (at $x = 0$) and maximum intensity at the three examined distances. This calculation used a 4 mW LG_{01} beam, blue-detuned by 50 GHz from the ^{85}Rb D_2 cooling transition ($5^2S_{1/2}(F = 3) \rightarrow 5^2P_{3/2}(F = 4)$) around 780.24 nm and diffracting from a 40-μm-diameter fibre core. The transition natural linewidth is $\Gamma/2\pi = 6.07$ MHz and saturation intensity (far detuned, linear polarised) is $I_{sat} = 2.50\,\mathrm{mW/cm^2}$ [101].

4.3.2 Sources of atom heating and guidance loss

The main source of heating in a guiding/coupling scenario using the conservative dipolar force is the spontaneous force caused by the same light beam. Even in a far-detuned scenario, when the dipolar force is dominant, some light scattering still occurs, and it can lead to an average force higher than gravity. To serve as comparison between dipolar and spontaneous forces, the case of a ^{85}Rb atom guided in a circular path in a fibre is analyzed. The trajectory of the atom confines it at the radius of the maximum gradient of a LG_{01} beam such that it is exposed to an intensity equivalent to 60% of its maximum. Figure 4.8 shows the acceleration caused by the action of the dipolar (blue trace) and spontaneous (red trace) forces (in units of *standard gravity*, g) from a single hollow beam on a ^{85}Rb atom as a function of its detuning.

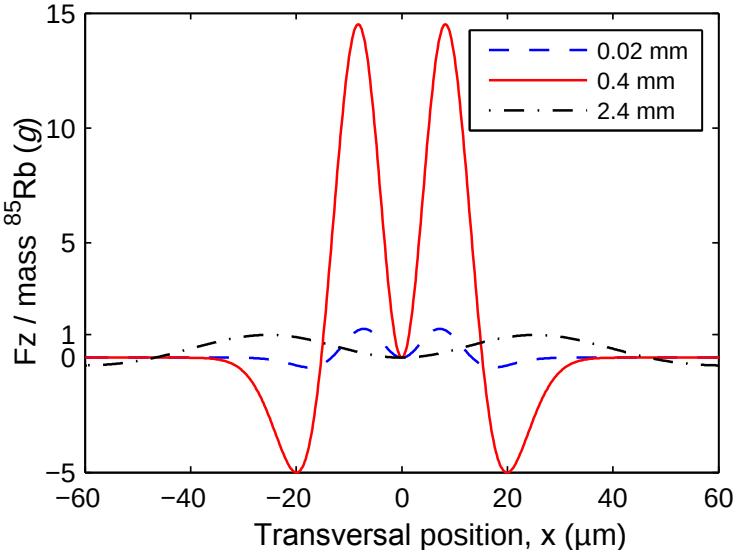

Figure 4.7: Axial component of the blue-detuned dipolar force (see Eq. 4.13) at three distances from the fibre end: 0.02 mm (blue dotted), 0.4 mm (red solid) and 2.4 mm (black dashed). The force is represented as ^{85}Rb acceleration in units of standard gravity. Positive values means repulsive while negative is an attractive force. The same physical parameters have been used as in Fig. 4.6.

The exact expression of the dipolar force (Eq. 3.18) is used to plot Fig. 3.3 represented in the close detuning range from 0 to −5 GHz. The figure shows the spontaneous acceleration is maximal on-resonance and the dipolar acceleration is null. As the frequency is detuned beyond 750 MHz, the dipolar force becomes superior and with further detuning becomes even stronger than the spontaneous force on-resonance because of the difference in magnitude over detuning.

Fig. 4.9 still compares both forces but in a semi-log representation for detuning from −5 to −1000 GHz. The approximate form for large detuning is used (Eq. 3.20). Since both forces arise from the same beam, they are rarely in true competition as the dipolar force is mostly radial and the spontaneous force acts in the direction of the beam propagation. Sometimes in a focused or diffracting beam, they can act together or compete. In a guiding scenario, the spontaneous force competes against gravity because it points upward. Note in Fig. 4.9 that the spontaneous force becomes inferior to gravity when the detuning reaches −180 GHz. From an earlier case for a circular trajectory, the highest energy guided atoms have a motion at the maximum intensity radius of the beam, so they have an energy 40% higher than the case considered before. By virtue of the linear relationship, a detuning of

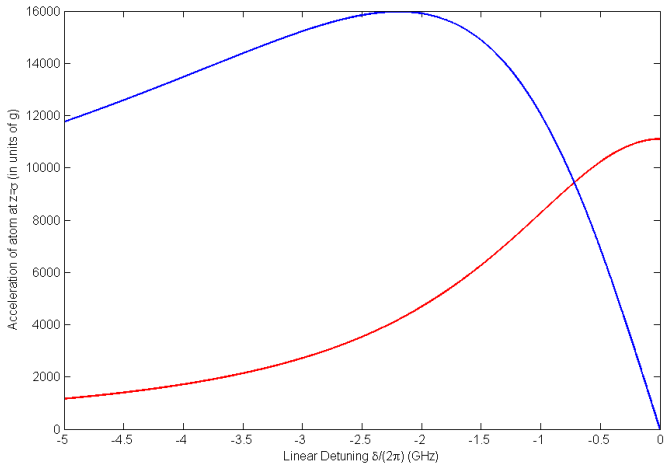

Figure 4.8: Comparison of the magnitude of dipolar (blue trace) and spontaneous (red trace) forces, in units of acceleration of ^{85}Rb, relative to the frequency detuning (from 0 to 5 GHz). Both forces are produced by a single collimated LG_{01} hollow beam, whereby an atom is confined in the maximum gradient of the beam and exposed to 60% of the maximum intensity at this same position. Spontaneous acceleration is maximal on-resonance. At around -0.75 GHz, both forces are equal and the dipolar force reaches its maximum at -2.2 GHz while the spontaneous force decreases as the inverse square of the detuning.

-300 GHz would be necessary to allow all coupled atoms to be guided through the fibre.

This spontaneous (or light scattering) force, detrimental to guiding, can be efficiently tuned off by coupling another counter-propagating guiding beam with an orthogonal polarisation thus cancelling the anti-gravity effect. It is essentially the configuration of an optical molasses beam but the frequency detuning difference prevents it from having any effective cooling or damping effect on the atom motion. However, in many experimental scenarios, it is impractical to implement two crossed polarisation counterpropagating beams. For example, in an experimental setup, the fibre is placed close to the bottom window and the hollow beam can be coupled with a lens placed at 100 mm outside the chamber. However, the large distance between the other extremity of the fibre and the top window would require the coupling optics and alignment servos to be placed within the chamber. Hence, detuning the beam further so that the spontaneous force is less than g is a much simpler solution. The disadvantage of using two beams is also that momentum-diffusion heating is doubled as well.

Although it is manifested as a separate effect, the second source of heating, *momentum diffusion* is a by-product of the spontaneous force. Its nature is a consequence of the deviation

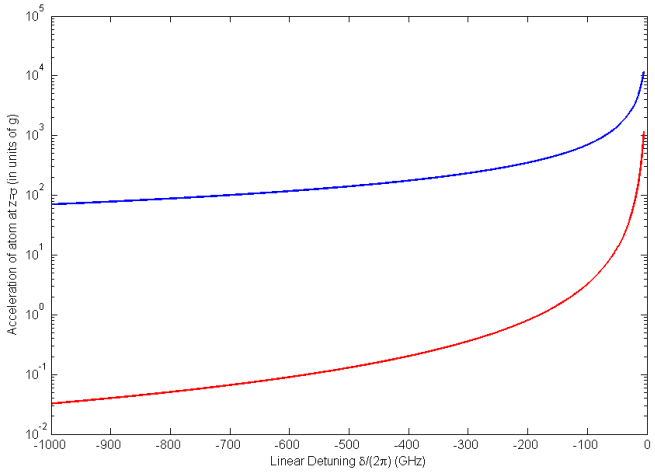

Figure 4.9: Comparison of the magnitude of dipolar (blue trace) and spontaneous (red trace) forces, in units of acceleration of ^{85}Rb, relative to the frequency in the mid to far detuning range (from 5 to 1000 GHz). Both forces are produced by a single collimated LG_{01} hollow beam, whereby an atom is confined in the maximum gradient of the beam and exposed to 60% of the maximum intensity at this same position. Both forces decrease with increasing detuning (away from resonance), but the dipolar force becomes relatively superior to the spontaneous force by a linear factor of the detuning. At 180 GHz, the spontaneous force becomes inferior to gravity.

from the statistical average of the number of expected atom recoils due to absorption and spontaneous emission of photons. The same validated approach to velocity shuffling in the MOT (see Eqs. 4.6,4.7) is used but adapted to a single beam version by removing the Q factor and factor 2 in front of the light scattering γ_s:

$$\Delta v_z(t) = \sqrt{1 + \frac{1}{3}} \frac{\hbar k}{m} \sqrt{\gamma_s t_s} \mathfrak{F}(0,1) \tag{4.14}$$

$$\Delta v_{x,y}(t) = \sqrt{\frac{1}{3}} \frac{\hbar k}{m} \sqrt{\gamma_s t_s} \mathfrak{F}(0,1) \tag{4.15}$$

where the two modifications are: Having a single beam with the factor 2 in front of the light scattering rate γ_s removed and the pre-factors are now 1 for the absorption in z and 1/3 for the contribution of random emissions in all 3 directions. The effect of these two heat sources is discussed in the next two sections.

Finally, the third source of heating is the viscous dipolar heating from Figure 2.2 and later discussed in Sec. 3.1.2. This effect, included in sisyphus cooling, presents particular

computing challenges because it is based on the excited state of the atom. This effect is mostly negligible until very high optical intensities (above $20\,\mathrm{MW/cm^2}$) are reached at small detuning. This effect is always negligible in scenarios of large-detuned guidance.

4.3.3 Initial conditions of the simulation model

A key objective of this research was to identify the best coupling efficiency using blue-detuned light with a realistic representation of the initial state. The coupling efficiency is defined as the ratio of the number of atoms that enter the fibre core over the total number of atoms loaded in the MOT. Due to the inaccuracy in the spatial distribution of simulated MOTs, the coupling simulation needs to start with a pre-defined MOT generated using the Monte Carlo method with a temperature of $25\,\mu\mathrm{K}$ such as can be achieved in a standard MOT setup [97]. The density variation is modelled as Gaussian ($\rho(r) = \rho_0 \exp(-r^2/\sigma^2)$) with the $1/e$ radius of the trap of $70\,\mu\mathrm{m}$, which can be produced experimentally with careful tuning of the optical and magnetic forces to optimize the trap spring constant [97, 131]. The simulation resulting from the starting point before the release of the atom coupling is shown in Fig 4.10. A computing domain of $1 \times 1 \times 20\,\mathrm{mm}$ was defined. To improve the visual aspect, the vertical scale was compressed by a factor of 8, which makes the MOT appear like a disc. Simulating 1000 to 2000 atoms at a time is a good compromise between computing efficiency, memory and accuracy of statistical results. The fibre can be defined to correspond to the one that will be used in experiments and the LG beam will diffract accordingly. The length of the fibre is also adjusted depending on the objective of the simulation. When only considering the coupling efficiency, a 5-cm-long fibre is used. When investigating in-fibre propagation and transit times, a 25-cm-long fibre model is generated. The hollow beam field diffracting from the fibre is represented by two red transparent cones. The outer cone and the cylinder inside the fibre are delimited by the maximum intensity radius of the LG beam. When the atoms reach outside this cone, they are no longer confined. The inner cone, just outside the fibre, is the $1/e^2$ intensity radius of the dark hollow region of the beam.

4.4 Atom coupling dynamics

This section undertakes a detailed examination of the atom trajectories to understand their dynamics in this system. The outcome is either one of the three classes: (i) atoms coupled into the fibre ("coupled"), (ii) those captured in the funnel but which do not enter the fibre ("trapped"), (iii) and those which immediately escape the funnel when released from the MOT ("escaped"). Sec. 4.4.1 analyzes atomic motion and then, adding the particular

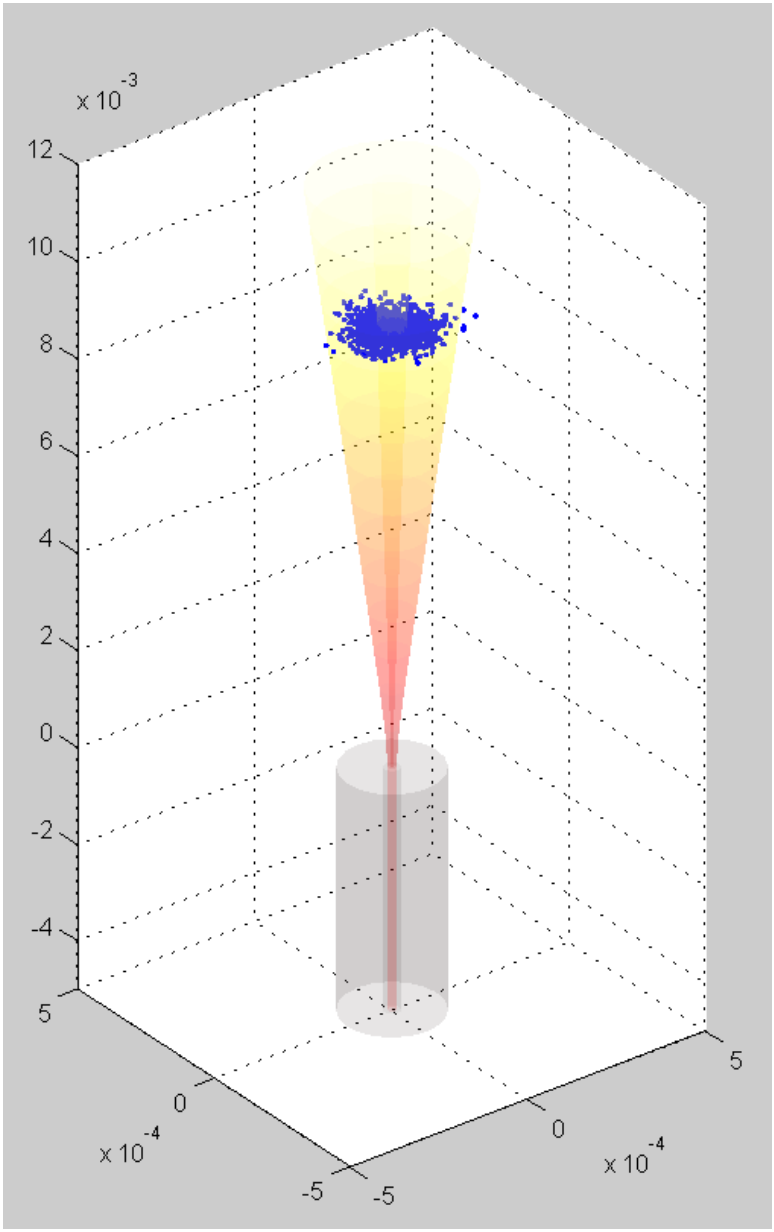

Figure 4.10: Screenshot capture of the initial conditions before release of the MOT in the atom coupling simulation model. A small MOT of 0.3 mm diameter and 1000 atoms is represented hovering 9 mm above a 5 cm-long hollow fibre with 40 μm core diameter. The red transparent cones show the maximum intensity and dark diameter of the LG_{01} beam diffracting from the fibre core.

details of a MOT released into an optical blue-detuned funnel in Sec. 4.4.2.

4.4.1 Motion of atoms in an optical dipolar potential

By considering atoms inside the fibre, whether guided in a blue-detuned collimated Laguerre-Gaussian beam or red-detuned Gaussian beam, their motion will be that of a particle trapped in a central, attractive and circular potential similar to the case of a test mass moving in the gravitational field of a point mass. More generally, for a central power-law potential $V \propto r^x$, only potentials in $x = -1$ (gravity) or $x = 2$ (harmonic) can sustain stable closed elliptical orbitals [132]. The optical confining potential follows a sigmoidal-shaped function of $r^2\ e^{-r^2}$. Therefore, atoms guided/loaded in the optical dipolar potential are found to have unstable orbitals as shown in Fig. 4.11. This figure displays characteristic orbitals of atoms falling into the optical funnel in a downward top view from the z-axis.

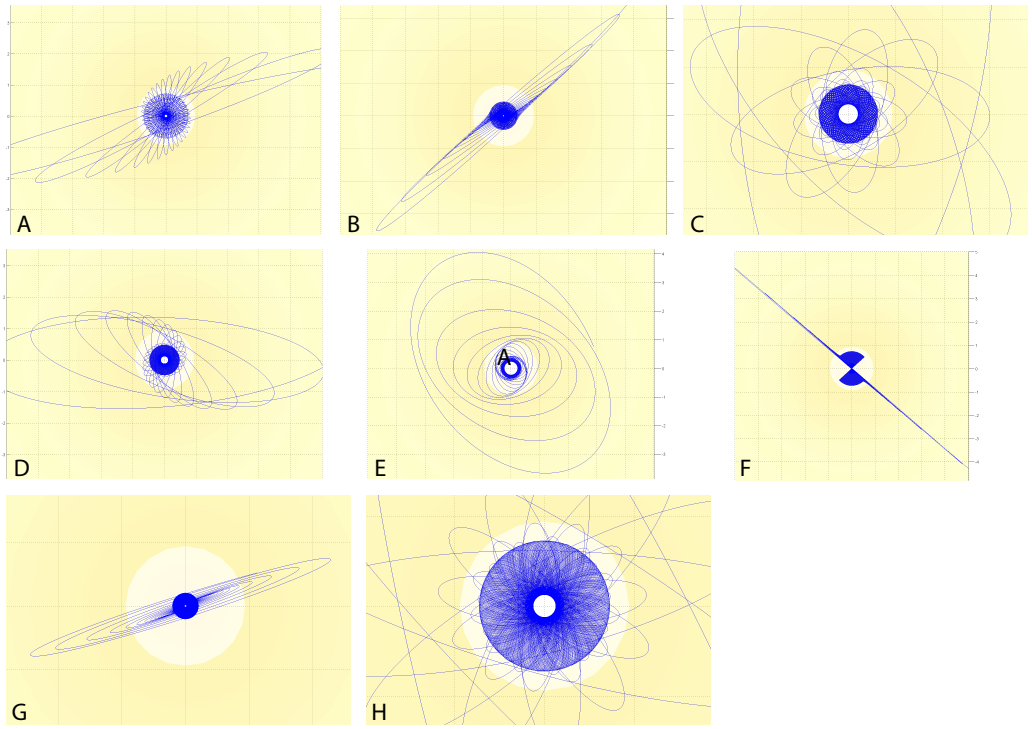

Figure 4.11: Top view of the characteristic orbital trajectories of atoms captured by the confining potential and coupled into the fibre.

Consider an atom falling into a diffracting potential. The atom will spiral into the light funnel, analogous to a ball moving on a hyperbolic funnel surface. As the diameter of the potential reduces towards the waist of the beam, the orbital velocity of the moving particle is seen to increase as is expected from the conservation of angular momentum. Unlike the ideal circular motion in a classic hyperbolic funnel, the orbital describes a precessing ellipse as seen

in Fig. 4.11. The precession acquired during the coupling is conserved once inside the fibre. Similar trajectories are also observed in collimated beam simulations, so the coupling is not responsible for precession but rather the *anharmonicity* of the confining potential. Depending on the initial conditions, simulated orbitals range from almost circular to extreme ellipses (close to a purely radial motion). They can be classified into one of the three categories: (I.) Almost-circular, (II.) Almost-linear and (III.) Precessing-elliptical. The third category is found to describe $> 95\%$ of coupled atoms. Figure 4.12 shows the 3 types of orbitals in 3D, from coupling to its movement within the fibre, in the same order they were presented.

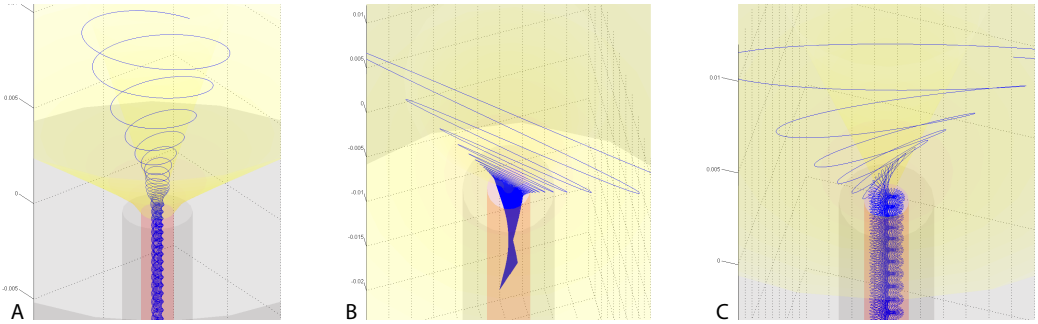

Figure 4.12: Path from the three types of orbitals are shown in 3D. (A) Almost-circular orbitals show very little precession. (B) Almost-linear orbitals usually have precession, like in this case, unless it is directly in line with the centre. (C) The most-common precessing-elliptical trajectories are easy to recognize with the initial coupling path and a flower-like pattern in the fibre core.

In the optical funnel, the axial motion is linked to the transverse velocity in a complex fashion. In the absence of axial forces in the funnel, i.e. where diffraction is absent or inside the fibre, all atoms accelerate downwards with gravity independent of their orbital motion. However, in locations where diffraction is significant, the tangential velocity assumes much greater importance. The orbital radius of a high tangential velocity atom needs to be larger in order to balance by the stronger radial forces available at that location. In this case, the atom will penetrate further into the high intensity areas of the beam and thus, the effective vertical acceleration delivered by the hollow-beam will become stronger. By this means, the optical funnel can couple tangential and axial motions of the atom and yield the complex orbits that are seen on Fig. 4.13 as well as the axial velocities illustrated in Fig. 4.14. The simulation time-step of $5\,\mu$s is carefully selected according to the physical parameters, to allow efficient computing while still maintaining a high resolution along the strongest gradients and the

smallest orbitals obtained within the fibre core. By comparison, the MOT simulation uses a 20 μs time-step because the large diameter beam gradients in free space are much smaller than within the fibre. Figure 4.13 shows the high-resolution orbital motion of atom within the simulated hollow optical fibre. Group (A#) of sub-Figures presents a top-view of their trajectories in a 5 cm-long fibre and group (B#) shows their corresponding path in 3D.

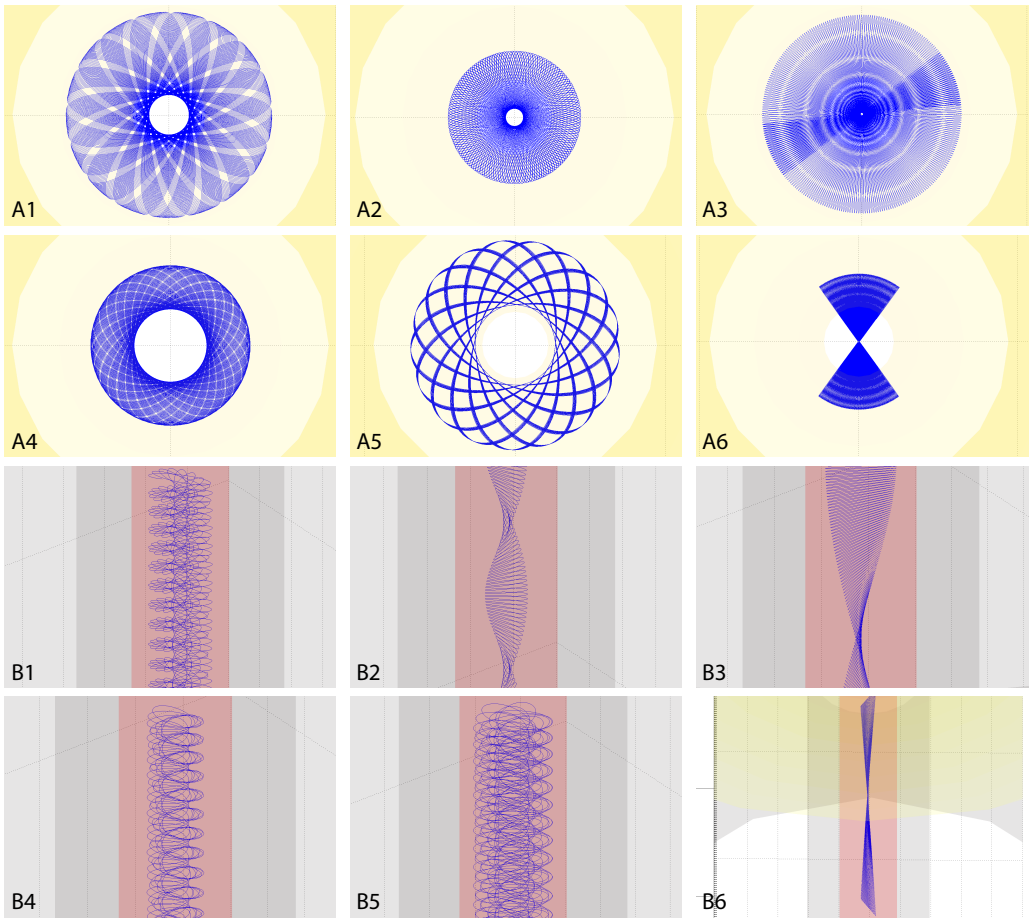

Figure 4.13: Guiding simulations show very high resolution of orbits within the fibre. The top-view of atom trajectories within 5 cm of fibre is represented in group A# while their corresponding 3D paths are shown in group B#.

The path integral of the axial force along the atom trajectory in the optical funnel, reveals the potential barrier that needs to be overcome in order to reach the fibre. Consequently, all atoms funnelled toward the fibre experience some deceleration that is dependent on their path trajectory. It is this complex interaction of their initial state energies (transverse, axial and gravitational potential) with the varying forces of the optical dipolar funnel which determines

whether or not they couple into the core. As a simplification, this simulation uses a detuning of 800 GHz where the heating forces have little effect on atom motion. However, atoms can be guided successfully at much lower detuning and this topic will be covered in-depth in the next section. Figure 4.14 presents the axial velocities of each atom as a function of distance from the fibre in a Monte Carlo atom coupling simulation. The atom-trajectories have been labelled on this figure according to the three possible outcomes: escaped from the funnel (green lines), guided into the fibre (blue lines), or trapped in a dynamic balance between gravity and the axial dipolar force (red lines). Once the guided atoms have gone through the repulsive axial potential barrier, they all start accelerating again inside the fibre by the action of gravity. The "trapped" atoms are pushed upwards and are recycled into the same near-triangular path of velocity-distance, being effectively trapped by the conservative potential.

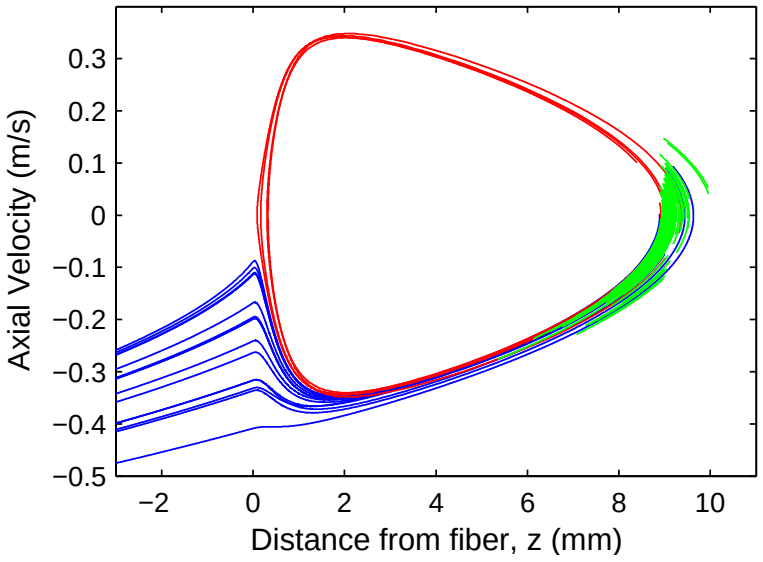

Figure 4.14: The axial velocity of each atom in the simulation is represented against its distance from the fibre. All atoms are released from 9 mm and exposed to a 52 mW/800 GHz blue-detuned LG_{01} beam with a 20-μm waist radius within the fibre. Negative distances represent positions within the fibre core from the coupling input. Each velocity path is color-coded by the final outcome of its atom: guided (blue/dark gray lines), trapped (red/medium gray lines), and escaped (green/light gray lines).

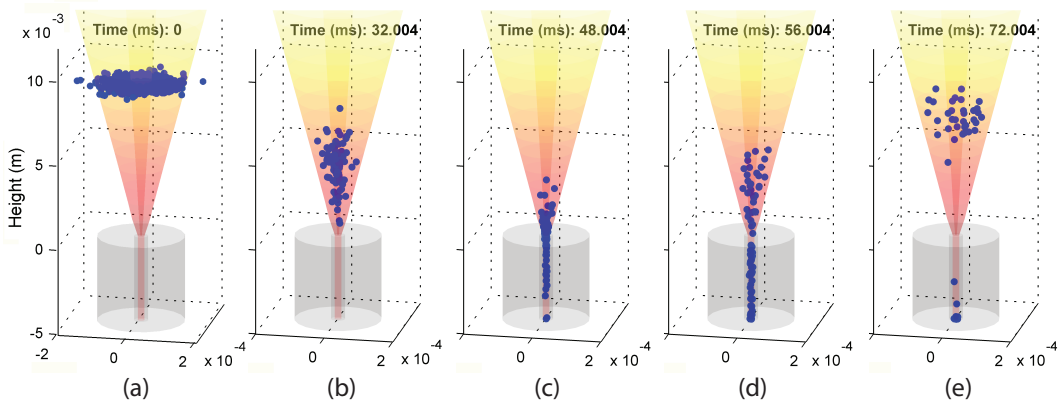

Figure 4.15: The dynamics of atomic coupling are represented with 5 snapshots taken during the simulation. The vertical axis is compressed by a factor of 15. The limits of confinement are represented by the outer light cone. The inside cone is delimited by the dark radius (peak intensity/e^2). (a) Atoms at release time from the cooling lasers, 9 mm away from the fibre. Their density distribution is a 3D Gaussian but the compressed vertical scale makes it appear like a disk. (b) 16% are loaded in the hollow-beam funnel. Their phase space is compressed as they approach the fibre. (c) Almost all atoms approach the fibre within 0.5 mm, with some of them already coupling into the core. (d) Atoms are separated into two energy-selective populations: the coldest 8% are guided into the fibre core, the other 8% are pushed away by the axial component of the dipolar force. (e) Atoms relax up until gravity forces them down again toward the fibre. This cloud of atoms is trapped in the gravito-optical bottle trap as long as their total energy is conserved in the system.

4.4.2 Atom dynamics in a microscopic optical funnel

Figure 4.15 displays five sequential snapshots of a 3D Monte Carlo simulation to fully illustrate the dynamics described. The figure is vertically compressed by a factor of 15 because the z axis spans over 17 mm while x and y axis are only 0.4 mm. In Fig. 4.15(a), the initial spatial distribution of atoms is a 3D Gaussian function (spherical); although they initially appear to be in a disk distribution due to the compressed z scale aforementioned. The confinement area is illustrated by the red cone colored from light yellow to red following the increasing trap potential. In simulations, the minimal efficient coupling distance required the radius of the maximum intensity of the beam, at MOT release location, to reach 1.8× the $1/e$-fold width of the MOT (as is the case in Fig. 4.15(a)). This effectively corresponds to releasing from the MOT $> 98\%$ of the atoms within the confinement limits of the funnel.

Atoms initially outside the red cone will be lost immediately. Atoms inside the cone can

escape only if they possess a transverse energy E_{Tr} greater than the trap potential depth, $U_0(z)$. The transverse energy of an atom at position *x, y, z* is defined as follows:

$$E_{Tr}(x, y, z) = E_{Kt}(v_x, v_y) + U(x, y, z) \tag{4.16}$$

where E_{Kt} is the kinetic energy in the plane perpendicular to the fibre/beam axis and $U(x, y, z)$ is the optical trap potential at the atom position calculated from Eq 4.11.

After the initial loss of the higher energy atoms in the distribution, in Fig. 4.15(b), the remaining cloud no longer exhibits a Maxwell-Boltzmann distribution. A compression of the cloud is observed as it falls in the funnel. Although the total energy of each atom is conserved as it falls, the conversion of gravitational potential energy into kinetic energy leads to a large increase in the velocity of the atoms. The diffraction of the funnel causes a conversion of the gain in axial velocity into an increase in the transverse energy. The simulation shows that the increase in the transverse energy is proportional to the decrease in the area defined by the locus of points of maximum intensity. That is, for a typical situation, with the MOT positioned 9 mm above the fibre, the radius of maximum confinement decreases by 160× from the MOT release to the entrance of the fibre. The transverse energy of each atom also increases by 160×. Fortunately, the trapping potential increases proportionally to the square of the decreasing fibre distance, which matches exactly the dependence of the transverse energy keeping the atoms in a trap of the same relative depth (ie. maximum transverse energy/optical potential depth is *approximately* constant).

Figure 4.15(c) shows the atoms falling toward the fibre in a cone-shaped cloud, coming very close to the fibre surface, until a separation into two populations occurs (Fig. 4.15(d) and (e)). The coldest fraction of atoms couple into the core, while others are repelled from the fibre. Continuation of the simulation shows that the repelled atoms execute the closed-cycle trajectories shown on Fig. 4.14 as the "trapped" atoms.

The principal determinant in the final state of the atoms is the initial transverse energy of the particle. The initial transverse energy of 1700 ^{85}Rb atoms was compared against their outcome in Fig. 4.16. It is shown that the coldest atoms (with lower initial transverse energy) couple into the fibre core (blue circles). Atoms with higher energy immediately escape the hollow-beam at the MOT release distance (green triangles). Atoms with transverse energy intermediate to these values penetrate the confining potential more deeply (red squares). These atoms have their axial velocity reversed before they reach the fibre. These atoms end up being trapped in an energy-selective gravito-optical bottle trap.

Similar gravito-optical traps based on blue-detuned hollow-beams have been previously reported [112, 133], although their intention was to trap the atoms whereas we are trying to

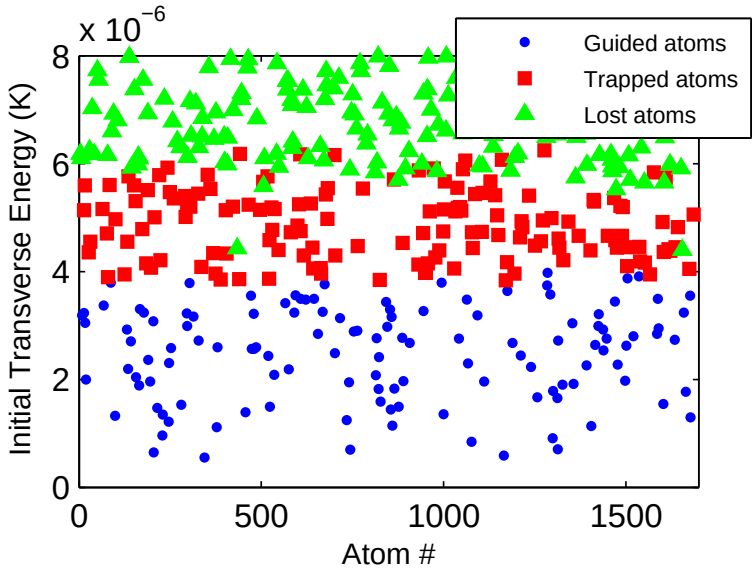

Figure 4.16: Initial transverse energy of 1700 ^{85}Rb atoms labelled in function of their simulation results: guided into the fibre (blue dots), trapped by the gravito-optical bottle effect (red squares) or escaped the hollow-beam (green triangles). The 3D Monte Carlo simulations had the following parameters: 25 μK, 200 μm diameter MOT launched at 9 mm into a LG_{01} beam of 40 μm diameter, 63 mW and 800 GHz blue detuning. Only escaped atoms with transverse energy below 8 μK are shown.

avoid this. Under our set of conditions, the axial component of the blue-detuned repulsive force, opposing gravity, is only effective for atoms with higher transverse energy. During the coupling experiment, the gravito-optical bottle trap effectively behaves as a hot-atom filter. As the potential is increased in strength a larger fraction of atoms fall into this "trapped" class. Obviously, this bottle trap effect should be carefully managed in order to achieve optimal coupling of atoms into the fibre core. This effect can also be used to only couple colder populations within the fibre, if the reduced fluorescence response is not beyond the detection threshold.

A deeper analysis of the dynamics showed that the transverse energy is not the only determinant of the eventual classification of the atom. The initial axial velocity can have a minor influence toward atoms with axial velocities at the extreme of the distribution. This causes an atom to fall into a class which was unexpected from their initial transverse energy alone. section 4.5 will consider how the experimental parameters influence the atom-distribution among the three classes and how the heating forces affect these results when working at closer detuning.

4.5 System properties: optimizing coupling efficiency

This section will focus on evaluating the coupling efficiency of our specific experimental arrangement. In particular, it will discuss the dependence of the efficiency on the light force ratio, MOT-fibre distance, fibre core diameter and the frequency detuning. It will also make a comparison of this hollow-core approach with an optimal coupling scheme based on red-detuned Gaussian beam coupling.

4.5.1 Optimal coupling efficiency discussion

In simulations with ^{85}Rb, realistic MOT parameters of $T = 25\ \mu$K were selected with the trap radius $\sigma = 70\,\mu$m using a standard setup [97]. The MOT is centered on the axis of a HC-PCF that guides a 40-μm diameter LG_{01} beam. The remaining degrees of freedom are the guiding laser light force ratio ($\kappa = P/\delta$) and the distance between the fibre and the MOT centre. The simulation shows that there is an optimal potential for maximum coupling at a

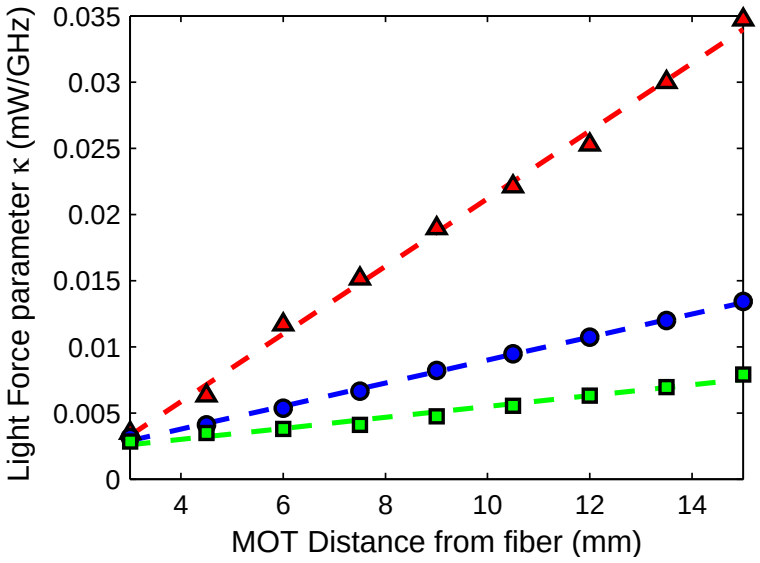

Figure 4.17: Atom coupling efficiency as a function of the force parameter of the blue-detuned hollow-beam and the distance the atoms in the MOT are released from the fibre. The optimal line (blue circles) shows the force relation with MOT distance to realize the best coupling efficiency. The low-force line (green squares) and high-force line (red triangles) represent the force-distance combination that would deliver a factor 2 reduction in the coupling efficiency.

given fibre-MOT spacing. This optimal value is shown by the line of blue circles in Fig. 4.17. Two other lines are shown in which the coupling fraction has fallen by a factor of two from

the optimal value. The relationship between the force necessary to maintain optimal coupling and the MOT distance is linear. This arises because it needs to compensate for the additional diffraction by increasing the beam power to maintain the equivalent initial conditions. The strength of the axial potential barrier that increases proportionally with κ, is a determinant factor in the coupling efficiency. Its effect on the coupling efficiency is compensated by the linear increase in gravitational potential energy with distance. The axial barrier therefore stays at the same relative strength for a given atom and the optimal coupling efficiency is maintained.

Optimal coupling as a function of the MOT-fibre distance

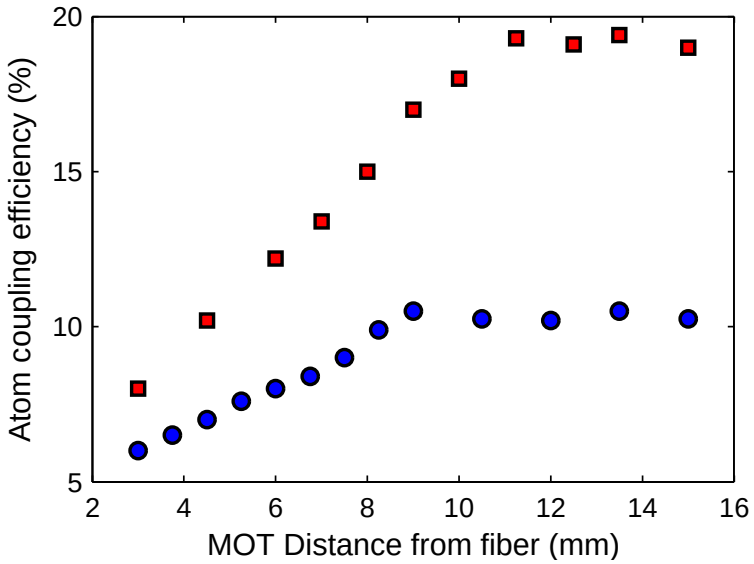

Figure 4.18: Monte Carlo simulation of the optimal coupling efficiency of a 25 μK, 200 μm diameter ^{85}Rb MOT launched from a fixed distance into: a 40-μm diameter (blue circles) and 50-μm diameter HC-PCF (red squares) guiding a blue-detuned LG_{01} beam.

Figure 4.18 shows the maximum atom coupling efficiency obtainable as a function of the distance from the MOT for two different fibre core radii. The analysis reveals that the best coupling efficiency can be achieved beyond a minimum distance. This value can be maintained for increasing distances. This distance is set when the radius of the diffracting funnel is at least 1.8× the size of the MOT. Below this threshold the Gaussian distribution of atoms in the MOT is trimmed by the funnel confinement limits. Even if the coupling efficiency can be maintained with longer distance, it is not desirable to do so because the increased light force

results in higher scattering rates (losses due to heating) in the fibre core. Therefore, it is best to work with the lowest force possible by selecting the shortest distance for optimal coupling efficiency. The minimum/optimal distance consistent with capturing the maximum fraction of the MOT is therefore determined by the guiding fibre core diameter. Results of 9 mm for a 40-μm core diameter and 11.25 mm for a 50-μm core were obtained. Smaller cores require shorter coupling distances because of increased diffraction.

Coupling efficiency as a function of the light force ratio

The fraction of coupled atoms as a function of the light force ratio in the hollow-core guide is displayed on Fig. 4.19 for the standard set of conditions presented. A fixed distance of 9 mm between the MOT and the 40-μm core hollow fibre is selected. The coupling efficiency

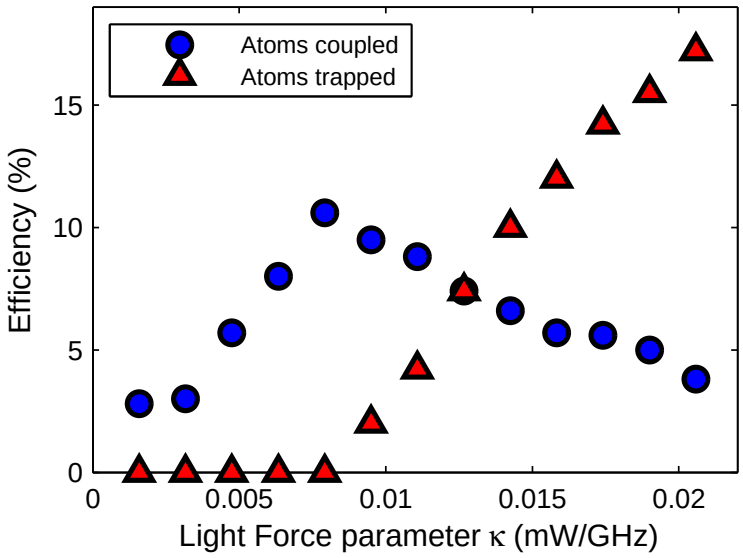

Figure 4.19: Releasing the MOT at 9 mm from the fibre, the coupling efficiency of ^{85}Rb atoms (blue circles) is illustrated in relation to the light force ratio. The trapping efficiency (red triangles) is also represented against the same light force. The best coupling efficiency is obtained when the light force is at the threshold of trapping atoms in the gravito-optical bottle effect.

increases up to a certain force, and then decreases as the fraction of trapped atoms grows. There is an optimal depth to the potential: This characteristic appears because a balance between the depth of the potential, in terms of atom capture, and the rise of a population of trapped atoms is necessary. The coupling-efficiency/light-force relationship shows the same

optimum with different MOT release distances and different fibre core radii. Thus, for a set distance and fibre core radius, the optimal coupling efficiency is always achieved with the maximal force just before or at the threshold of the appearance of a few trapped atoms. The fraction of trapped atoms rises much faster because not only are guided atoms converted into trapped atoms but the increase in force also increases the fraction of atoms initially captured at the release of the MOT. Nonetheless, their higher transversal energy means they cannot be converted into coupled atoms either.

Scaling of coupling efficiency with fibre core diameter

If the objective is to couple a large number of atoms into a fibre, it is clearly an advantage to work with larger core fibres. With a larger core, there is less diffraction (diffraction angle is inversely proportional to the radius) and this results in a naturally weaker axial force. Comparing different fibre core radii, the maximum coupling efficiency and minimum coupling

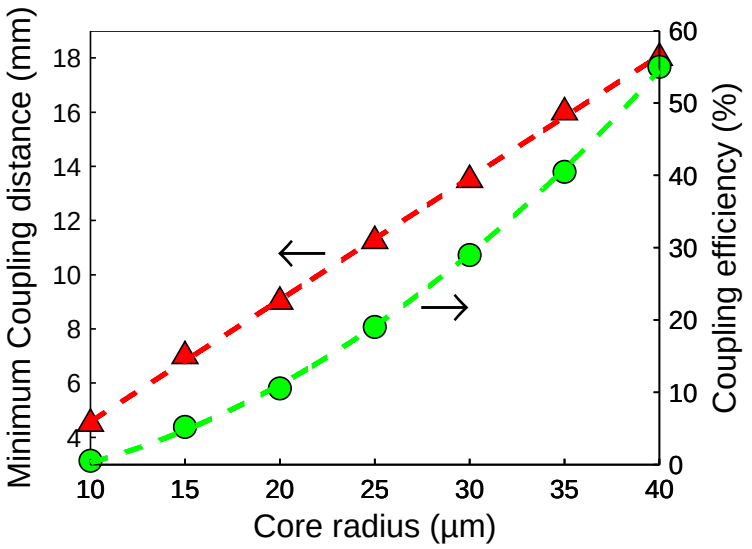

Figure 4.20: On the left axis, minimum coupling distance to achieve the best coupling efficiency is represented as a function of the fibre core radius (red triangles). On the right axis, the best coupling efficiency achieved with a particular fibre core radius is shown (green circles). The red dashed line is a linear fit of the distance-radius relationship and the green dashed line is a quadratic fit to the coupling efficiency.

distance to achieve that efficient coupling are displayed for a range of realistic fibre core sizes in Fig. 4.20. Our simulations have shown that the maximum coupling efficiency is linearly

proportional to the fibre hollow-core area, whereas the minimum coupling distance is linearly related to the core diameter. For best coupling efficiency, the minimum coupling distance is achieved (with a LG_{01} beam) when the radius of maximum intensity of the diffracting hollow-beam is equal to 1.8× the diameter of the MOT. Hence, for this fixed funnel radius, the relationship of the distance with the fibre core radius is $d = 1.8\sigma/tan(\theta)$, where d is the coupling distance and θ is the diffraction angle of the hollow-beam (inversely proportional to the core radius). The minimum distance is therefore a linear function of the fibre core radius. With increasing core dimensions, the maximum light force that can be applied is limited by the axial dipolar force (the gravito-optical bottle effect), as reported in Sec. 4.5.1. It is observed that increasing κ proportionally to r^3 maximizes the coupling efficiency. The quadratic increase in the coupling efficiency with core radius (shown in Fig. 4.20) is a combination of the decreasing axial force by $1/r$ and the linear increase of the gravity potential energy (due to increasing the minimal distance linearly with r).

4.5.2 Analytical estimation of optical scattering in the guiding beam

The difference in light scattering between atoms guided in a conventional red-detuned Gaussian beam and a blue-detuned hollow-beam is investigated. For a frequency detuning *large* compared to the atomic linewidth and at low saturation, the scattering rate per atom can be expressed:

$$R = \frac{\Gamma}{4}\frac{\Omega^2}{\delta^2} = \frac{\Gamma^3}{8\delta^2}\frac{I}{I_s} \tag{4.17}$$

In both guiding arrangements, the cold atoms will be concentrated around the central axis depending on their initial transverse energy. In the blue-detuned guide, the atoms spend the predominant time in the dark whereas, in the Gaussian beam, they are exposed to the maximum intensity. The light scattering rates of atoms is compared in repulsive and attractive potentials during the process of coupling and then, guiding inside of a HC-PCF. An identical maximum potential and a detuning of 50 GHz from resonance is used in both cases. Light scattering rates are calculated using two different methods.

The first method explicitly simulates the scattering rates of atoms trajectories described in the guiding potential, while the second method calculates the average light intensity in the volumes explored by atoms of a specific energy. Then this is used to represent the average scattering rates. Both techniques predict that only a small fraction of scattering events (less than 8% of the total) occur during the coupling phase and hence, this phase is ignored in our calculations. Figure 4.21 compares the relationship between light scattering rates and the coupled atom transverse energy, using this first technique, for a Gaussian (black squares)

and a LG_{01} trap beam (green triangles). The expected behavior that a hollow-beam guide has much lower scattering rates than a Gaussian guide is observed, except for atoms with a transverse energy close to the guiding potential.

Figure 4.21 also displays the expected scattering rates from a simple model (the second method) that averages the beam intensity over the area of confinement of atoms of a particular transverse energy. The radius of that area is determined by a trapping potential that is equal to the transverse energy of the atoms. The calculation of the light scattering rates for the Gaussian (red line) and LG_{01} beam (blue line) shows excellent agreement with the light scattering rates obtained from the atoms simulated in the numerical SC-VV model. Thus, this investigation shows that blue-detuned hollow-beam guides are superior in their guidance of *cold* atoms because of the reduced scattering rates while maintaining an equivalent guiding potential. It was also observed that for different optical trap depths, the ratio of scattering rates between Gaussian and hollow-beam, for a given transversal energy, is maintained.

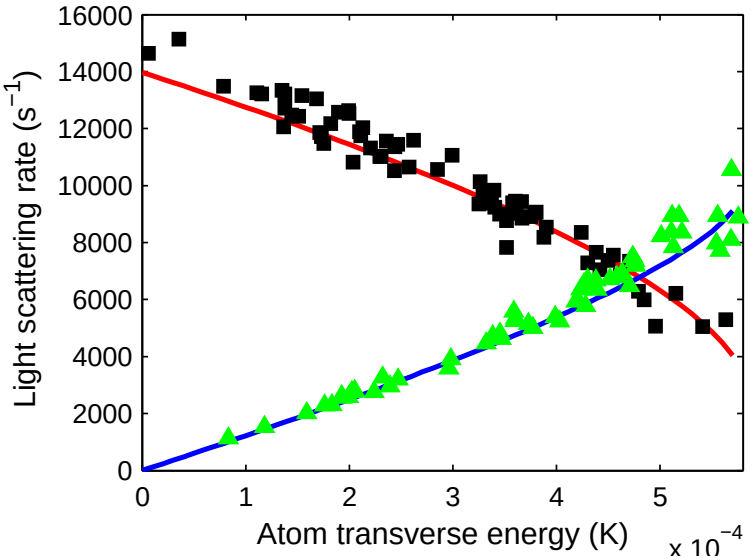

Figure 4.21: Light scattering rates of cold atoms guided in a HC-PCF by an attractive Gaussian potential (upper red curve and black points) and by a repulsive hollow-core potential (lower blue curve and green points). The expected scattering rates are calculated by a statistical method (smooth curves) and by examination of the scattering rates through the explicit trajectory of the atoms simulated in the model (points). The two methods show excellent agreement. Simulated parameters are: 9-mm MOT-fibre distance, 40-μm core diameter, 0.57 mK trapping potential depth in the core, and 50 GHz detuning.

4.5.3 Effects of light scattering and momentum diffusion on coupling and guiding atoms

Most of our previous simulations have been conducted at a detuning where heating effects do not interfere with optimal coupling and guidance. At smaller detuning, the effects of light scattering (average effect of the spontaneous force) and momentum diffusion are complimentary and quite remarkable because captured atoms are now ejected during the coupling and trapping process.

Light scattering is a force that directly opposes gravity, following the laser beam propagation, and it is at its strongest inside the fibre core. At its strongest, even atoms that are coupled into the fibre can be stopped after some distance and pushed out, creating a new subclass of trapped atoms labelled "ejected". In collimated beam guidance, light scattering can be important enough to completely oppose gravity and prevent atoms from falling in the beam. When the scattering rate is weaker, it does not induce any loss but slows guided atoms within the fibre so that they accelerate only at a fraction of g.

Momentum diffusion acts by adding random pushes to the velocity of the atom, as demonstrated in the MOT simulations. In coupling simulations, atoms being funnelled are quite energetic and the contribution of momentum diffusion is to increase their kinetic energy over time. For most coupled atoms, it has no noticeable effect, except that their orbitals increase slightly during guidance in the fibre. However, for atoms at the frontier between the coupled and trapped classes, the random recoils are enough to push them over the edge of the potential barrier and escape the optical funnel. This happens during guidance in the fibre as well. Observed in the simulation videos, the effect gives the impression that a few atoms spin out of control during funnelling or when they just reach inside the fibre. In the analysis, it induces loss in the trapped atom population 4× more than in the coupled/guided atom population. Over time, momentum diffusion takes away more and more atoms, whether they are guided or trapped.

For example, at 50 GHz detuning, for the optimal light force ratio (0.0675) from a MOT launched at 9 mm, the simulation without any heating gives a coupling efficiency of 9.6% with 0.2% atoms trapped. When light scattering is taken into account, the coupling efficiency reduces to 5.5% and the trapped population increases from null to 5.3%, which shows that nearly half of atoms coupled are now converted to trapped atoms. Considering guidance within the fibre, nearly 1.5% from the 5.5% of atoms are "ejected" and do not reach the end of the 5 cm-long fibre. When momentum diffusion is also included, there is a noticeable change as many atoms are seen spinning out of control in the funnel and escape. The coupling

efficiency is slightly affected, down to 4.8% (a 0.7% loss) but the trapped population is down to 2.2% (a 3.1% loss). By prolonging the simulation so that the trapped population bounces twice (∼170 ms), 20 additional atoms are lost out of 22. This example shows the general effect of these heating forces, nonetheless, they can be mitigated by detuning the frequency and using higher optical power.

Previously, the "heat-free dynamics" of atom coupling with a 40 μm-diameter LG_{01} beam were analyzed with a detuning of 800 GHz. To reach an optimal coupling, a light force ratio of 0.0675 must be followed which requires 54 mW of optical power. Experimentally, this is not always practical: when taking into account the power budget, the experiment would require a laser output power of 250 mW. Therefore, how close a detuning is needed while maintaining a reasonably good efficiency? If one wants to guide in a fibre, a detuning of 290 GHz, keeps momentum diffusion losses negligible and an average spontaneous acceleration inferior to 1 g. Optimal coupling is reached with 20 mW of optical power. Without guidance in a fibre, coupling and funnelling atoms is achieved with minimal losses at a detuning of 180 GHz, the coupling efficiency is back to optimal (around 9.5%). However the highest energy atoms funnelled are exposed to 1.4 g at the tightest point. Back at 800 GHz, effects of momentum diffusion and light scattering are not observable in our given configuration.

As a general recipe for specific simulation parameters, the nearest detuning useable is when coupling efficiency is equivalent to heat-free simulations and the strongest spontaneous acceleration is less than gravity. Further detuning is still desirable to minimize momentum diffusion effects and losses during guidance but that is ultimately determined by the optical power available in the vacuum chamber (coupled through the fibre).

4.5.4 Model validation and comparison with red-detuned Gaussian beams

Our model was tested against the experimental data of atom guiding efficiency from Mestre et al. [57]. The Rb atoms were guided using collimated blue-detuned LG modes of order 1 to 12. Because their model did not take into account the light scattering loss, they added an empirical loss factor fitted against their experimental data. Our model does take into account this loss but to be comparable to their data, we deactivated these functions, and applied the same light scattering loss factor to our simulated results. Table 4.2 shows the excellent agreement with their experimental data. The model was also applies to the cold atom coupling experiments reported recently by Bajcsy et al. [22] (summarized in Sec. 2.5). Their initial loading configuration was reproduced as a spatially uniform disk distribution of 440 μm diameter, 1 mm from the fibre, with a temperature distribution equal to that of

Beam order	Exp. guiding eff.(%)	Our model calculation (%)
LG_0^1	0.8	1.4
LG_0^3	7.5	8.1
LG_0^5	13.5	12.75
LG_0^9	18.0	18.3
LG_0^{12}	17.5	19.1

Table 4.2: Comparison between experimental data from Mestre et al. [57] and the model prediction in the guiding efficiency of Rb atoms in collimated blue-detuned LG beams of various orders.

the MOT. A coupling efficiency of 1.5% was simulated at best compared with their 0.3% obtained experimentally. That calculation assumed no loss in the MOT loading process and no light scattering loss during the red-detuned Gaussian coupling.

When comparing the coupling efficiency of the blue-detuned hollow-beam with a red-detuned Gaussian beam, the latter has the advantage of a larger confining area (no confinement limits) and the axial dipolar force is attractive, which does not produce a gravito-optical trapping effect and therefore facilitates coupling. Using the same fibre and identical trap depth potential in the guide, the best coupling efficiency obtained with a red-detuned Gaussian beam was shown to be a factor 4 more efficient (46%) than the blue-detuned LG_{01} beam (11%) when using a 40-μm diameter fibre.

Nonetheless, the blue-detuned hollow-beam is potentially more useful in some circumstances for guidance of cold atoms because of reduced light scattering rates for an identical trapping depth (see Sec. 4.5.2) and the guiding laser does not need to be strobed in antiphase with the probe laser, in order to make measurements within the fibre.

4.6 Summary and future improvements

This chapter presented a model of laser atom cooling and simulations aimed at efficient coupling of atoms from a MOT into a hollow-core photonic-crystal fibre using a blue-detuned LG_{01} beam. In contrast to previous approaches, only a single beam is required to achieve both efficient coupling and guiding within the fibre. The key goal are to guide atoms in locations with minimum light intensity in order to minimize shifts of the internal states, and to minimise de-coherence associated with light scattering.

It was shown that, with a blue-detuned hollow-beam funnel, there is a minimum efficient

coupling distance, which can be simply calculated from the measured parameters of the MOT and the fibre core radius. The model identified a new gravito-optical bottle trapping effect that is significant for the coupling dynamics, when using a low-order, blue-detuned hollow-beam funnel. This trapping effect must be carefully managed to optimize coupling efficiency. Optimal atom coupling conditions were identified for a fixed MOT-fibre separation and fibre core radius. Optimal coupling is achieved when using the highest light force possible before the appearance of trapped atoms. This result disputes the naive expectation that strong guiding forces will lead to maximum in-coupling to the fibre. In contradiction with this expectation, we find that there is an optimal potential depth that will maximize the coupled fraction from the MOT.

Investigation into the heating forces have shown that they do not affect the dynamics of the coupling system when the detuning is enough so that the light scattering force is less than $1\,g$. At this detuning, momentum diffusion will also be weak but will still take away a fraction of atoms coupled and increase the energy of guided atoms. For guidance over 5 cm, further detuning is necessary.

For our example of a $40\,\mu$m core diameter HC-PCF with a LG_{01} guide beam in-coupled, a detuning of 290 GHz is necessary to prevent rejection of atoms by the light scattering force. With 20 mW of optical power, optimal coupling efficiency is reached for a MOT-fibre separation of 9 mm. Momentum diffusion still takes away atoms over time and this effect can be completely cancelled with a detuning of 800 GHz (and 54 mW optical power), the simulation showing "heat-free" dynamics with no noticeable effect of these two forces at this optimal light force. Under these conditions, simulations showed that 10% of ^{85}Rb can be coupled and guided over 5 cm from a $25\,\mu$K, 0.3 mm diameter MOT. The coupling efficiency is very sensitive to the fraction of the MOT contained within the maximum intensity radius of the beam at the release height. However, it is not very sensitive to the MOT temperature, where less than an order of magnitude reduction of the coupling efficiency was measured when the temperature was increased to $150\,\mu$K.

As a general note, if one can afford to use more laser power, then further detuning is advantageous to minimize momentum diffusion losses both during coupling and in-fibre guiding. A first order hollow beam is advantageous over a Gaussian beam, a higher order beam is even better within the fibre but its increased diffraction makes it nearly useless during the coupling phase. Larger core fibres could achieve better coupling efficiency but would require higher light force and experimental constraints would force trading-off power for a reduced detuning, which is not desirable to minimize light scattering losses.

In the next experimental section, the model was used frequently to understand the experimental observations of the atom dynamics as well as improving the performance.

CHAPTER 5 THE EXPERIMENTAL MAGNETO-OPTICAL TRAP

During this thesis, the largest part of the experimental work was focused on the design and construction of the MOT setup. Here is a brief outline of the main elements of our experimental MOT design:

- An octagon vacuum chamber (25 cm diameter by 18 cm wide) was selected to have vertical clearance for a 10 cm straight fibre below the MOT. The chamber featured 8 window ports and 2 large side windows for easy optical access to the MOT. For experiments, all windows were occupied by the laser inputs, the two cameras and the photo detector.

- The cooling beam setup used six polarisation-maintaining (PM) optical fibres to provide six independent cooling beams. This choice made the setup and alignment more complex but also provided the experimenters with freedom to fine tune the MOT shape, position and launch parameters.

- A few turns anti-Helmholtz coils were built to provide ultrafast magnetic field decay. Instead of using wires, we used hollow copper tubes to provide a powerful cooling design where water would circulate all through the coils.

- Three Helmholtz pairs of coils were set up around the chamber to take care of the cancellation of the earth's magnetic field and other stray fields in the centre.

- Two cameras were used for observation and imaging of the MOT. One overhead TV camera provided real-time imaging of the MOT (at 15 fps) for alignment. For imaging, a triggered CCD photo-camera with a zoom tele-objective was implemented to capture MOT dynamics during experiments.

- Three independent lasers were used in the experiment to provide four different frequencies to achieve the tasks of cooling, re-pumping, probing and guiding the rubidium atoms.

- The cooling and frequency stabilisation loop of the re-pump laser was the most critical part of the setup. Many experimental schemes were tested but the best results were obtained with the modulation transfer spectroscopy (MTS) setup. MTS provided an error signal shifted by 180 MHz from ^{85}Rb cycling transition. The less stable re-pump

laser, a homemade Littrow cavity, was frequency locked in a Master-Slave configuration to benefit from the better stability of the commercial laser used for cooling. A complex two-stage servo-controller implementing a phase-locked feedback loop was used to convert the MTS error signal into modulation of the laser pump intensity and the piezo controller of the external cavity grating for both lasers.

- Ultrafast and stable frequency control and tuning of the cooling and probe beam was achieved using two acousto-optic modulators (AOMs) in a double-pass cat-eye interferometer configuration to produce frequency-insensitive beam alignment.

- An *Arduino Mega* microcontroller board was used to implement scripts of the experimental procedures and timing control of the magnetic field current, the laser cooling, guiding and probing frequencies (through their AOMs) and their mechanical shutters, as well as the CCD camera trigger.

In the following section and subsections the design and characterisation of the experimental setup is described. In the second section, the imaging setup, the MOT characterisation and the experimental results of the atom cloud guidance is presented.

5.1 Designing and building the MOT

Depending on the experimental goals, there are many ways to build a magneto-optical trapping system. In this section, we will describe accurately and completely, how our system was built as well as the interconnections of the subsystems. As a roadmap for this task, we have represented a schematic build of our system in Fig. 5.1. Each subsystem (A-H), later identified as stages will be detailed in their respective subsections to complete the system description of this section, except for stage H (hollow beam generation and coupling), which will be discussed in the next chapter.

5.1.1 The vacuum system and Rb source

The UHV vacuum chamber selected for our research program was the Extended Spherical Octagon chamber by Kimball Physics inc. (model MCF800). It has 8×1.5 inch viewports (windows) and 16×0.75 inch viewports around the octagon and 2×8 inch windows on each side. The 16 smallest viewports were sealed shut without windows for economy. The windows were not antireflection coated, although it would have been ideal to minimize the background light inside the chamber and prevent specular reflections off the windows, it would also have

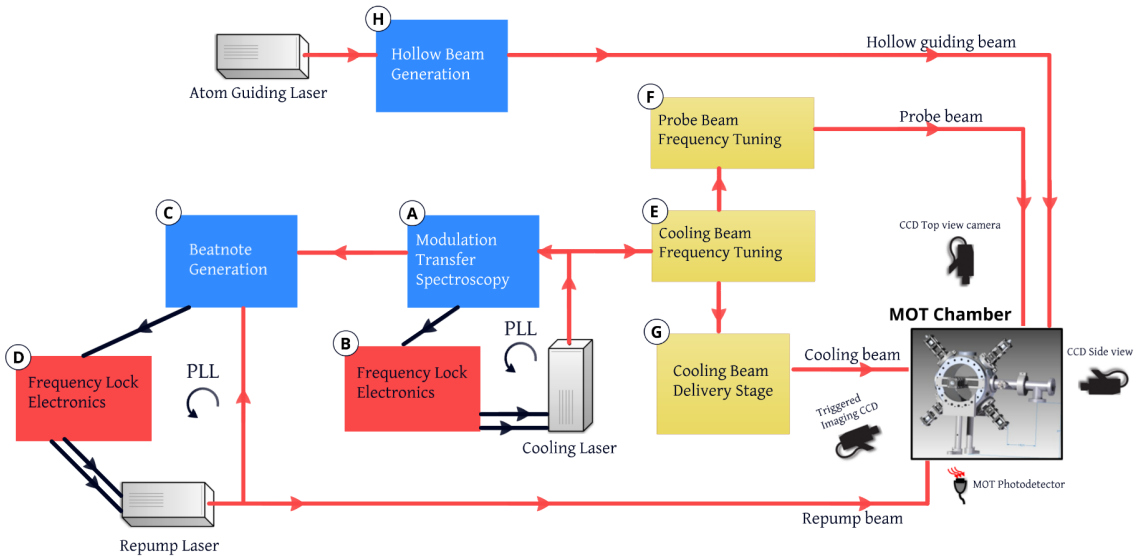

Figure 5.1: Schematic of the MOT system built in Frequency Standards and Metrology labs at University of Western Australia. Arrows indicates the flow of photons, electrical currents and data. Lines in red (black) represent optical (electrical) interconnections. Functional stages of operations are labeled A-H and their internal components will be illustrated by a figure in the following subsections.

been a very costly solution. The inner surface is electro-polished to ensure minimal out-gassing under vacuum. One of the horizontal viewports is used to attach the long steel vacuum arm tube that contained the indirect rubidium source (an oven getter), the ion pump, the optionally attached mechanical pump and the fibre and optics that deliver the re-pump beam. The chamber, the vacuum pump arm and the beam delivery structures are illustrated in the CAD drawing of Fig. 5.2. The mounted large beam fibre collimator, the 2× telescope and the quarter wave plate are all attached together to the chamber viewports in a typical cage-mount construction. The two copper wires sticking out of the vacuum arm are the power terminals that will deliver the electrical current in the feed through component holding the Rb getter oven (the atom source). The second getter oven through a smaller viewport is not represented in this drawing.

Prior to the first vacuum, all the parts involved in sealing the joints: silver plated copper gaskets, silver plated screws and flanges were cleaned in an ultrasonic bath. The 4-step cleaning procedure involved taking each part into consecutive ultrasonic baths of soapy water, distilled water, acetone and methanol for 15 minutes each. The parts were then jet-dried out of the final bath to prevent drying white marks. Flanges with and without windows were

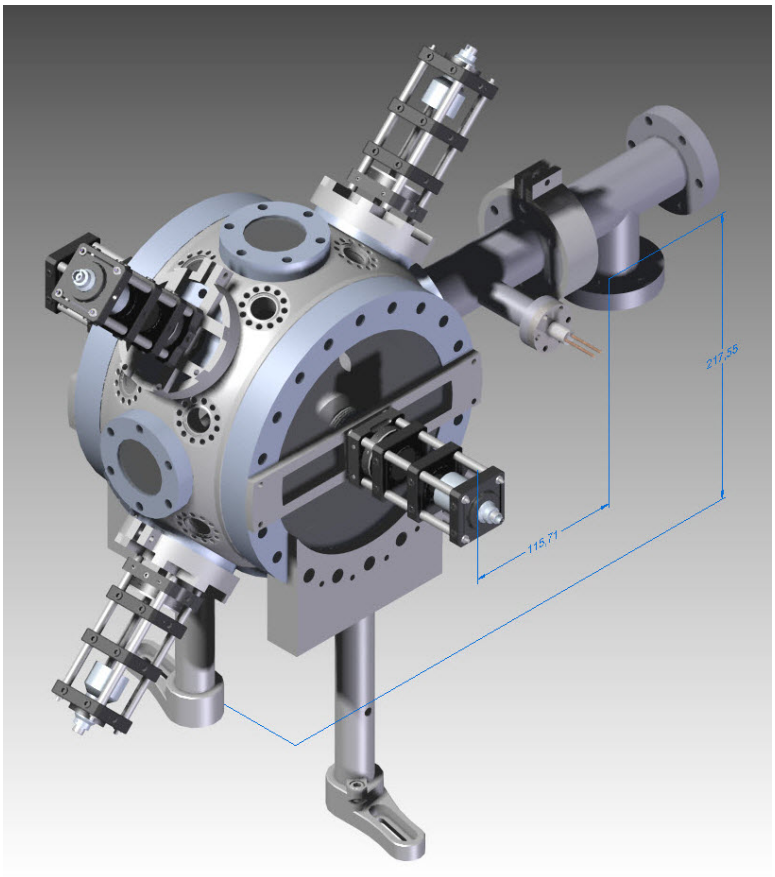

Figure 5.2: CAD drawing of the assembled UHV chamber. The two 1.5" dia. posts supporting the chamber on the optical table are shown. The cage-mounted collimated beam delivery optics is composed of a large diameter fibre collimator mount followed by a 2× telescope and a quarterwave plate. The long steel tube fixed horizontally is the vacuum arm to which the turbo and ion pump are connected. The 2 copper wires sticking out are the power terminals for the Rb getter oven.

attached to the octagon following a procedure to ensure that the screws were evenly tightened.

The primary vacuum of 10^{-5} Torr is obtained using a turbomolecular pump backed with a mechanical oil pump. This vacuum is then followed by a bake-out procedure that consists of using a radiative element heater and wrapping the vacuum system in foil to maintain a temperature > 50°C for 4-5 days. During the bake-out, a gas spectrometer (Stanford Research System RGA) is attached to the system to keep track of the out-gassing of the parts. The bake-out is stopped when the vacuum pressure is dominated by hydrogen while oxygen and nitrogen leaks are an order of magnitude below. After system cool down, the turbo pump is pulled out and the ion pump is activated.

The ultrahigh vacuum is maintained by a 20 litres/sec Duniway Triode Vacion pump (IPC-0065) running continuously to maintain a vacuum of 10^{-8} Torr or less before Rb is introduced in the system. The pressure gauge (Duniway) minimum was 10^{-8} Torr so the overall pressure in the system could be even slightly less when the needle is at the bottom of the dial. The ion pump was wrapped with heating tape around it to maintain its temperature above 35°C in order to prevent Rb from condensing in the pump. Figure 5.3 shows a photo of the octagon chamber when the desired vacuum was reached.

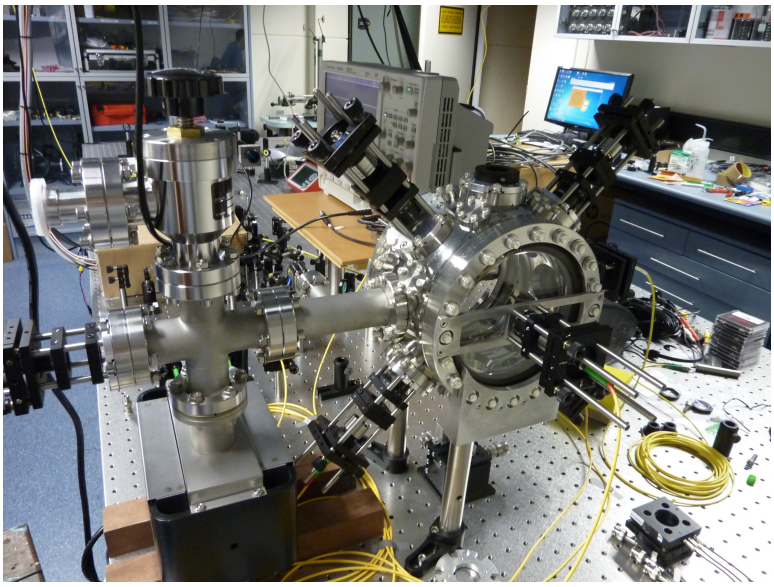

Figure 5.3: Octagon Chamber under ultrahigh vacuum mounted on the optical table.

The Rb atom source was an alkali metal dispenser (getter oven made by SAES Getters inc.). The getter is a small 2 cm long reservoir containing a few milligrams of Rb/Alkali blocked over its length by a fine diameter wire. When heated through by AC or DC current, the wire cracks open the reservoir and provides heat to the reduction reaction to release pure alkali atoms in the chamber. When the wire cools down, the reservoir is sealed again preventing out-gassing of atoms/molecules to the vacuum. The ovens are spot welded to the feed-through part providing current.

Initially all Rb was absorbed by the walls of the vacuum arm and chamber. It took one week running the dispenser at 3.5 A before Rb made its way into the main chamber and was able to build sufficient pressure to observe its fluorescence with a laser on-resonance. Since breaking the vacuum requires considerable time and effort to repump the environment to a high vacuum, 3 getter ovens were installed: one indirect source with a double-oven in the vacuum arm and a backup direct single oven feed-through in one of the smaller 0.75 inch

viewports of the octagon. We preferred the indirect source to ensure that all background atoms in the chamber are close to room temperature and the MOT is not exposed to a stream of high velocity Rb.

5.1.2 The lasers systems

In order to produce and operate the MOT, three different laser frequencies are used for cooling, repumping and probing/guiding/imaging the atoms. First, somewhat uncollimated 150 mW of light was generated with an external cavity grating in conjunction with a narrow linewidth semiconductor laser (Sacher Lasertechnik) at 780.24 nm. In order to achieve the required stability, the laser pump intensity and the grating were actively stabilized, to electrically generate an error signal obtained from a spectroscopic setup using a Rb gas cell, frequency offset by 180 MHz. Details are provided in sections 5.1.5 to 5.1.7. The laser was de-tuned slightly to the red of resonance, close to its true cycling transition (−186 MHz), using a double-pass AOM in a cat-eye interferometer configuration. An external isolator was used, which let out around 80 mW partly because of beam clipping at the input and output despite attempts to collimate the beam with two cylindrical lenses. From this laser, about 3 mW was diverted to probe the atom cloud. Its frequency was tuned independently using a second AOM cat-eye interferometer.

The second frequency source was a "homebuilt" semiconductor laser diode with a typical external Littrow cavity design. The design was similar to the ones published by MacAdam et al. [103] and Hawthorn et al. [134]. The Toshiba diode produced 50 mW at 785 nm but was cooled down with a thermoelectric cooler (TEC) to around 17°C to generate 780.24 nm radiation. The back plate was also held slightly warmer (23°C) than ambient (20°C). Both were actively stabilized by TECs controlled in a PID-based temperature servo. Additional temperature and sound isolation was achieved by putting the laser in double-insulated wooden boxes sitting on a vibration damping base layer (Sorbothane). Still, this repumping laser was affected by stability issues when operated independently and found that the best solution was to lock it against the frequency stabilized signal from the Sacher (cooling) beam. The re-pump resonance was obtained through an electronic offset of the error signal. More details about the repump laser frequency stabilisation and offset are given in the slave lock section 5.1.6.

The third laser was a fibre-coupled Ti:Sapphire narrow linewidth single mode laser (Coherent MBR 110). It served mainly as the guiding beam, where powers up to 100 mW were available. Frequency stabilisation and tuning were far less important than for the previous

two lasers because it was used in far-detuned guidance, from 10 to 800 GHz to the blue or red regions of resonance.

5.1.3 Magnet design and characterisation

The large anti-Helmholtz coils

Large anti-Helmholtz coils were built with a radius corresponding to the large observation windows of the vacuum chamber so that they were as unobtrusive as possible. Custom aluminium mounts were designed and fabricated at the UWA workshop to mount both coils orthogonally and optimally aligned with the chamber's centre. The distance-to-radius ratio to obtain a spherical quadrupole with minimum distortion is $d/R = \sqrt{3} \cong 1.73$ [96], where d is the distance between the two coils and R is the radius of the coil. Our coils had an average radius of 112 mm and the total separation (measured from the centre of each coil) was 209 mm, which results in a $d/R = 1.86$, as close to the ideal spherical quadrupole condition as we could obtain given the mechanical constraints of chamber and the coils mounts. One feature of our design was the use of hollow insulated copper tubes such that they are optimally water-cooled. This allows to design coils with very low inductance having just a few tens of turns and which are driven by high currents (50-100 A). They were fabricated so that each large coil consisted of 21 turns of hollow copper tube with an inner/outer diameter of 1.5/3.15 mm (3.75 mm with insulated polymer coating). The total resistance of each coil was 0.0625 Ω at room temperature but it increased with rising temperatures during their operation.

The coils are supplied with a 600 W programmable DC power supply (Agilent N5741A) with a maximum output of 100 A at 6 V. The coils were connected in series to the power supply with heavy duty copper cables (7/1.70, 16 mm^2, 76 A rating) to ensure a constant and equal current through both coils. The maximum field of each coil was measured independently with a calibrated Teslameter (based on a Hall Effect probe) and the results are displayed in Table 5.1. The Table also shows the total power dissipated through both coils. Even with only a slight difference observed between the two coils, because the position of the zero crossing point of the magnetic field is a critical parameter to control, it became necessary to compensate for it. This was achieved using the Helmholtz pair field cancelling coils in-line with the large coils.

Large coils field modelling

The coils can be easily modelled in the anti-Helmholtz pair configuration with their experimental parameters by simply using the short coil formula for each coil and summing the

Table 5.1: Magnetic field produced for each coil as a function of current. The average power dissipated by the two coils together is also calculated.

Current (A)	B - Coil 1 (G)	B - Coil 2 (G)	Coils power dissipation (W)
10	11.4	11.3	12
20	23.6	23.3	44
30	36.3	35.9	122
40	50.6	49.7	178

total magnetic field in space along the z-axis:

$$B(z) = \frac{\mu_0}{4\pi} \frac{N_i I_B 2\pi R^2}{(R^2 + z^2)^{3/2}} \tag{5.1}$$

Where N_i is the number of turns of wire in the electromagnet and I_B is the electrical current driving the coil. The position along the magnetic axis is defined z. From this formula, the field produced by two coils of opposite current separated by distance d is modelled. Figure 5.4 shows the field produced by the large anti-Helmholtz coils described earlier. The magnetic

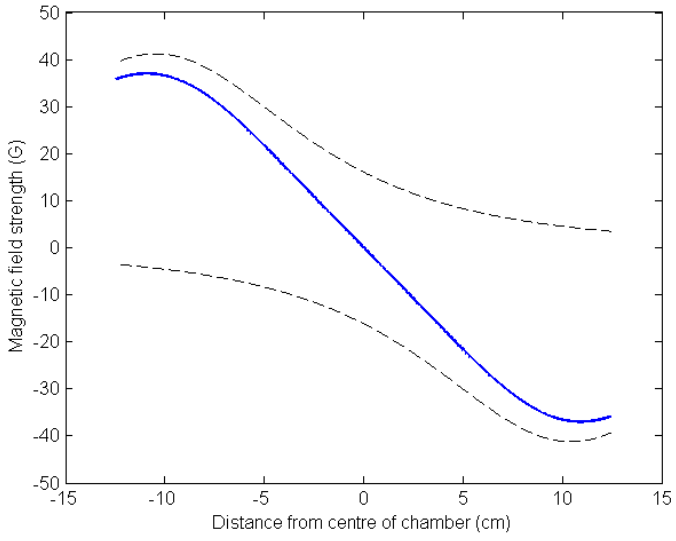

Figure 5.4: Calculated magnetic field produced by the two coils in anti-Helmholtz configuration, driven at 35 A and separated by 209 mm (solid line). The individual magnetic field produced by each coil is also shown (dashed line).

field gradient appears uniform over a large distance but the plot of the gradient of this field (see Fig. 5.5) shows the distortion caused in the centre by the slightly larger than optimal separation distance of our coils. Still, the gradient of the field varies by ±1.2% over 10 cm.

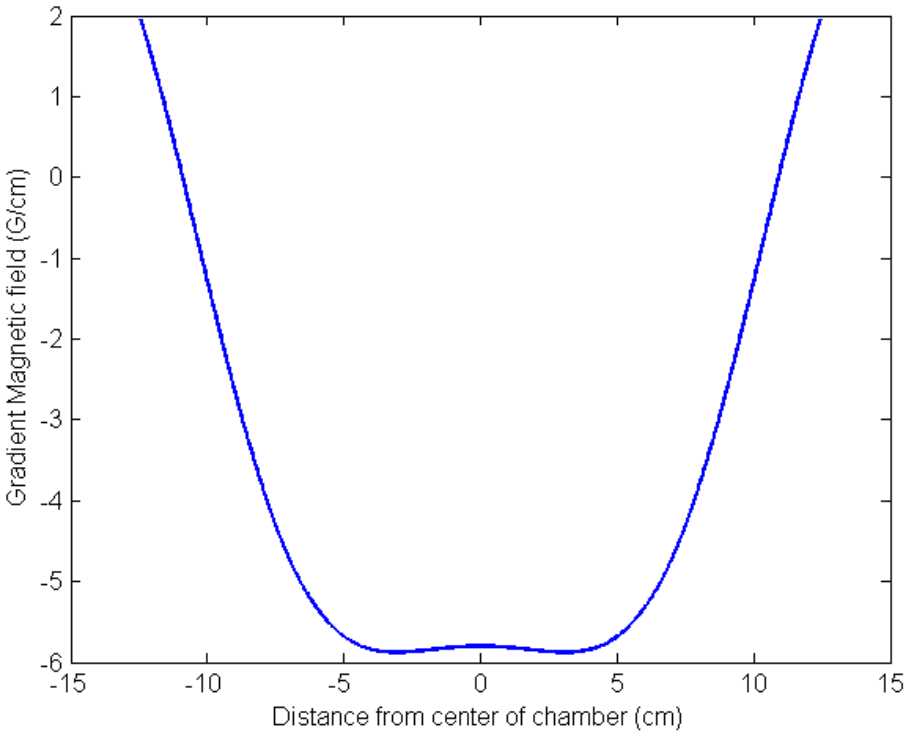

Figure 5.5: Calculated magnetic field gradient as a function of the position produced by the two coils driven at 35 A and separated by 209 mm in an anti-Helmholtz configuration. The gradient of −5.84 Gauss/cm produced is constant over a distance of 5 cm from either side of the zero crossing point, showing ±1.2% of variation over this region.

The gradient in the centre can also be calculated analytically. Taking the derivative of the field for two coils separated by distance d at an equal distance from the centre, we obtain the gradient of the magnetic field in the centre of the chamber:

$$\nabla B = 100 N_i I_B \frac{d}{R} \left(\frac{d^2}{R^2} + 4 \right)^{-5/2} \left(\frac{48 \mu_0}{R^2} \right) \tag{5.2}$$

From the parameters of our coils, we obtain an on-axis gradient of −5.84 G/cm at 35 A. This driving current is often used in our experiments because it is the highest driving current that does not require water cooling of the coils and it is sufficient to produce a robust MOT. The gradient in the perpendicular direction is −2.92 G/cm because Maxwell's equation $\nabla \cdot \mathbf{B} = 0$

implies that the gradient in a plane r perpendicular to the coils' axis is half the magnitude obtained along the coils' axis.

Coils' inductance and magnetic field decay

In many experiments with the MOT and especially for coupling atoms, it is necessary to be able to quickly dissipate the magnetic field so that unbalanced decay between the coils and the eddy currents it generates have as little effect as possible on the trapped atoms. How quickly the field decays is a function of the current fall-time, Δt. However, the inductance produces an EMF kick as a reaction to the current rate of change:

$$V_{peak} = -L\frac{\Delta I_B}{\Delta t} \tag{5.3}$$

where L is the total inductance of the coils. Hence, the key to having a quick decay is to handle the back EMF produced with as little resistance as possible.

Thus, having very low inductance coils is necessary for fast decay of the magnetic field when the current is turned off, which is why our coils were designed with only 20 turns. Calculating the inductance can be a complicated task for irregular geometries. No analytical formula exists for calculating the inductance of a coil of tubular wire and to obtain an accurate value requires numerical calculations with the finite element method. However, we can obtain a good approximation by calculating the inductance of a short coil of round wire with a section equivalent to the section of the tube:

$$L = N_i^2 R\mu_0 \left[\ln\left(\frac{8R}{a}\right) - 2\right] \tag{5.4}$$

where a is the electrical wire radius. In our approximation, the wire radius is $a = \sqrt{r_{out}^2 - r_{in}^2}$. Thus, we obtain an inductance of 0.28 mH for each coil and 0.56 mH for the whole system.

As a simple approach, we first chose to shunt off the coils although this meant a much slower field decay because there are no elements to dissipate the back EMF quickly. The programmable Agilent power supply can also suppress the coil current by shunting a 1 mF capacitor across the power terminals, although it is not designed for quick decay because a capacitor is too slow compare with a transient voltage suppressor diode (TVS). This is how the magnetic field was dissipated in all the experiments for this thesis. Appendix III presents a circuit designed to improve the magnetic field dissipation.

During MOT operation, the slow decay (of the order of tens of milliseconds) transfers kinetic energy into the atom cloud during the transition to the optical molasses stage. It also makes the overall system more sensitive to stray magnetic fields and alignment of the

coils. At its worst, it can accelerate the MOT into a preferential direction; at best, it only raises the overall temperature by a few μK over what could have been achieved. To minimize heating, identical coils were built and a considerable amount of time spent in achieving an optimal alignment.

The decay of the magnetic field across the coils was measured using a calibrated Teslameter and an oscilloscope to monitor the peak back EMF voltage. Figure 5.6 shows the normalized magnetic field decay for 4 driving currents: 3, 6, 25 and 36 A. The decay time for the magnetic field to fall to 5% of its value was measured to be 23 ms. The decay time is independent of the driving current and differences were observed mainly due to the signal being lost in the noise floor when the coils were driven at lower current values.

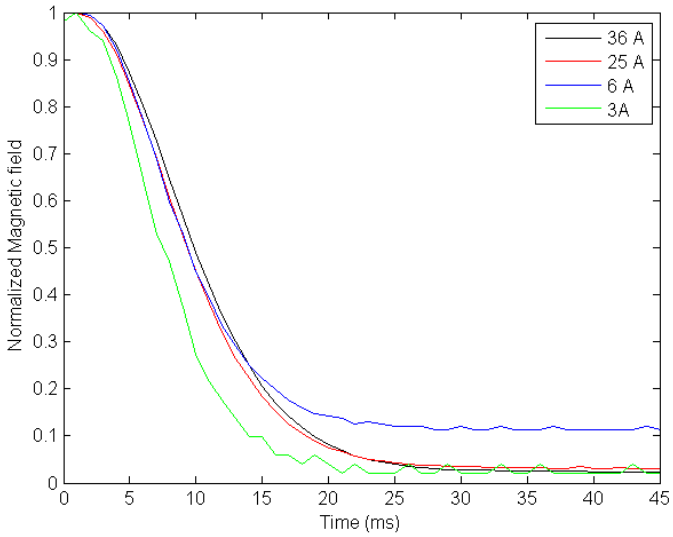

Figure 5.6: Decay of the magnetic field produced by the coils driven at 3, 6, 25 and 36 A. The field was measured in the centre of the coil at its maximum magnitude. Current was shut off by shunting a large capacitor across the power terminals of the Agilent N5741A power supply. The normalized magnetic field decayed in the same time regardless of the driving current. Differences are mainly due to variable noise floor and sensitivity to stray magnetic fields during measurements of very weak fields.

Stray magnetic fields cancelling

An important step in obtaining a cold MOT is the ability to cancel any residual magnetic field that may appear in the centre of the chamber and that is not sourced by the

anti-Helmholtz coils. The stray magnetic fields from the ion pump, 30 cm away, were first evaluated with the Teslameter. Although, a field of 10 G was measured in contact with the pump, the field magnitude was not detectable by our Teslameter at this distance at several locations.

A 20 l/s Triode ion pump (Duniway IPC-0065) was used to maintain a high vacuum. The documentation gives specific values at several distances of the stray magnetic field from the pump. The centre of our chamber was 25 cm away from the pump flange and 6 cm above which yield a stray field < 0.1 G in a direction along the z-axis toward the lasers. In Perth, the magnetic field of the earth (measured in 2010) was 0.58 G with a horizontal orientation almost perpendicular to the z-axis of the Anti-Helmholtz coils and at an inclination of 66° upwards [135].

The Helmholtz cancelling coils were made of 58 turns of 0.65 mm diameter (22 AWG) insulated copper wire. Each of the six coils were carefully wound to be identical and a final resistance of $0.66 \pm 0.01\Omega$ was obtained for all of them. They had a radius of 36 mm and a separation of 257 mm. They are very far from the Helmholtz condition for a uniform field ($d/R = 2$) which would be impractical to satisfy given the dimensions of our chamber. With the known parameters of the fabricated coils, the magnetic field produced by a pair of those coils with a current of 1 A was calculated. Figure 5.7 shows a maximum field of 9.88 G in the centre of the coil and 0.42 G in the centre of the chamber. The magnetic field is reasonably constant around this point showing a variation of less than 5% for up to 1.3 cm away from the centre (Gradient up to 0.03 G/cm). Given the size of a typical Rb MOT (< 2 mm across), this uniformity is acceptable. The field in the centre of these coils was then measured at room temperature with a Teslameter with a current of 1.0 A obtaining a maximum magnetic field of 9.4 G, which is in good agreement with the calculations made earlier at the design stage.

The six cancelling coils were fixed directly against the chamber in custom designed mounts in the same position and axis as the fibre output ports. Each pair is connected in series to get the same constant current in both, which are identical enough to produce an equivalent magnetic field. The cancelling coils setup around the vacuum chamber are illustrated in Fig. 5.8.

Initially, we cancelled the stray magnetic fields through observation alone. This means that we produced a MOT and observed it with a TV CCD camera at maximum gain, so we could get to 25 fps (real time display). With all cancelling coils at zero, we shut off the field of the large coils and immediately observed the MOT moving in a preferential direction. This is

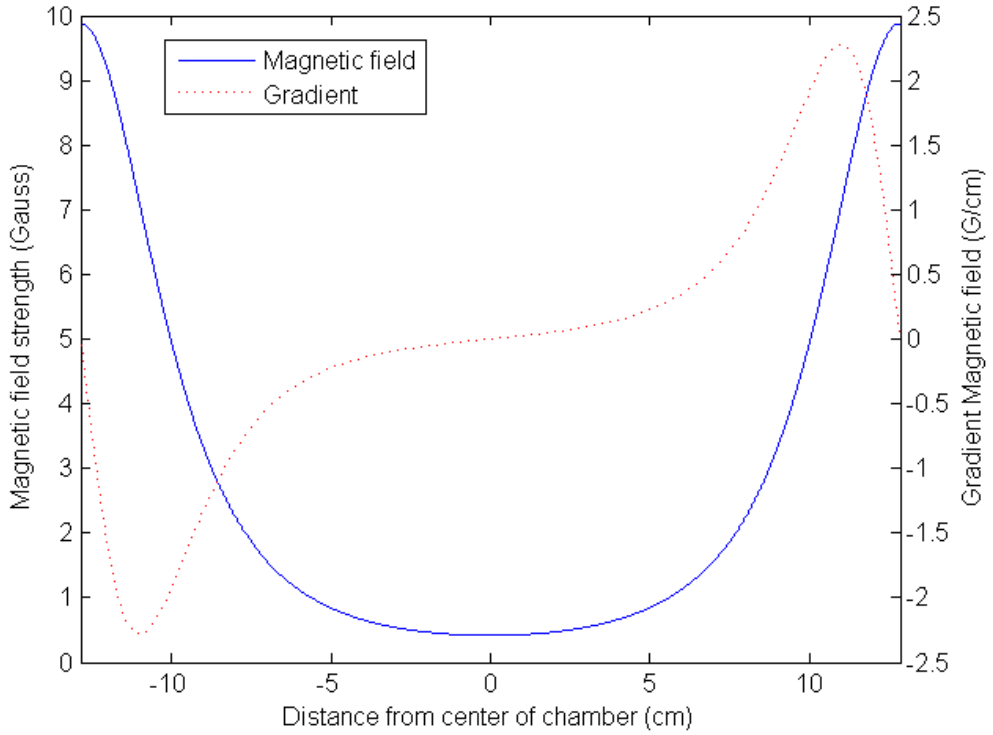

Figure 5.7: Calculated magnetic field and its gradient produced by a pair of coils in Helmholtz configuration. The field is calculated after the following parameter: current of 1 A, 58 wire turns, radius of 37 mm and coils distance 257 mm. Maximum field is 9.88 G and in the centre of the chamber is 0.42 G. The field gradient is null in the centre.

the effect of the stray magnetic fields mainly, although there is some component of dependence on the non-uniform decay of the magnetic field in the large coils and the alignment of the cooling beams. Then the current in the pairs and the alignment of the optical beams (to keep the MOT in the centre) are tweaked iteratively until a MOT is obtained that falls with gravity. However, we can see there are still some remnants of stray fields present because the MOT decays in a whirlwind-like motion when the fields of the large coils are shut off. Hence, the currents and magnetic field values are obtained as shown in Table 5.2. These settings, shown as an example, by using a 35 A current in the large coils, are dependent on the magnetic field of the coils and on the alignment of the cooling beams. This is a tell-tale sign that we are not only cancelling static external stray magnetic fields, but also finding some equilibrium condition valid for the whole system.

Later, the exact values that would be required to cancel the Earth's magnetic field was

Table 5.2: Driving current (magnetic field produced in the centre) of the Helmholtz pair of magnetic field cancelling coils in the experiment. These are compared with current settings that would be necessary to cancel the Earth's magnetic field in Perth.

Coils pair	Experimental		Model	
	Current (A)	Magnetic field (G)	Current (A)	Magnetic field (G)
Diagonal Trim 1 (M1A, M1B)	-0.78	-0.33	-1.3	-0.54
Diagonal Trim 2 (M2A, M2B)	0.68	0.28	0.48	0.20
Horizontal Trim 3 (M3A, M3B)	0.41	0.17	0	0

modelled. The ion pump manufacturer's specifications gives a stray magnetic field in the centre of the chamber that is less than 0.1 G Westward so it is negligible in our model. The two diagonal trims of the vacuum chamber are along the magnetic North-South axis (see Fig. 5.8), which means there is no residual magnetic field to cancel in the large coils axis (Trim 3, East-West axis). The earth's magnetic field was then decomposed over the diagonals Trim 1 and 2 (respectively 0.54 G and -0.20 G) and the current settings of the magnetic field cancelling coils were chosen to produce the opposite field in the centre.

When we tried the modelled values experimentally, we could not get the MOT to decay neutrally (without translational or spinning motion) during magnetic field shut down. That demonstrates that the cancelling coils are also compensating for the uneven decay, temporary stray fields that appear during shutdown and/or unbalanced forces due to misaligned cooling beams. The cancelling coils are also used to position the zero-crossing of the magnetic field with the overlap centre of the beams. When using only the modelled parameters the MOT is severely misaligned with the cooling beams. The experimental parameters in Table 5.2 gave the best results.

5.1.4 Stage G: optical delivery, cooling beam polarisation and alignment

When the cooling beam is frequency stabilised and shifted to the optimal red-detuning frequency for trapping ^{85}Rb , it is fed into stage G. The goal is to efficiently couple the laser light into the right polarisation axis of the PM fibres and simultaneously distribute the power equally among the outputs of the 6 PM fibres. In order to achieve this task, the optical delivery stage following Fig. 5.9 was built.

An iris is used to eliminate multiple reflections and secondary beams coming from the previous stages. A compact 2× telescope (-50 / $+100$ mm) is used which expands the

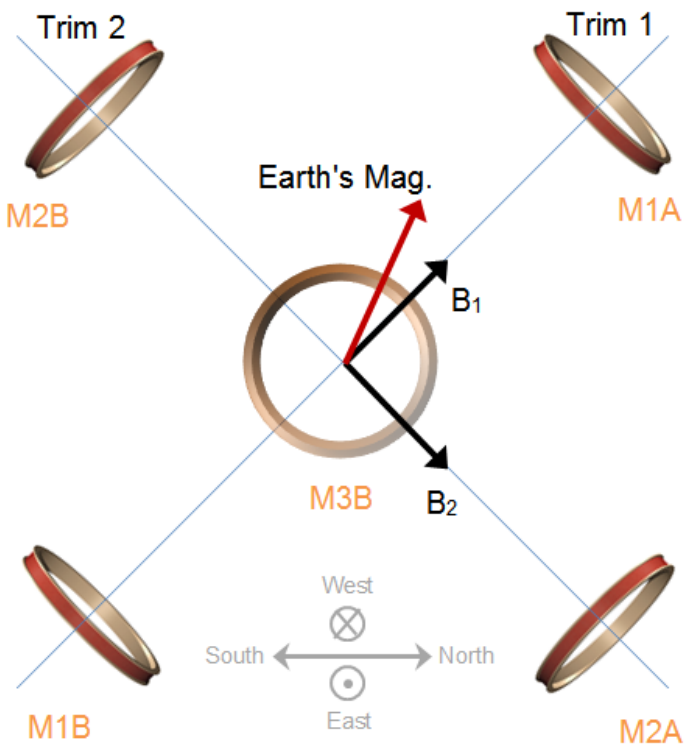

Figure 5.8: Cancelling coils setup around the vacuum chamber. When driven with positive current, Trim 1 (Trim 2) pair generates magnetic field B_1 (B_2) in the centre. The Earth's magnetic field orientation is also displayed 21° upwards from B_1 (or 66° upwards from the horizontal).

beam diameter back to 2 mm and further corrects the collimation. The beam is divided into 3 equal beams using 3 polarising beam splitters (PBS) in cascade where the power reflected/transmitted by each is adjusted using the half-wave plate (HWP) in front of them. With the cooling laser, an initial output power of 144 mW, 60 mW is obtained at the entrance of stage G. This resulted in 17.5 mW in each of the three beams and a coupling efficiency around 51% was achieved in each fibre equipped with an 11 mm collimator (Thorlabs CFC-11x). The 1×2, 50/50 PM couplers took care of splitting the 3 input beams into 6 equal optical outputs. This yielded output beams of 4.5 mW from each of the 6 fibres mounted on the octagon chamber. The power could be easily reduced by rotating the neutral density gradient filter ring inserted just after the 2× telescope, power attenuation is monitored relative to the transmitted beam power at the end of the 3 PBS.

The cage-mounted optics between the fibre mount and the chamber, as shown in Fig. 5.2,

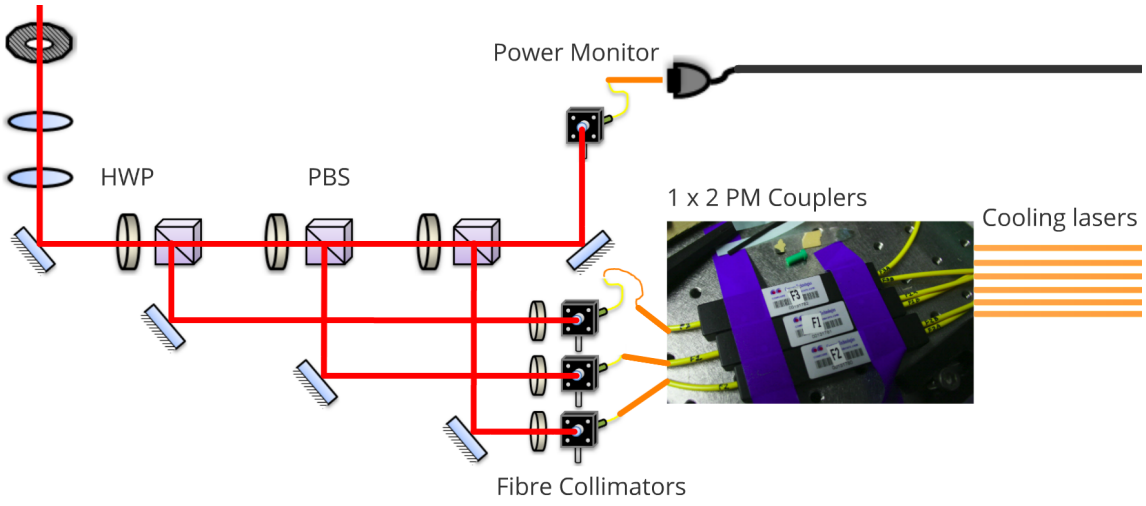

Figure 5.9: Stage G: optical delivery system that takes the input cooling beam and splits it in 3 equal beams and couples it along the stress axis of polarisation maintaining fibres. 1×2 PM couplers take care of splitting the 3 inputs into 6 equal output power cooling beams.

was an air-spaced doublet collimator (Thorlabs F810APC-780, f=36 mm) fixed to a kinematic alignment mount, a 2× telescope (25 / 50 mm) to expand and correct the collimation and a quarter wave plate (QWP) to circularize the beam polarisation. The output beam was measured at 12.1 mm diameter with a commercial knife-edge beam profiler (Thorlabs). With this beam, we were able to deliver optical intensities up to 4.1 mW/cm^2 or almost $3\,s_0$ (see Eq. 3.21).

The only difference with the repump beam is that we used a 2.5× telescope to produce a 15 mm diameter beam and it delivered 5 mW of power. We later tested with MOTs in several conditions that 0.5 mW was the repump power threshold for optimal performance.

Polarisation setup and control

To ensure adequate linear polarisation preservation by the fibres, great care was taken in launching the linearly polarised light into the correct stress axis of the fibres using a HWP in front of each collimator lens. Although we knew the approximate stress axis because of the connector key position, we fine-tuned the launch axis by applying mechanical vibrations in the fibre to test the stability of the guided mode. If the beam's polarisation axis was not coupled parallel or perpendicular with the stress axis, it was affected by the birefringence induced by curvature in the fibre that translated into crosstalk between the guided modes.

The output of the polarisation control fibre was then re-collimated, enlarged and cir-

cularised in the right handedness with a QWP using a cage mount fixed to the chamber viewport. The circularisation was initially set in a separate setup by moving the whole cage mount to another location on the optical table. A linear polariser and a detector were installed at the cage mount end. We used the optics property that an ideally circularised beam would always transmit the same power regardless of the linear polarisation orientation. By continuously rotating the linear polariser, the QWP was rotated until the power transmitted was constant. This technique to align the QWP ensured we had optimal circularly polarised beams.

There are two solutions of QWP angular orientation, each producing either a right-handed or a left-handed circularly polarised beam. The QWP from Ninja Optics used in the setup didn't have the axis labelled so it was not possible to determine the polarisation absolutely. In the MOT setup however, we can inject the current in the coils in both directions to shift the magnetic field slope so ultimately we only needed to label our polarisation arbitrarily but consistently. The handedness is determined by adding a fixed QWP (at any angle) immediately after the correctly aligned QWP and just checking which of the two possible linear polarisation orientations that comes out. For that purpose we choose the vertical polarisation to be left-handed and the horizontal one is right-handed.

Each fibre in the radial cooling beams, labelled F1A, F1B, F2A, F2B, was set to the same left-handed polarisation. Identical circularly polarised beams become oppositely polarised when counter propagating. The axial cooling beams F3A, F3B were set to right-handed polarisation. This choice is arbitrary, the only prescription is that the circular polarisation of axial and radial beams, named after the magnetic coil geometries, are opposite as defined by the direction of the beam propagation. To produce a MOT, the magnetic field polarisation required is not known because of the arbitrary choice of left or right-handed circular polarisation. So when ready to produce a MOT, both current directions through the coils had to be tested to find out the correct orientation.

Cooling beams alignment

To align the six circularly polarised beams in counter-propagating pairs, we used 0.8 mm pinholes that can be inserted anywhere in the cage mount. The first pinhole was mounted in front of the collimator to create a very small centre beam. The orientation of the beam was then aligned so it goes through the second pinhole in the opposing cage-mount. Flooding the chamber with Rb, the overhead and side cameras were then used to check the alignment and make adjustments to both alignment and the on-resonance frequency lock (see image from

the side camera, Fig. 5.10 A). The small white spot in the centre of the crossed beams is the axial cooling beam facing the camera. Figure 5.10 B shows the full size of the cooling beam relative to the beam with a pinhole. The repump beam was also aligned with the cooling beams overlap. The pinholes made sure that the cooling beam overlaps were aligned in the chamber's geometrical centre.

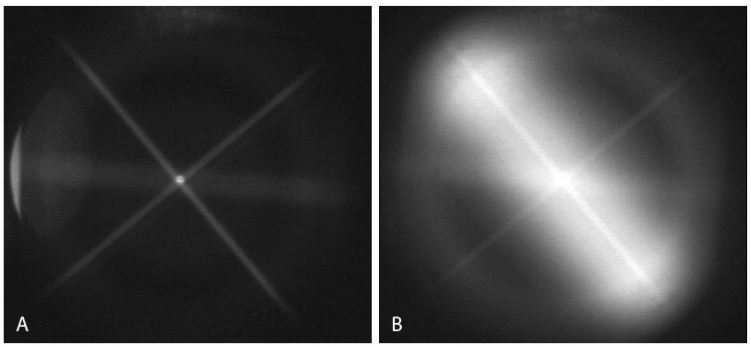

Figure 5.10: A. Alignment of the cooling beams with a camera replacing one of the axial beam. The bright white spot is from the pinholed axial beam facing the camera. B. One of the radial beam pinhole was removed to show the fluorescence of the 12 mm diameter beam relative to the pinholed beams. The larger and fainter horizontal beam is the repump.

Unfortunately the perfect alignment with the MOT produced strong interference amongst the beams leading to a poor and unstable MOT. After re-alignment of the optical beams and trimming of the magnetic field zero-crossing while reading the MOT intensity at the photodetector, the largest intensity MOT was found to be produced by an optimum misalignment. This misalignment created a larger overlap volume, although each beam was not perfectly balanced by its counter-propagating beam. This larger capture volume produced the largest MOT but also important internal currents of atoms, caused by unbalanced forces, resulting in a very hot ensemble. Our goal being a cold MOT, we settled down to a minimal misalignment, enough to erase interference to produce a spherical cloud. An image from the top-view camera, with pin-holed beams, shows the interference-free optical alignment after optimization with the MOT (see Fig. 5.11) and the resulting MOT shown in Figure 5.22.

Magnetic field zero-crossing alignment

It is also possible to optically align the zero-crossing of the magnetic field relative to the beams overlap. The zero-crossing is the position in the magnetic field spatial gradient where its value is null. Using only the axial or radial beam, a clear dark line can be observed where

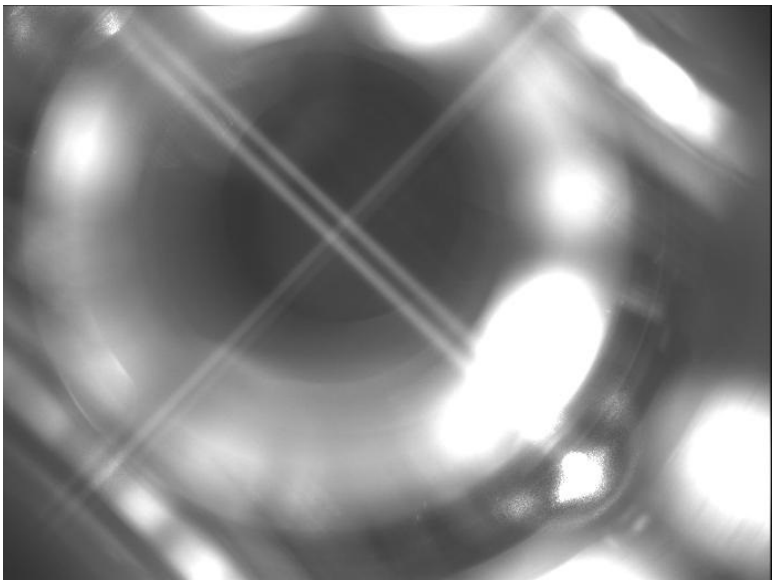

Figure 5.11: Image from top-view camera of the cooling beam alignment after optimizing with the MOT to eliminate interference and produce an ideal round MOT.

the magnetic field zero crosses the beam path. By trimming the current in one of the large coils or the magnitude of the stray fields with the cancelling coils, the zero-crossing of the magnetic field can be precisely positioned in the cooling beam overlap centre. Using the magnetically induced dark line in the fluorescence (see Fig. 5.12) and alternating between the axial and radial beam lines, the magnetic field zero was then positioned in the centre of the chamber and the cooling beam overlap.

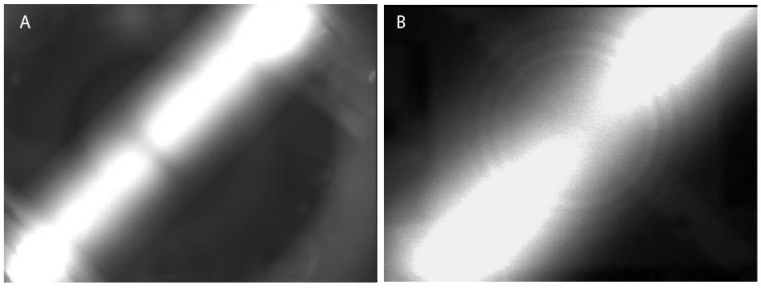

Figure 5.12: Optical alignment of the magnetic field zero-crossing inducing a dip in Rb fluorescence caused by the cooling beam. A. Axial beam B. Radial beams.

5.1.5 Stages A-B: cooling laser frequency locking and stabilisation

Stage A: modulation transfer spectroscopy

A modulation transfer spectroscopy (MTS) technique was implemented, as introduced in subsection 3.5.7, to produce an ultra-stable frequency lock. The experimental setup we built is illustrated in Fig. 5.13 . The critical component was to set the correct balance of pump and probe intensity by turning the HWPs in order to obtain a good MTS signal.

A Novatech DDS was used to generate a 10 MHz sinusoidal modulation signal. This signal was amplified, fed into a mini-circuit bias-Tee that adds a 12 V bias to the sine wave. When this biased 10 MHz signal is coupled to a VCO, a 180 MHz signal is generated with a 0.8 V amplitude at a 10 MHz modulation rate (in order to separate the MTS signal from the DC signal later). This processed signal is then used to modulate a double-pass AOM to shift the frequency of the optical signal (this beam would become the pump). After the double-pass, and the four-wave mixing process with the probe in the Rb gas cell, the 10 MHz MTS signal has its atomic spectrum shifted by the carrier frequency shift of the AOM. This is detected with the ac photodetector at +180 MHz in this case.

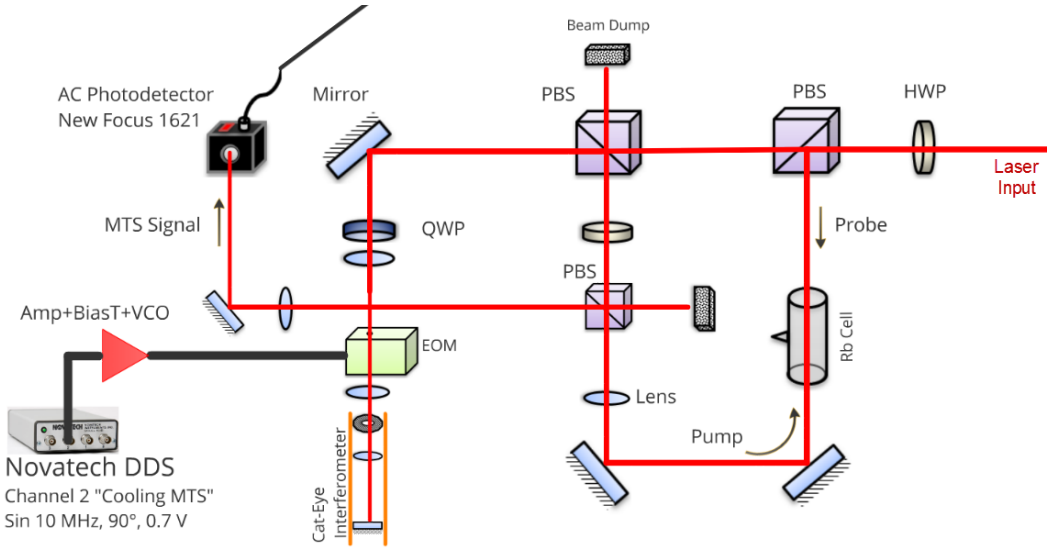

Figure 5.13: Stage A: Optical and electrical setup to produce a modulation transfer spectroscopy (MTS) signal. Red lines are free space optical beam paths. The black line is an electrical link.

Stage B: frequency lock servo controller

At stage B, shown in Fig. 5.14, the 10 MHz MTS signal is amplified and compared with a 10 MHz LO with an RF mixer in order to extract and demodulate its quadrature component. Figure 5.15 shows the MTS spectrum (blue, bottom trace) and the SAS spectrum (red, top trace) obtained under the same conditions.

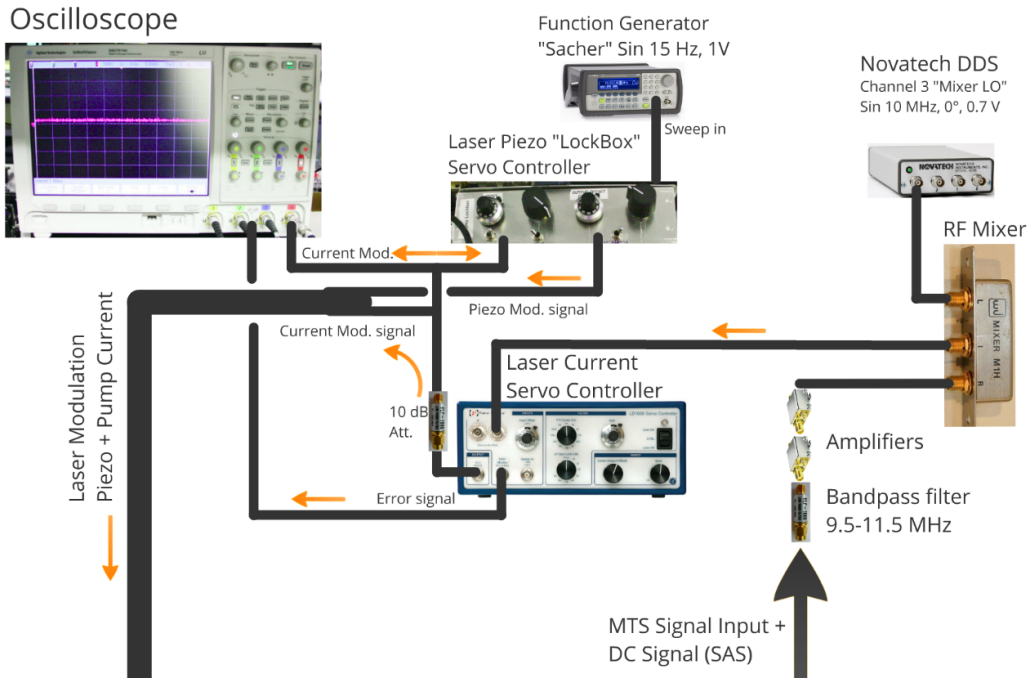

Figure 5.14: Stage B: Electrical demodulation processing of the MTS signal into an error signal used to lock the laser frequency to the fixed frequency offset of rubidium cycling (cooling) transition. Servo controllers feedback circuits are used to convert the error signal into pump intensity current and piezo modulations of the cooling laser.

The error signal is processed by two integrating feedback circuits. A fast 30 kHz servo loop is designed to control the cooling laser pump current in order to keep the laser frequency locked relative to ^{85}Rb cycling transition (with an offset of +180 MHz). The fast loop circuit (New Focus servo controller LB1005) is used to compensate for high frequency noise, mechanical vibration and acoustic pickup. The second stage is a slow 20 Hz loop is used to compensate for slow drifts of frequency like those caused by temperature variations. This second stage was a home-built servo controller (lockbox) as the bandwidth was too high on the commercial servo. The servo controller I/O and circuit diagram are presented in Fig. 5.16.

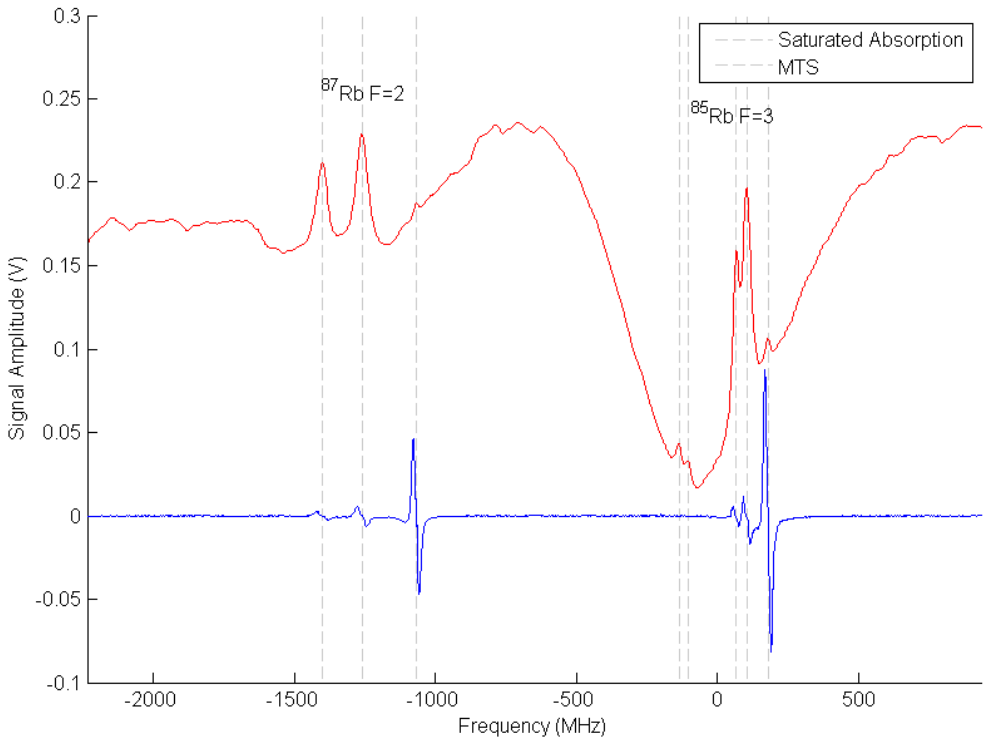

Figure 5.15: Comparative frequency spectrum of the saturated absorption DC signal (red trace, top) and its MTS signal obtained at 10 MHz (blue trace, bottom).

5.1.6 Stages C-D: repump laser "slave configuration" frequency lock

Stage C: heterodyne beatnote generation

Owing to lock stability of the MTS signal, a frequency lock for the repump laser was built as a frequency offset from the much more stable cooling resonance frequency. A fast AC photo-detector was used to convert the heterodyne beat signal between the two optical signals (around 384 THz) into a lower frequency electrical signal. Overlapping both beams into free space in order to get a good beat signal was challenging and unstable into freespace. To resolve this, the beat note generation stage was modified in order to use optical fibres and a 2×1 fibre coupler. Each beam was individually coupled into their respective coupling port (see Fig. 5.17) and waves combined into the fundamental mode of the fibre. A wavemeter was used with one laser at a time to assist in tuning the laser into the right cavity mode so they stayed within frequency locking range. The beat note was set to 2.73 GHz, which corresponds to the repump resonance frequency minus the cooling resonance (shifted up by

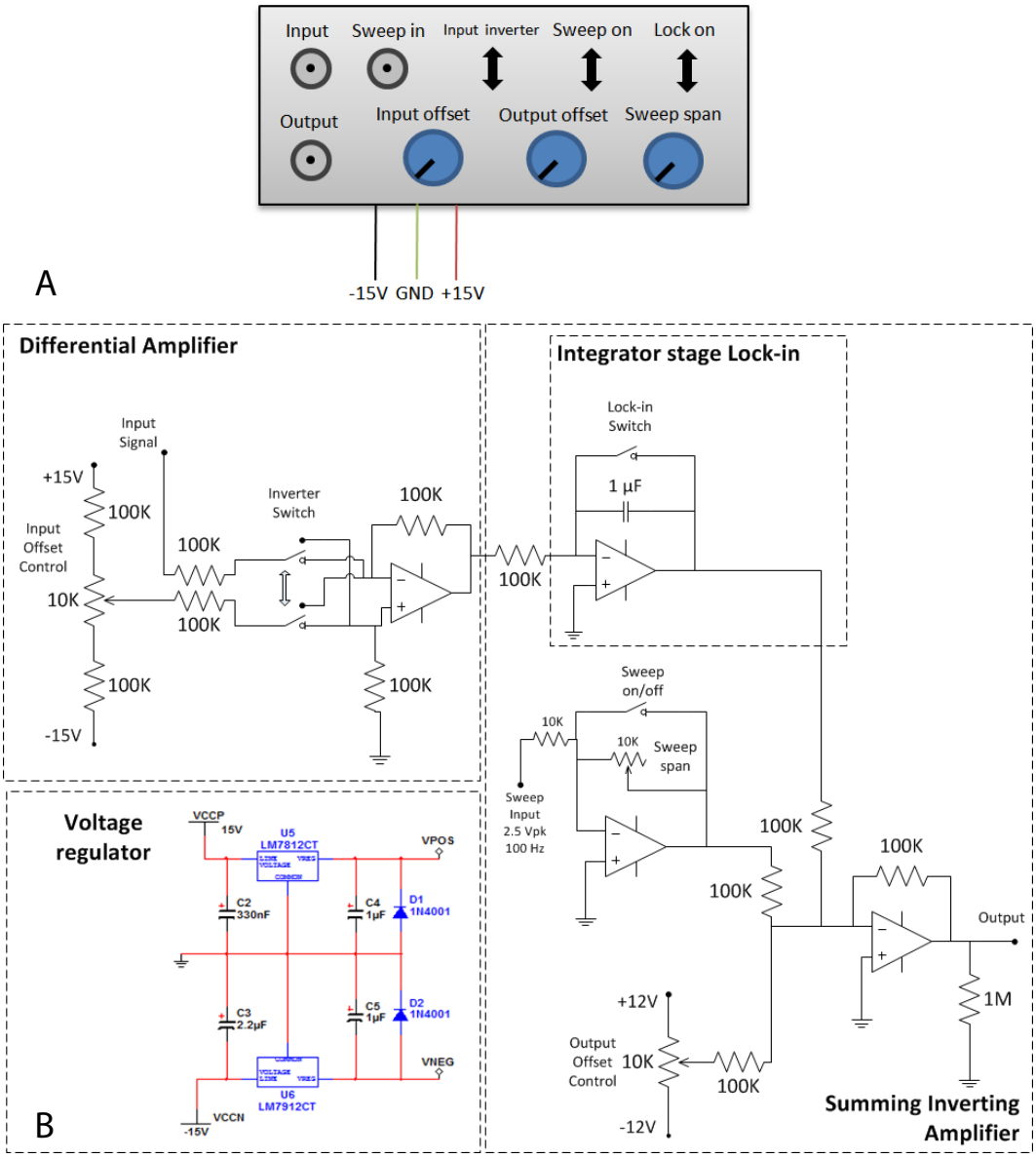

Figure 5.16: A. Inputs/Outputs of our servo controller. B. The circuit purpose is to produce a small bandwidth, very slow feedback loop that is used to compensate for slow drifting changes like small temperature variations. The voltage regulator part was used to immune the circuit to quick voltage spikes caused by other devices connected on the 15 V rail.

+180 MHz).

The stability of the frequency lock was measured by acquiring the data from the generated beat note on an electrical spectrum analyzer. Figure 5.18 shows the beat note signal of one acquisition including its two 10 MHz modulation sidebands. Data was acquired every

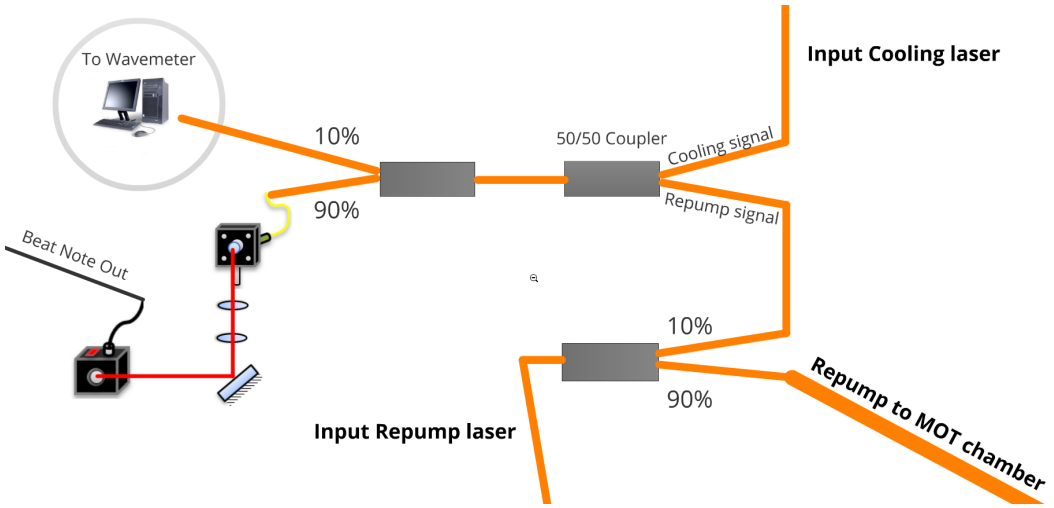

Figure 5.17: Stage C: Setup of optical fibres connections (orange links) used to generate a heterodyne beating signal around 2.73 GHz between the cooling and repump laser beams. The copropagating beams are collimated out of the fibre and into an AC photodetector (red line) acting as an RF mixer.

10 seconds during 10 minutes. The full-width half-maximum of the heterodyne beat note is 5 MHz $\pm$ 0.3 and its average frequency was 2.761 GHz. The standard deviation of the distribution of its locked frequency was 0.52 MHz.

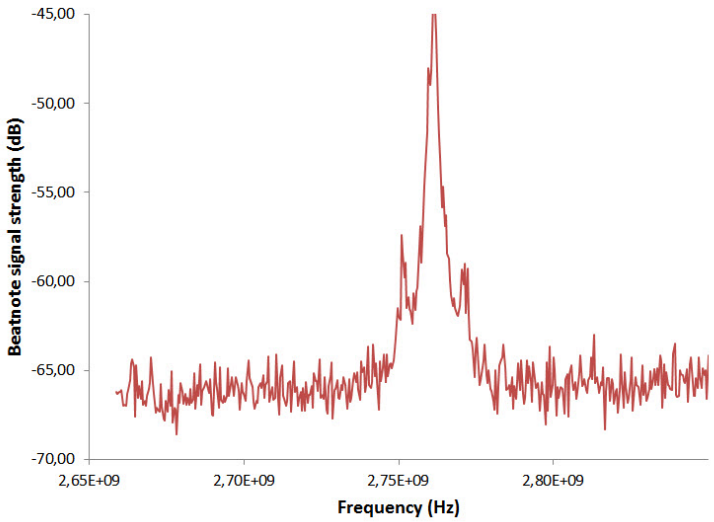

Figure 5.18: Signal of the heterodyne beatnote at 2.76 GHz generated by the repump and cooling beams. Modulation sidebands of 10 MHz from either side are also visible.

Stage D: frequency lock electronics

This stage was built according to Fig. 5.19 and had the same purpose as stage B: to demodulate the signal, generate an error signal for the feedback loop that modulates the laser pump and piezo actuator. The error signal is a signal that goes through zero at the desired frequency and gives a positive or negative response so that the current and piezo can be modulated accordingly to bring the laser back to the desired frequency, often called the lock point. However there is a major difference with Stage B because the signal is modulated around 2.73 GHz instead of 10 MHz. The difference between the repump and cooling laser transitions is 2.91 GHz [101], but the frequency of the cooling spectrum is shifted by the MTS stage by +180 MHz, which reduces the difference between the two signals to 2.73 GHz. An analog circuit PLL frequency synthesizer card (Analog Devices ADF4108) is used to mix and down convert the beat note to a frequency in the tens of MHz range. The PLL card needs a 100 MHz reference to function which was provided by the group's hydrogen Maser. The RF through port was sent into a frequency analyser to show the beat note and determine from its shape if the laser was stable or if it was close to a mode-hop, which frequently happened. Using the N-divider output port, one of the sideband MTS signal was mixed down to 20.1 MHz (N=136) and fed into the RF port of the mixer. The lock point was determined by the frequency of the function generator LO. A frequency of 20.1 MHz puts the lock point exactly on the repump transition resonance and changing that value detunes the lock point to the red or blue part of the resonance. The IF output of the mixer is the final MTS error signal. A bandpass filter is used to filter out the main beatnote and the other sideband which were unused. After the error signal generation the rest of the circuit, with the two stage integrators, is identical to stage B. The most common cause of the repump for falling out of frequency lock was caused by the mode-hops of the laser diode.

5.1.7 Stage E-F: frequency tuning with acousto-optic modulators

Stage E: cooling beam frequency shift back near resonance

Once the cooling laser has been frequency-locked at the AOM offset resonance transition, we need to tune it back close to resonance, compensating the +180 MHz shift in frequency, before insertion into the MOT chamber. This was done with an AOM which had a full-width half maximum tuning bandwidth of 60 MHz centred at 80 MHz for the first order. It is therefore not possible to frequency shift a beam by 180 MHz in a single pass, but it can be done in a double-pass. The double-pass also has the advantage of compensating for the first

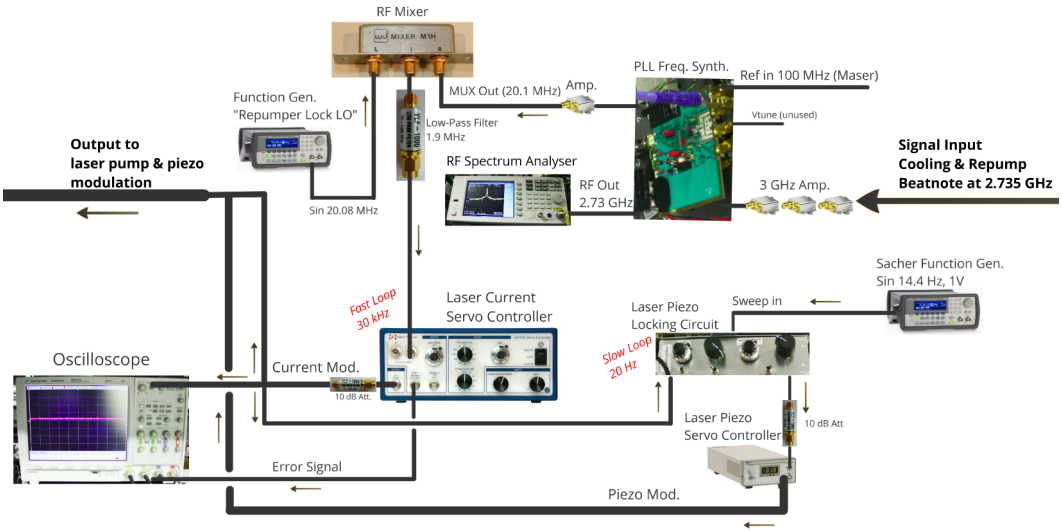

Figure 5.19: Stage D: Electrical demodulation setup that down converts the beat signal and processes it into an error signal. A two-stage servo controller is then used to modulate the pump intensity and the piezo actuator of the repump laser.

order deviation which is around 2° for an 80 MHz shift of orders ±1.

In the optical setup of Fig. 5.20, a cat-eye-interferometer was built which determines the output beam orientation, after double-passing through the AOM, and is insensitive to the modulation frequency of the AOM. Before the AOM, a HWP is used to adjust the power reflected toward the probe beam setup. We characterised our polarising beam splitter performance and obtained at best 93% transmittance, 5% reflectance and 2% of loss, which is strongly affected by the purity of the polarisation of our laser. Hence, with 100 mW of input power, 5 mW was transmitted to stage F (probe frequency tuning) and the rest was transmitted through a 0.5× telescope, shrinking the beam to a diameter of 1 mm, improving the overall conversion efficiency of the AOM.

The AOM was modulated between 93 to 100 MHz and angled to maximize the power shift into the −1 order. Once optimally aligned, we obtained a first pass efficiency of 91% and double-pass efficiency of 72%. The double pass through the aligned QWP rotates the input polarisation by 90° when its fast axis is at 45° of the input linear polarisation axis. As a result of this rotation, the output beam is now reflected by the PBS and we obtained 60 mW of light detuned to the cooling transition between −6 to −20 MHz or more depending on the AOM modulation which is controlled by the Novatech direct digital synthesizer (DDS) of a desired frequency signal. The frequency could be shifted in a few microseconds but large frequency

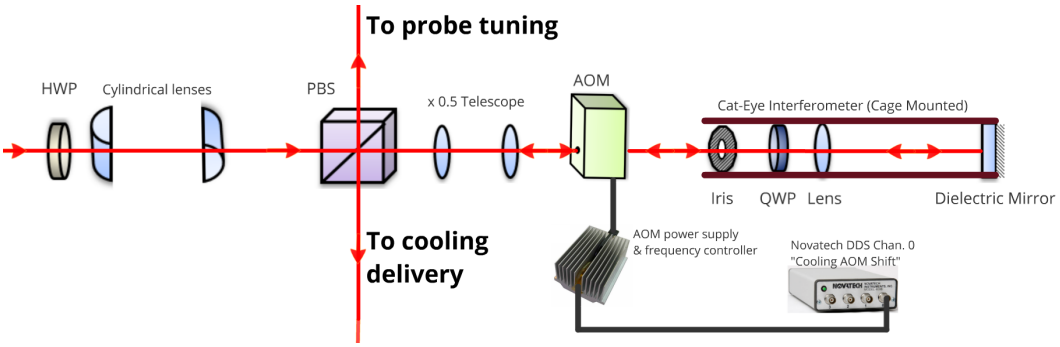

Figure 5.20: Stage E: Optical setup of the AOM cat-eye interferometer that shifts the cooling beam frequency back to near resonance (3-20 MHz red-detuned) and distributes the beam into the probe generation stage (before shifting) and the cooling delivery stage (after shifting).

shifts also affected the transmitted power so the design of experiments had to compensate for this change. By turning off the modulation, the optical beams could also be shut off quickly but doing so for longer than 50 ms affected the temperature stability of the AOM after which it required several seconds to get back to the same power transmitted.

The cat-eye interferometer was built in a cage-mount fixed to a kinematic mount attached to a single-post holder. Towards the end of the study presented in this thesis a new custom-built mechanical mount was designed in the physics workshop to address instability issues of the post holder mount to improve the overall experiment reliability through time.

The few mW transmitted through the PBS after the double-pass were directed back toward the laser cavity. With a single isolator stage, we had to align it optimally in order to protect the laser from the instability caused by this back injection. It worked at the limit of acceptability and it was necessary to frequently tune its alignment to stabilize the laser mode. For this kind of power return, a second isolator would have been ideal or, a more economical solution; the use of an optical fibre circulator before stage E would have also improved this system.

Stage F: probe beam generation and frequency tuning

This stage was built similarly, see Fig. 5.21, to the previous stage E, but only received 5 mW of optical power. The double-pass and DDS control of the AOM modulation allowed coupling of 2 mW of light on-resonance to the cooling transition frequency of ^{85}Rb. Control of the probe for direct or shadow imaging often involved attenuating the power before the fibre collimator using neutral density filters and/or detuning the probe frequency in order

to prevent saturation of the image. Sometimes, when needed for large area direct imaging, more power was diverted from Stage E to get up to 10 mW in the probe beam.

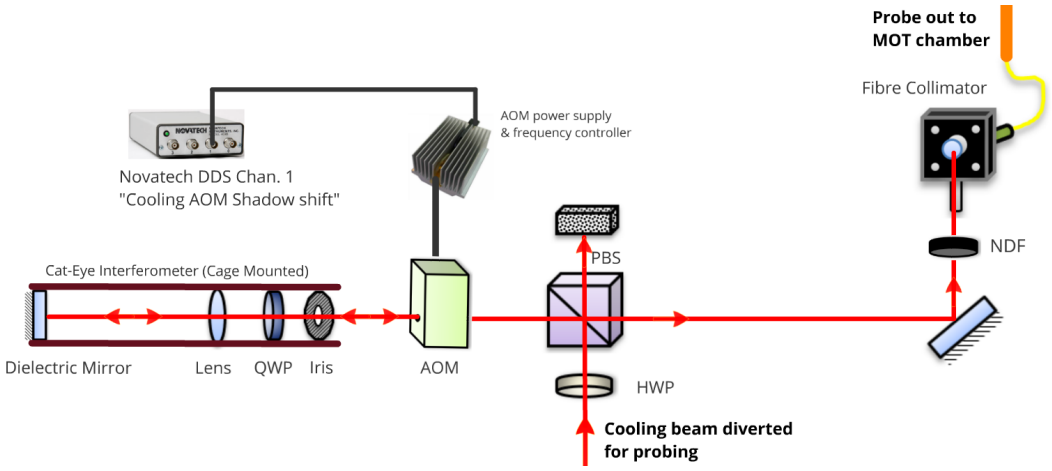

Figure 5.21: Stage F: Optical setup used to tune the frequency close to or on-resonance with an AOM and couples the frequency shifted light into an optical fibre for delivery to the octagon vacuum chamber.

5.2 MOT imaging and characterisation

5.2.1 Observation and first measurements of the MOT

When the final MOT apparatus including all systems was assembled, obtaining the first MOT was still challenging. The solution was mainly a combination of having the circular polarisation of the radial beams orthogonal to that of the axial beams and producing simultaneously the correct magnetic field polarisation. Figure 5.22 shows the view of the MOT from the top camera. The beams and magnetic field were aligned to produce the best uniformity MOT while still being cool.

Figure 5.23 shows an unsaturated image of the MOT taken by the JAI CCD camera with a teleobjective lens (135 mm) on the horizontal plane at 45° off the axis of the coils. After a calibration process explained in Sec. 5.2.2, the $1/e^2$ diameter of this MOT was measured to be 0.89 mm horiz., 1.14 mm vert. with an average size of 1.01 mm. The MOT size depends on many parameters: the number of atoms, the light force, the magnetic field gradient and the MOT temperature. We used only a field gradient of 4 G/cm here, produced by 30 A, which is weak for MOT standards (up to 20 G/cm), mainly because of limitations by the design of the coils having too few turns and running too hot with currents above 35 A.

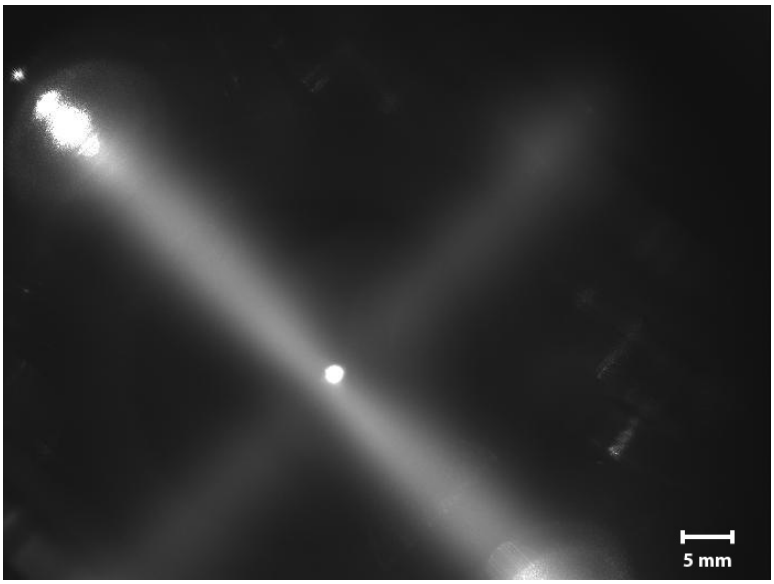

Figure 5.22: Cloud of ^{85}Rb in a MOT taken from top-view with the CCD astro-camera. The cooling beams and magnetic field were aligned to produce the ideal, uniform distribution in space.

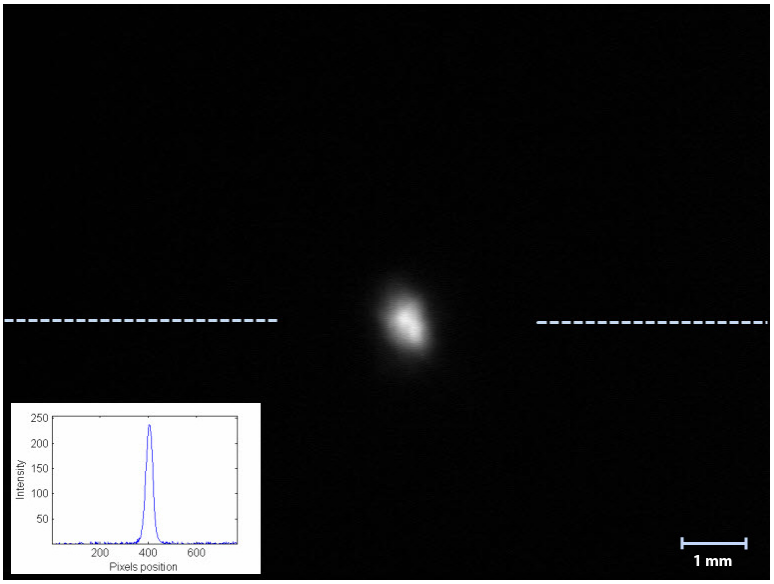

Figure 5.23: Unsaturated image of ^{85}Rb MOT taken with a JAI-CVM50 CCD camera from the horizontal plane with a 135 mm teleobjective lens. The $1/e^2$ diameter of the MOT was 0.89 mm horiz. by 1.14 mm vert. (Inset) Intensity profile of the MOT along the dashed line.

Calculating the number of atoms in a MOT

Counting atoms in a MOT is accomplished by a calculation from measurements of the cloud fluorescence, the detector solid angle and the scattering rate of photons. Beforehand, the photodetector was cross-calibrated by comparing its reading with a calibrated power meter in the same intensity range as exposed to in experiments. The result of this five-point calibration gave a conversion scale C = 0.92 μW/V. The following expression was developed to calculate the number of atoms (N_{MOT}) and it will be demonstrated with a typical example from the experimental measurements of the MOT:

$$N_{MOT} = \frac{(P_{MOT} - P_{BG}) \cdot C}{(\gamma_s \hbar\omega \cdot \Omega/4\pi)} \tag{5.5}$$

where the numerator is the differential power (300 - 165 mV) multiplied by the conversion scale above. The fluorescence of the MOT (P_{MOT}) captured over the solid angle of the lens was measured at 124 μW. When measuring the partial MOT radiated intensity (which is the differential intensity, with and without a MOT), one must be careful to keep the background radiation constant while disabling the MOT. While keeping all the lasers locked on, turning off the magnetic field was sufficient to obtain a precise background reading (P_{BG}).

The denominator is composed of two terms. First, the power radiated per atom is a product of the 6-beam light scattering rate (photons/s·atoms) [93]:

$$\gamma_s = \frac{\Gamma}{2} \frac{6I/I_s}{1 + 6I/I_s + 4(\delta/\Gamma)^2} \tag{5.6}$$

and $\hbar\omega$ is the energy per photon (J/photon). The units of the term $\gamma_s \hbar\omega$ is therefore in Watts/atom. In the example, we had the intensity for each laser I = 2.22 mW/cm^2 and a detuning $\delta = -12$ MHz, and with the rest of the atomic constants of ^{85}Rb, we obtained 1.57×10^{-12} W/atom.

The second term is the solid angle ratio over the whole space. The solid angle subtended by a cone of height d and radius r, where d is the lens-MOT distance and r is the lens aperture radius:

$$\Omega_{cone} = 2\pi(1 - cos\theta) \tag{5.7}$$

where $\theta = arctan(r/d)$. In the example, we had a 12.7 mm radius lens and it was at 110 mm from the MOT. So the ratio of the total power detected is 0.33%. Inserting those results back into Eq. 5.5, we obtained 2.36×10^7 atoms in the MOT.

Steck also proposed a different formula [101], based on the same principles but for use with a CCD camera instead of a calibrated photo detector or power meter. We found equivalency

between these parameters:

$$\frac{N_{counts}}{t_{exp} \cdot \eta_{count}} \equiv \frac{\Delta P \cdot C}{\hbar\omega} \tag{5.8}$$

where N_{counts} is the integrated number of counts recorded on the CCD chip, t_{exp} is the CCD exposure time, η_{count} is the CCD camera efficiency (in counts/photon). Both terms are a calculation of the photon flux, i.e. the number of photons detected per unit time over the solid angle of light collected by the detector optics.

A second slight discrepancy of our approach compared to Steck's analysis is in the calculation of the solid angle of the light detected [101]:

$$d\Omega = \frac{\pi}{4}\left(\frac{f}{(f/\#) \cdot d_0}\right)^2 \tag{5.9}$$

Where f is the focal length of the lens, f/# is the lens f-number = f/D (aperture diameter), d_0 is the lens-object distance. The resulting solid angle calculated with Steck's gave the same result as Eq. 5.7.

Observation of a MOT secondary ring

When the MOT is made of a large number of atoms and reaches a certain critical density, it exhibits a ring of atoms that are ejected from the MOT's fundamental mode into a another mode due to the internal pressure of photons fluorescence re-capture [84]. The system did not have a strong enough magnetic field gradient but it was possible to produce such a secondary ring mode in the MOT by increasing the density of the atoms by reducing dynamically the size of the trapped volume. We started by obtaining a steady state MOT in a very low Rb pressure environment (several seconds to obtain a full MOT). Then by moving the alignment of two beams closer, it reduced the MOT trap volume without initially reducing their trapped atom numbers which expelled some of them into a secondary ring as shown in Fig. 5.24.

5.2.2 Cold atoms imaging techniques

When probing room-temperature atoms, as in a Rb vapor cell, the highest fluorescence occurs for a particular isotope ground state when the probe is tuned to the peak of its Doppler line. For example, for ^{85}Rb F=3 transition, it is at $-13\,$MHz from its cooling transition frequency.

When the same atoms are cooled to their Doppler temperature or less, the strongest fluorescence response occurs at the resonance with its cooling transition. However, the atoms are never probed on resonance because the challenge of imaging the MOT is to detect the

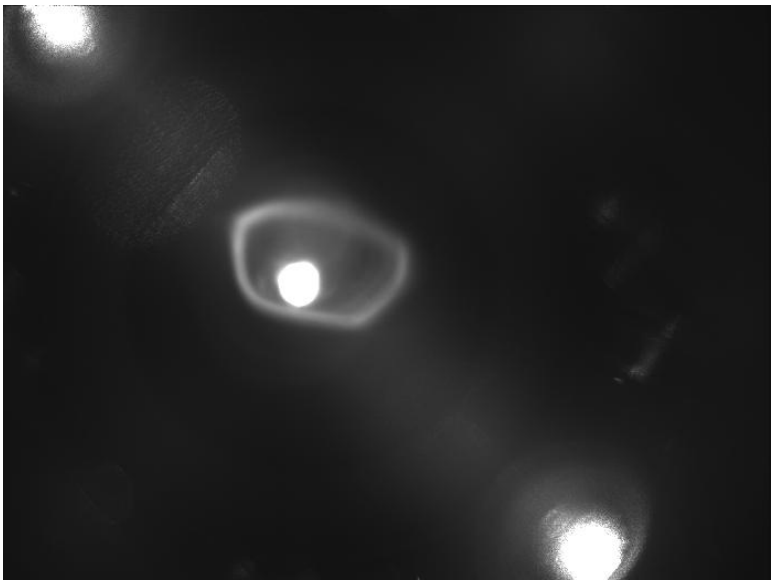

Figure 5.24: Observation of a MOT secondary ring by reducing the trap volume of a large MOT.

atom cloud without perturbing its position and spatial distribution. Special care has to be taken to ensure that the effect of the probe on the atoms is minimal but at the same time be able to detect them, even at lower densities to at least allow precise thermal expansion measurements.

Depending on the experiment, it is necessary to be able to apply different imaging techniques to ensure proper detection. Essentially, three imaging schemes were developed: fluorescence imaging with the six cooling beams, shadow, and fluorescence imaging using an independent probe beam. Post-processing is applied to produce differential images where background artefacts were subtracted, the image smoothed and the pixel colouring scale was modified to enhance contrast.

The common approach in all dynamic measurements during an experiment is to only expose the atoms to the imaging probe, after a specified delay, for the shortest time necessary to create an image snapshot. The experiment is then repeated, the MOT is reconstructed in less than 3 seconds and the probe is triggered with an increased delay (usually a few milliseconds later) before capturing a new image. The motion of the atoms in an experiment is recorded in a video from which each frame corresponds to a delayed capture of a different "run" of the same experiment. In all cases, the exposition time of the camera is identical and synchronized with the probing time.

The cameras and optics

The performance of the imaging system is also intrinsically linked to the camera used. A CCD sensor was selected mainly because they are low cost and relatively low-noise devices for imaging low-light exposures compared with similarly priced CMOS systems. New expensive CMOS cameras can be more sensitive while having a larger dynamic range but they are also pricier. Over the length of the project, various cameras were tested with multiple objectives. The image quality was really good using an Astro-camera with a cooled sensor, as in Fig. 5.12 A, but it was ultimately too slow for the needs of the experiment.

For the project a JAI-CVM50 industrial CCD camera was mostly used with a 768×576 pixels and a 135 mm teleobjective lens. When focused on the MOT position at 40 cm, a frame height of 9.0 mm was measured with a ruler imaged at the same distance and thus, obtained a calibrated scale of 0.016 mm/pixel. The same camera was also used without a lens for all beam profiling tasks where the scale was the pixel pitch of the sensor ($8.6 \times 8.3 \mu$m/pixel). However, this camera system was bulky on our table and it was complicated to shape a trigger signal accepted by the camera; ultimately a smaller and better performing CCD camera was bought for the purpose.

Toward the end of the project, two CCD cameras (Chameleon series from Point Grey Inc.) replaced the JAI-CVM50. The sensors were 640×480 pixels with a 7.5 μm pixel pitch. Chameleon A was set with a 25 mm lens that had a frame height of 34 mm at the MOT focus (with a calibrated scale of 0.071 mm/pixel). Chameleon B had a much larger field-of-view with a 6 mm lens; however, MOT sizes were not measured with it, so it was not necessary to calibrate its scale. Both were easily triggered using an Arduino Mega I/O microcontroller board.

In all cases, the spontaneous force is an important perturbation factor that must be managed, and ideally mitigated, by the imaging scheme employed. In the following subsections, each imaging scheme will be described.

Fluorescence imaging with cooling beams probe

To measure the MOT temperature, the thermal/ballistic expansion technique detailed in [92] - Appendix A was applied. The standard configuration of the cooling beams, with all three pairs of beams counter propagating with orthogonal polarisations, is ideal for minimizing spontaneous forces. By flashing the cooling beams after a determined expansion time, clear images of the cloud even at lower densities were captured. For temperature measurements, we determined that probing atoms by flashing the cooling beams yields the best results because

the cloud motion is mainly within the trap volume, as opposed to atom guidance experiments.

In this imaging technique, the probe timing and control is realized at the AOM stage which is triggered by the Arduino microcontroller. The imaging protocol starts by shutting down the current of the cooling beams and magnetic coils simultaneously, wait for a variable time i (ms), where i is the thermal expansion phase duration for a particular run of the experiment. During the wait, the beam frequency is shifted for the imaging probe; after i ms, simultaneously trigger the camera exposure and flash the cooling beams for the exposure duration (or longer). The frequency of the cooling beams is shifted closer to resonance in order to minimize the exposure time and obtain a sharp image. However, probing too close to resonance disturbs the cloud, regardless of the intensity; better results were obtained by always detuning further than $\Gamma/2$ to the red (-3 MHz).

For reference, the largest MOT produced, but not the coldest, is obtained with beams around 1 to 2 times the saturation intensity and detuned 2 linewidths to the red (-12 MHz). The shortest on-off-on cycle duration achieved was 8 ms (see Sec. 5.2.3) because of internal delays in the system. This delay affects both the minimum duration of i (the expansion delay) and the shortest length of the probe flash. The exposure time is not limited by the length of the probe flash because it is set at the camera, so in most cases, only the first 150 μs of exposure were recorded. The ideal light force to achieve good fluorescence intensity without excessively heating the atoms during the camera exposure was to use a detuning no closer than -4 MHz when the cooling intensity of the each laser beam is set to 3 mW/cm^2 (around $2\,\mathrm{I}_{sat}$). We determined that too much light force is used when there are signs of disturbance and detuning the probe further fixes these issues. The signs are, for example, the MOT appearing off-centred or its spatial distribution is changed (its expansion appears to be non-isotropic, exotic or unbalanced). Still anisotropic expansions are not uncommon either and are not automatically a sign of disturbance by the probe but rather of internal dynamics of the cloud, so one must exert caution in selecting the right amount of light force.

To verify and measure the imaging probe disturbance, interference (if any) with the cloud natural "dark motion", a MOT freefall experiment was realized. It consisted of measuring the vertical position of the centre of the expanding atom cloud in freefall. The position was automatically determined from each image taken by a 2D Gaussian fitted to the data using the Levenberg-Marquardt algorithm (a more robust version of least-squares fitting, especially with noisy images). The horizontal position was also monitored but there was no shifting. In Fig. 5.25, the equation of movement of an object falling with $g = 9.8\,\mathrm{m/s^2}$ (red line) was fitted to the vertical position as a function of time of the MOT falling (blue dots). A good

agreement was found between the two. This measurement was repeated with the independent fluorescence probe, described in the following Sec. 5.2.2, to assess its perturbing interaction with the cloud.

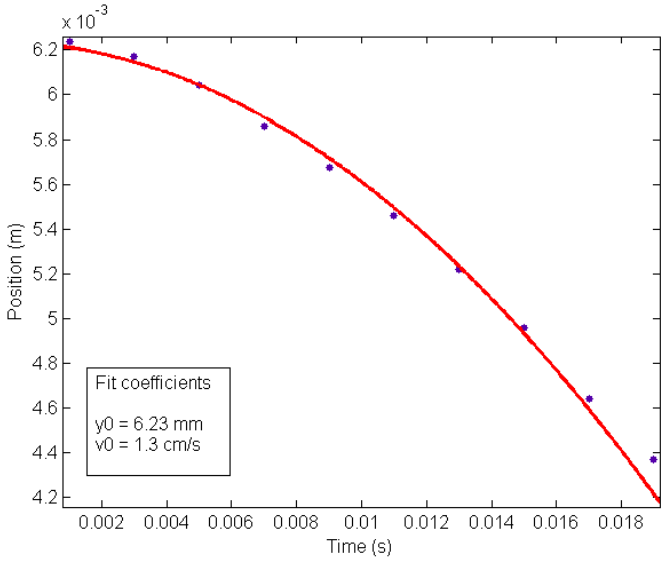

Figure 5.25: Test of the gravitational acceleration of a ^{85}Rb MOT released and probed with a flash of the cooling beams detuned at $-4\ MHz$. The blue dot marker is the vertical position of the expanding MOT fitted with a 2D Gaussian. The red line is the motion equation fit of an object falling with normal gravity.

Fluorescence imaging with independent probe

When a probe beam that is not counterbalanced by an equivalent orthogonally polarised beam is used, the effect of the spontaneous force is dramatic and significant even for exposures as short as 150 μs. So it is necessary to use a much weaker light force to minimize this effect. In this setup, using the MBR laser as the probe, a mechanical shutter was used to turn the beam on/off. The mechanism had a 5 ms internal triggering delay and thus, the minimal probe duration is de facto 5 ms.

However, this does not restrict us from exposing for shorter durations to record an image. Nonetheless, the weaker fluorescence response, compared to when using the six cooling beams probe flash, required exposure times of 5 ms or more to produce a clear image of the cold atoms. The probe, coupling from underneath the chamber, was initially designed as a single linearly polarised vertical beam, which is ideal for imaging free-falling guided atoms across

the whole chamber. A much weaker single beam at 0.2 mW and with a 6 mm diameter (0.7 mW/cm^2, 4 times weaker than a single cooling beam) was used at several detunings to test several light force values.

When in freefall from the MOT, the optical molasses (OM) interacts strongly with the probe, even at detunings that made detection very difficult (> -15 MHz). The position of the molasses after 6 ms of freefall and 5 ms of exposure always ended up 2 mm above the initial starting position without trace of fluorescence at or below the starting position. Figure 5.26 shows differential images of the OM at several detunings. The first image to the left is the initial MOT before release. The following images are all snapshots after 6 ms of freefall with the probe tuned at $+1.9, 0, -1.8, -3.6, -5.1, -6.5$ and -7.6 MHz. The cloud seemed unaffected by the reduced force, always being at the same position with only its fluorescence response becoming less intense with larger detuning. The intensity profile along the vertical axis, shown in Fig. 5.27, shows an abrupt rise in fluorescence on the side facing the laser with the fuorescence trailing off on the opposite side. This particular distribution is interpreted to be caused by the imaging beam pushing strongly against the atom cloud. By comparison, the vertical intensity profile of OM after 9 ms of freefall was imaged for 150 μs with the six cooling beam flash probe.

Fig. 5.28 shows the intensity profile which also represents the spatial distribution of the atoms along this axis. The fluorescence signal (blue trace) and the Gaussian fit (red trace) are in good agreement with each other, as opposed to the case when the atoms are exposed to a single vertical probe beam.

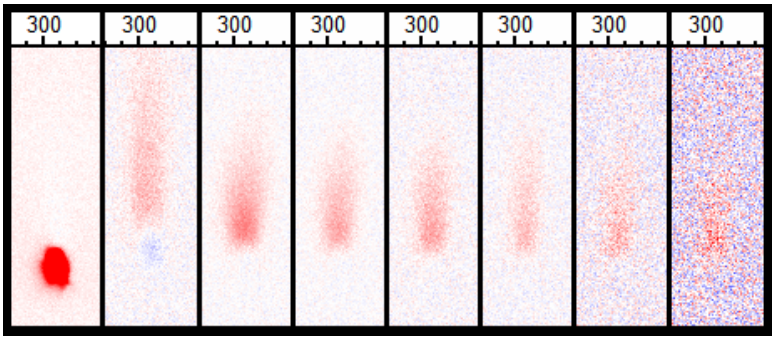

Figure 5.26: MOT freefall experiment differentially imaged with a single polarised beam opposing gravity. First snapshot on the left shows the MOT before release. Following snapshots are all 5 ms exposures of the cloud after 6 ms of freefall at detunings of (left to right): $+1.9, 0, -1.8, -3.6, -5.1, -6.5, -7.6$ MHz. Red is higher intensity than background reference, blue is lower.

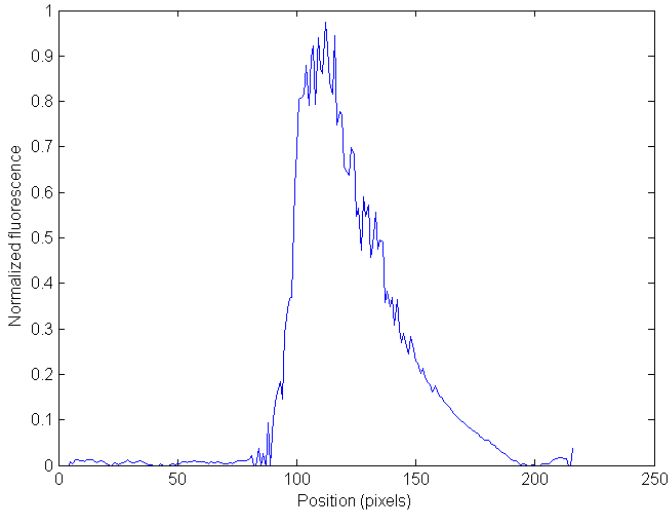

Figure 5.27: Vertical intensity profile of the atom cloud after 6 ms of freefall and 5 ms of exposure, when exposed to a single linearly polarised beam probe (0.7 mW/cm^2, -1.8 MHz).

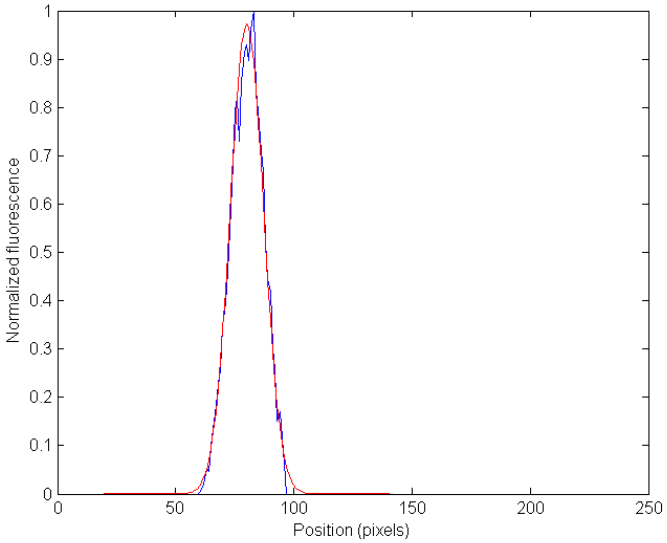

Figure 5.28: Vertical intensity profile of the atom cloud after 9 ms of freefall and 150 μs of exposure. The cloud was exposed by flashing the six cooling beams. The intensity profile (blue trace) and Gaussian fit (red trace) are in good agreement.

Our hypothesis was that the atoms were pushed up by 3 mm in a lot shorter time than the exposure which started 6 ms after freefall began. This is possible as the maximum spon-

taneous force can easily be a few thousands of g. The average spontaneous force acceleration is $\hbar k\Gamma/(2mg) = 1700g$ which could move a MOT by 3 mm in 0.6 ms. The upward movement Doppler shifts the probe beam reducing its force acting on the cloud after this initial push. From the results, it is clear that a beam with unbalanced spontaneous forces cannot be used to image cold atoms vertically.

We tested a second scheme in which the beam was simply retroreflected. However, the polarisation of the reflected beam was left unchanged (parallel) in one case and shifted orthogonally in the second case with a double-pass QWP. To improve fluorescence response, the intensity was also increased by a factor of 5 (from 0.2 to 1 mW). The MOT freefall is compared between the two imaging polarisation configurations. The differential post-processed images are shown in Fig. 5.29 using 7 snapshots each at 6 ms intervals except for the last one at 8 ms. As in the previous case, the colouring range (contrast) was optimized to identify the cloud position.

It can be observed that in the parallel polarisation case (bottom frames), the OM does not accelerate following standard gravity. In the case of orthogonal polarisations (top frames) the cloud can be clearly seen falling. By fitting a 2D Gaussian surface to the fluorescence in each frame, we obtain the cloud's central position. The cloud's acceleration is found to be 6.3 $\mathrm{m/s^2}$. The experiment was repeated with a probe light force 5 times weaker (at 0.2 mW) and obtained just a slightly faster acceleration of 7.0 $\mathrm{m/s^2}$. This result is not surprising, although two balanced counterpolarised beams should be non-interacting with the MOT freefall, as in the six cooling beam probe flash case, there is still important heating effects occuring (friction) which can be on the scale of gravity or even more important. However, there is a difference with the latter case; the absorption of the upward beam in the MOT creates a shadow in the retroreflected downward beam intensity. It is this imbalance that leaves an upward component of the spontaneous force that reduces the MOT's gravitational acceleration. A solution is to use two independent beams of equal power instead of retroreflecting a single beam.

Alternatively, it is important to note that when the atoms were probed in a direction perpendicular to their movement (with a horizontal beam), the interaction with the probe was much less noticeable. Measurements of acceleration of the thermal expansion or guidance in a collimated beam were in agreement with expected gravitational acceleration. However, this is at the expense of having a much reduced imaging window, determined by the beam diameter, so both imaging axis have their advantages and limits.

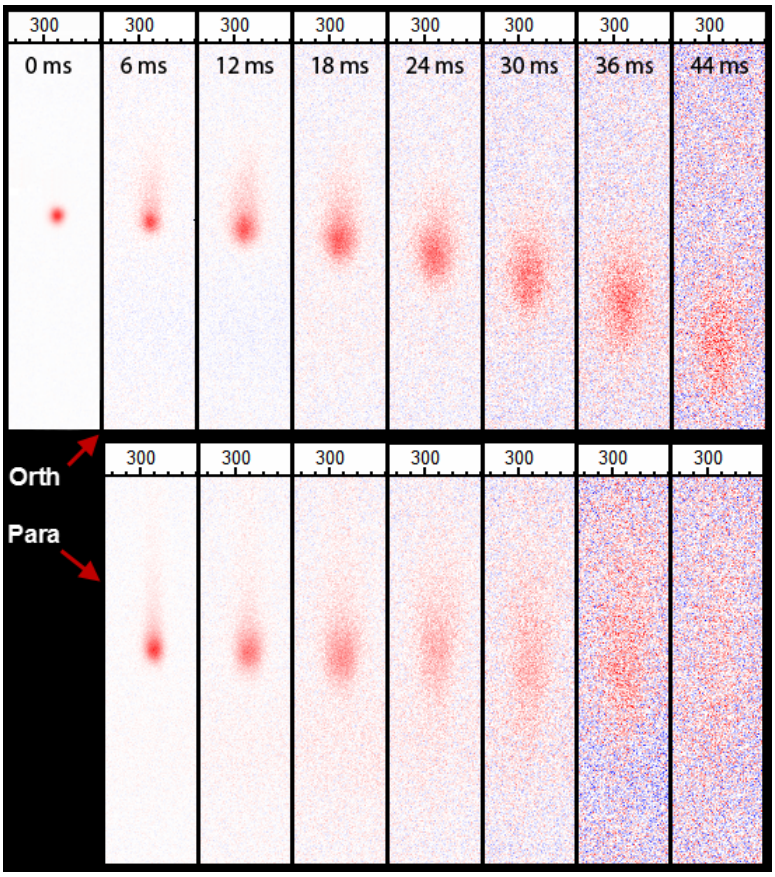

Figure 5.29: MOT freefall experiment differentially imaged with two vertical counterpropagating linearly polarised beams. Two cases are examined where beams have parallel and orthogonal polarisation. First snapshot on the left shows the MOT before release. Following snapshots are all 5 ms exposures of the cloud after freefalls of; respectively, 6, 12, 18, 24, 30, 36 and 44 ms in both polarisation configurations.

Shadow imaging

Shadow imaging is the reverse approach to fluorescence imaging in which absorption of light is measured rather than atomic fluorescence. A weak well-collimated laser beam, tuned on-resonance (or very close to it) is used to expose the cloud. A camera placed in the beam's path at the other end detects the laser probe directly. The light is absorbed where there are atoms creating a 2D "shadow" projection in the camera image. The denser the cloud, the darker is the shadow. The differences with fluorescence imaging being that the shadow beam uses intensities orders of magnitude weaker and requires the camera to be always aligned with the beam, which also causes interference fringes.

This technique presents several advantages: it is not destructive and there is no concern about the influence of the spontaneous force component. It is ideally suited for continuous exposure, real-time imaging, as well as camera triggered exposures. It is more sensitive to very low atomic densities compared to fluorescence imaging.

The main disadvantage of this technique is that the dynamic range is very limited. The image is plain dark (like the background) in most cases and it is difficult to balance exposure and gain across a wide range of densities. The image is also disturbed by interferences (multiple diffractions/Fresnel rings) collected through optics of the system because a coherent beam was used directly for imaging.

In our shadow imaging system, the camera was equipped with the 135 mm lens positioned 40 cm away from the MOT position (frame vertical height: 9 mm). The beam, coming from Stage F output, was collimated to 2.8 mm diameter with an F260 large aperture collimator and then it was expanded using a long 2.5× telescope (with 50 and 125 mm PCX lenses). The resulting beam had a $1/e^2$ diameter of 7.0 mm, ideally an even larger beam up to 20 mm is preferred. Later the beam size was improved slightly with a 175 mm lens, reaching a diameter of 10 mm. Figure 5.30 shows the resulting shadow imaging from a MOT optimized for size. Subset A is the image of the 7 mm beam without the MOT and subset B shows the shadow produced by the MOT. Subset C is the clearer differential image produced by post-processing and subset D is the absorption intensity profile of the beam through the centre. In this example, the camera gain was carefully adjusted as was the laser intensity in order to enhance the signal against the background of the CCD.

To evaluate the degree of interference in this technique, heating of the MOT by the probe beam was measured for the "worst case scenario" when the cloud is thermally expanding at release, while under continuous exposure of the shadow beam probe. Temperature measurements did not need to be calculated every time, rather the release-and-recapture (R&R) data was used to compare the recaptured fraction of atoms against the case without shadow beam exposure. This technique is explained fully in Sec. 5.2.4. The shadow probe did not play any role in the detection of the cloud fluorescence because the R&R technique uses a photodetector placed at the bottom viewport of the chamber (orthogonal to the shadow beam propagation axis).

The release-and-recapture protocol measured the recaptured fluorescence after turning off the cooling beams for delays of 4 to 56 ms, moving by increments of 4 ms. After each recapture, a 5-second wait was sufficient for the MOT to return to its steady state. In Fig. 5.31, the no-probe case with shadow probes of 20, 5 and 1 μW (intensities of respectively 52, 13 and

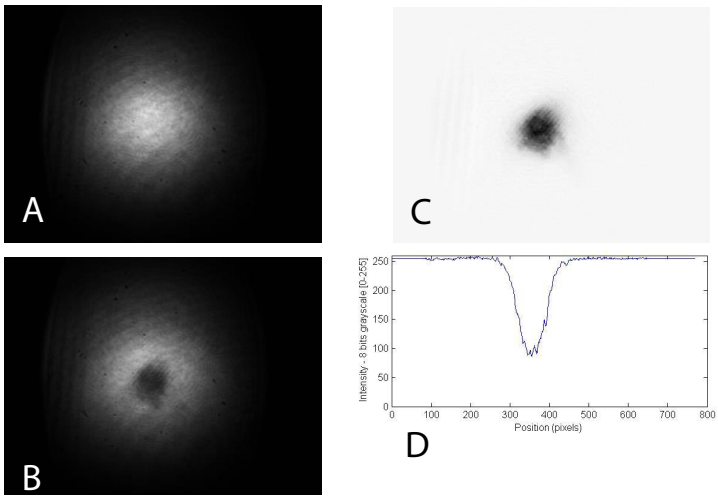

Figure 5.30: Shadow imaging of a large ^{85}Rb cloud in a magneto-optical trap. Subset A and B shows the background image and the MOT shadow projected. Subset C is the post-processed image obtain by differentiating B with A. The dark profile of the beam was taken horizontally through the centre, as shown in subset D the image was not dark-saturated.

$2.6\,\mu\mathrm{W/cm^2}$) are compared. The red dashed line represents the background fluorescence detected when the cooling beams are on and locked at -12 MHz detuning but without a MOT (by reversing the magnetic field polarity). The red circles are comparative markers showing the recaptured fluorescence across all four cases.

Starting with $20\,\mu$W, tuned on-resonance, the R&R data showed clearly how the MOT was heated up: its recaptured intensity being at the background level in less than 12 ms of expansion. This demonstrated that the atoms are expelled much faster from the trap when the shadow probe is on. With the $5\,\mu$W probe, all the atoms were lost in 36 ms. For reference, without the influence of the shadow probe, the cold atom cloud in the MOT takes 56 ms to escape the trap volume completely. Using a variable neutral density filter disk before coupling into the fibre of Stage F, the power was reduced down to $1\,\mu$W in order to eliminate the heating effects on the MOT. By increasing the CCD gain close to maximum, shadow images could still be clearly recorded although noisier. By applying this technique, we were able to tune the shadow imaging setup so that it was not noticeably heating cold ^{85}Rb atoms.

The sensitivity of this detection was further improved to the shot noise limit when measuring the phase shift of the shadow beam instead of its intensity. Dr. Phil Light from our research group pioneered this technique [136].

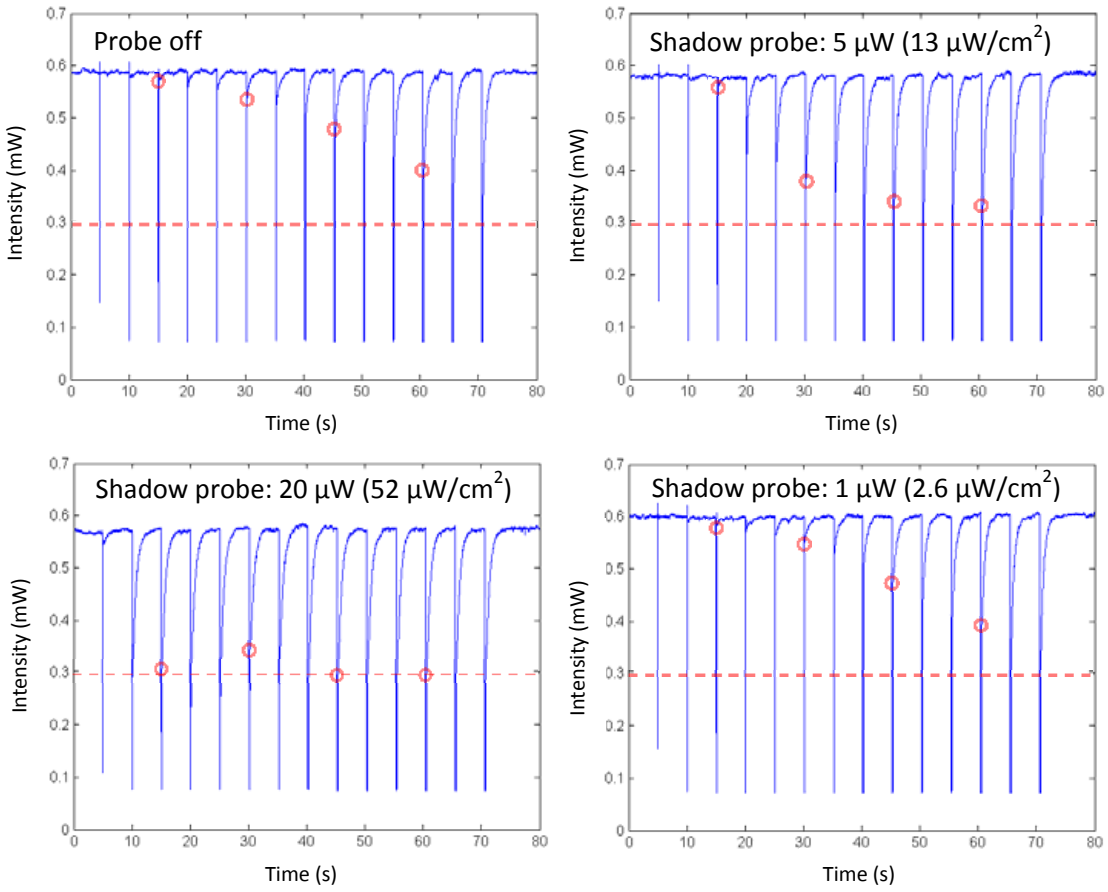

Figure 5.31: Fluorescence through time of a MOT released-and-recaptured in order to qualitatively evaluate its temperature. In this test, the MOT was released with delays from 4 to 56 ms, by 4 ms increments and 5 s to reach steady state between R&R measures. We compared the recaptured fraction of an unexposed MOT with continuous exposure to shadow beam probes of 20, 5 and 1 μW in a 7 mm beam. The red circle markers identify points of comparison of the captured fluorescence across all the cases. Only the 1 μW beam was not interfering with the cold atom cloud.

Imaging techniques summary

During the course of this thesis and the development of the cold atoms research program, three imaging techniques were developed and tested, while being particularly focussed on determining and mitigating the influence of the imaging probe on the measurement.

Flashing the cooling beams as a probe is the easiest technique to use and also has a very minimal influence on the duration of the exposure. With the combined intensity of the six

beams, excellent resolution of the atom cloud expansion was achieved for exposure times around 100 μs. This technique was particularly well suited to track the position of the cloud during ballistic expansion and realizing precise temperature measurements with it. Gravity freefall measurements combined with horizontal monitoring confirmed that the probe was not acting on or disturbing the atoms. However, the observation window was limited to the trap volume.

Shadow probe is designed as the least invasive imaging procedure and when the power is minimized, allows for continuous exposure of the atom cloud without any perceivable heating. It is well suited for real time observation but only works in one axis because the camera needs to be in the beam path in order to capture the cold atoms shadows. It was used for aligning the MOT in real-time observation, and to produce ballistic expansion videos. However, the 1D configuration and small diameter made it unsuitable to observe atoms during guidance experiments where observation over several centimetres was required. An improvement would be to make the beam elliptic in order to continue using this type of imaging but it would still not be suitable for guidance experiments over longer distances.

The most challenging imaging approach was the independent fluorescence probe. Using a single beam is unsuitable in most cases and that beam needs to be counterbalanced by an equal intensity orthogonally polarised beam. The atom cloud freefall measurements showed that for suitable imaging intensities, even a retroreflected polarisation shifted beam is not an ideal solution because the shadow of the cloud creates an imbalance of intensity in the reflected beam and therefore allows a portion of spontaneous force to act on the atom and reduce the gravity's pull. Still, it was possible to get good imaging of atoms guided in a collimated beam and focused through a hollow beam but difficulties encountered cannot rule out the possibility of the imaging beam having a physical impact, thus invalidating experimental results. However, this technique can be applied over different imaging axes (vertical, horizontal) and will definitely help to investigate dynamics of cold atoms guidance. The necessary conclusion is that two independent, balanced and counterpropagated imaging probes are required to get quality imaging.

5.2.3 Timing and remote control of the experiment subsystems

One critical aspect of the system performance for measuring temperatures or guidance in cold atoms experiments is to be able to remotely control the power and frequency of all the beams and probes. Equally critical is to shut off the magnetic fields quickly and in-sequence to perform the experiments. A good example of these requirements is to be able to

work with very cold atoms; one must produce optical molasses from the MOT. The optical molasses (OM) cooling protocol [92, 94], also called by researchers "polarisation gradient cooling" (PGC), a bit of a misleading name, sets the standard for the timing and remote control requirements of most systems. This specific cooling protocol was applied to produce OM in this thesis:

1. All lasers locked. Repump is on. Magnetic field is on. [Time = 0]
2. Cooling beams turned on. MOT formation. [Wait 3 s]
3. Turn magnetic field off.
4. Cooling beam frequency shifted to -50 MHz, intensity/4.
5. OM cooling controlled expansion. [Wait 5 - 15 ms]
6. Cooling beams switched off. [Wait i ms]
7. Probe atoms & Trigger camera exposure [0.1 - 10 ms].

To implement OM cooling and following temperature thermal expansion measurements, R&R measurements or more complex atom guidance experiments, an Arduino Mega microcontroller board was used as the central commanding unit to execute operation protocols written in the form of program scripts (sketches in the Arduino IDE). Getting the precise timing required careful analysis because of internal delays and limitations of each subsystem that had to be carefully measured (see Table 5.3). Fortunately, we did not have to worry about the time to send and receive signals because these would be received and transmitted in a few tens or hundreds of microseconds over USB connections depending on the length of the commands. Initially significant delays were encountered over the DDS command serial connection. Previously, it was mentioned that the minimum delay to shift the frequency and shutoff the cooling beams was 8 ms. It was found that, using a higher bitrate to communicate with the DDS, this delay was reduced to less than 2 ms. Table 5.3 summarizes the delays and execution speed of the MOT control systems.

5.2.4 Temperature measurements

To measure the atoms cloud temperatures two techniques were used: Release-and-Recapture (R&R) and thermal/ballistic expansion. A third technique, yielding results similar to ballistic expansion but that requires much less post-processing of the data, is the time-of-flight

Component	Delay
Serial command to DDS	< 2 ms
AOM frequency shift execution	< 20 μs
Mechanical shutter delay	5 ms
Mechanical shutter speed	< 1 ms
Camera Trigger	10 μs
Arduino smallest delay	1 μs
Magnetic field decay to >5%	30 ms

Table 5.3: Summary of the timing and control delays of components in the MOT and its imaging system.

method (TOF) [90, 92]. However the optical setup required two counterpropagating sheet beam positioned below the MOT which were not implemented due to the limited space available around the chamber.

Release-and-recapture

The temperature measurement technique called release-and-recapture (R&R), pioneered by Harold Metcalf et al. [90], was introduced as the most accessible means of measuring a cloud temperature. It consists of simply shutting off the cooling beams ("the release") and then after a delay i (time in milliseconds), firing them back on, starting the MOT trap again ("the recapture"). The key here is to measure the "recaptured fraction": the fluorescence signal of the cloud immediately at recapture divided by the steady state fluorescence signal of the MOT (including the background fluorescence from the beams). Measurements are obtained by repeating this procedure for delays of 8 ms up to 60 ms (or when the recaptured fraction is equal to the steady state fluorescence. The fluorescence background is obtained by reversing the magnetic field polarisation to prevent the formation of the MOT but keeping the laser locked at the trapping and cooling frequency. Results are discussed in Sec. 5.2.2, Fig. 5.31.

The Monte Carlo ballistic expansion model was developed and calculated the fit of the recaptured fraction as a function of the release delay i (in ms) and thus, derived the temperature of the cloud. Figure 5.32 shows results obtained on one of the early MOT's produced in this thesis, yielding temperatures of 300 μK.

However, to derive the temperatures, two experimental parameters needed to be specified

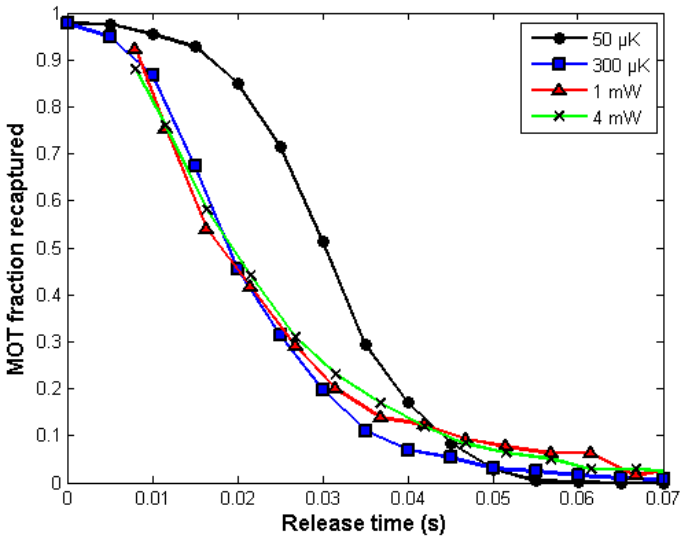

Figure 5.32: Results of the recaptured fraction of atoms in the MOT as a function of release time for trapping beams of 1 mW (red triangles) and 4 mW each (green x). Two Monte Carlo R&R model simulation of the same experiment with cloud temperatures of 300 μK (blue squares) and 50 μK (black circles) were also plotted to evaluate the cloud temperature.

with important uncertainties: the initial $1/e^2$ cloud radius and the trap volume, which is deduced from the well-known beam radius, but is affected by the beam alignment. For this technique to yield good results, significant effort must be invested in reducing these uncertainties. At this point, the estimated error was over $\pm 150\,\mu$K. Still, this technique is useful and was used during optical/magnetic alignment to evaluate the immediate, real-time impact of experimental parameter adjustments on the cloud temperature. It is the quickest relative measurement of an atom cloud temperature developed in this thesis.

Thermal expansion

This technique to measure the temperature of a cold atom cloud is similar to the previous release and recapture at the only difference it requires a well-triggered CCD camera. An initial image is taken of the trapped atom cloud, then the cloud is released for time X, and simultaneously probed and imaged using the cooling beam flash imaging technique for 2 ms intervals, as described in Sec. 5.2.2. This technique was first used by Steven Chu et al. [92] in *Appendix B* of their famous 1989 experimental paper on the first investigation and explanation of sub-Doppler cooling. They calculated the ballistic time-evolution of the

released atoms density, $n(r,t)$, assuming initial Gaussian density distribution ($n_0(r)$), as its convolution with Maxwell-Boltzmann Green's function:

$$n(r,t) = \frac{exp(r^2/2\sigma^2)}{(2\pi\sigma^2)^{3/2}} \tag{5.10}$$

where the Gaussian distribution variance (the cloud size parameter) is:

$$\sigma^2 = \sigma_0^2 + k_B T t^2/m \tag{5.11}$$

and σ_0 is the initial distribution variance (before expansion), T is the cloud temperature, t is the time of the ballistic expansion and m is the atomic mass.

With this formula, the cloud temperature is simply obtained by fitting Eq. 5.11 to the cloud distribution variance (expanding radius data) as a function of time. The latter is obtained by fitting a 2D Gaussian distribution function to each CCD image taken. The fitting parameters for the equation are: σ_0 and T. The temperatures are calculated independently for the vertical and horizontal axes. As mentioned earlier, it is not unusual to obtain different temperatures along each axis.

Although this may seem like complex processing, the whole calculation was automated using a Matlab program that read images in batch using fine-tuned automated fitting algorithms and produced the temperature results immediately after the measurement. The measurement procedure and control of the whole MOT system, was also automated with an Arduino sketch program. The cloud temperature could be obtained at any time by any operator in less than 2 minutes with only 2 button clicks (start Arduino temp measurement, launch Matlab temperature analysis). The program used a *Levenberg-Marquardt* 2D Gaussian fitting algorithm written that automatically low-pass noise filtered the image when its signal to noise ratio was getting low. More precisely the best and most consistent results were obtained using a pixel-wise adaptive Wiener method based on statistical estimates from the local neighbourhood of each pixel.

Using this technique, several measurements of the produced MOT were realized. The MOT was produced using detunings of -2Γ (-12 MHz). For the strongest laser intensity produced in the experiment (3.5 mW per beam), a temperature of 78 μK was obtained, see Fig. 5.33. In this figure, the 3 small inset CCD images of the thermally expanding MOT are imaged at 0, 4 and 10 ms. The program always produced such a figure at the output to allow the experimenter to evaluate the quality of the fit and quickly notice convergence errors.

With a weaker MOT of 1.3 by 1.9 mm produced using 1 mW beams and with the other parameters kept identical, the temperature dropped down to 61 μK. Then production of

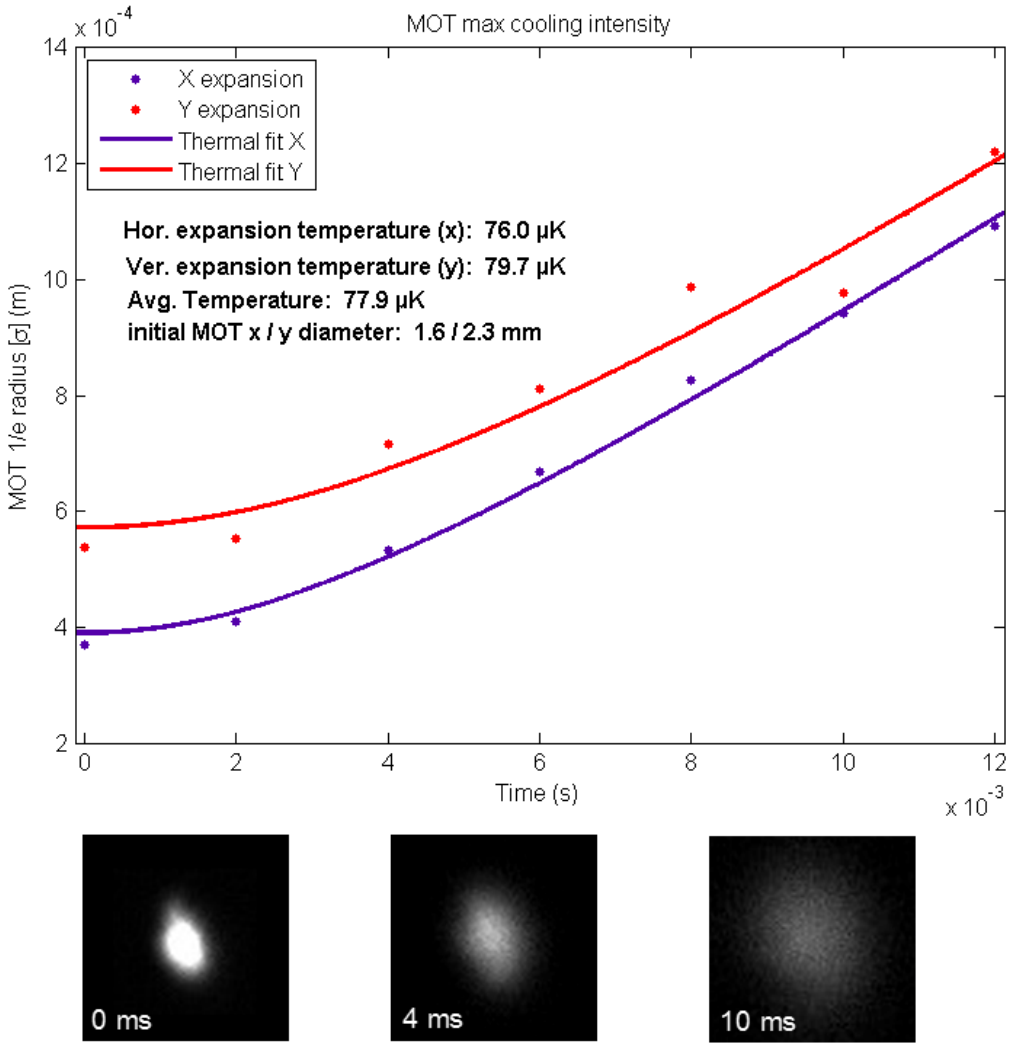

Figure 5.33: Curve fits of the MOT radius vs. the expansion time for horizontal and vertical profiles. The temperatures in x, y are shown above as well as the average of the two (78 μK). Below, the 3 small insets are some of the original CDD images of the MOT (at 0, 4 and 10 ms), the Gaussian function was fitted to. The MOT of 1.6 mm by 2.3 mm diameter was produced with cooling beams of 3.5 mW, 12 mm diameter and 12 MHz red-detuned.

optical molasses (OM) was achieved by shutting down the magnetic field and detuning the cooling beam frequency for 12 ms before proceeding to temperature measurements. Several patterns were evaluated whereby the frequency of the beam was ramped or stepped over the 12 ms. A quick ramp produced a 23 μK MOT, a slower ramp for 20 ms produced a cooler, larger MOT at 14 μK. The best results were obtained by just stepping the frequency to 32 MHz and having the power dropped by 65% (the AOM being less efficient at this

frequency helped). The total power was thus reduced by a factor of 7.5 for 12 ms with no magnetic field present. This protocol produced the coldest and smallest atomic molasses at 9 μK and 1.0 mm diameter, see Fig. 5.34.

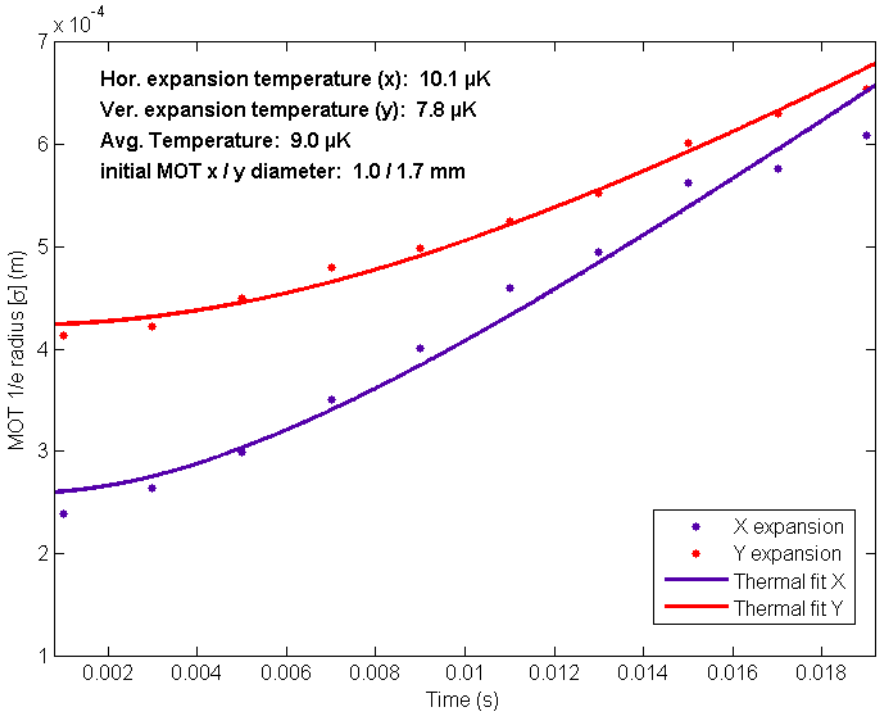

Figure 5.34: Coldest optical molasses obtained from a strong-force MOT (at 3.5 mW each beam). The beams are detuned from 12 to 32 MHz and power is dropped by 65% to 1.2 mW, cooling force is reduced by a factor of 7.5 for a duration of 12 ms, then the thermal expansion technique is applied to obtained the average measured temperature of 9 μK.

5.3 Guiding cold atoms

Three essential preliminary guiding experiments were performed prior to guiding atoms in a fibre. These allowed us to improve our detection/imaging and the required timing control essential to control atoms.

5.3.1 Red-detuned horizontal gaussian guide in free space

In the first experiment, a red-detuned Gaussian beam was used to guide a cold atom cloud released from a MOT. The guide beam was produced by the CW tunable ring Ti:sapphire

laser (Coherent MBR-110) described earlier. The optimal Gaussian beam profile was obtained after reflection off a computer-generated phase mask produced by a spatial light modulator (SLM) in stage H of the setup (described in Sec. 6.3). This allowed troubleshooting the entire setup and the beam control of this stage, through a simpler guidance experiment.

The beam was raised horizontally by two 45° silver mirrors in a periscope setup, and introduced horizontally through one of the only available viewports (opposite to the repump beam using the other horizontal viewport). With this particular setup, there is no availability to install a mirror on the opposite end (or a second laser beam of orthogonal polarisation) to cancel the spontaneous force effect.

A 2-mm diameter beam was initially used but, because of the challenges for the initial alignment, the experiment was simplified by expanding the beam to a diameter of 28 mm. To compensate for the large size, 66 mW of optical power was used delivering an intensity of $10.7\,\mathrm{mW/cm^2}$ and a relatively weaker intensity gradient than would have been obtained with a smaller beam. The guidance force being relative to the detuning, 5 values were evaluated: -1, -10 and -30 GHz to the red and $+1$, $+10$ GHz to the blue as well to test anti-guiding. The correct frequency was obtained by tuning the MBR using the wavemeter data. The advantage of working in far detuning is that the wavelength does not have to be precisely controlled and actively stabilised. Simply detuning by $+0.02$ Å from the cooling frequency for every -1 GHz of detuning was required to setup the guide beam.

Now for the actual experiment, an optimized size MOT was produced without going into a cold optical molasses phase (also referred in this thesis by polarisation gradient cooling phase). After a couple seconds of charging the trap, a steady state MOT was obtained. First, the beams and magnetic field were quickly shut down. Simultaneously, the Gaussian guide beam was introduced into the chamber. To minimize any interference at this point, the shadow beam imaging technique was used to minimize the variables that could interfere with the experiment. The camera was triggered after the prescribed guidance time to produce a short exposure (< 2 ms) in the selected timeframe. The guidance was run repetitively to capture an image of the experiment every 250 μs and generate a 14 ms-long video of the guidance. When the Gaussian beam was set at -1 GHz, no guidance was observed and the MOT was rapidly pushed out of the frame, evidence that the spontaneous force, left unbalanced, is still remarkably strong at this detuning and superior to the dipolar force. At -10 GHz, guidance of the MOT was observed but the push of the spontaneous force steered the atoms to move into the beam propagation direction. Figure 5.35 shows 4 frames of the guidance video at 0.25, 2.25, 3.25 and 5 ms. The image was differentially subtracted from

the background and enhanced to accentuate contrast through post-processing. The fading observed at half the distance of the frame is mainly due to the shadow beam imaging probe limited range of exposure (about the radius of the probe beam) rather than losses. Moving the probe further away showed that guidance was achieved. Looking carefully at the video, a small fraction of the cloud is seen as ballistically expanding un-captured by the guidance beam. This class of "lost" atoms was also identified through simulations.

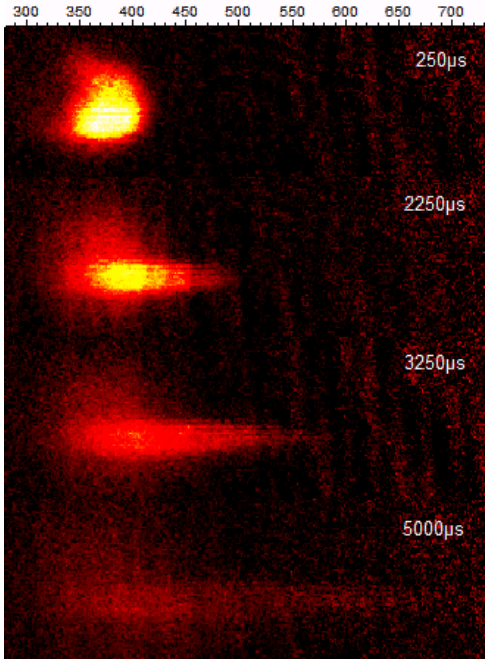

Figure 5.35: Four selected frames at 250, 2250, 3250 and 5000 μs from the video of the guidance of a cloud of cooled ^{85}Rb atoms are shown side-by-side in a vertical stack. The single 10 GHz red-detuned Gaussian beam of 66 mW and 28 mm diameter was produced through the same setup used to generate the Laguerre-Gaussian hollow beam.

The beam at -30 GHz did not have any apparent effect and atoms were quickly lost due to ballistic expansion and gravity's pull. The beam at $+1$ GHz (blue-detuned) produced identical results dominated by the spontaneous force. At $+10$ GHz, the result showed anti-guiding combined with the spontaneous force push in the beam's propagation direction. The atom cloud expanded and moved away from the laser in a moon crescent shape where most atoms quickly escaped the beam path but some initially lost atoms lingered for a longer time outside of the beam.

5.3.2 Collimated blue-detuned guidance

In the following experiment, LG_{01} blue-detuned guidance was realized in the vertical axis in order to image the guidance over a longer distance as opposed to the horizontal guidance realized in the previous subsection. A top view camera was used to realize a tighter alignment within the beam centre.

The coupling of the beam into the chamber was modified for this second experiment. Fluorescence imaging was implemented to image the atoms across the chamber. To this end, both the probe and the guide beam were polarised, aligned and combined in a single beam using a polarising beam splitter close to the bottom viewport of the chamber. Both beams were vertically aligned into the chamber using a mirror in a kinematic mount. However, the probe beam was not reflected at the top so the spontaneous force was left unbalanced. Imaging was also made easier by using Point Grey Chameleon cameras in "high gain" to replace the older JAI CV-M50 CCD camera. The exposure time with these cameras could be significantly reduced from [10-15] ms down to [0.5-2.0] ms. The higher gain also allowed a reduction in the power of the probe beam which overall resulted in reducing the negative effects of independent single beam fluorescence imaging.

During these experiments, electronic issues with the SLM of stage H temporarily prompted a replacement with a reflective spiral phase-plate of order 5 to generate a hollow beam. This optical element was fabricated from an aluminium mirror using a commercial diamond turning point optical surface shaping apparatus (at the Australian National University). However, the beam obtained from the spiral phase plate was not a pure LG_{05} as it also contained higher order harmonics (of the same parity) commonly generated by this technique [57]. So it was only a temporary solution as large NA multimode beams are more likely to suffer from optical aberrations leading to a non-dark non-hollow beam at the focal point when coupled into a hollow fibre.

A 50 mW guide beam with a diameter of 16 mm and detuning of between +5 GHz (780.23 nm) and +40 GHz (780.16 nm) was used. The MOT was also colder than in the previous step by implementing a cold optical molasses phase. The MOT was measured to be around 35 μK during these experiments.

To acquire the images of the guided atoms, cold optical molasses were produced, then cooling beams were turned off and the hollow guide beam switched-on. After waiting i ms, camera triggered and probe fluorescence beams switched-on, in a loop with the delay i being increased by 5 ms every iteration. Selected frames of the atom cloud guided over 22.5 mm during 66 ms are shown in Fig. 5.36. The first four frames were 5 ms apart to show the

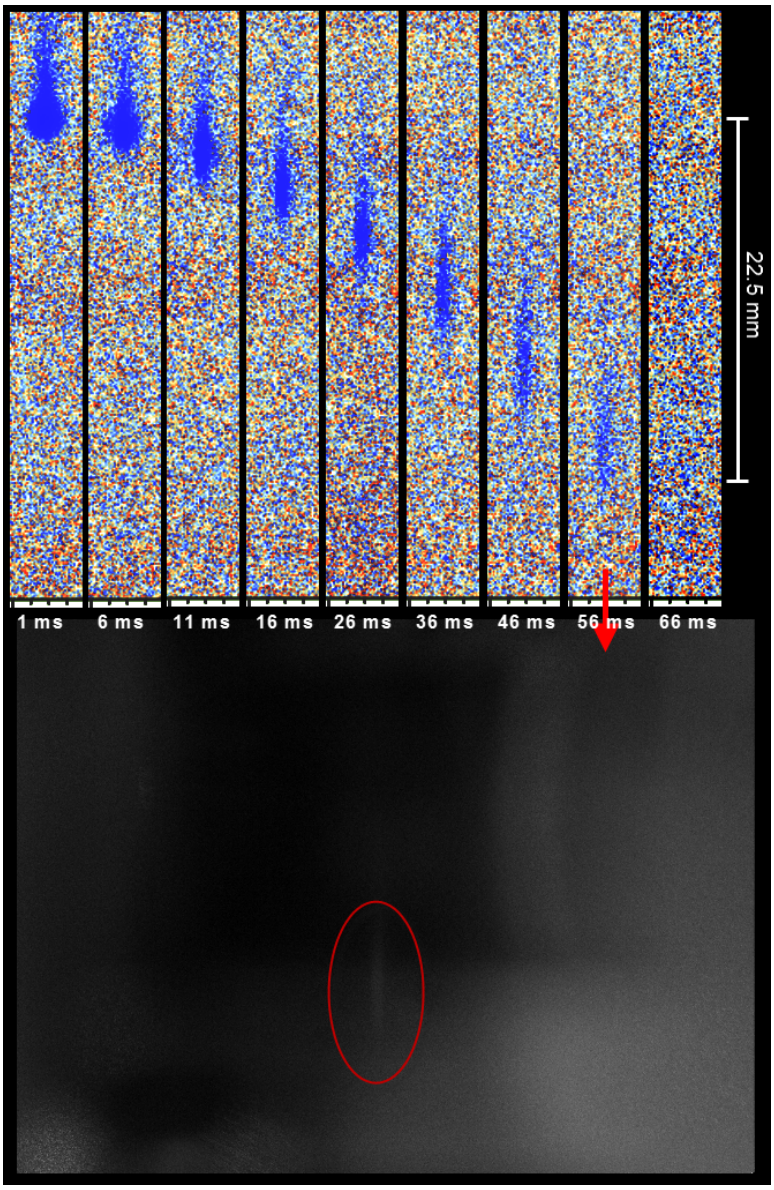

Figure 5.36: Imaging of cold ^{85}Rb atoms released from a MOT into a collimated LG_{05} blue-detuned hollow beam. Atoms travelled over 22.5 mm in 66 ms in a 16 mm diameter beam of 50 mW with 20 GHz detuning. (Top) 9 differential images contrast-enhanced at 1, 6, 11, 16, 26, 36, 46, 56 and 66 ms. (Bottom) Raw image from CCD camera showing the blurred reflection of light against the the background limiting the imaging at the bottom of the range. The red ellipse indicates the position of the guided atoms in the unprocessed image captured after a delay of 56 ms.

formation of the guided class of atoms, and then showed frames 10 ms apart for guidance over the imaging distance. Each image is background subtracted and contrast enhanced by

using a technique of "histogram saturation". This enhancement was executed with Adobe Photoshop's automatic level adjustments.

First, it was noticed that the cloud was almost invisible in the last frame; this was introduced to show the most problematic element of this imaging setup. In the bottom of Fig. 5.36, the original frame captured at 56 ms is shown. The white fluorescence on the right side and bottom is due to reflection off the metallic structure mounted against the chamber's large window to support the cancelling coils and the cooling beam cage-mounted optics. When the atom cloud is in front of this structure, it disappears against the strong background reflection off this metallic support piece. It could have been mounted vertically to prevent this problem but it would have necessitated a complete disassembly of the chamber to correct the issue which could not be afforded at this point in time.

One also notices that in unhindered freefall, the atom cloud centre-of-mass should have travelled 42 mm in 66 ms and not a mere 22.5 mm. The vertical motion of atoms had a calculated acceleration of $5.2\,\mathrm{m/s^2}$. This was not surprising as previous experiments by Mestre et al. [57] also showed their atom cloud travelled only 10 mm in 45 ms. This is caused by the spontaneous force component slowing down the atoms vertically when they penetrate the field. It can also be seen that the forefront of the distribution seemed to accelerate normally with gravity.

To further analyse this behaviour, simulations of the experiment were performed reproducing all known parameters as precisely as possible. The vertical motion of atoms, their freefall, was analysed in relation to their transversal energy, i.e. how far they penetrate the guiding field. It showed that the more they interact with the field (deeper penetration linked with higher transversal energy), the slower they accelerate downward. The simulations showed excellent agreement with measured statistical centre of the cloud distribution ($4.95\,\mathrm{m/s^2}$ for the case illustrated). Guide beam intensity were also found, in agreement with simulations, that results in a stationary centre of the atom cloud (that would not fall), but the distribution itself would elongate up and down through time.

5.3.3 Guiding through a focused hollow beam

Following previous experiments, the next step before coupling the atoms in a fibre was to guide them through a focused beam. The coldest and smallest optical molasses were only realized after these experiments, so these experiments still used larger and warmer optical molasses similar to the collimated guidance experiments. The hollow beam was generated using the fifth-order ($10\,\pi$) spiral phase-plate instead of the SLM.

A 175 mm plano-convex lens was positioned just before the beamsplitter cube combining both probe and guide beam and coupling them in the chamber from the bottom viewport with a 45° mirror. The lens was positioned to align the beam focus 10 mm below the MOT. The laser frequency was locked on-resonance, the input power was maximized and the Rb density was also increased to improve the beam fluorescence and identify its focal point position. Figure 5.37 shows the focused beam imaged using the two Chameleon cameras with their focal position optimized approximately 10 mm below the MOT centre. Subsets (A) and (C) shows the Gaussian beam and hollow beam in Chameleon A view respectively. Subset (B) shows the same fifth-order hollow beam imaged by Chameleon B, a larger field-of-view camera. In all cases, the focal point indicated by the red square, is just slightly above the reflection off the metal support of the horizontal cancelling coil. Both Gaussian and hollow beams were going through the same optics system to ensure that their focal point would be at the same position.

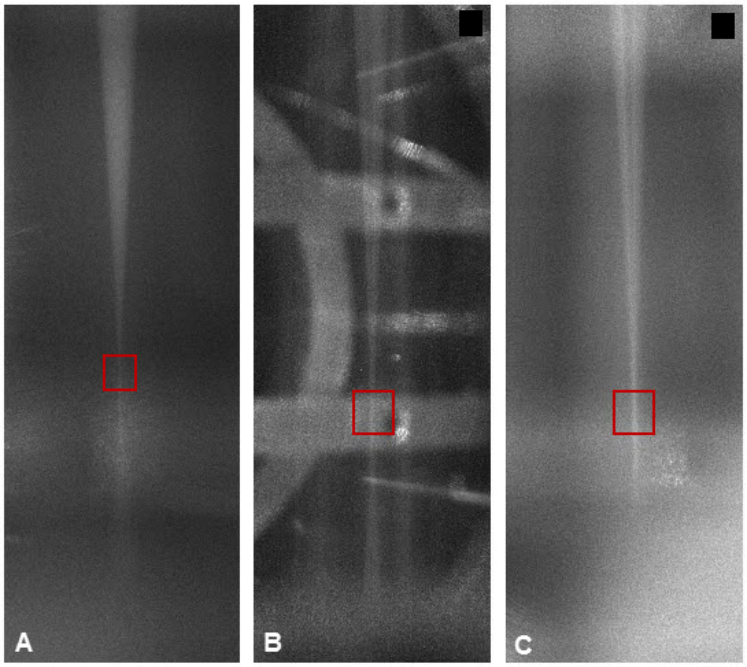

Figure 5.37: CCD captures of the focused guide beams against a dense background of ^{85}Rb, red squares indicate the approximate focal point. (A) 12 mm diameter Gaussian beam focused by a 175 mm lens taken with Chameleon A camera. (B) 12 mm diameter focused hollow beam taken with Chameleon B, and the same beam taken by Chameleon A in subset (C).

When setting up this experiment, the uniformity and temperature of the MOT was opti-

mized and several cameras were used to improve the alignment. Several attempts were made to see the atoms funnelling toward the focus before being expelled to the side; re-alignment of the beam and re-positioning the MOT solved these issues. Imaging the weak fluorescence going through the focus against the bright background required post-processing of every frame taken. The technique developed involved removing background light with an image subtraction between the captured frame and the reference frame (a Rb fluorescence background without a MOT). Differential images were then enhanced through histogram saturation, an imaging technique involving grey level automatic adjustments. When the signal is weak, it is difficult to distinguish the atom cloud position because the fluorescence signal is overcame by the laser light reflections off the metallic parts in background and back to the camera. However, when looking at the stills in sequence, it is easier to distinguish the cloud fluorescence in motion against the static background and to see atoms funnelling through the focus. It was also found that background differentiation often erases valuable fluorescence signals. From the raw captures, atom ensembles often appear after focus as an organised rapid trickle of the noise. Afterwards, histogram saturation was only used as a post-processing operation without background subtraction that was able to enhance this signal visible in the raw data. Two experiments are analysed below.

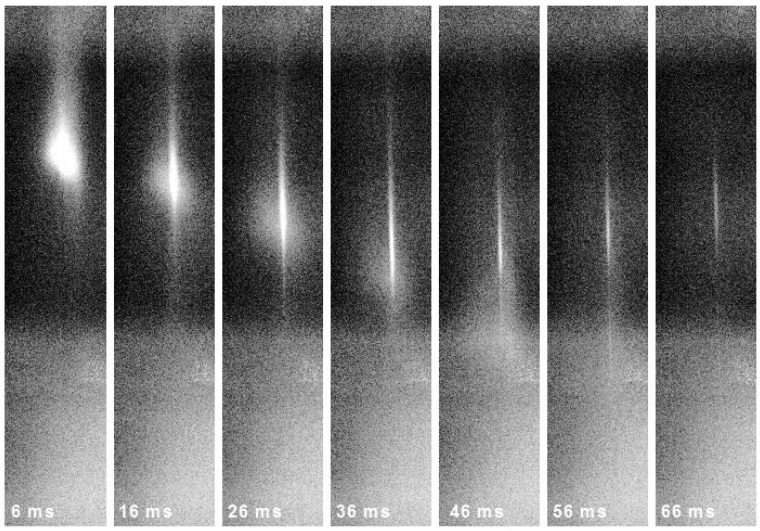

Figure 5.38: Imaging of cold optical molasses released 10 mm above a focused LG_{05} beam, 12 mm diameter, 50 mW and 20 GHz detuned. 7 frames 10 ms apart shows all three groups of atoms: lost, trapped and guided.

First, when the focused LG_{05} beam was detuned at +20 GHz (780.201 nm), all three

groups of atoms initially identified in our modelling paper [36] and in the modelling Chapter 4 of this thesis were observed. Figure 5.38 shows 7 selected frames of the experiment imaging sequence, 10 ms apart. In the experiment, the cold optical molasses are released about 10 mm above the focal point of the blue-detuned hollow beam. Through the frames, a cloud of lost atoms is seen expanding and going through the beam as if falling just ballistically. The rest of the atoms are initially funnelled but around the focal point, from 46 to 66 ms, they are seen being separated in trapped and guided distributions. In the 56 ms frame, the lowest intensity in the image, before the two distributions are clearly separated, is where the focus was identified in Fig. 5.37. The guided atoms falling through are observed even beyond 66 ms but its necessary to observe it in time-sequence in order to distinguish the weak fluorescence signal from the static background noise. The experimental parameters of this experiment were modelled as closely as possible and resulted in 0.6% guided, 12.8% trapped and 86.6% lost.

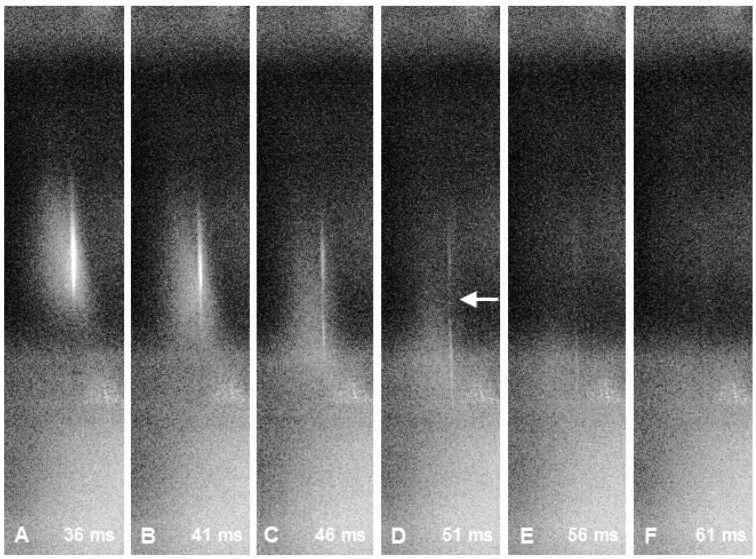

Figure 5.39: Same experiment as the previous at 30 GHz detuning. This time we only show the critical part of the experiment with 6 frames starting at 36 ms and 5 ms apart. Similar distribution of atoms is initially funnelled but more atoms end up guided through and trapped atoms are lost after focus.

A comparative guidance through the focus was produced by keeping all the same experimental parameters but reducing the optical force by detuning the frequency to +30 GHz (780.183 nm). To show the separation point in more detail, frames were selected 5 ms apart from 36 ms onward. The experimental initial conditions being the same; the frames at the

same time from release are comparable between different run of the experiment. The distribution of atoms and lost cloud position in this 36 ms frame is almost identical to the 36 ms frame of the experiment at 20 GHz. Continuing with the comparison, at 46, 51 and 56 ms, the atoms guided are more intense at 20 GHz but afterward the trapped atoms are quickly lost. The model analysis also showed that the proportion of guided atoms becomes more important at 30 GHz going up to 2% and the amount of trapped atoms is almost the same at 15% which agrees with frames comparison at 36 ms.

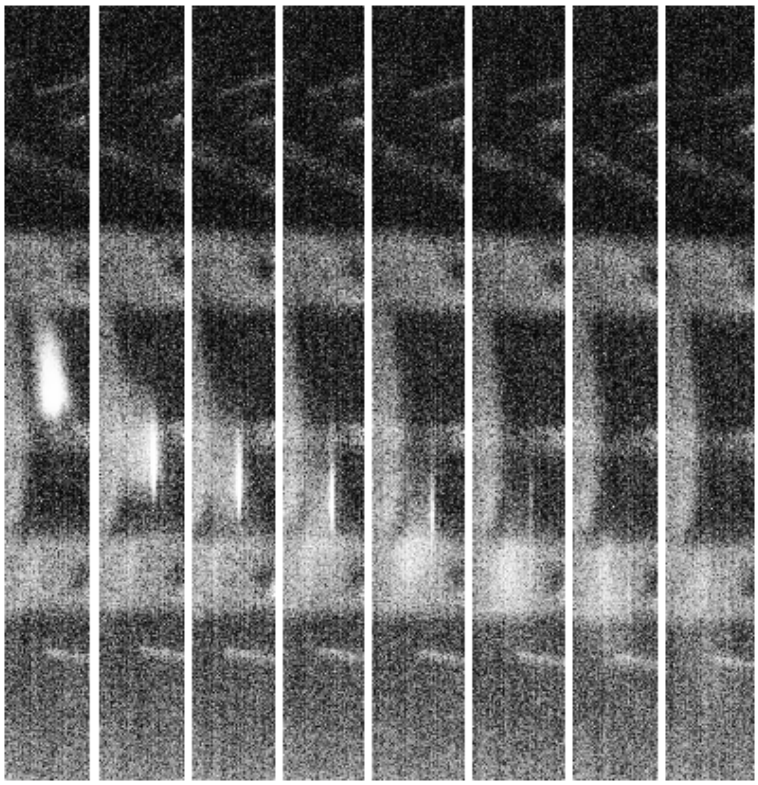

Figure 5.40: Same experiment at 30 GHz detuning but imaging over a wider field-of-view using Chameleon B. Frames are respectively at 1, 36, 41, 46, 51, 56, 66, 76 ms. The last two frames show that in a still frame the very weak fluorescence against the bright background makes the guided atoms invisible but in an animated sequence we can see the trickle of noise revealing their presence.

Fig. 5.40 shows the same experiment of focussing through the fifth order hollow beam at +30 GHz detuning but from the *Chameleon B* camera point of view. First, the initial 1 ms frame is shown followed by the 36 ms frame and onward by 5 ms timestep except for the last two using 10 ms steps to show the extent of the guidance. It appears like there is no signal

in the last two frames but through an animated sequence, this trickle of noise from the weak fluorescence against the static background becomes visible. In this experiment at 30 GHz, the guided atoms are even seen below the metallic support, while in the experiment run at 20 GHz they are not seen, which is further evidence that more atoms are guided through the focal point of the hollow beam with less force, following our model prediction.

Guidance at 40 GHz detuning was also investigated and the ratio of guided atoms decreased back to what was observed at 20 GHz following predictions of the model (0.8%) without visible trapped atoms. Imaging sequences taken after re-alignment showed that guidance was not occurring anymore so it served to demonstrate how critical the alignment can be to the success of the experiment. It is also a variable the model doesn't take into account, assuming that atoms and beam are perfectly centred. The absence of trapped atoms has been shown in two missed experiments where they were expected but, because of a bad alignment, the trapped distribution is ejected on the side when it approached the focal point of the hollow.

5.3.4 Summary of results

Overall in this section, guidance was achieved in collimated beams and through a focused hollow beams. The level of control and the precision required to achieve the experimental goals exceeded expectations but were found to be manageable. Methods to diagnose misalignments were also developed from imaging data of the attempts. Post-processing of the image data was optimized to enhance very weak fluorescence amid the laser lit background. With close to optimal alignment, good guidance was obtained and compared for 3 different optical forces (20, 30 and 40 GHz detuning). The qualitative comparisons of atoms funnelled and guided through the focus were supported by the quantitative results of the numerical modelling reproducing these experimental conditions. Both experiment and simulations identified the optimal detuning to achieve the best atomic coupling (+30 GHz). This agreement further confirmed the adequacy of using our developed numerical model to determine the experimental parameters. Optical misalignment and beam imperfections not modelled were also found to be more critical in accounting for the trapped and coupled atom group distributions. The experiment yielded smaller number of atoms than simulated but without affecting the optimal parameters, just resulting in more overall losses due to misalignment and imperfections.

With these results we feel confident in continuing toward fibre coupling and guidance. A step forward is also to improve the imaging scheme by using two counterpropagating

orthogonal polarisation probe beams and removing reflective metal parts from the background by changing the cancelling coil holder design or reorganizing the position of elements outside the chamber to allow for a better camera angle. To guide atoms in a fibre, it will also be necessary to use the SLM with a lower order single mode beam for reasons discussed in Chapter 6.

CHAPTER 6 GENERATION AND COUPLING OF A LG_{01} BEAM IN A HOLLOW CORE FIBRE

In this chapter, the part of the project involved with the guidance of the hollow beam and the technique used to produce it will be discussed. In the first section the development of the fibre leading to the final fibre selected along with its specifications and performance data will be presented. In the second part, the spatial light modulator, the computer generated phase mask and their results are described. Next, how the first two parts are put together in the experiment setup along with the control elements necessary to integrate it with the complete MOT system is shown. The last part presents the particular coupling method developed to achieve efficient coupling and single-mode guidance of the LG_{01} beam.

6.1 Fabrication and imaging of atom guiding hollow core fibres

The primary goal of this Thesis was to develop the concepts and techniques that would allow longer distance guiding of atoms at the scale of the lab (above one metre). The elected direction to achieve this goal was to work with a high efficiency, low loss hollow core optical fibre instead of using a capillary which is only useful for distances of a few centimetres, as has been used by every other research group on atom guidance.

Polymer optical fibres presented interesting advantages in producing unique ring suspended core fibres (a geometry not possible in silica fibres due to their lack of flexibility). The microstructured polymer optical fibre (mPOF) group at the Australian Technology Park in Sydney, offered access to its facilities to develop an atom guiding fibre in polymer. The initial concept was to couple laser light in the suspended ring and atoms would be guided by the blue-detuned evanescent field leaking into the hollow core. The guided modes of the fibre were modeled using a home-built fibre mode solving computer program (ABC-FDM), which was used to maximize evanescent field penetration in the core and identify single mode guiding conditions in the ring. Figure 6.1 shows the modeled suspended ring fibre cross-section. The color-map shows the electric field intensity where red is null and blue is max. A weakness was revealed for this geometry as it always remained multimoded. To achieve a single-mode operation, the fibre core wall needed to be sub-micron thick (0.78 μm precisely) for the hollow core diameters required to guide large amount of atoms.

In parallel to the modelling, fabrication techniques were developed to produce the suspended ring fibre and a PC/PMMA bi-material fibre to explore index contrast simultaneously.

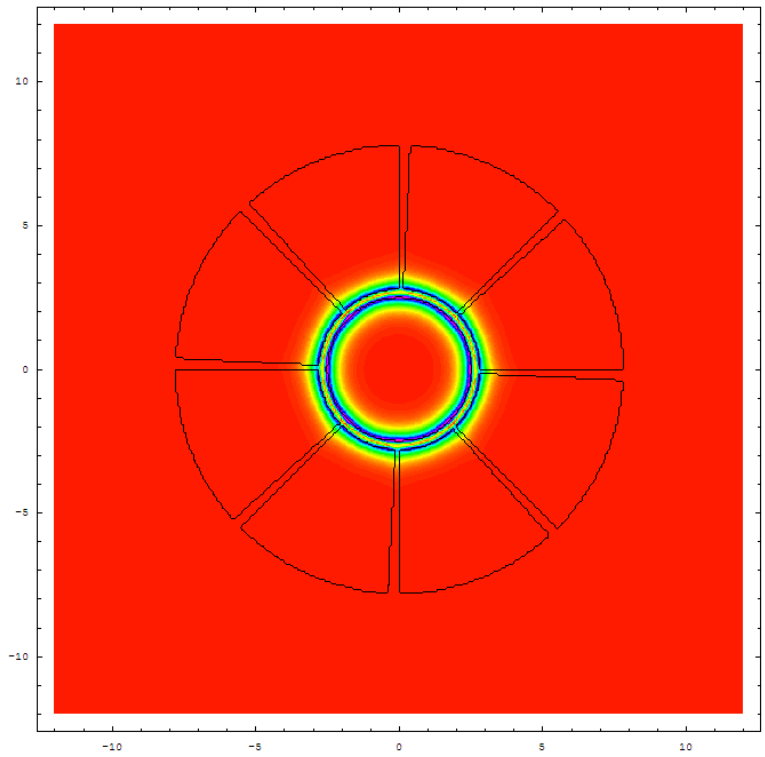

Figure 6.1: The solutions for the guided modes solved using the ABC-FDM program for a suspended ring fibre design. The 31μm wide ring guiding the light and its supporting triangle bridges of 1 to 3 μm are made of PMMA. The hollow core is 25 μm diameter.

Generally, fibres are made from a preform of a few centimetres in diameter (in silica) to several tens of centimetres (in polymer), which is heated and drawn to a fibre in a single step. With microstructured fibres built from a stack of straws, it is necessary to use a two-stage draw. The preform (10 cm dia.) is drawn to a "cane" (0.5 cm dia.) that is then re-sleeved into a thick-walled tube (4-10 cm dia.) depending on the final desired core size. This new preform-cane is then re-drawn into a fibre. With PMMA MPOF, a technique was developed using slight air pressure in the core, and low pressure to vacuum in the cladding to fine tune the collapse of the microstructure. This technique allows the production of a kagome-style or honeycomb-style cladding from the same stack of straws with great success [137]. Kagome fibres are a type of microstructured optical fibres in which the cladding features are in a characteristic "star of David" pattern (see Fig. 6.3 A, D, D_2, E). This microstructure enhances mode-separation, higher order mode guidance and guided wavelength range [138] compared to a classical "honeycombed" photonic crystal fibre (PCF) (see Fig. 6.3 B & C).

Fig. 6.2 shows four photoraphs at various stages of the suspended ring atom guiding

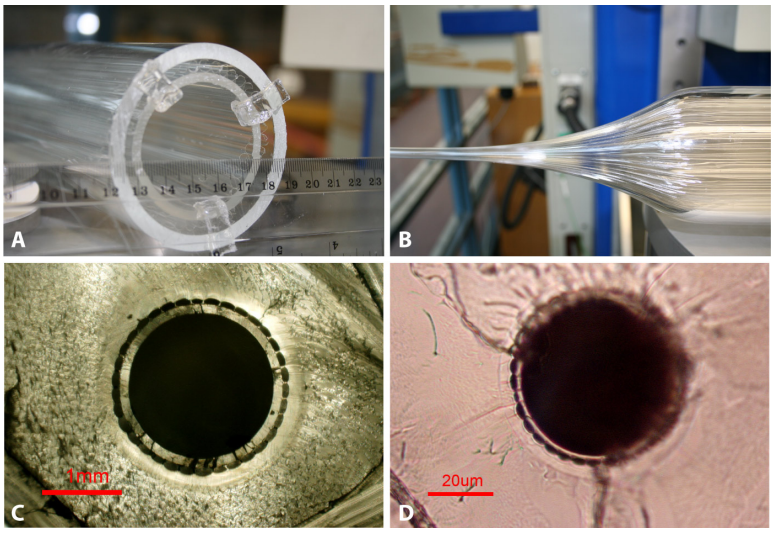

Figure 6.2: Photographs of the fabrication of our suspended ring mPOF. A. 7-cm diameter stacked-straw preform assembled before drawing. B. The preform is drawn into a 5-mm diameter cane while applying pressure in the core and vacuum in the cladding. C. Microscope image of the 2-mm diameter hollow core cane after re-sleeving (draw stage with less than 5% reduction in diameter). D. Microscope image of the fibre core after the final draw (50 μm dia. core, 1 μm thick ring, 0.2 μm thin Y-bridges).

mPOF. Photo A shows the stacked-straw preform. Photo B shows the preform drawn to a 5-mm cane and photo C is a microscope image of the cane cross-section using a pressurised core and vacuum in the cladding. Photo D is a microscope image cross-section of the final fibre. This fibre has a 50-μm diameter hollow core with a 1-μm thick ring supported by Y-shaped 200 nm thick bridges. The bridges increase the ring mode isolation and the performance was compared with initial models and integrated in a new model. These results were discussed in a 2009 publication [139]. The fibre shown in D was made as a proof-of-principle to show that the large core single-mode suspended ring design could be fabricated. However, coupling laser light into the ring mode is dependent on extremely difficult alignment and yields abysmal efficiencies (0.2%). This design was dropped for fibres that could support a hollow mode in the hollow core (c.f. Alexander Argyros's thesis [140]). Instead of using a TE-mode, which is difficult to guide in band gap fibres, Laguerre-Gaussian (LG) modes were chosen instead. Hollow beam generation will be discussed along with our results in the Sec. 6.2.

When developing the kagome 1083-nm guiding fibre structure (for metastable Helium at that time), too many simultaneously guided and coupled modes posed an issue. One proposed solution was to use a fibre with the desired wavelength at the edge of the bandgap. Higher

order modes do not guide well in this region and this creates better mode separation[137], but the analysis indicated an additional loss caused by surface roughness that couples modes and increases cross-talk/mixing even close to the bandgap. The solution was to minimize surface roughness in PMMA mPOF fibres, leading to the "high stress - cold draw - no post-draw annealing" process [141, 142]. Improvements in the decreasing mPOF transmission losses by a factor of 3 were the result, and thus led to the fabrication of the lowest loss mPOF at 0.14 dB/m at 650 nm [142], below bulk PMMA material loss, but still not sufficient to guide a single-mode hollow beam (even $<$ 10-cm length). This was due to the significant mode-mixing that occurred over the equilibrium length, mostly caused by lossy modes, a feature commonly encountered in mPOF [143].

Silica microstructured fibres are a more mature technology which does not suffer from the limitations of mPOF. Several kagome guiding fibres in silica were provided by Prof. Fetah Benabid (University of Bath, UK), and tested as potential candidates for guiding a hollow beam at 780 nm and suitable for guiding cold Rb atoms. The coupling technique used, hollow beam guiding efficiency and shape will be further discussed in Sec. 6.4. Here we will briefly summarize the methodology used and characteristics of the fibres tested. The data from our fibres was compiled in Table 6.1 and a scanning electron microscope (SEM) image was made of each fibre's cross-section in Fig. 6.3.

Fibres A-D were made out of silica while fibre E was optical grade PMMA with material loss of 0.97 dB/m@780 nm. Each fibre evaluated was coupled with plano-convex lenses from 50 mm to 175 mm focal length with an input beam size from 1.5 mm to 6 mm $1/e^2$ diameter in order to find the most efficient coupling with rigorous alignment and beam-walking. The bare fibre was mounted on a Thorlabs 3-axis micrometre controlled alignment stage. The coupling lens was also moved in all 3-axis in order to control and minimize the focused beam propagation axis relative to the fibre optical axis. Lengths of 40 cm were used except for fibre D (kagome #7, Fig. 6.3 D-D_2) where we only had a 10 cm sample. Gaussian and LG_{01} coupling efficiency and the transmitted modes were measured for each fibre. Moreover, coupling efficiencies were only measured when we had more than 1 mW of absolute transmitted power. All measurements were done with a 780.24 nm laser.

Table 6.1: Specifications, coupling performance and the guiding characteristics of each hollow core fibre, Rb atom guiding candidates, tested. Fibre A-D are made of silica while fibre E is made of polymer (optical grade PMMA). SEM cross-section images of the fibres are shown in Fig. 6.3.

Fibre Description	Fig. 6.3 ref	Cladding type	Hollow core type	Mode content	Core diameter	Cpl/Guid Gaussian	Cpl/Guid LG01	Fabricator	Date
Kagome #1, large core	A	Kagome	19-cell	Multimode	70 μm	80%, mixed modes	mixed modes	F. Benabid, Bath	2010
Ovoid core, low loss	B	PCF	7-cell	Multimode	20 / 25 μm	34%, mixed modes	mixed modes	F. Benabid, Bath	April 2011
Indian Fibre, commercial sample	C	PCF	7-cell	Single-mode	7.5 μm	55%, Mode preserved	37%, Converted to Gaussian	NKT Photonics HC-800-01	2009
Kagome #7, hex core	D, D2	Kagome	single cell	Multimode	45 / 53 μm	76%, Mode preserved	43%, Mode preserved	F. Couny, Bath	2010
mPOF, PMMA	E	Kagome	7-cell	Multimode	35 μm	44%, mixed modes	34%, mixed modes	R. Lwin, Sydney	2011

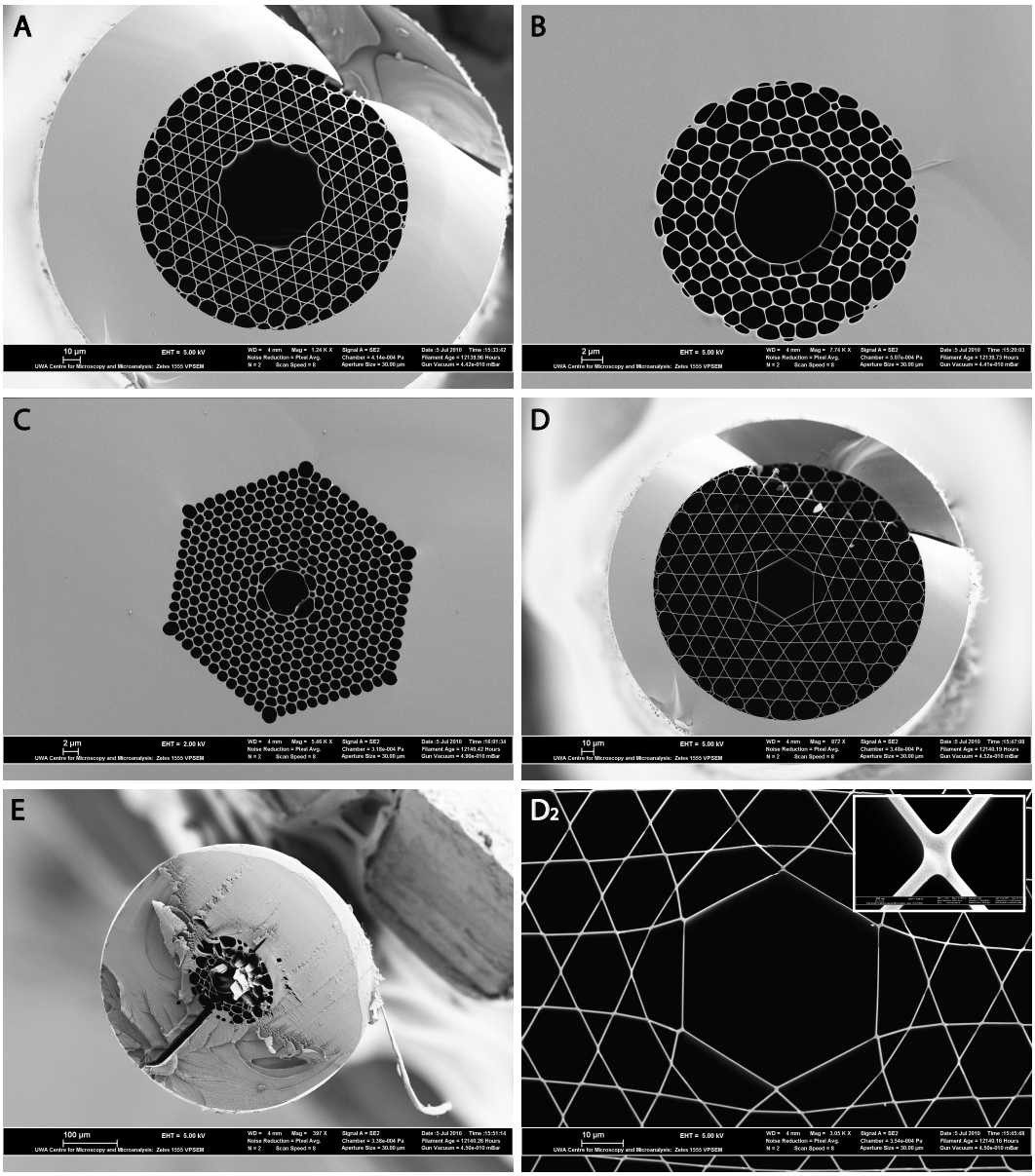

Figure 6.3: SEM cross-section images of the hollow core "Rb atom guiding" fibre candidates. Each of the fibre A-E data and performance is given in Table 6.1.

We were able to obtain optimized coupling efficiency with each fibre but only fibre D preserved the hollow mode and was therefore selected for the rest of the project. It was insensitive to mechanical vibrations, to local heating with a soldering iron and to bending to a radius larger than 10 cm, preserving the guided hollow beam. The coupling was very critical and with a beam path over 3 metres from laser to fibre, it was strongly affected by air currents causing the transmitted mode to oscillate and fluctuate in intensity. When we

used a single-mode fibre to transport the beam closer and a box over our setup, it eliminated these fluctuations.

The mPOF fibre E was causing important mode-mixing, was very sensitive to bend and had a very multimoded guidance even above 1 meter. In the image we see it was not cleaved properly. For mPOF, cutting the fibre under tension using a hot knife is the most appropriate method to get repeatable quality cleave. Fibre A, with the largest core, was the most efficient to transport power but was also slightly mixing the coupled mode in about 10 minima and maxima distributed randomly and sensitive to vibrations and bending. Fibre B was the least efficient without a surprise because of its non-circular core. Finally we found the commercial single-moded PCF (fibre C) and smallest core fibre to be very efficient and robust at guiding a Gaussian beam and any other mode was quickly converted over 1 cm into its fundamental low loss Gaussian mode.

It is particularly challenging to predict whether a given multimode microstructured fibre will preserve or mix modes because it not only depends on the crystal lattice structure but is affected by minute details like the width of the lattice walls, their defects and the surface roughness, all characteristics difficult to simulate accurately. Especially for kagome PCF fibre, the fabrication is as much an art as it is a technique and a design. However, we found that when the Gaussian mode is preserved and easy to couple into the fibre, it is indicative of well-achieved mode separation that could result in preserving higher order modes as well (see Sec. 6.4).

The light guiding capability of fibre D was also assessed by the signal transmission vs. wavelength plotted in Fig. 6.4 provided by Dr. Benabid (University of Bath, UK). This shows the broad guidance of this fibre from 650 to 1200 nm with peak efficiency at 1100 nm. Guidance at 780 nm is approximately 10 dB below the maximum.

6.2 LG beam generation using computer-generated holograms with a liquid-crystal spatial light modulator

In the initial design of the project, the hollow beam generation part looked as if it would be a small part of the project compared with the fibre design and fabrication, producing and focusing cold atoms into this fibre. We started by producing a simple intensity interference mask. The fork mask is the natural interference pattern produced by a hollow beam intersecting a Gaussian beam with angle γ (see Fig. 6.5.A). We printed interference films on transparent paper and with a high resolution 4800 dpi negative photography film printer. We also tested sinusoidal gradient interference films and binary films. We found that laser

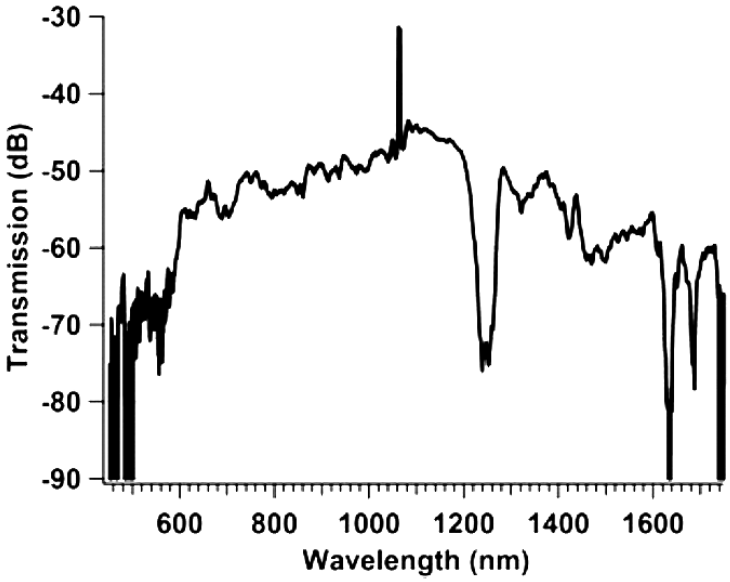

Figure 6.4: Light guiding efficiency of fibre D (kagome type cladding, hollow core diameter 45 μm) as a function of the light wavelength. This fibre guides best from 650 to 1200 nm with peak transmission at 1100 nm.

printed binary masks (Fig. 6.5.B) produced more efficient masks, 48% in order zero and 15% in each of the first order, because of the stronger contrasts between black and white (Fig. 6.5.C). Higher resolution negative photo films had lower difference between transmitted power in "white" and "black" pixels transmitting 85% in 0-order and 5% in each first order. However this technique produced very noisy hollow beams with a -16 dB contrast between the dark and maximum intensity regions measured with a pinhole. The important noise and poor resolution obtained by interference masks led to a change in the approach toward optical phase control techniques, a more efficient way of producing hollow beams.

An optical hollow beam with low purity results in uncontrolled excitation of many core and cladding modes in the fibre [35]. In order to excite a single higher-order mode to a high degree of efficiency (>50%), an holographic mask technique that allows a higher degree of control over the beam order, purity, propagation and spatial distribution was selected. To this end, a phase-only liquid crystal spatial light modulator was used.

Encoding phase and amplitude into a phase-only filter was pioneered by Kirk and Jones in 1971 [144]. They used a holographic technique where they encoded the desired phase directly but used a function of the frequency carrier wave (grating) to encode the amplitude. It worked well with analog filters but was considered un-useable with pixelated discrete phase

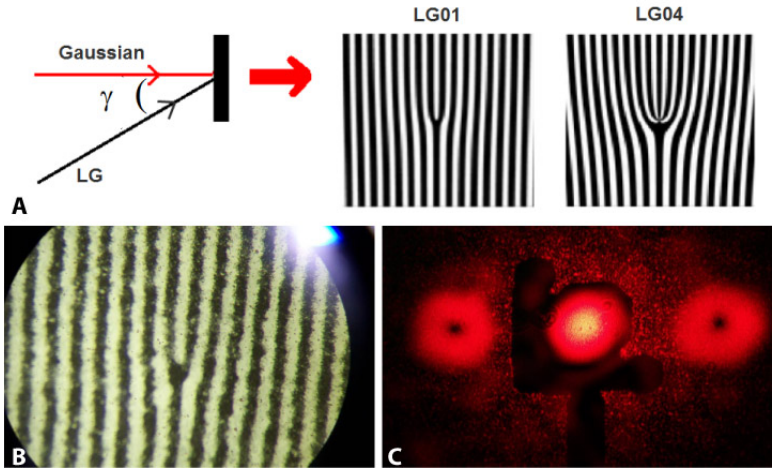

Figure 6.5: Producing LG_{01} using an intensity interference mask. A. Setup used to record the mask interference pattern. Mask is then generated by computer and laser printed at 3000 dpi on a 5 mil polyester film. B. Microscope image of the 3×3 mm, order 1 mask with a 160 μm period. C. Hollow beams produced by a 633-nm TEM_{00} beam passing through the interference mask.

modulators like SLM. It was also not the most efficient technique to transfer power into the light field. Phase-only encoding techniques were regularly used with SLM and it was assumed that LG beams generated with SLM could not achieve mode purities higher than 0.85 [145].

In 1999, Davis et al. [146] developed a technique to produce computer-generated holograms (CGH) that would encode complex, and arbitrary, scalar light fields both in intensity and phase using phase-only transformations without modifying the carrier grating phase. Following this approach, Arrizon et al. [147], [148], [149] developed highly efficient complex phase encoding algorithms by taking into account the discrete array nature of the spatial light modulator.

From all these results, a Laguerre-Gaussian beam generation was implemented and their approach modified using a sinusoidal grating. To generate a single beam with as much power as possible in a single order, a blazed grating phase function in the hologram was implemented. Here the used CGH phase encoding functions are summarised. The mathematical details can be found in Arrizon et al. [147]. 4 CGHs were implemented to compare the formation of LG_{0m} beams:

Type I, based on Davis et al. [146], defines the CGH phase modulation ψ as a product of

a function of the amplitude $f(a)$ with the phase of the desired beam ϕ:

$$\psi(a, \phi) = f(a(x, y)) \cdot \phi(x, y) \tag{6.1}$$

To obtain a valid solution of the CGH phase function ψ, encoding the amplitude $a(x, y)$ and phase $\phi(x, y)$ of the desired beam, a solution to the phase-encoded amplitude function $f(a)$ must be found. An effective method is to express the light field transmitted by the hologram $h(x, y) = exp(i\psi)$ as a Fourier series in the domain of ϕ. For the type I above, the q-th order Fourier coefficient solution is a *sine cardinal* function: $c_q^a = sinc[q - f(a)]$.

Type II phase encoding function (and following III), is based on Arrizon et al. [147]:

$$\psi = \phi + f(a) \cdot sin(\phi) \tag{6.2}$$

Its Fourier coefficient is: $c_q^a = J_{q-1}[f(a)]$. Where J_q is a integer order Bessel function. For example, the desired LG_{01} beam will be found in the first order, q = 1, and the Fourier coefficient encoding its amplitude c_1^a will be a zeroth-order Bessel function J_0.

Type III is:

$$\psi = f(a) \cdot sin(\phi) \tag{6.3}$$

Its Fourier coefficient is: $c_q^a = J_q[f(a)]$. Following the above example, $c_1^a = J_1[f(a)]$. We will further discuss these CGH types below, when presenting the results obtained with the SLM.

Finally the type IV is based on Kirk and Jones [144], where it is mathematically different to type I-III because it encodes amplitude into the grating instead of the phase function but the encoding approach is most similar to type I because it uses the *sine cardinal* function.

Fig. 6.6 plots the different functions that are composed together to obtain the computer generated hologram as a complex construction of phase and amplitude of a LG_{01} beam. The target amplitude is a function that ranges from 0 to 1 while the phase is the characteristic helicoidal pattern of a Laguerre-Gaussian beam. In a first order azimuthal beam, there is only a single 2π phase shift in a 360° revolution. The carrier phase grating is a product of a blazed grating function with the target phase of the beam, which creates a forked mask similar to the one in Fig. 6.5. The bottom row of Fig. 6.6 is the resulting CGH projected on the SLM to produce the target beam using algorithms types I to IV (per discussion above).

In order to assess the accuracy of the CGH projected on an SLM to produce a Laguerre-Gaussian beam the mode purity of the light field must be analysed. The mode purity is evaluated numerically by comparing the electric field amplitude with the theoretical beam profile desired. Ando et al. [150] compared the ability of the 4 types described above to generate a pure LG_2^1 beam (see results in Fig. 6.7). They found that types I-III generate

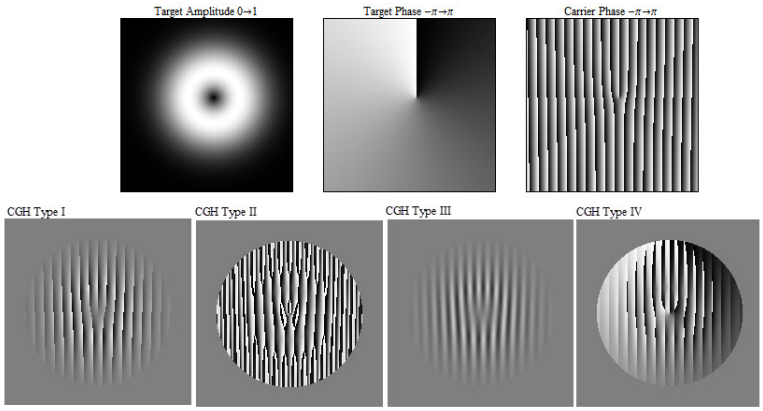

Figure 6.6: Stages into the generation of LG_{01} CGH mask. The top row shows the target amplitude and phase and the blazed grating encoded with the target beam phase. The bottom row plots the result from the processing of the target amplitude and carrier phase grating according to one of the 4 types presented.

hollow beams with mode purity between 0.92 and 0.996 for grating periods between 5 and 12 pixels with type II being generally better across that range. Kirk's method (type IV) yields better mode purity than type I-III and close to 0.98 when the carrier grating period was below 5 pixels (see Fig. 6.7). However, type IV has also poor conversion efficiency compared to the other methods. These results show that using these types with their optimal period grating on a SLM can produce a pure single-mode Laguerre-Gaussian beam ($\eta > 0.99$). They also confirm that lower order beams have better mode purity generally.

A spatial light modulator (HEO1080P by HoloEye, Germany, loaned by Prof. Arrizon from INAOE, Mexico), which is a model without a high efficiency mirror was used for this purpose. Figure 6.8 illustrates the 2D CMOS array which diffracts the light from the incoming beam after it is transmitted by the cover glass, the electrode and the liquid crystals.

With a zero phase shift mask, a 40% loss was measured, so that only 60% of the input power is reflected. The phase bandwidth of the hologram as rendered by the SLM is much lower than the pixel resolution of the SLM because of the limitation in resolving sharp phase changes. This limitation comes from the effect of the electric field produced by a pixel on its neighbors. Thus, phase dislocations/strong contrasts in the hologram, as in a blazed grating implementation, lead to errors in the rendering of the holograms by the twisted nematic liquid crystals of the display. So a less efficient sinusoidal grating was used to separate the desired beam into two equal orders (+1, -1), although only a single order was used. The best conversion to a LG_{01} beam in +1 order was 24% using Prof. Victor Arrizon type II "Bessel

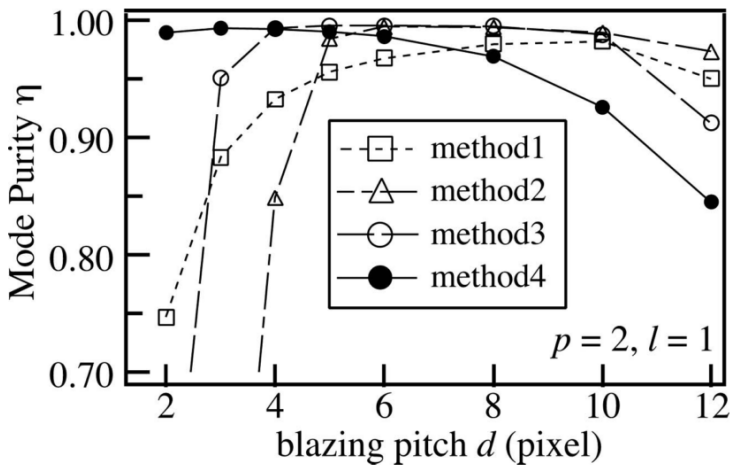

Figure 6.7: Comparison of complex valued phase-only computer generated holograms produced on a liquid crystal spatial light modulator. Mode purity η of beam LG_2^1 is evaluated numerically as a function of the grating period d on the SLM measured in pixels. Figure from [150].

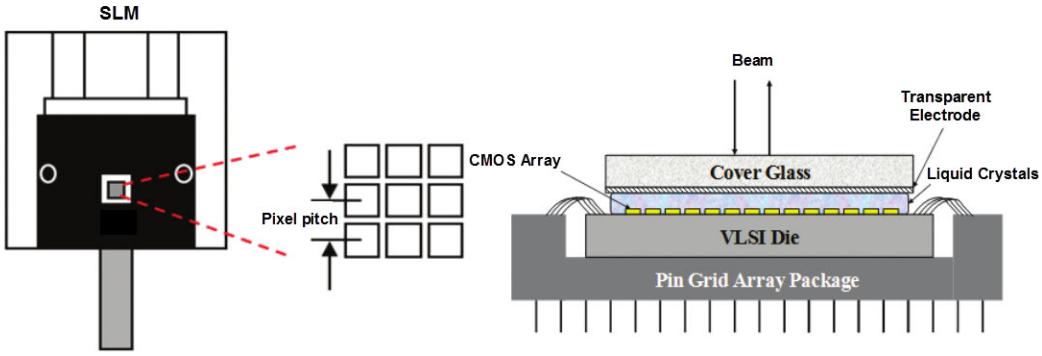

Figure 6.8: Anatomy of a liquid crystal spatial light modulator showing the CMOS array causing diffraction.

zero" hologram. Considering the 40% loss from the diffraction off the phase control array, only 14% of the input beam power was transferred into the hollow beam. The SLM had to be upgraded to a more efficient unit because of this low efficiency.

With the new SLM (model: XY Nematic Series 512 at 1064 nm by Boulder Nonlinear Systems (BNS), Colorado, USA) much higher efficiency with a 100% fill factor due to the high efficiency mirror was achieved which prevents diffraction of the laser beam on the electronic CMOS array that controls the liquid crystal orientation. This new SLM had a much higher

phase bandwidth and was able to produce high phase contrasts from one pixel to the next, which made it possible to generate efficient blazed gratings in the hologram. Its display was 7.68 mm square with 512 pixels for a pixel pitch of 15 μm. The damage threshold for this device is high (5W/cm^2), which translates to 157 mW for a 2 mm diameter beam. However the liquid crystal orientation can be affected by local heating due to the laser beam power slightly below that limit.

However, this SLM was an economy "B model" which had a non-uniform liquid crystal display. At a wavelength of 780 nm, close to 4π phase modulation across the full modulation range of the SLM was possible. A uniform polarised illumination of the SLM display (when it was turned off) was performed and is shown in Fig. 6.9. It was easy to see that the display's uneven thickness was important at this wavelength causing destructive interference, hence the dark fringes observed in the reflected beam. A simple solution was to limit the beam size to 3 mm and use the SLM off-centre. A visual c# program allowed the position of the centre of the CGH to be moved to wherever it was needed on the display for that purpose but also for pixel-by-pixel alignment which is easier to control by software than by steering the beam.

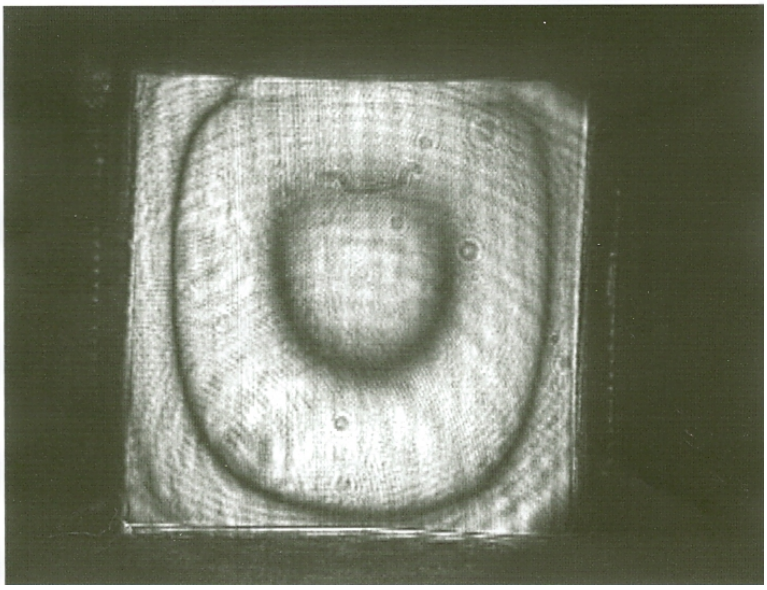

Figure 6.9: Capture image of the SLM display uniformly illuminated with vertically polarised light at 785 nm.

The BNS SLM had also an enhanced phase resolution encoding of the hologram in 16 bits using a 24 bits RGB signal. The image was divided into 2 channels of 8 bits, where the green signal was displayed in the 8 most significant bits and the red signal used the 8 least

significant bits. Figure 6.10 shows the resulting type II LG_{01} 16-bit greyscale CGH image converted to a 24-bit RGB image.

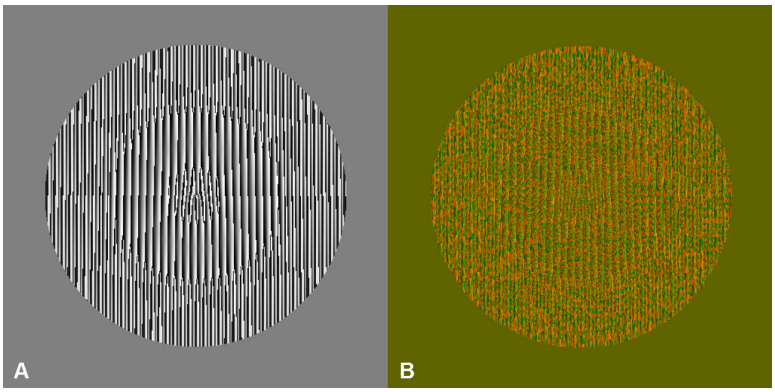

Figure 6.10: Comparison of a LG_{01} type II CGH with an 11-pixels period encoded in a 16-bit greyscale image (left) with its 24-bit RGB conversion (right). Note the absence of blue in the image so there is only 16-bit of data.

6.3 Stage H: experimental setup for generation and coupling of the hollow beam

One aspect that had not been addressed in Ando et al. [150] study and which is of major importance for atom guiding is the power conversion efficiency into the hollow mode. Once the CGH was able to produce LG beams, the power conversion efficiency of the different types of CGHs were compared. The stage H, illustrated in Fig. 6.11, was built on the same optical table as the rest of the MOT. For free space atom guidance experiments, the output of stage H was fed directly underneath the MOT chamber through the viewport or coupled into the fibre inside the chamber using a final plano-convex lens and a 45° mirror on a kinematic mount (not shown). After the laser isolator, the beam was circularised and resized to achieve optimal coupling into the SMF (HP780) using focus-adjustable collimators. The output produces a 1.5 mm beam that is scaled 2× to a 3 mm diameter Gaussian beam with a telescope made of a 100-mm focal plano-convex lens (PCX) and a 50-mm plano-concave lens (PCV). The beam is vertically polarised with a HWP and has excellent polarisation purity to be used directly on the SLM. Optionally, a linear polariser could be inserted before the HWP. The beam is resized (optionally) and steered by the CGH on the SLM display and the reflected modes are propagated 60 cm before being far enough to be separated using a 0.8 mm iris as a mode selector. An optional telescope was used to enlarge the beam for free space guidance, however, when coupling into fibre D, the best efficiency was with the 3 mm

beam and no telescope before the final coupling PCX lens. After the fibre, the beam shape was monitored and power transmitted simultaneously using a HWP and PBS at the output to only redirect 1% of the beam toward the camera.

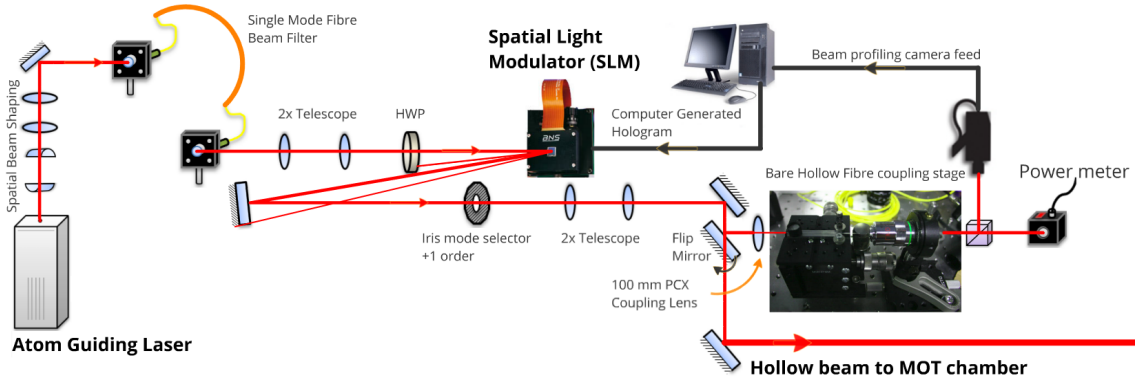

Figure 6.11: Stage H - Experimental setup to generate and couple a hollow beam into a hollow fibre or feeding the beam directly into the chamber.

Figure 6.11 represents the final setup used to angle the SLM surface 5° from the normal to the input Gaussian beam. However, initially the beam was coupled into the fibre using the SLM display normal to the input beam. The reflected modes were separated from the input beam by using a non-polarising beam splitter (NPBS), the last optical element inserted before the SLM. This setup produces very circular modes with the high efficiency; but the NPBS also causes 75% loss. Normally an anti-reflection coated polarising beam splitter (PBS) is used with a quarter-wave plate (QWP) to achieve less than 5% loss. However, a PBS cannot be used with an SLM because it requires the input beam to be linearly polarised at 0° (vertically), so it forbids the use of a QWP to separate the reflected modes by shifting its polarisation.

Fig. 6.12 shows all the orders reflected by an LG_{01} CGH of type I, II and III imaged with JAI-CVM50 CCD camera with fixed exposure and gain from one CGH type to the next. The camera was placed a few milimetres behind the focal point of a modified setup where we placed a 1× telescope in the beam path after reflection from the NPBS. Along with the image data, Table 6.2 lists the CGH relative power distribution among the orders. Note that the target beam is designed to be diffracted in the first order. Higher orders will feature beams of a higher order as well (±2 order = LG_{02}, etc.).

In the setup, each mask was carefully exposed to the same input beam power so that efficiencies could be compared on an optical power basis as well. Type IV was eliminated

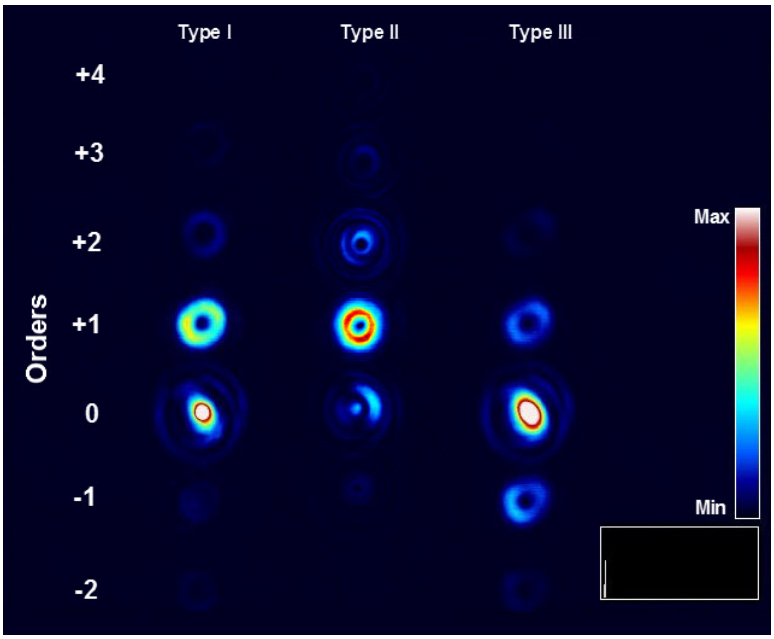

Figure 6.12: Imaging of LG_{01} CGH diffracted orders for type I, II and III. Input beam power, beam angle normal to the surface, CCD camera exposure and sensor gain was kept constant across measurements. Relative diffraction efficiencies are listed in Table 6.2.

early on because of poor conversion efficiency and low mode purity with high resolution CGHs. From the data, Type II is by far the most efficient CGH both in terms of mode quality and power conversion efficiency into target mode (52%). This was expected because of the "Bessel J_0" encoding of the phase function. With the Bessel function, higher orders decrease sharply in intensity resulting in very little power being transferred into orders higher than 1 in the hologram. However, even with filtering of a single order in the Fourier plane, there is inevitable cross-talk from higher orders into the first order due to the nature of the Fourier transformation of phase signals, which is a convolution of the signal with itself. This results in a weak first order frequency noise that cannot be eliminated.

We can see that conversion efficiency into the +1 order is also down to 45%, reduced by 7%, when the beam is incident at 5° to the SLM surface. The zeroth order is also reduced proportionally by the same amount which is more likely caused by a combination of loss and power transfer into higher orders. However, this loss is largely offset by the gain in eliminating the need for the NPBS (which caused an additional 75% power loss).

Ando et al. [150] used a top hat beam (or flat-top depending on your inclination), which is ideal in terms of conversion efficiency for a CGH producing a hollow beam. However, when considering the whole system, the small efficiency gain from a top hat beam is offset by the

Table 6.2: Diffraction efficiency of CGH type I, II, II at 5° and III for LG_{01} beam. The target beam is designed to diffract in the first order.

Orders	Type I	Type II	Type II at 5°	Type III
+2	4%	9%	10%	1%
+1	25%	52% (10% laser input)	45% (35% laser input)	8%
0	63%	18%	10%	80%
-1	2%	2%	1%	8%

loss in converting the Gaussian to a top hat beam using a special density filter. This could be a performance upgrade to consider in the future by doing this conversion efficiently with a combination of aspheric lenses. Currently, SLMs can generate a good top hat beam.

In the previous measurements, for optimal mode purity, a carrier grating period of 11 pixels was used. To come to this conclusion, the LG_{01} beam generation with CGH type II was used and compared the +1 modes with only the carrier grating period varying from 3 to 12 pixels. Resulting beams are compared side-by-side in Fig. 6.13. For this CGH we can see that the mode shape is best when the grating period is from 10 to 12 pixels. Above 12 pixels the target mode starts collecting noise from its neighboring modes.

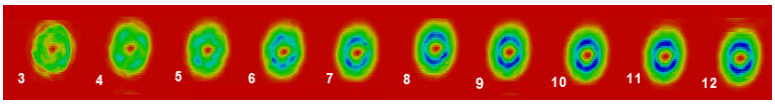

Figure 6.13: Imaging of LG_{01} beam generated with a type II CGH with grating periods varying between 3 and 12 pixels. Better resolved beam is achieved when the grating period is between 10 to 12 pixels. In this colormap, red is the minimum intensity (0) on the color scale and progress to blue at the maximum intensity (255).

6.4 Coupling LG beams into a large core hollow kagome fibre

In the first section of this chapter, a review of the fibres tested was presented and it was found that fibre D was the only one supporting a single higher-order hollow mode. In this section these results will be explained in greater detail to help guide future researchers into

reproducing and improving the results.

Because of the limitations of the thick and imperfect SLM display model used in these experiments, the input beam diameter on the SLM was limited to 3 mm. Controlling the output beam, with a mask support radius of 2.5 mm for the CGH, it produced a hollow beam of 5.1 mm in $1/e^2$ diameter. The beam profile, recorded as the Gaussian distribution variance σ of the intensity profile, was measured at 1250 μm with a Thorlabs rotating slit beam profiler as well as with our CCD camera and our own software beam profiler.

A 50/50 NPBS was used in front of the SLM in order to produce the best beam quality. Having the beam normal to the surface minimizes phase shift encoding errors. For mode separation, instead of using a 60-cm long propagation distance as shown in Fig. 6.11, a 1$\times$ telescope was inserted composed of 2 $\times$ 50-mm PCX lenses with a 200 μm pinhole at their common focal point. An AR-coated 100-mm PCX lens was used to couple power into the fibre core.

Further efforts were deployed to produce a more efficient coupling. The first step was to ensure that the laser beam was horizontal. After the last mirror before the coupling stage, 3 iris evenly distributed over 2 metres were inserted, all set at precisely the same height. The laser beam level and angle were aligned using two mirrors on kinematic mounts. Irises were swapped during alignment to make sure that they were at the same height, adjustments were performed. After alignment, a lens was inserted after the last mirror and with two of the irises kept in position, the lens x-y position (in the plane normal to the laser propagation) was adjusted to ensure that the laser beam was going through the optical centre of the lens.

Then, the coupling stage was installed at approximately 100 mm from the PCX lens. The fibre was mounted on a v-grooved bare fibre platform fixed to a *MicroBlock 3-Axis Positioner w/ Differential Micrometre* (Thorlabs MBT616D). An iris fully closed at 10 mm from the fibre input was inserted. Its role was to prevent us from "walking" the beam out of alignment. A modified "walk-the-beam" alignment technique was utilised with the additional steps of re-centering the fibre in x-y plane and moving it forward-to-backward in the optical axis. Z-translation was then used to observe the alignment of the beam relative to the fibre core optical axis. This was particularly helpful to achieve a precise in-axis coupling of the beam power. A pure single mode (Gaussian or hollow) was excited when the movement in z did not shift the beam out of alignment in the core over a few millimetres.

During alignment the Gaussian fundamental (LG_{00}) mode and the LG_{01} mode were swapped and "walked" into a single guided mode. The fundamental mode reached 76% transmission through 10-cm of fibre D with a 2.7 mm diameter input beam. Once achieved,

the coupling was fairly resistant to variations in input beam size, maintaining 68% efficiency for 1.8 mm to 73% efficiency for 3.2 mm diameter. Figure 6.14 shows the input LG_{01} beam (top row) with unsaturated (left) and maximum power exposure (right). The bottom row displays the transmitted hollow beam after 10-cm through the fibre, also unsaturated (left) and saturated (right). The LG_{01} mode was best coupled at 43% through fibre D for an input of 5.1 mm. Similarly, good coupling efficiency was obtained across a range of input sizes from 4 mm input dia. (38%) to 6 mm input dia. (40%), with efficiency falling off sharply outside this range. The hollow beam diameter was controlled by the CGH support radius r parameter, from 1.5 to 3.0 mm, within our CGH generation software.

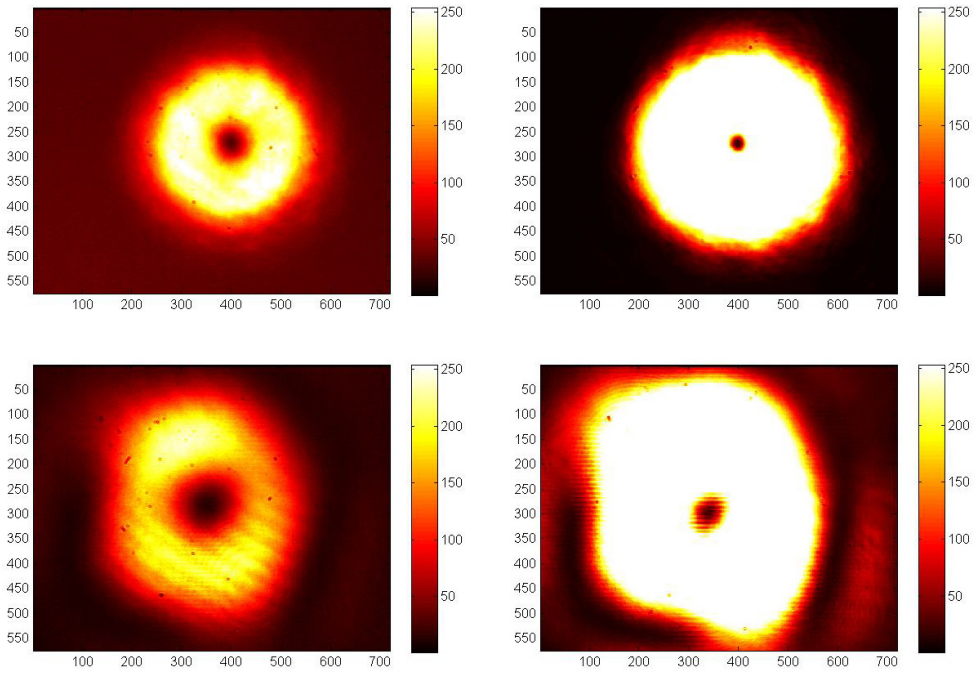

Figure 6.14: Imaging of the input 5-mm LG_{01} beam after the SLM and before the final coupling lens (top row). After coupling this beam with a 100-mm PCX lens through fibre D, the transmitted beam is attenuated and imaged on the CCD camera (bottom row). Left column shows the beams when imaged unsaturated using density filters. Right column shows the extreme of imaging saturation, with less filtering, enhancing the darkest parts of the beams.

Coupling the beam with 75-mm and 125-mm PCX lenses using only the Gaussian mode was inefficient, which was indicative that the native mode field diameter (MFD) of this fibre

was not well-matched. Not having a MFD specification to compare it to, a similar commercial fibre (fibre C) was used which had a MFD of 5.5 vs. 7.5 μm core (or 73% of the filling of the core diameter). The most efficient Gaussian beam radius was found to be around 1.5 mm for fibre D, the calculated spot size with a 100-mm focal length lens, using Gaussian optics formula:

$$\omega_0' = \frac{\lambda f}{\pi \omega_0} \tag{6.4}$$

Where ω_0' is the spot size radius, f is the focal distance of the coupling lens and ω_0 is the input beam radius before the lens. The depth of focus is the distance $2z_0$ (on either side of the focus) over which the spot size increases by a factor $\sqrt{2}$:

$$2z_0 = \frac{2\pi\omega_0'^2}{\lambda} \tag{6.5}$$

From these equations, we calculated a focal spot diameter of 33 μm. Assuming the same 73% MFD-to-core ratio as from other PCF, we obtain a core size of 49 μm. This is exactly the average core diameter of fibre D, which proved that the 100-mm PCX with the 3-mm Gaussian mode input diameter matches exactly the MFD of fibre D. The depth of focus is 2.1 mm, which is indicative of a focal distance that is not too critical to achieve good coupling.

For the hollow beam generation, the LP_{01} mode transmitted through a single mode fibre as an input beam was selected on the SLM, because it was symmetrically round. The SLM was normal to the input beam propagation and produced a very circular hollow mode (x-to-y diameter ratio was less than 2% difference). To dramatically reduce power loss, the setup was re-arranged and the blazed grating direction of the SLM set at a 5° angle. Despite losing a bit of power efficiency (-7%), it cut down on losses post-SLM due to the removal of the NPBS. However, the hollow beam became slightly oval, with x-to-y variations up to 8%. When coupling this hollow mode to the fibre, a better efficiency (54%, +11% improved) was achieved but with fewer modes, hence the improved power coupling. It was found that beam symmetry was a key parameter here; however 8% is not too large a variation, suggesting it could be corrected optically, with cylindrical lenses, without having to use an NPBS.

Additionally, we coupled LG_{11} but the single mode transmitted at the end of the fibre was a LG_{01}. It failed to guide a single hollow mode with azimuthal order $\ell > 1$. In Fig. 6.15, we show the LG_{02} beam at the input (left) and its transmitted mode though fibre D (right). We found that the transmitted distribution closely matched that of a Hermite-Gaussian HG_{11} mode in that case.

Imaging of the beams was performed with the JAI-CVM50 CCD camera that had a non-AR coated protective window before the sensor which caused important beam interferences

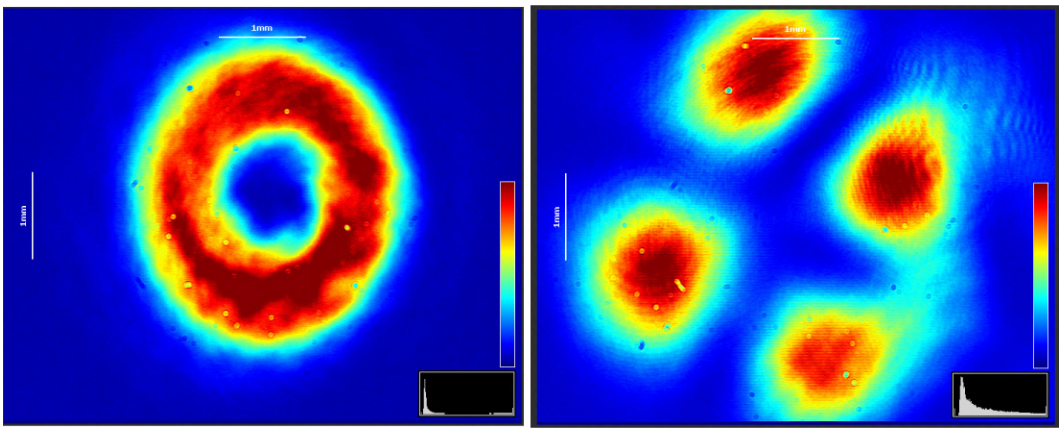

Figure 6.15: Best attempt at coupling a higher order mode in fibre D. (left) The input LG_{02} beam generated. The black-and-white image was color coded by our beam profiler software to enhance the scale. (right) The transmitted beam in a quadrupole power distribution reminiscent of the HG_{11} mode.

like a linear grating. Its period and orientation depended on the angle of the beam relative to the sensor window. A beam profiler ascertained that the beam quality was a lot better than appears from the imaging results generally showcased in this Thesis.

The camera also had quite a limited dynamic range which required constantly attenuating the input beam using density filters which also made the beam distribution noisier with more interference fringes and diffraction points due to dust and optical defects. The dynamic range and attenuation made small beam power variations appear larger than they really are. In Fig. 6.14, is shown (left) the unsaturated image of the transmitted hollow beam at 1% of its total power, compared with an image of the beam at 50% transmission (right). By comparing the saturation power of points in the image as the power is increased, the azimuthal power variations of the transmitted hollow beam is calculated to be between 5 to 8%.

In order to mount the fibre vertically, inside the chamber, a 100-mm long steel fibre holder was designed and fabricated. Figure 6.16 shows renderings of the 3D CAD model on the left. The top rendering illustrates how the fibre holder is designed to integrate into the complete assembly where we used the CAD model from our chamber's manufacturer. The holder attaches in the viewport grooves using the "groove grabbers" part from the manufacturer also (in gold). The large collimated laser beams were also placed in the model to ensure the holder is not interfering with the beam propagation but will deliver the fibre as close to coupling position (which was designed to be at 10 mm from the MOT centre). To minimize optical disruption, the fibre extended 5 mm beyond the tapered end of the holder. At the

bottom, the fibre is aligned with the end of the holder and comes as close as 2 mm from the bottom window viewport. The bottom left rendering shows the view of the fibre in the holder from the bottom viewport and the input beam's point-of-view. The part was designed so that the fibre, when sitting in the v-groove is aligned in the centre of the viewport within the precision of the fabrication from *UWA physics and engineering workshop*. Figure 6.16 (right) is a photo of the completed fibre holding tower with its groove grabbers mounted.

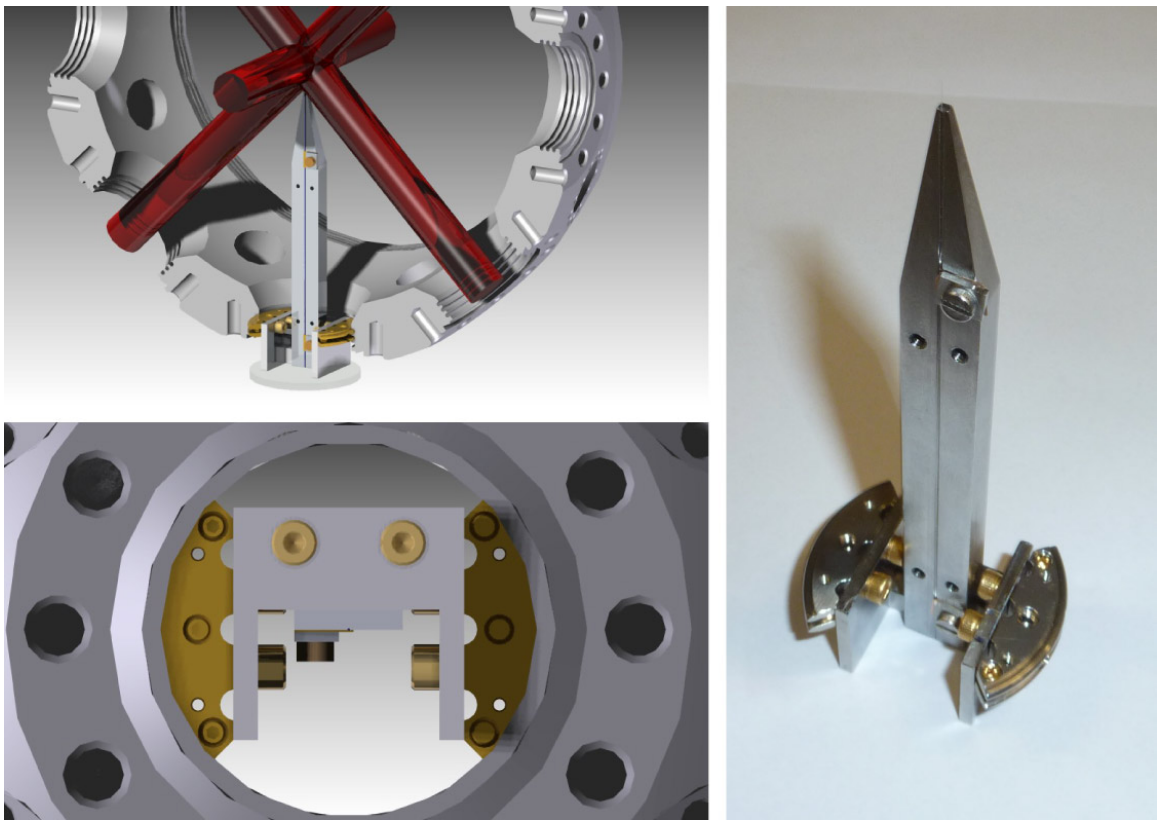

Figure 6.16: Design and fabrication of the fibre holder used to mount the fibre vertically up to 10 mm below the MOT and in the geometric centre of the viewport. (Top-left) CAD rendering (in Siemens Solid Edge) of the 100-mm high fibre holder mounted with groove grabbers in the octagon chamber assembly. Cooling beams were also placed to ensure no parts of the holder were disrupting the beam's propagation. (Bottom-left) Same rendering in a bottom view corresponding to the coupling input and showing the fibre in the geometric centre of the chamber's viewport. (right) Photo of the fabricated fibre holder with its groove grabbers.

The holder was designed as vacuum friendly with all tapered holes going through the part completely. The four holes on either side of the groove were designed to help mount a curved

grooved metal piece that will be used to test atom guidance in a fibre when bent to a precise curvature radius. The holder also uses no rubber, polymer, grease, glue or magnets to hold the fibre in the groove because of degassing issues critical to high vacuum experiments in atomic physics. The fibre is held by a 0.5 mm sheet of spring copper that is curved and held to the fibre holder with a square nut and screw. Ideally the fibre holder and all screws should be silver coated, minimizing outgassing in vacuum, but no parts in the prototype were.

One of the critical steps that was left before vacuum mounting of the fibre, was removing the fibre polymer jacket to better minimize degassing to the chamber. An efficient way of doing this without risking any damage to the cladding is by burning the polymer. However with a hollow fibre of large core, there were concerns of filling the core ends with soot that would then disrupt coupling and atom transmission. One way of solving this would be to seal each end in solid silicone, burn the jacket off, and then remove the silicone and a millimetre of jacket left at each end with a razor blade. This technique should be validated with less precious and rare fibres of similar or larger core sizes. Also the ends should be imaged using a SEM to ensure no residues are left in the core after the final cleaning step.

This concludes our efforts into developing the techniques to prepare for coupling and guiding cold atoms into the hollow core fibre.

CHAPTER 7 CONCLUSIONS

During the course of this thesis, blue detuned atom guidance in space has been demonstrated in a collimated beam as well as through a tight focused hollow beam. In order to achieve these goals, a MOT had to be built from scratch (with the concentrated work of Dr. Philip S. Light). To support this work, a model that allows to simulate dense cold atoms to a temperature of $10\,\mu$K was developed. This work was done to allow the complex simulation of cold atomic coupling into a hollow fibre using only gravity and a single diffracting hollow beam and identifying the best conditions to achieve it. A hollow core microstructured silica fibre was identified and demonstrated to support guidance of a single first order hollow mode through a very efficient coupling technique. To achieve this, it used a high purity LG_{01} mode generated with high efficiency using a computer generated hologram rendered on a liquid-crystal spatial light modulator.

7.1 Summary

A simulation framework was developed based on a unique, particle-based Monte Carlo approach for atom cooling and guiding experiments. Our model implemented in 3D space for the first time to our knowledge, momentum diffusion, a known but previously ignored heating (loss) mechanism. The model achieved realistic results and predictions such as the temperatures of the MOT in the linear regime and heat-related losses of atoms in a gravito-optical trap. Most importantly the objective of the simulation model was to support experimental research in testing new geometry and unorthodox experiments which are very difficult to simulate in quantum mathematical models or with empirical formulae. The model was applied to the simulation of the coupling of cold atoms from a MOT optically funnelled into a hollow core fibre guiding a single mode hollow beam.

This approach to modelling also demonstrated the quality of being able to represent cold atoms using multimedia, in which complex atomic behavior such as capturing atoms in optical molasses (without a magnetic field) or heat losses taking the form of atoms spinning out of a blue detuned laser funnel could be visualised. Hence, there has been strong interest from a scientific software company to continue the development toward professionnal cold atom simulation software for both academic and research applications.

At the same time a complete MOT system was built from scratch with features such as:

- MOT octagon vacuum chamber with 8 viewports and 2 large side windows for improved

optical access

- Six optical cooling beams delivered into the chamber directly from single mode PM fibres at 45° from the plane which frees the x, z axis through larger viewports for detection imaging, probing, atom control beams and easier fibre mounting and alignment.
- A cooling laser locked to the rubidium cooling frequency using modulation transfer spectroscopy
- A re-pumping beam slave-locked to the cooling laser using a heterodyne beatnote with a low frequency VCO generated offset to lock to the repump frequency. This strong slave lock allowed the use of a less stable, less expensive, in-house laser diode system for optical re-pumping
- Anti-Helmholtz coils built to produce close to ideal spherical quadrupole magnetic field to be intrinsically fast with only 21 turns and very low inductance of only 0.28 mH. These can produce field gradients of 4 G/cm at 35 A and could produce over 10 G/cm at 100 A. To achieve sufficient cooling, hollow copper tubes were used to carry water as an active cooling system.
- Three pairs of Helmholtz field cancelling coils to produce a local field of 0.4 G along each axis in the centre of the chamber, easily sufficient to cancel the earth's magnetic field and stray fields from the ion pump
- Remote controls of coils, camera triggers, EOM, AOM and mechanical shutters to perform experiments controlled through an open hardware Arduino microcontroller board which simplified and accelerated development of experiments automation and data acquisition system
- Development of 3 imaging techniques: cooling beam fluorescence, probe fluorescence and shadow imaging each with their own advantages to support the current and future experiments

With this system a stable MOT of ^{85}Rb with 10^7 atoms was produced and a polarisation gradient cooling scheme implemented to obtain a cold atom cloud down to 9 μK. The guided cold atoms released from the MOT, and later the cold atom molasses through a horizontal red detuned Gaussian beam and vertical blue detuned hollow beam, achieved results similar to those found in the literature [57].

The critical experiment to prepare for optical coupling of atoms into a hollow fibre was also realised. We demonstrated funneling and coupling of atoms through a focused hollow beam that followed a similar divergence and coupling distance to the experiment with a fibre. The experiment used 3 different detunings (optical forces) and we successfully observed transmitted, lost and trapped atom groups as predicted in our model [36]. The coupling results were in excellent agreement with the simulations and it was found that both showed that the optimal coupling force was at 30 GHz. The model was also used as a diagnostic tool when coupling was not working, therefore demonstrating its usage in supporting experimental work with cold atoms in future control experiments.

Simultaneously, a fibre to support rubidium atom guidance over long distances was identified and tested at UWA. Several silica fibre candidates were tested and identified for the purpose. Hollow core, single-cell defect, Kagome crystal cladding silica fibres were shown to support a single-mode LG01 mode necessary to guide atoms.

LG_{01} hollow beams were generated with a spatial light modulator by implementing complex valued phase-only computer generated holograms. Since significant power is required to guide the atoms in the far blue-detuned regime, a Gaussian to hollow-beam conversion efficiency of over 50% was achieved with this technique as well as a 35% global efficiency (from SLM input beam to coupling the hollow beam in the chamber). In addition, a coupling efficiency of LG_{01} mode at 43% (and 76% for the Gaussian mode) was achieved while fulfilling the requirement for coupling with a long focal length lens. This is necessary to keep all the optics outside the vacuum chamber when coupling to the fibre inside.

7.2 Future directions

The work in this Thesis began with designs and developed techniques in microstructured polymer optical fibres which led to several publications and contributions to the field [139, 141, 142] that finally ended up outside the scope of this Thesis with the change in direction in our application to better performing hollow-core silica fibres (through our collaboration with *Bath University, UK*).

For future developments, it would be useful to extend the work presented in this thesis to develop a fibre that could achieve better mode separation, which would facilitate the launch conditions necessary to excite a single hollow mode. To that end, a photonic band-gap cladding would be more efficient than a Kagome cladding which intrinsically supports lossy modes.

Higher order modes have been proven to cause less heating, so a fibre that could support a

second order or third order hollow beam with low loss would be useful into achieving superior atomic guidance over long distances. Our model showed that higher order modes diffract more strongly which reduces the optimal coupling distance while increasing the amount of compression heating in the funnel. A possible way to reduce that, would be to keep two pairs of cooling beams in the horizontal plane, with much reduced intensity, during the optical funnelling stage to mitigate some of the compression heating occurring.

Aside from demonstrating the long distance guidance of atoms in a hollow core fibre (not just a capillary), we would seek to test how well the atoms can be guided in a bent fibre, something that has not been done since the work of Renn et al. [49, 63, 64] at JILA in Colorado.

The software developed in this thesis could be easily adapted to model a dark hollow beam trap or the effect of a hollow beam replacing one of the six cooling beams. Fundamental statistical physics research could also be done to further develop its core algorithm and extend its functionality beyond the linear regime. We see atom-atom interactions as a next logical step into developing the physical effects that will be taken into account.

The next step in the evolution of this model could be even more interesting with regard to studying the performance and developing better schemes. Particularly, these specific improvements are suggested:

- Developing a semiclassical model to implement viscous dipolar heating
- Integration of the atom coupling simulation into the MOT simulation
- Capability to simulate more complex atom coupling schemes like optical elevator by adding planar cooling beams, sheet beams and magnetic fields
- Replace ideal Laguerre-Gaussian guiding beams by the real intensity distribution of the fibre and modelling its diffraction out of the fibre.
- Modelling curved fibres and simulate guidance performance
- Integrate transit time analysis to post-simulation routines to produce a figure of expected fluorescence over time at the fibre output

We look forward to the development of this Thesis into future works to contribute in the field of cold atom physics and help achieve new milestones in the fibre guidance of atoms.

REFERENCES

[1] M. Takeda and M. Kujawinska, "Lasers Revolutionized Optical Metrology", *SPIE Professional*, no. October, 2010.

[2] C. J. Davisson, "The Diffraction of Electrons by a Crystal of Nickel", *Bell System Technical Journal*, vol. 7, Jan. 1928, p. 90–105.

[3] H. Rauch and S. A. Werner, *Neutron interferometry*. Oxford: Clarendon Press, 2000.

[4] J. T. Cremer, M. A. Piestrup, C. K. Gary, R. H. Pantell and C. J. Glinka, "Biological imaging with a neutron microscope", *Applied Physics Letters*, vol. 85, no. 3, 2004, p. 494.

[5] R. Cook and R. Hill, "An electromagnetic mirror for neutral atoms", *Optics Communications*, vol. 43, Oct. 1982, p. 258–260.

[6] J. Bjorkholm, R. Freeman, A. Ashkin and D. Pearson, "Observation of Focusing of Neutral Atoms by the Dipole Forces of Resonance-Radiation Pressure", *Physical Review Letters*, vol. 41, Nov. 1978, p. 1361–1364.

[7] J. Nellessen, J. Werner and W. Ertmer, "Magneto-optical compression of a monoenergetic sodium atomic beam", *Optics Communications*, vol. 78, no. 3-4, 1990, p. 300–308.

[8] T. Pfau, C. Kurtsiefer, C. S. Adams, M. Sigel and J. Mlynek, "Magneto-optical beam splitter for atoms.", *Physical review letters*, vol. 71, Nov. 1993, p. 3427–3430.

[9] D. Keith, M. Schattenburg, H. Smith and D. Pritchard, "Diffraction of Atoms by a Transmission Grating", *Physical Review Letters*, vol. 61, Oct. 1988, p. 1580–1583.

[10] R. M. Godun, M. B. D'Arcy, G. S. Summy and K. Burnett, "Prospects for atom interferometry", *Contemporary Physics*, vol. 42, no. 2, 2001, p. 77–95.

[11] T. L. Gustavson, P. Bouyer and M. a. Kasevich, "Precision Rotation Measurements with an Atom Interferometer Gyroscope", *Physical Review Letters*, vol. 78, Mar. 1997, p. 2046–2049.

[12] C. Champenois, M. Büchner and J. Vigué, "Fringe contrast in three grating Mach-Zehnder atomic interferometers", *The European Physical Journal D - Atomic, Molecular and Optical Physics*, vol. 5, Feb. 1999, p. 363–374.

[13] A. Peters, K. Y. Chung and S. Chu, "High-precision gravity measurements using atom interferometry", *Metrologia*, vol. 38, Feb. 2001, p. 25–61.

[14] C. Ekstrom, J. Schmiedmayer, M. Chapman, T. Hammond and D. Pritchard, "Measurement of the electric polarizability of sodium with an atom interferometer", *Physical Review A*, vol. 51, May 1995, p. 3883–3888.

[15] M. H. Anderson, J. R. Ensher, M. R. Matthews, C. E. Wieman and E. A. Cornell, "Observation of Bose-Einstein Condensation in a dilute atomic vapor.", *Science*, vol. 269, July 1995, p. 198–201.

[16] J. Dalibard and C. Cohen-Tannoudji, "Laser cooling below the Doppler limit by polarization gradients: simple theoretical models", *Journal of the Optical Society of America B*, vol. 6, Nov. 1989, p. 2023.

[17] C. E. Wieman, "Inexpensive laser cooling and trapping experiment for undergraduate laboratories", *American Journal of Physics*, vol. 63, no. 4, 1995, p. 317.

[18] M. Zhan, K. Li, P. Wang, L. Kong, X. Wang, R. Li, X. Tu, L. He, J. Wang and B. Lu, "Cold Atom Interferometry", *Journal of Physics: Conference Series*, vol. 80, Sept. 2007, p. 012047.

[19] D. Keith, C. Ekstrom, Q. Turchette and D. Pritchard, "An interferometer for atoms", *Physical Review Letters*, vol. 66, May 1991, p. 2693–2696.

[20] J. Lawall and M. Prentiss, "Demonstration of a novel atomic beam splitter", *Physical Review Letters*, vol. 72, Feb. 1994, p. 993–996.

[21] D. C. Aveline, R. J. Thompson, N. Lundblad, J. M. Kohel and L. Maleki, "Loading, guiding, and manipulating neutral atoms in atom chip magnetic traps", in *2006 Conference on Lasers and Electro-Optics and 2006 Quantum Electronics and Laser Science Conference*, p. 1–2, IEEE, 2006.

[22] M. Bajcsy, S. Hofferberth, T. Peyronel, V. Balic, Q. Liang, A. Zibrov, V. Vuletic and M. D. Lukin, "Laser-cooled atoms inside a hollow-core photonic-crystal fiber", *Physical Review A*, vol. 83, June 2011, p. 1–9.

[23] S. Okaba, T. Takano, F. Benabid, T. Bradley, L. Vincetti, Z. Maizelis, V. Yampol'skii, F. Nori and H. Katori, "Lamb-Dicke spectroscopy of atoms in a hollow-core photonic crystal fibre.", *Nature communications*, vol. 5, Jan. 2014, p. 4096.

[24] D. J. Harris and C. M. Savage, "Atomic gravitational cavities from hollow optical fibers", *Physical Review A*, vol. 51, May 1995, p. 3967–3971.

[25] R. G. Dall, S. S. Hodgman, A. G. Manning, M. T. Johnsson, K. G. H. Baldwin and A. G. Truscott, "Observation of atomic speckle and Hanbury Brown-Twiss correlations in guided matter waves.", *Nature communications*, vol. 2, Jan. 2011, p. 291.

[26] D. Meschede and H. Metcalf, "Atomic nanofabrication: atomic deposition and lithography by laser and magnetic forces (Topical Review)", *Journal of Physics D: Applied Physics*, vol. 36, 2003, p. R17–R38.

[27] W. Williams and M. Saffman, "Two-dimensional atomic lithography by submicrometer focusing of atomic beams", *Journal of the Optical Society of America B*, vol. 23, no. 6, 2006, p. 1161.

[28] K. G. H. Baldwin, "Metastable helium: atom optics with nano-grenades", *Contemporary Physics*, vol. 46, no. 2, 2005, p. 105–120.

[29] C. Christensen, S. Will, M. Saba, G.-B. Jo, Y.-I. Shin, W. Ketterle and D. Pritchard, "Trapping of ultracold atoms in a hollow-core photonic crystal fiber", *Physical Review A*, vol. 78, no. 3, 2008, p. 033429.1–033429.4.

[30] M. Bajcsy, S. Hofferberth, V. Balic, T. Peyronel, M. Hafezi, A. Zibrov, V. Vuletic and M. D. Lukin, "Efficient All-Optical Switching Using Slow Light within a Hollow Fiber", *Physical Review Letters*, vol. 102, May 2009, p. 1–4.

[31] M. Hafezi, D. E. Chang, V. Gritsev, E. a. Demler and M. D. Lukin, "Photonic quantum transport in a nonlinear optical fiber", *EPL (Europhysics Letters)*, vol. 94, June 2011, p. 54006.

[32] B. Paredes, A. Widera, V. Murg, O. Mandel, S. Fölling, I. Cirac, G. V. Shlyapnikov, T. W. Hänsch and I. Bloch, "Tonks-Girardeau gas of ultracold atoms in an optical lattice.", *Nature*, vol. 429, May 2004, p. 277–81.

[33] A. Gorshkov, J. Otterbach, E. Demler, M. Fleischhauer and M. D. Lukin, "Photonic Phase Gate via an Exchange of Fermionic Spin Waves in a Spin Chain", *Physical Review Letters*, vol. 105, Aug. 2010, p. 1–4.

[34] S. Vorrath, S. Möller, P. Windpassinger, K. Bongs and K. Sengstock, "Efficient guiding of cold atoms through a photonic band gap fiber", *New Journal of Physics*, vol. 12, Dec. 2010, p. 123015.

[35] T. G. Euser, G. Whyte, M. Scharrer, J. S. Y. Chen, A. Abdolvand, J. Nold, C. F. Kaminski and P. S. J. Russell, "Dynamic control of higher-order modes in hollow-core photonic crystal fibers", *Optics Express*, vol. 16, no. 22, 2008, p. 17972–17981.

[36] J. Poulin, P. Light, R. Kashyap and A. Luiten, "Optimized coupling of cold atoms into a fiber using a blue-detuned hollow-beam funnel", *Physical Review A*, vol. 84, Nov. 2011, p. 053812–1–10.

[37] P. N. Lebedev, "Untersuchungen uber die Druckkrafte des Lichtes", *Annalen der Physik*, vol. 6, 1901, p. 433.

[38] E. F. Nichols and G. F. Hull, "A Preliminary Communication on the Pressure of Heat and Light Radiation", *Physical Review (Series I)*, vol. 13, no. 5, 1901, p. 307–320.

[39] V. S. Letokhov, "Translational atomic motion in a single-frequency standing light wave", *JETP Letters*, vol. 7, 1968, p. 272.

[40] A. Ashkin, "Acceleration and Trapping of Particles by Radiation Pressure", *Physical Review Letters*, vol. 24, no. 4, 1970, p. 156–159.

[41] A. Ashkin, "Atomic-Beam Deflection by Resonance-Radiation Pressure", *Physical Review Letters*, vol. 25, no. 19, 1970, p. 1321–1324.

[42] A. Ashkin, "Trapping of atoms by resonance radiation pressure", *Physical Review Letters*, vol. 40, no. 12, 1978, p. 729–732.

[43] S. Chu, L. Hollberg, J. E. Bjorkholm, A. Cable and A. Ashkin, "Three-Dimensional Viscous Confinement and Cooling of Atoms by Resonance Radiation Pressure", *Physical Review Letters*, vol. 55, no. 1, 1985, p. 48–51.

[44] S. Chu, J. Bjorkholm, A. Ashkin and A. Cable, "Experimental Observation of Optically Trapped Atoms", *Physical Review Letters*, vol. 57, July 1986, p. 314–317.

[45] C. Salomon, J. Dalibard, A. Aspect, H. Metcalf, C. Cohen-Tannoudji and C., "Channeling atoms in a laser standing wave", *Physical Review Letters*, vol. 59, no. 15, 1987, p. 1659–1662.

[46] V. I. Balykin, Y. E. Lozovik, Y. B. Ovchinnikov, A. I. Sidorov, S. V. Shulga and V. S. Letokhov, "One-dimensional localization of atoms in a standing spherical light wave", *Journal of the Optical Society of America B*, vol. 6, no. 11, 1989, p. 2178–2187.

[47] M. A. OlShanii, Y. B. Ovchinnikov and V. S. Letokhov, "Laser guiding of atoms in a hollow optical fiber", *Optics Communications*, vol. 98, 1993, p. 77–79.

[48] J. Dalibard and C. Cohen-Tannoudji, "Dressed-atom approach to atomic motion in laser light: the dipole force revisited", *Journal of the Optical Society of America B*, vol. 2, Nov. 1985, p. 1707.

[49] M. J. Renn, A. A. Zozulya, E. A. Donley, E. A. Cornell and D. Z. Anderson, "Optical-dipole-force fiber guiding and heating of atoms", *Physical Review A*, vol. 55, no. 5, 1997, p. 3684–3696.

[50] S. Marksteiner, C. M. Savage, P. Zoller and S. L. Rolston, "Coherent atomic waveguides from hollow optical fibers: quantized atomic motion", *Physical Review A*, vol. 50, no. 3, 1994, p. 2680–2690.

[51] H. Ito, K. Sakaki, T. Nakata, W. Jhe and M. Ohtsu, "Optical potential for atom guidance in a cylindrical-core hollow fiber", *Optics Communications*, vol. 115, 1995, p. 57–64.

[52] H. S. Pilloff, "Enhanced atom guiding in metal-coated, hollow-core optical fibers", *Optics Communications*, vol. 143, 1997, p. 25–29.

[53] M. V. Subbotin, V. I. Balykin and D. V. Laryushin, "Laser controlled atom waveguide as a source of ultracold atoms", *Optics Communications*, vol. 139, no. June, 1997, p. 107– 116.

[54] L. Pruvost, D. Marescaux, O. Houde and H. T. Duong, "Guiding and cooling of cold atoms in a dipole guide", *Optics Communications*, vol. 166, no. 1-6, 1999, p. 199–209.

[55] B. T. Wolschrijn, R. A. Cornelussen, R. J. C. Spreeuw and H. B. v. L. van den Heuvell, "Guiding of cold atoms by a red-detuned laser beam of moderate power", *New Journal of Physics*, vol. 4, Sept. 2002, p. 69.

[56] Y. Song, D. Milam and W. T. Hill III, "Long, narrow all-light atom guide", *Optics Letters*, vol. 24, no. 24, 1999, p. 1805–1807.

[57] M. Mestre, F. Diry, B. Viaris de Lesegno and L. Pruvost, "Cold atom guidance by a holographically-generated Laguerre-Gaussian laser mode", *The European Physical Journal D*, vol. 57, Jan. 2010, p. 87–94.

[58] A. E. Leanhardt, A. P. Chikkatur, D. Kielpinski, Y. Shin, T. L. Gustavson, W. Ketterle and D. E. Pritchard, "Propagation of Bose-Einstein Condensates in a Magnetic Waveguide", *Physical Review Letters*, vol. 89, no. 4, 2002, p. 040401.1–4.

[59] M. P. A. Jones, C. J. Vale, D. Sahagun, B. V. Hall and E. A. Hinds, "Spin Coupling between Cold Atoms and the Thermal Fluctuations of a Metal Surface", *Physical Review Letters*, vol. 91, no. 8, 2003, p. 080401.

[60] A. Dutt, S. Mahapatra and S. K. Varshney, "Capillary optical fibers : design and applications for attaining a large effective mode area", *Journal of the Optical Society of America B*, vol. 28, no. 6, 2011, p. 1431–1438.

[61] Y. Song, *Hollow beam atom tunnel*. PhD thesis, University of Maryland, 1999.

[62] H.-R. Noh and W. Jhe, *Atom Optics with Hollow Optical Systems*. Elsevier science, 2002.

[63] M. J. Renn, D. Montgomery, O. Vdovin, D. Anderson, C. Wieman and E. Cornell, "Laser-Guided Atoms in Hollow-Core Optical Fibers", *Physical Review Letters*, vol. 75, Oct. 1995, p. 3253–3256.

[64] M. J. Renn, E. A. Donley, E. A. Cornell, C. E. Wieman and D. Z. Anderson, "Evanescent-wave guiding of atoms in hollow optical fibers", *Physical Review A*, vol. 53, no. 2, 1996, p. 648–651.

[65] D. Muller, E. A. Cornell, D. Z. Anderson and E. R. I. Abraham, "Guiding laser-cooled atoms in hollow-core fibers", *Physical Review A*, vol. 61, 2000, p. 033411.1–6.

[66] H. Ito, T. Nakata, K. Sakaki, M. Ohtsu, K. I. Lee and W. Jhe, "Laser Spectroscopy of Atoms Guided by Evanescent Waves in Micron-Sized Hollow Optical Fibers", *Physical Review Letters*, vol. 76, no. 24, 1996, p. 4500–4503.

[67] H. Ito, K. Sakaki, W. Jhe and M. Ohtsu, "Evanescent-light induced atom-guidance using a hollow optical fiber with light coupled sideways", *Optics Communications*, vol. 141, 1997, p. 43–47.

[68] R. G. Dall, M. D. Hoogerland, K. G. H. Baldwin and S. J. Buckman, "Guiding of metastable helium atoms through hollow optical fibres", *Journal of Optics B: Quantum and Semiclassical Optics*, vol. 1, 1999, p. 396–401.

[69] G. Workurka, J. Keupp, K. Sengstock and W. Ertmer, "Guiding of metastable neon atoms in hollow-core optical fibers", *Technical Digest - European Quantum Electronics Conference*, 1998, p. 235–236.

[70] P. Engels, S. Salewski, H. Levsen, K. Sengstock and W. Ertmer, "Atom lithography with a cold, metastable neon beam", *Applied Physics B: Lasers and Optics*, vol. 69, 1999, p. 407–412.

[71] R. G. Dall, *Optical guiding with bright sources of cold metastable helium.* PhD thesis, Australian National University, 2004.

[72] J. A. Swansson, R. G. Dall and A. G. Truscott, "An intense cold beam of metastable helium", *Applied Physics B: Lasers and Optics*, vol. 86, no. 3, 2007, p. 485–489.

[73] R. F. Cregan, B. J. Mangan, J. C. Knight, T. A. Birks, P. S. J. Russell, P. J. Roberts and D. C. Allan, "Single-Mode Photonic Band Gap Guidance of Light in Air", *Science*, vol. 285, no. 5433, 1999, p. 1537–1539.

[74] T. Takekoshi and R. J. Knize, "Optical Guiding of Atoms through a Hollow-Core Photonic Band-Gap Fiber", *Physical Review Letters*, vol. 98, 2007, p. 210404.1–4.

[75] R. J. Knize and T. Takekoshi, "Optical Guiding of Atoms through a Hollow-Core Photonic Band-Gap Fiber", in *Quantum Electronics and Laser Science Conference (QELS)*, vol. 1, (San Jose), p. 2, 2008.

[76] F. K. Fatemi, M. Bashkansky, E. Oh and D. Park, "Efficient excitation of the TE(01) hollow metal waveguide mode for atom guiding.", *Optics express*, vol. 18, Jan. 2010, p. 323–32.

[77] J. Pechkis and F. K. Fatemi, "Cold atom guidance in a capillary using blue-detuned, hollow optical modes.", *Optics express*, vol. 20, June 2012, p. 13409–18.

[78] S. Ghosh, A. Bhagwat, C. Renshaw, S. Goh, A. L. Gaeta and B. Kirby, "Low-Light-Level Optical Interactions with Rubidium Vapor in a Photonic Band-Gap Fiber", *Physical Review Letters*, vol. 97, July 2006, p. 023603.

[79] C. Perrella, P. Light, T. Stace, F. Benabid and A. Luiten, "High-resolution optical spectroscopy in a hollow-core photonic crystal fiber", *Physical Review A*, vol. 85, Jan. 2012, p. 012518.

[80] E. A. J. Marcatili and R. A. Schmeltzer, "Hollow Metallic and Dielectric Waveguides for Long Distance Optical Transmission and Lasers", *Bell System Technical Journal*, vol. 43, no. 4, 1964, p. 1783.

[81] A. Bjarklev, J. Broeng and A. Sanchez Bjarklev, *Photonic Crystal Fibres*. Boston: Kluwer Academic Publishers, 2003.

[82] C. Townsend, N. Edwards, C. Cooper, K. Zetie, C. Foot, A. M. Steane, P. Szriftgiser, H. Perrin and J. Dalibard, "Phase-space density in the magneto-optical trap", *Physical Review A*, vol. 52, Aug. 1995, p. 1423–1440.

[83] C. J. Foot, *Atomic Physics*. Oxford University Press, 2005.

[84] H. Metcalf and P. van Der Straten, *Laser cooling and trapping*. New York, USA: Springer-Verlag, graduate t ed., 1999.

[85] V. I. Balykin and V. S. Letokhov, *Atom Optics with Laser Light*. CRC Press, 1995.

[86] E. Raab, M. Prentiss, A. Cable, S. Chu and D. Pritchard, "Trapping of Neutral Sodium Atoms with Radiation Pressure", *Physical Review Letters*, vol. 59, Dec. 1987, p. 2631–2634.

[87] A. E. Leanhardt, T. A. Pasquini, M. Saba, A. Schirotzek, Y. Shin, D. Kielpinski, D. E. Pritchard and W. Ketterle, "Cooling Bose-Einstein condensates below 500 picokelvin.", *Science (New York, N.Y.)*, vol. 301, Sept. 2003, p. 1513–5.

[88] J. P. Gordon and A. Ashkin, "No Title", *Physical Review A*, vol. 21, 1980, p. 1606.

[89] C. Cohen-Tannoudji, J. Dupont-Roc and G. Grynberg, *Atom-Photon Interactions*. New York, USA: Wiley, 1992.

[90] P. Lett, R. Watts, C. Westbrook, W. Phillips, P. Gould and H. Metcalf, "Observation of Atoms Laser Cooled below the Doppler Limit", *Physical Review Letters*, vol. 61, July 1988, p. 169–172.

[91] P. J. Ungar, D. S. Weiss, E. Riis and S. Chu, "Optical molasses and multilevel atoms: theory", *Journal of the Optical Society of America B*, vol. 6, Nov. 1989, p. 2058.

[92] D. S. Weiss, E. Riis, Y. Shevy, P. J. Ungar and S. Chu, "Optical molasses and multilevel atoms: experiment", *Journal of the Optical Society of America B*, vol. 6, Nov. 1989, p. 2072.

[93] D. A. Steck, "Rubidium 87 D Line Data", tech. rep., 2010.

[94] C. Monroe, W. Swann, H. Robinson and C. E. Wieman, "Very cold trapped atoms in a vapor cell", *Physical Review Letters*, vol. 65, Sept. 1990, p. 1571–1574.

[95] A. M. Steane and C. J. Foot, "Laser Cooling below the Doppler Limit in a Magneto-Optical Trap", *Europhysics Letters (EPL)*, vol. 14, Feb. 1991, p. 231–236.

[96] P. Kohns, P. Buch, W. Süptitz, C. Csambal and W. Ertmer, "On-Line Measurement of Sub-Doppler Temperatures in a Rb Magneto-optical Trap-by-Trap Centre Oscillations", *Europhysics Letters (EPL)*, vol. 22, June 1993, p. 517–522.

[97] C. D. Wallace, T. P. Dinneen, K. Y. N. Tan, a. Kumarakrishnan, P. L. Gould and J. Javanainen, "Measurements of temperature and spring constant in a magneto-optical trap", *Journal of the Optical Society of America B*, vol. 11, May 1994, p. 703.

[98] F. Pereira Dos Santos, H. Marion, S. Bize, Y. Sortais, a. Clairon and C. Salomon, "Controlling the Cold Collision Shift in High Precision Atomic Interferometry", *Physical Review Letters*, vol. 89, Nov. 2002, p. 233004.

[99] M. Merimaa, T. Lindvall, I. Tittonen and E. Ikonen, "All-optical atomic clock based on coherent population trapping in 85Rb", *Journal of the Optical Society of America B*, vol. 20, no. 2, 2003, p. 273.

[100] S. Knappe, P. D. D. Schwindt, V. Shah, L. Hollberg and J. Kitching, "A chip-scale atomic clock based on 87 Rb with improved frequency stability", *Optics Express*, vol. 13, no. 4, 2005, p. 1249–1253.

[101] D. A. Steck, "Rubidium 85 D Line Data", tech. rep., 2010.

[102] R. L. Barger, M. S. Sorem and J. L. Hall, "Frequency stabilization of a cw dye laser", *Applied Physics Letters*, vol. 22, no. 11, 1973, p. 573 – 575.

[103] K. B. MacAdam, A. Steinbach and C. E. Wieman, "A narrow-band tunable diode laser system with grating feedback, and a saturated absorption spectrometer for Cs and Rb", *American Journal of Physics*, vol. 60, no. 12, 1992, p. 1098–1111.

[104] K. L. Corwin, Z. T. Lu, C. F. Hand, R. J. Epstein and C. E. Wieman, "Frequency-stabilized diode laser with the Zeeman shift in an atomic vapor.", *Applied optics*, vol. 37, May 1998, p. 3295–8.

[105] G. Jundt, G. T. Purves, C. S. Adams and I. G. Hughes, "Non-linear Sagnac interferometry for pump-probe dispersion spectroscopy", *The European Physical Journal D - Atomic, Molecular and Optical Physics*, vol. 27, Dec. 2003, p. 273–276.

[106] G. C. Bjorklund, M. D. Levenson, W. Lenth and C. Ortiz, "Frequency modulation (FM) spectroscopy", *Applied Physics B Photophysics and Laser Chemistry*, vol. 32, Nov. 1983, p. 145–152.

[107] R. W. P. Drever, J. L. Hall, F. V. Kowalski, J. Hough, G. M. Ford, a. J. Munley and H. Ward, "Laser phase and frequency stabilization using an optical resonator", *Applied Physics B Photophysics and Laser Chemistry*, vol. 31, June 1983, p. 97–105.

[108] E. D. Black, "An introduction to Pound-Drever-Hall laser frequency stabilization", *American Journal of Physics*, vol. 69, no. 1, 2001, p. 79.

[109] J. H. Shirley, "Modulation transfer processes in optical heterodyne saturation spectroscopy.", *Optics letters*, vol. 7, Nov. 1982, p. 537–9.

[110] D. J. McCarron, S. a. King and S. L. Cornish, "Modulation transfer spectroscopy in atomic rubidium", *Measurement Science and Technology*, vol. 19, Oct. 2008, p. 105601.

[111] R. Raj, D. Bloch, J. Snyder, G. Camy and M. Ducloy, "High-Frequency Optically Heterodyned Saturation Spectroscopy Via Resonant Degenerate Four-Wave Mixing", *Physical Review Letters*, vol. 44, May 1980, p. 1251–1254.

[112] J. Yin, Y. Zhu and Y. Wang, "Evanescent light-wave atomic funnel: A tandem hollow-fiber, hollow-beam approach", *Physical Review A*, vol. 57, no. 3, 1998, p. 1957–1966.

[113] H. S. Pilloff, "The effect of the van der Waals interaction on the excited state for atom guiding in metal-coated, hollow-core optical fibers", *Optics Communications*, vol. 179, 2000, p. 123–127.

[114] P. Roberts, F. Couny, H. Sabert, B. Mangan, D. Williams, L. Farr, M. Mason, A. Tomlinson, T. Birks, J. Knight and P. St J Russell, "Ultimate low loss of hollow-core photonic crystal fibres.", *Optics express*, vol. 13, Jan. 2005, p. 236–44.

[115] G. Sagué, E. Vetsch, W. Alt, D. Meschede and a. Rauschenbeutel, "Cold-Atom Physics Using Ultrathin Optical Fibers: Light-Induced Dipole Forces and Surface Interactions", *Physical Review Letters*, vol. 99, Oct. 2007, p. 1–4.

[116] F. K. Fatemi and M. Bashkansky, "Cold atom guidance using a binary spatial light modulator.", *Optics express*, vol. 14, Feb. 2006, p. 1368–75.

[117] X. Xu, V. G. Minogin, K. Lee, Y. Wang and W. Jhe, "Guiding cold atoms in a hollow laser beam", *Physical Review A*, vol. 60, no. 6, 1999, p. 4796–4804.

[118] X. Xu, Y. Wang and W. Jhe, "Theory of atom guidance in a hollow laser beam: dressed-atom approach", *Journal of the Optical Society of America B*, vol. 17, no. 6, 2000, p. 1039–1050.

[119] B. Smeets, R. W. Herfst, E. te Sligte, P. van der Straten, H. C. Beijerinck and K. A. H. van Leeuwen, "Laser-cooling simulation based on the semiclassical approach", *Journal of the Optical Society of America B*, vol. 22, no. 11, 2005, p. 2372.

[120] H. Yan-Xu, L. Yong-Hong, Z. Chun-Hong, L. Shu-Jing and W. Hai, "Realization of High Optical Density Rb Magneto-optical Trap", *Chinese Physics Letters*, vol. 26, Feb. 2009, p. 023201.

[121] M. Towler, "Quantum Monte Carlo: accuracy, generality, and scalability", in *Scuola Normale, Pisa*, p. 51, 2014.

[122] A. L. Garcia, *Numerical Methods for Physics*. Englewood Cliffs, NJ, USA: Prentice Hall, 2000.

[123] K. Molmer, "Friction and diffusion coefficients for cooling of atoms in laser fields with multidimensional periodicity", *Physical Review A*, vol. 44, Nov. 1991, p. 5820–5832.

[124] J. Javanainen, "Polarization gradient cooling in three dimensions: comparison of theory and experiment", *Journal of Physics B: Atomic, Molecular and Optical Physics*, vol. 27, Feb. 1994, p. L41–L47.

[125] Y. Castin and K. Molmer, "Monte Carlo Wave-Function Analysis of 3D Optical Molasses", *Physical Review Letters*, vol. 74, May 1995, p. 3772–3775.

[126] A. M. Steane, G. Hillenbrand and C. J. Foot, "Polarization gradient cooling in a one-dimensional sigma + - sigma - configuration for any atomic transition", *Journal of Physics B: Atomic, Molecular and Optical Physics*, vol. 25, Nov. 1992, p. 4721–4743.

[127] W. D. Phillips, "Laser Cooling, Optical Traps and Optical Molasses", in *Fundamental Systems in Quantum Optics*, Les Houches Summer School, 1992, p. 165.

[128] C. Gerz, T. W. Hodapp, P. Jessen, K. M. Jones, W. D. Phillips, C. I. Westbrook and K. Molmer, "The Temperature of Optical Molasses for Two Different Atomic Angular Momenta", *Europhysics Letters (EPL)*, vol. 21, Feb. 1993, p. 661–666.

[129] A. M. Steane, M. Chowdhury and C. J. Foot, "Radiation force in the magneto-optical trap", *Journal of the Optical Society of America B*, vol. 9, Dec. 1992, p. 2142.

[130] N. Friedman, A. Kaplan and N. Davidson, "Dark optical traps for cold atoms", in *Advances in Atomic Molecular and Optical Physics, vol. 48* (B. Bederson and H. Walther, eds.), vol. 48, Academic Press, 2002, p. 99–151.

[131] W. Petrich, M. H. Anderson, J. R. Ensher and E. A. Cornell, "Behavior of atoms in a compressed magneto-optical trap", *Journal of the Optical Society of America B*, vol. 11, Aug. 1994, p. 1332.

[132] J. M. Danby, *Fundamentals of celestial mechanics*. Willmann-Bell, Inc., 2nd editio ed., 1988.

[133] Y. B. Ovchinnikov, I. Manek, A. I. Sidorov, G. Wasik and R. Grimm, "Gravito-optical atom trap based on a conical hollow beam", *Europhysics Letters*, vol. 43, Sept. 1998, p. 510–515.

[134] C. J. Hawthorn, K. P. Weber and R. E. Scholten, "Littrow configuration tunable external cavity diode laser with fixed direction output beam", *Review of Scientific Instruments*, vol. 72, no. 12, 2001, p. 4477.

[135] NOAA, "World Magnetic Model", 2010.

[136] P. S. Light, C. Perrella and a. N. Luiten, "Phase-sensitive imaging of cold atoms at the shot-noise limit", *Applied Physics Letters*, vol. 102, no. 17, 2013, p. 171108.

[137] M. C. J. Large, L. Poladian, G. Barton and M. A. van Eijkelenborg, *Microstructured Polymer Optical Fibres*. New York: Springer, 2008.

[138] P. Ghenuche, S. Rammler, N. Y. Joly, M. Scharrer, M. Frosz, J. Wenger, P. S. J. Russell and H. Rigneault, "Kagome hollow-core photonic crystal fiber probe for Raman spectroscopy", *Optics Letters*, vol. 37, no. 21, 2012, p. 4371–4373.

[139] A. Docherty, L. Poladian, A. Argyros, M. Large, J. Poulin and R. Kashyap, "Increasing the numerical aperture of large-core microstructured polymer optical fibers using a 'Y'-bridge cladding", *Journal of Lightwave Technology*, vol. 27, no. 11, 2009, p. 1610–1616.

[140] A. Argyros, *Bragg reflection and bandgaps in microstructured optical fibres*. PhD thesis, The University of Sydney, 2006.

[141] J. Poulin, A. Argyros, R. Kashyap and M. Large, "Fabrication and Characterisation of a Large-core Bridged Air-clad High Numerical Aperture Microstructured Polymer Optical Fibre", in *Proceedings of the International Conference on Plastic Optical Fibers*, (Turin, Italy), p. 131–134, 2007.

[142] A. Argyros, R. Lwin, S. G. Leon-Saval, J. Poulin, L. Poladian and M. C. J. Large, "Low Loss and Temperature Stable Microstructured Polymer Optical Fibers", *Journal of Lightwave Technology*, vol. 30, Jan. 2012, p. 192–197.

[143] G. Barton, M. V. Eijkelenborg, G. Henry, N. Issa, K.-f. Klein, M. Large, S. Manos, W. Padden, W. Pok and L. Poladian, "Characteristics of Multimode Microstructured POF Performance", in *Plastic Optical Fibre Conference 14-17 september*, no. 3, (Seattle), p. 81–84, 2003.

[144] J. P. Kirk and A. L. Jones, "Phase-Only Complex-Valued Spatial Filter", *Journal of the Optical Society of America*, vol. 61, Aug. 1971, p. 1023.

[145] Y. Ohtake, T. Ando, N. Fukuchi, N. Matsumoto, H. Ito and T. Hara, "Universal generation of higher-order multiringed Laguerre-Gaussian beams by using a spatial light modulator", *Optics Letters*, vol. 32, no. 11, 2007, p. 1411.

[146] J. A. Davis, D. M. Cottrell, J. Campos, M. J. Yzuel and I. Moreno, "Encoding Amplitude Information onto Phase-Only Filters", *Applied Optics*, vol. 38, Aug. 1999, p. 5004.

[147] V. Arrizón, U. Ruiz, R. Carrada and L. González, "Pixelated phase computer holograms for the accurate encoding of scalar complex fields", *Journal of the Optical Society of America A*, vol. 24, no. 11, 2007, p. 3500.

[148] V. Arrizón, U. Ruiz, G. Mendez and A. Apolinar-Iribe, "Zero order synthetic hologram with a sinusoidal phase carrier for generation of multiple beams", *Optics Express*, vol. 17, Feb. 2009, p. 2663.

[149] V. Arrizón, D. Sánchez-de-la Llave, U. Ruiz and G. Méndez, "Efficient generation of an arbitrary nondiffracting Bessel beam employing its phase modulation", *Optics Letters*, vol. 34, Apr. 2009, p. 1456.

[150] T. Ando, Y. Ohtake, N. Matsumoto, T. Inoue and N. Fukuchi, "Mode purities of Laguerre-Gaussian beams generated via complex-amplitude modulation using phase-only spatial light modulators", *Optics Letters*, vol. 34, Dec. 2008, p. 34.

[151] D. Budker, D. F. Kimball and D. P. DeMille, *Atomic Physics*. Oxford University Press, 2nd ed., 2008.

[152] N. Bhaskar, J. White, L. Mallette, T. McClelland and J. Hardy, "A historical review of atomic frequency standards used in space systems", in *Proceedings of 1996 IEEE International Frequency Control Symposium*, p. 24–32, IEEE, 1996.

[153] K. Honda, Y. Takahashi, T. Kuwamoto, M. Fujimoto and K. Toyoda, "Magneto-optical trapping of Yb atoms and a limit on the branching ratio of the 1 P 1 state", *Physical Review A*, vol. 59, no. 2, 1999, p. 934–937.

[154] E. S. Shuman, J. F. Barry and D. Demille, "Laser cooling of a diatomic molecule.", *Nature*, vol. 467, Oct. 2010, p. 820–3.

[155] J. H. V. Nguyen, C. R. Viteri, E. G. Hohenstein, C. D. Sherrill, K. R. Brown and B. Odom, "Challenges of laser-cooling molecular ions", *New Journal of Physics*, vol. 13, June 2011, p. 063023.

APPENDIX I REVIEW OF THE QUANTUM MECHANICAL MODEL OF THE ATOM

Atomic structure

A first approximation of the quantum mechanical model of the atom was first discovered by Niels Bohr. His model was a spectacular result in the fashion that it was able to explain fundamentally the meaning of the Rydberg constant (already known empirically) and to accurately predict the energy levels corresponding to the lines of the hydrogen spectrum using this formula:

$$E_n = -hcR_\infty \frac{Z^2}{n^2} \tag{I.1}$$

where h is Planck's constant, c is the speed of light, R_∞ is Rydberg constant, Z is the atomic number (of protons) and n is the energy level considered. But the model was not working for more complex atoms. Bohr's model invented the concept of electron orbitals. The electrons are not localized particles orbiting around the nucleus anymore, like in the Rutherford model of the atom, but rather wavefunctions in a central potential. The electron wavefunction can be described as a probability of presence of the electron during a "measurement event". It is these electronic wavefunctions, called orbitals, which interact with the nucleus and the other electron wavefunctions that define the basic energy levels of the atom. To obtain the energy levels of an atom, one must find the eigenvalues by solving the complete Hamiltonian of the Schrödinger equation, a complex calculation that is easily validated by spectroscopic measurements.

In the quantum model of the atom, each electron must have a unique quantum state. This is a direct consequence of the fermionic nature of electrons translated into the *Pauli exclusion principle*. The quantum state is defined from the eigenvalues of a complete set of commuting observables (or operators) (CSCO). These observables form a basis in which every system state is defined uniquely. Each eigenvalue from each operator is expressed as a function of a variable that is used as a label for the eigenstate and called quantum number. Before considering spin-orbit interaction and other finer interactions, the electron quantum state is composed of four quantum numbers: the principal quantum number (n), the orbital angular momentum (l), the projection of the orbital angular momentum (m_l), and the projection of the spin (m_s).

To a first approximation the atom energy levels are essentially described by shells and

orbitals (also called subshells). Shells are labeled after the principal quantum number n, which is an integer number starting with 1. Physically, it represents the energy levels emerging from the most fundamental interaction of a single electron in the central isotropic electrostatic field of the nucleus, as described in Bohr's formula (Eq. I.1). Each shell contains $2 \cdot n^2$ unique states that can be occupied by electrons. The separation of energy levels into orbitals comes from the consideration of the central potential being screened by the presence of the other electrons. This is the symmetric part of the electron-electron interactions. Orbitals are labeled after their orbital angular momentum quantum number l following spectroscopic notation. Each integer value of l, that starts with 0, has a letter assigned to it in the following order: s for sharp, p for principal, d for diffuse, f for fine, g, h, ... (following alphabetical order). Each orbital contains $2 \cdot (2l+1)$ electronic states. In a given shell, there are always n orbitals with l values from 0 to $n-1$. Within an orbital, the electronic states are composed of spin projection values m_s of +1/2 and -1/2 for each angular momentum projection m_l having integer values from -l to l.

Note that these quantum numbers are just simplified expressions of the eigenvalues of operators. The eigenvalue of L_z is $m_l\hbar$, S_z is $m_s\hbar$ and $\mathbf{L}$ is $\sqrt{l(l+1)}\hbar$.

For an atom in its ground state, each shell is not necessarily filled fully before electrons starts occupying states in the next shells. Each shell-orbital pairs are filled in order of lowest energy first. This order, empirically defined by *Aufbau rule*, is in order of increasing value of $n+l$. When two pairs of shell-orbitals are equal, the one with the lowest n comes first. Note that there are very few exceptions to this rule and those exceptions only concern atoms with very high Z (total number of protons).

The electronic configuration of an atom, in the ground state, is the list of each shell-orbitals containing an electron in the notation $nl^{\#e-}$ where the superscript is the number of electrons. The electronic configuration of rubidium ($Z = 37$) is $1s^2 2s^2 2p^6 3s^2 3p^6 4s^2 3d^{10} 4p^6 5s^1$.

Considering the atom as a whole, its energy state can be simply described using the total of the projection of orbital momentum of each electron $M_l = \sum_i m_{l_i}$ and total projection of spin $M_s = \sum_i m_{s_i}$ where i is an integer that goes up to the total number of electrons. This labeling of atomic states is known as the Russell-Saunders or L-S coupling scheme. M_l, M_s are always zero in a full shell-orbital pair, so this notation only comes to considering the sum of m_s and m_l in the unfilled shell-orbitals. Note that some authors use notation L and S instead of M_l and M_s but it can lead to confusion with the observables L^2, L_z, S_z and quantum number l and spin value s.

How electrons distribute, to minimize energy, in a given unfilled shell-orbital level is gov-

erned by Hund's rule. Electrons distribute to maximize M_s, if many possible configurations, choose the ones that maximize M_l. If there is still multiple configurations, these are all equal energy and the state is therefore referred as a *doublet*, *triplet state* and so on, according to the number of possible configurations that yield the same state energy.

Because of yet unaccounted fine and hyperfine interactions, the energy levels in an atom are not labeled in this notation because more global parameters are taken into account. The *ground state notation* that builds upon the L-S coupling scheme [151] is used instead.

Fine, hyperfine interactions and the ground state notation

Further perturbations of the energy levels are calculated by consideration of the complex fine and hyperfine interactions. The principal fine interaction is the spin-orbit coupling that describes the interactions of an electron spin with the nucleus electric field. The changes are more dramatic because the observables basis upon which the quantum states L^2, L_z, M_s are constructed, no longer commute with the Hamiltonian, but with the total angular momentum $\mathbf{J} = \mathbf{L} + \mathbf{S}$. The eigenvalue of $\mathbf{J}$ is $\sqrt{J(J+1)}\hbar$ where its associated quantum number J is simply the possible integers or half-integers only of positive values between $|M_s - M_l|$ and $M_s + M_l$. The lowest value of J in this ensemble yields the lowest energy state. There is also the J_z operator with eigenvalues $m_J\hbar$ where the quantum number of the projection of total angular momentum is an integer with values comprised from $-J$ to J.

The quantum state of the atom is now described in a new CSCO basis: $\mathbf{J}^2$, its momentum projection observable J_z, and the P parity transformation observable whose eigenvalues are ± 1 based on the parity of the angular momentum L.

The new notation was built as an hybrid of the previous scheme and total angular momentum j

$$n^{2M_s+1}M_{lj} \tag{I.2}$$

Back to the case of rubidium, the last unfilled orbital is $5s^1$. $M_s = \frac{1}{2}$ and $M_l = 0$, therefore $j = \frac{1}{2}$, its only possible value so there is no fine structure splitting of this level. The ground state of Rb is then $5^2S_{1/2}$ for all its isotopes.

Now there is another splitting of each $j-$*sublevel* that can occur, it is typically an order of magnitude weaker than the fine interaction and it is called hyperfine interaction. It comes from either or both the interaction between the nuclear magnetic dipole with the magnetic moment of the electron and the quadrupolar nuclear electric moment with the electric field gradient of the electrons. There are also other types of hyperfine interactions but they are less common. In hyperfine structure, the spin of the nucleus I and the total angular momentum

of the electron J are interacting. Thus, a new operator is defined: $\mathbf{F} = \mathbf{I} + \mathbf{J}$. The possible levels are labeled by its quantum number F, which have positive integer or half-integer values of $\{|I - J|, ..., I + J\}$. Similarly to j, the lowest value of F will yield the lowest energy state. The hyperfine F number is just added to the ground state notation (Eq. I.2). In the case of ^{85}Rb, I=5/2 and j=1/2 so F=2,3. With ^{87}Rb, I=3/2 and j=1/2 so F=1,2 [93, 101].

APPENDIX II ATOM CANDIDATES FOR LASER COOLING

For laser cooling to work, the atom is placed in a state where it effectively behaves as a single electron atom. In this state, it doesn't have to deal with more complex multi-electron processes and it can constantly recycle the free electron in the closed transition to be affected by the cooling force. A practical restriction to atoms that can be laser cooled is also the availability of a continuous wave (cw) laser with a narrow linewidth tuneable at the cycling frequency.

Up to now, 14 atom species have been used in laser cooling and atom optics research. They can be grouped in 4 categories: alkali metals, (metastable) rare gases, alkaline-earths and complex structures. Their main optical and atomic properties are listed in Table II.1 along with hydrogen included for comparison as it is the most studied and simple atomic structure. Cooling of hydrogen has only been limited by the lasers available for its closed-transition wavelength (122 nm).

Alkali metals (Li, Na, K, Rb, Cs) are all ideal hydrogen-like candidates for laser cooling, which accounts for their popularity in the field, as they have an electronic structure of completely closed inner shells with a single valence electron in the last shell. Particularly, rubidium (Rb) is by far the most laser cooled atom and has been stated by many as a "workhorse" of atomic physics. The main reason for its popularity is its cooling transition D-line that lies in the near infrared (780 and 795 nm) where cheap and performant semiconductor laser diodes are available. This doesn't justify alone the popularity of Rb because other alkalis are all within range as well as shown in Table II.1. Other factors include their convenient vapor pressure at low melting temperature, for a metal, which allows for well-controlled Rb pressure using affordable mini oven dispensers (SAES Getters, UK). Here affordability is a major selling point if it is compared with its nearby cousin Cesium (Cs). It is also the reason why GPS satellites use Rb cells for their frequency standard instead of Cs [152]. The first demonstrations of laser cooling at Bell Labs were accomplished with Sodium atoms [43, 44, 86] but its cooling transition at 589 nm (yellow) proved to be not as convenient for other labs which developed their research programs around Rb. The first Bose-Einstein Condensate was realized with ^{87}Rb [15].

The rare gases (He, Ne, Ar, Kr, Xe) are all closed shell electronic structures but have the particularity of being excitable to a metastable state by electric discharge. When one s-electron is excited to an upper level state in this manner (not dipolar coupling), its decay

back to the ground state, through dipolar coupling, is forbidden by quantum mechanical selection rules. The atom therefore behaves effectively as a one-electron hydrogen-like atom with the metastable state acting like an effective ground state. The metastable state lifetime can be as short as 20 seconds in Neon and last as long as 8000 seconds in the case of Helium [28].

Alkaline-earths (Mg, Ca, Sr, Ba) are more difficult to work with because of their higher melting point but are interesting in the context of special applications and mainly used in the development of optical atomic clocks. Ytterbium is also similar to strontium and was trapped for the first time in 1999 [153]. It's an atom interesting for its weight making it a slow-mover and because it has a pair of states suitable for an atomic clock transition at a friendly 578 nm wavelength.

The "complex structures" category used to have only Chromium (Cr) which is used in atomic deposition lithography to create conductive nanostructures [26]. Now they feature also diatomic molecules which were thought impossible to laser cool because of their complex structures and vibrational and rotational energy levels. In 2010, Shuman et al. demonstrated the cooling of strontium monofluoride (SrF) [154] leading the way in the creation of the subfield of molecular laser cooling. Over 10 good candidates for laser cooling have also been identified with BH^+ and AlH^+ showing the most promising potential [155]. Nonetheless, cooling molecules is much more demanding experimentally with each molecule requiring between 6 to 10 repump lasers to compensate for the multiple forbidden/weak transitions surrounding its closed transition.

By looking at the atomic cooling transitions of elements in the first three categories of Table II.1, for the same column of the periodic table, the transitions are the same with only the n-level being increased from one row to the next. This illustrates how similar atomic fine structures are, within one family of atoms, even if their energies are quite different.

Table II.1: Atomic constants and optical parameters of 15 atoms that can be cooled and trapped by direct Doppler laser cooling. In this table, λ is the cooling transition wavelength, τ is the excited state lifetime, Γ is the decay rate or natural linewidth (FWHM), T_D and v_D are the Doppler temperature and velocity and I_s is the saturation intensity of the cycling transition excited by circularly polarized light. *Data from [84, 93, 101].*

Atom	λ (nm)	τ (ns)	$\Gamma/2\pi$ (MHz)	T_D (μK)	v_D (cm/s)	I_s (mW/cm^2)	Cooling transition
^{85}Rb	780.24	26.24	6.07	145.57	11.94	1.67	$5^2S_{1/2}F=3 \rightarrow 5^2P_{3/2}F'=4$
^{87}Rb	780.24	26.24	6.07	145.57	11.80	1.67	$5^2S_{1/2}F=2 \rightarrow 5^2P_{3/2}F'=3$
Li	670.78	27.1	5.87	141	41.1	2.54	$2^2S_{1/2} \rightarrow 2^2P_{3/2}$
Na	588.99	16.2	9.82	236	29.2	6.28	$3^2S_{1/2} \rightarrow 3^2P_{3/2}$
K	766.49	26.4	6.03	145	17.5	1.75	$4^2S_{1/2} \rightarrow 4^2P_{3/2}$
Cs	852.11	30.52	5.21	125	8.8	1.10	$6^2S_{1/2} \rightarrow 6^2P_{3/2}$
H	121.57	1.6	99.47	2387	444	7237	$1^2S_{1/2} \rightarrow 2^2P_{3/2}$
He*	1083.03	98.04	1.62	38.96	28.44	0.17	$2^3S_1 \rightarrow 2^3P_2$
	388.86	106.83	1.49	35.75	27.25	3.31	$2^3S_1 \rightarrow 3^3P_2$
Ne*	640.22	19.5	8.16	196	28.4	4.07	$3s[3/2]_2 \rightarrow 3p[5/2]_3$
Ar*	811.53	30.2	5.27	126	16.2	1.29	$4s[3/2]_2 \rightarrow 4p[5/2]_3$
Kr*	811.29	28	5.68	136	11.6	1.40	$5s[3/2]_2 \rightarrow 5p[5/2]_3$
Xe*	881.94	34	4.68	112	8.4	0.89	$6s[3/2]_2 \rightarrow 6p[5/2]_3$
Mg	285.21	2.0	79.57	1910	81	448	$3^1S_0 \rightarrow 3^1P_1$
Ca	422.67	4.5	35.37	849	42	61.2	$4^1S_0 \rightarrow 4^1P_1$
Sr	460.73	4.98	31.96	767	27	42.7	$5^1S_0 \rightarrow 5^1P_1$
Cr	425.33	31.8	5.00	120	13.9	8.50	$4a^7S_3 \rightarrow 4z^7P_4$

APPENDIX III FAST COIL ENERGY DISSIPATION

A fast coil energy dissipation is defined as $< 100\,\mu$s in atomic physics. A dedicated circuit is necessary to dissipate the back EMF and protect the power supply. We have designed a circuit, shown at Fig. III.1, using a power MOSFET (more precisely an IGBT: Insulated Gate Bipolar Transistor) as the interrupt to shutoff the current in less than $1\,\mu$s. This circuit was designed following guidelines given by Dr. Lincoln Turner (Monash U.) and further support for the details of the circuit was given by Dr. Mitja Nemec (UWA). Assuming a maximum

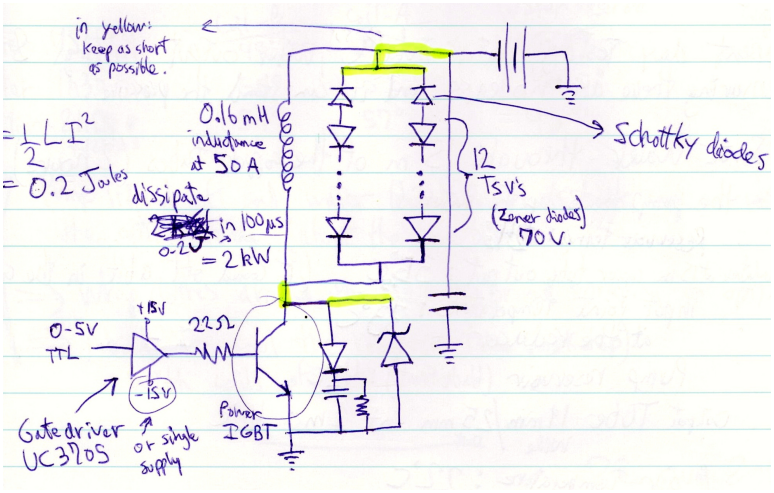

Figure III.1: Circuit designed to dissipate the magnetic field energy of our coils with two parallel lines of 12 TVS in series. The circuit was designed to be able to dissipate the magnetic field induced by a current of up to 100 A in less than $66\,\mu$s.

current of 100 A, the time to dissipate the current in the coils depends on how high we can raise the peak voltage. To this end, we used two lines of 12 transient voltage suppressors (TVS), which are specialized Zener diodes that can dissipate a large amount of power very quickly. By connecting them in series we increase the breakdown voltage from 70 V to 840 V. We used two lines to divide the current so as not to exceed the maximum current rating of 100 A and to increase the TVSs lifetimes. The decay time is then calculated with Eq. 5.3 to obtain $66\,\mu$s. The maximum power that can be dissipated by each TVS is 2 kW. The power to dissipate from the coils is calculated as the energy stored divided by dissipation time:

$$P = \frac{LI^2}{2\Delta t} \tag{III.1}$$

In this case we obtain 42 kW which is 1.75 kW per TVS. The circuit has not been fabricated yet due to its high cost, thermal management of the components and likely time needed to implement a digital remote controller. In most experiments, the coils are repeatedly turned on and off every minute which requires superior cooling capabilities.

APPENDIX IV COILS WATERCOOLING SYSTEM

As we previously explained, our original approach to cooling the coils was to circulate cooling water through the copper tubes forming the coils. To design the watercooling system, we had to analyse our coils in terms of hydraulics, hydrodynamics and thermodynamics to answer the most basic practical questions:

- How much flow we need to keep our coils cool?
- What is the minimum pressure head we need for our pump to make this work?
- Where do we get the water?

The essential of our analysis was that we had very small pipes so the only way to work was to keep the flow laminar (i.e. non-turbulent). This eliminated the Hazen-Williams model of waterflow through pipes and we selected the more hydrophysical Darcy-Weisbach model of Newtonian fluids laminar flow. Each coil was to be driven in parallel because the bottleneck of our system was the pump head pressure not its flowrate. We calculated flowrates of our system as a function of head pressure loss. The best pump available and adequate for a lab environment was a 35 m head pressure pump, which we calculated would produce a flow of 2.4 ml/s through each coil.

For the thermodynamic part of the model, we assumed an ideal heat transfer between the copper tube and the water flowing inside. Balancing units, we built this intuitive heat transfer equation that the temperature of water at the output is the thermal power divided by the mass flowrate times its calorific capacity:

$$\Delta T = \frac{P}{\rho Q C} \tag{IV.1}$$

where P is the thermal power (W), ρ is the fluid density (1 kg/l for water), Q is the flowrate (l/s) and C is the calorific capacity (4186 J/°C kg).

Given a current of 50 A producing 150 W of heat in each coil, we calculated a temperature raise of 16°C at a rate of 2.4 ml/s for each coil (heating 16 l/hour in total), which would be suitable given we wouldn't continuously run the magnets, at such a current, for more than a few hours per day.

For the cooling water source, we couldn't use the university refrigerated cooling water circuit because the water is "dirty" and would end up clogging our tubes very quickly. We settled into using a 60 litres tank of clean water.

Table IV.1: Temperature of the watercooled magnetic coils (driven at 50 A) and the 60 litres water reservoir over time.

Time@50 A (min)	Coil A	Coil B	Water reservoir
5	37	38	27
45	47	49	35
90	53	55	40.5
120	57	59	43

The system was assembled with swagelok fittings and teflon tape to make sure there would be no leaks. The final setup is shown in Fig. IV.1 and IV.2. We let the water run for several hours and found that all the joints were dry. We then started driving the coils at 50 A for 10 minutes, flowrate was 2.2 ml/s, the reservoir temperature was 24.5°C and the water temperature at the coils output was 41°C. The flowrate and the temperature raise of 16.5°C are both in strong agreement with the predictions of our hydrodynamics and thermodynamics model.

However, when running the pump continuously, we noticed it started heating up considerably adding more heat into the water than expected. Running both coils at 50 A, we monitored their temperature as well as the water tank in Table IV.1. After 2 hours, the pump tripped off and water started leaking at the junction with the coils, spraying water all over the optics on the table. The solution to prevent this accident from reproducing was to cool the water in the reservoir, however given the costs involved we decided to abandon this avenue for the time of this thesis and drive the coils at a maximum current of 35 A and not allowing them to stay above 50°C in which case we stopped the current to allow them to cool. However, during a long day of experiments, they would still warm the octagon chamber enough to create a constant increase of the Rb pressure which was a constant annoyance of our system but one we could work with. A solution we didn't get around to do is to build a second set of "slow" coils which could generate a strong magnetic field gradient of 10 G/cm for a weak current (< 1 A). These slow coils would be used whenever a fast field turnoff is not required.

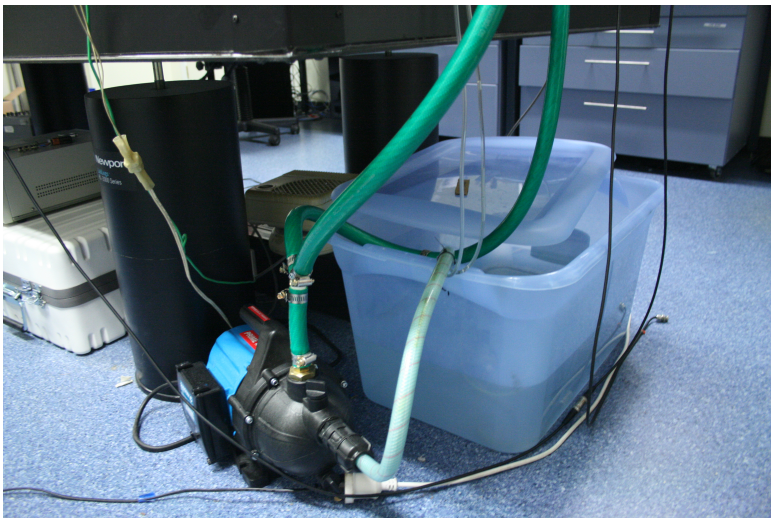

Figure IV.1: Photo of the 35 m of head waterpump and its connections to the water reservoir and up toward the coils.

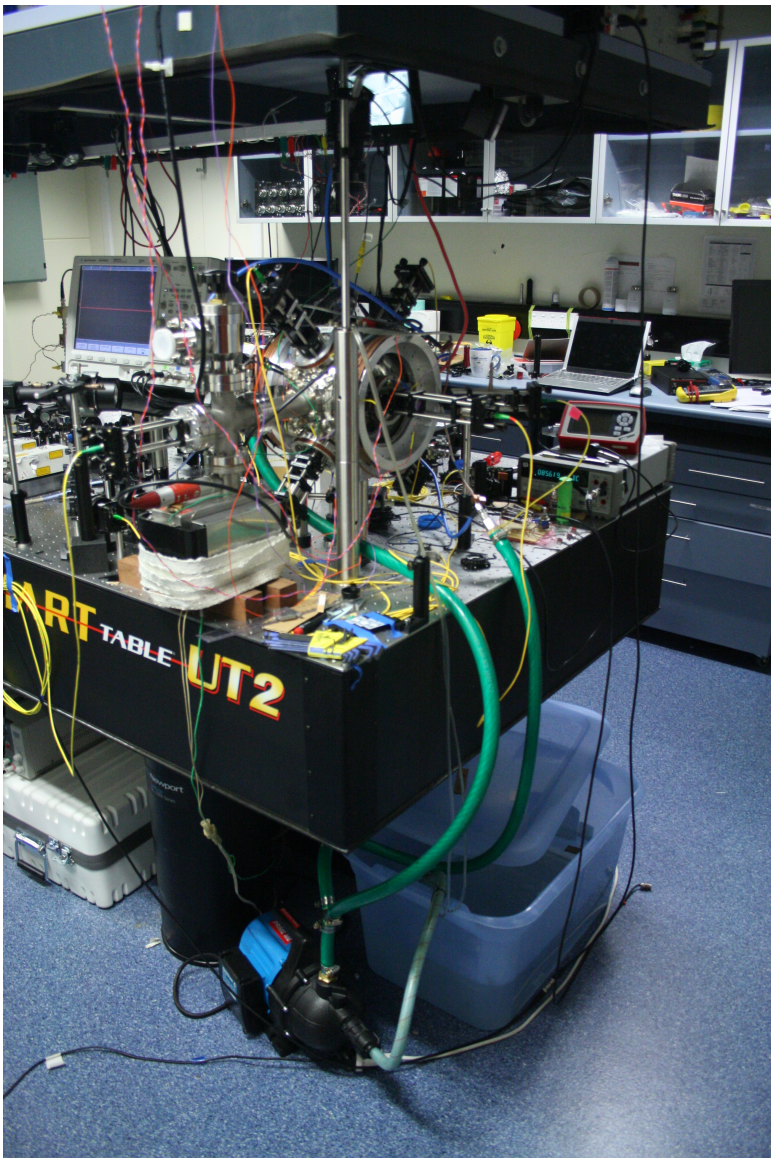

Figure IV.2: Photo of the lab setup showing the coils connected to the water pump on the input through the green tubes. At the output, 25 mm transparent tubes are used to return water to the water reservoir.